

ADSORPTION OF CO AND H₂ ON TRANSITION
METAL CLUSTERS, INSIGHTS FROM VIBRATIONAL
SPECTROSCOPY AND DENSITY FUNCTIONAL THEORY

ADSORPTION OF CO AND H₂ ON TRANSITION
METAL CLUSTERS, INSIGHTS FROM VIBRATIONAL
SPECTROSCOPY AND DENSITY FUNCTIONAL THEORY

ADSORPTIE VAN CO EN H₂ AAN OVERGANGSMETAAL CLUSTERS,
INZICHTEN VERKREGEN MET VIBRATIESPECTROSCOPIE EN DICHTHEIDS FUNCTIONAAL THEORIE

(met een samenvatting in het Nederlands)

PROEFSCHRIFT

ter verkrijging van de graad van doctor aan de Universiteit Utrecht
op gezag van de rector magnificus, prof. dr. J.C. Stoof, ingevolge het
besluit van het college voor promoties in het openbaar te verdedigen
op woensdag 8 oktober 2008 des middags te 4:15 uur

door

INGMAR SWART

geboren op 5 december 1980, te Opsterland

Promotor: Prof. dr. ir. B.M. Weckhuysen

Co-promotoren: Dr. F.M.F. de Groot
Dr. A. Fielicke

Het in dit proefschrift beschreven onderzoek werd mede mogelijk gemaakt met financiële steun van de Nederlandse Organisatie voor Wetenschappelijk Onderzoek (NWO).

"Equipped with his five senses, man explores the universe around him and calls the adventure Science"

Edwin Powell Hubble

Cover photograph taken by the author
ISBN: 978-90-393-4899-4

Contents

1	General Introduction	11
1.1	Catalysis	12
1.2	Cluster Science	15
1.3	Adsorption of H ₂ and CO on Transition Metals	17
1.4	Scope and Outline of this Thesis.....	20
2	Infrared Multiple Photon Dissociation Spectroscopy and Theoretical Concepts	23
2.1	Infrared Multiple Photon Dissociation Spectroscopy.....	24
2.2	Experimental.....	25
2.2.1	Free Electron Lasers.....	25
2.2.2	The Molecular Beam Machine.....	28
2.3	Theoretical methods	30
2.3.1	Basic Principles of Electronic Structure Theory.....	30
2.3.2	Density Functional Theory.....	33
2.3.3	Geometry Optimization	34
2.3.4	Vibrational Frequency Calculations.....	35
3	Adsorption of Multiple H₂ Molecules on 3d Transition Metal Clusters	39
3.1	Introduction.....	40
3.2	Experimental	42
3.3	Theoretical Method	43
3.4	Results and Discussion.....	44
3.4.1	Complex Composition	44
3.4.2	Scandium.....	46
3.4.3	Vanadium	49
3.4.4	Iron	51
3.4.5	Cobalt.....	53
3.4.6	Nickel	55
3.4.7	Comparison of Hydrogen Binding Geometries	58
3.5	Conclusions	60
4	Adsorption of a Single H₂ Molecule on Nickel Clusters	63
4.1	Introduction.....	64
4.2	Experimental.....	64
4.3	Theoretical Method.....	65
4.4	Results and Discussion.....	65
4.5	Conclusions	73

5	Effects of Co-adsorption of H₂ and CO on Cobalt Clusters	75
5.1	Introduction	76
5.2	Experimental	77
5.3	Results and Discussion	77
5.4	Conclusions	82
6	Effects of Co-adsorption of H₂ and CO on Vanadium Clusters	85
6.1	Introduction	86
6.2	Experimental	86
6.3	Theoretical Method	87
6.4	Results and Discussion	87
6.5	Conclusions	96
7	On the Effect of Charge on the Binding of CO in Rhodium Carbonyls: From Bridging to Terminal CO	99
7.1	Introduction	100
7.2	Theoretical Method	100
7.3	Results and Discussion	101
7.4	Conclusions	108
8	A Vibrational Spectroscopic and Density Functional Theory Investigation of Cationic Cobalt- and Nickel-Carbonyl Clusters in the Gas-Phase	111
8.1	Introduction	112
8.2	Theoretical Method	114
8.3	Results and Discussion	115
	8.3.1 Complex Compositions	115
	8.3.2 Vibrational Spectroscopy and DFT results	117
8.4	Conclusions	124
	Summary and Concluding Remarks	127
	Samenvatting	133
	Bibliography	137
	Appendix A	147
	Appendix B	163

Appendix C	171
List of Publications.....	183
Acknowledgements.....	185
About the author	187

Chapter 1

General Introduction

1.1 Catalysis

The term 'catalysis' was introduced by the Swedish chemist Jöns Jakob Berzelius in 1835 to characterize phenomena observed by a variety of chemists in the 18th and 19th century.^[1, 2] These included the enhanced conversion of starch into sugars in acidic environment and the observation that combustion of certain gasses is facilitated by metallic platinum. However, mankind has used catalytic processes for many millennia before the term 'catalysis' was introduced. Examples of catalytic processes that have been used for several thousand years include the conversion of wine into acetic acid by fermentation and the manufacturing of soap from fats and bases. Berzelius postulated that a 'catalytic force' is active during certain reactions. At that time, the theory of atoms and molecules had not yet been formulated and hence no molecular understanding of reaction rates was possible. The formulation of the theory of chemical equilibria by Jacobus Henricus van 't Hoff was instrumental in the development of a framework for catalyst development. This ultimately led to the modern day definition of a catalyst: A catalyst is a substance that is added to a reaction mixture to increase the rate of a chemical reaction without being consumed by the overall reaction.

Catalytic processes have a tremendous effect on modern day life. Nearly all transportation fuels and around 80% of all chemical products (e.g. plastics, fertilizers, etc.) that are manufactured today are produced in catalytic processes.^[3] Catalysts may be gasses, liquids or solids and can be classified according to their physical state or by the nature of the reactions that they catalyze. In homogeneous catalysis, the catalyst is molecularly dispersed in the same phase as the reactants, usually in the gas- or liquid-phase. In contrast, in heterogeneous catalysis, the catalyst and the reactants are in different phases. Usually the catalyst is a solid while the reactants are in the gas- or liquid-phase. Many heterogeneous catalysts consist of finely dispersed transition metal (oxide) nanoparticles on or in an inert support material. A schematic representation of such a catalyst is shown in Figure 1.1.

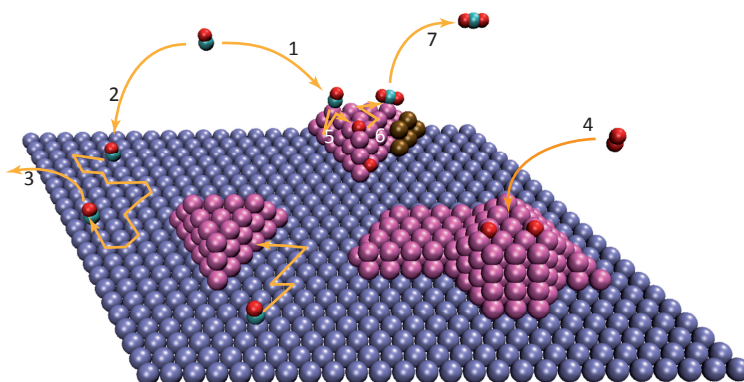


Figure 1.1. Schematic overview of a heterogeneously catalyzed reaction. The catalytically active particles are shown in pink, the support in blue and a promoter in ochre. Numbers indicate possible elementary reaction steps (see text).

The performance of a catalyst is greatly influenced by its composition. Not only the elemental composition, but also the size and shape of the nanoparticles determines how well a catalyst performs. Because of the small size of the nanoparticles, a significant fraction of the constituent atoms are located on the surface of the particles and many atoms are located on edges, rims, and step sites. Despite the small size, a variety of crystallographic facets might be present on a single particle. In many cases, different atomic coordination will result in different catalytic performance. Next to the metal particles, also the support material itself can influence the activity and/or the selectivity of the catalyst. The catalytic performance can often be greatly improved by adding other elements in small quantities. These so-called promoter materials can influence the structure and/or the electron density of the catalytically active particles. In fact, the charge state/electron density of a catalyst often plays a key role in determining the catalytic activity, as illustrated by the catalytic reactions in Table 1.1.

Table 1.1. Some catalytic reactions that demonstrate the importance of the charge state/electron density on catalytic performance. The δ^- and δ^+ indicate partially negatively and positively charged particles, respectively.

Catalytic Process	Catalyst	Proposed Active Site	Reference
Oxidation of CO	Au on metal oxides	$\text{Au}^{\delta^-} / \text{Au}^0 / \text{Au}^{\delta^+}$	[4-8]
	Pt / zeolite Y	Pt^{δ^-}	[9]
	Rh / $\text{Ce}_{0.7}\text{Zr}_{0.3}\text{O}_2$	Rh^{δ^+}	[10]
Hydrogenation of CO	Co / Mn / TiO_2	Co^{δ^+}	[11, 12]
	Cu / K	Cu^{δ^+}	[13]
	Pd / SiO_2	Pd^{δ^+}	[14]
Water gas shift reaction	Au / CeO_2	Au^{δ^+}	[15, 16]
Ammonia synthesis	Fe / K	Fe^{δ^-}	[17]
Hydrogenation of α, β unsaturated aldehydes	Cu / S / Al_2O_3	Cu^+	[18, 19]
	Au / S / ZnO	Au^+	[19, 20]

For many catalyzed reactions, the overall reaction actually consists of many elementary reaction steps. A typical sequence is shown in Figure 1.1. First, the reactants have to diffuse to the catalyst and subsequently adsorb. They can either adsorb directly onto the catalytically active particle (1) or on the support material (2) and diffuse toward the metal particle. Of course, species adsorbed on the surface can also desorb (3). When molecules bind to the catalyst, they can either bind molecularly (1) or they can dissociate upon adsorption (4). The reactants then have to find a site where the actual reaction occurs, possibly followed by other reactions (5), diffuse away (6) and the product(s) should finally desorb from the surface to regenerate the catalyst (7). Hence, many different variables influence the overall

catalytic reaction, making it complex to obtain detailed insight into, e.g. the sites where the actual reactions occur, and the precise sequence of the many possible elementary reaction steps.

To systematically improve existing catalysts and to develop new catalysts, fundamental knowledge about the elementary reaction steps that take place in catalyzed reactions is required. Such information can be obtained in several ways. One approach is to apply (advanced) analysis techniques on the catalytic process under investigation. The main advantage of this approach is that information on the actual catalytic mechanism is obtained. Despite the ever-increasing number of (spectroscopic) tools available to study catalysts under reaction conditions, the main difficulty remains the complexity of many heterogeneously catalyzed systems. In 1922 the American chemist Irving Langmuir phrased an alternative approach as follows^[21]:

'Most finely divided catalysts, such as platinum black or activated charcoal, etc, must have structures of great complexity, and it is probable that the atoms are attached to each other in the form of branching chains so that there are hardly any groups of as little as three or four atoms, which are as closely packed as they would be in the crystalline solid. In order to simplify our theoretical consideration of reactions at surfaces, let us confine our attention to reactions on plane surfaces. If the principles in this case are well understood, it should then be possible to extend the theory to the case of porous bodies.'

Hence, catalytic systems have been modeled by the interaction of molecules with well-defined single crystal surfaces in ultra high vacuum. This opens up the use of analysis techniques that cannot be used to study industrial catalysts under reaction conditions. These techniques can provide information that is otherwise inaccessible. Indeed, surface science studies have been instrumental for the elucidation of several catalytic reaction mechanisms, including the ammonia synthesis process over iron based catalysts and the conversion of CO and NO_x species in automotive exhaust gas catalysts.^[22] The importance of surface science studies has also been recognized by the awarding of Nobel prizes in Chemistry to Irving Langmuir (1932) and Gerhard Ertl (2007).

The simplicity of single crystal surfaces allows for in-depth studies of reaction mechanisms. However, it also implies that single crystal surfaces cannot account for all the distinct sites present in real catalysts, all of which may have different reactivity. Examples of such sites include certain coordinatively unsaturated atoms and atoms located on the particle-support interface. Hence, there exists a materials gap with on the one hand the complexity of a heterogeneous catalyst and on the other hand the simplicity of single crystal surfaces. Another limitation stems from the fact that many surface science studies are performed at low pressures, whereas the pressures used in actual catalytic reactions are often quite high. Since reaction mechanisms can depend on pressure, it is not a-priori clear whether or not a reaction mechanism derived from surface-science studies is also taking place on the actual catalyst. This is often referred to as the pressure gap. As should be clear from the

above, both surface science studies and catalytic studies have their advantages and disadvantages. Hence, they should be regarded as complementary approaches to obtain the desired information.

1.2 Cluster Science

In the early 1980's, the field of transition metal cluster science emerged with the development of molecular beams of clusters consisting of tens up to hundreds of metal atoms. Inherent of the small size, a significant fraction of the constituent atoms are located on the surface of the cluster, i.e. these atoms are coordinatively unsaturated. Heterogeneously catalyzed reactions often take place on such atoms. A good example is the oxidation of CO over a single coordinatively unsaturated ruthenium atom on a $\text{RuO}_2(1,1,0)$ surface.^[23] Furthermore, the atomic arrangements in clusters can be different compared to those in bulk materials, potentially resulting in a different coordination. Atomic coordination different from that of the bulk material is also found at surface defects (e.g. steps and kinks). Hence, next to single crystal surfaces, metal clusters in the gas-phase provide a complementary system to obtain fundamental insight into the reactions of molecules with solids. One of the main advantages of cluster studies is that experiments can be performed on well-defined systems. As a result, cluster studies are ideally suited to provide size dependent information on a variety of important phenomena, including adsorbate binding geometries, co-adsorption effects, and electron density/charge state dependent binding of adsorbates. Furthermore, by comparing clusters in the gas-phase with supported clusters of the same size, information on the effect of the support material can be obtained. Hence, cluster studies can provide useful information about phenomena relevant for heterogeneous catalysis although they suffer from the same materials and pressure gap as surface science studies.

Clusters, consisting of tens up to hundreds of atoms are intermediate between atoms/molecules and bulk. Clearly atoms/molecules and bulk materials have different properties and it can therefore be expected that interesting (and useful) phenomena might be observed for clusters. For particles larger than ~ 100 nm, the material properties are independent of particle size and such particles can therefore be regarded as small pieces of bulk material. Upon decreasing the particle size to the ~ 1 -100 nm range, several properties of materials scale as a function of size (see Figure 1.2). However, this does not necessarily apply to all properties. For example, it has been shown that the optimal Co particle size in Co based Fischer-Tropsch catalysts is 6-8 nm.^[24] Increasing or decreasing the particle size lowers the catalytic activity. When particles become even smaller, one enters the regime where quantum effects are dominant and properties like reactivity, magnetic moment and ionization potential do not smoothly scale with size anymore but critically depend on particle size. In this size range, dramatic changes can occur by adding or removing just a single atom (see Figure 1.2). Examples include the unique capability of Fe_4^+ to convert small hydrocarbons into benzene^[25, 26] and the large changes in reactivity

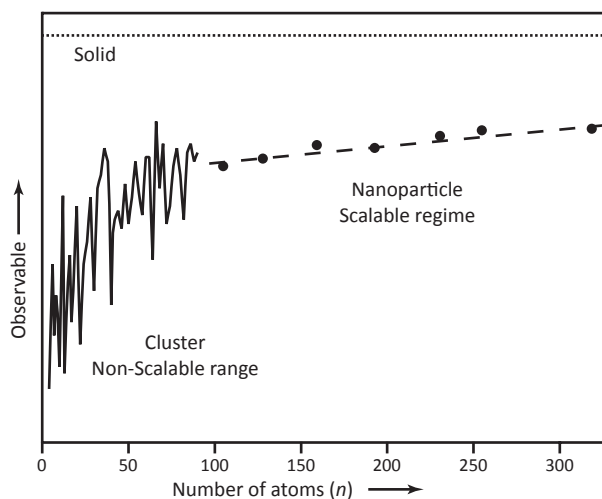


Figure 1.2. The value of an observable depends on the size of the particle. The solid line indicates the quantum regime, the dashed line the scalable size range and the dotted line represents the value of the observable for bulk material.

of cationic iron, cobalt and nickel clusters toward hydrogen as a function of cluster size.^[27] Another example is the size dependent hydrogenation of toluene by iridium clusters.^[28]

One of the central questions in cluster science is therefore ‘How large must a cluster be before its properties resemble those of the bulk material?’ It has become clear that the approach to bulk behavior critically depends on the property and on elemental composition. For example, binding energies rapidly converge as a function of size, while ionization potentials and electron affinities do not. This is consistent with the idea that chemical bonds are mainly local phenomena, whereas ionization potentials and electron affinities are not.

Another advantage of cluster studies is that due to their small size, cluster complexes can be modeled directly by both electronic structure methods and dynamical calculations. Hence, there has been an intimate interplay between experimental and theoretical investigations since the early days of cluster science. On the one hand, experimental studies have benefited enormously from the advances in theoretical chemistry and on the other hand qualitative experimental results, e.g. thermochemistry, photoelectron and vibrational spectroscopy, provide benchmark data for theoretical models.

A comparison between catalytic, surface science and cluster science with respect to several different properties is given in Table 1.2. Cluster- and surface science studies should be regarded as complementary approaches to obtain information about phenomena relevant for heterogeneous catalysis.

Table 1.2. Comparison between catalytic, surface science and cluster science studies.

Property	Supported Nanoparticles	Surface Science	Cluster Science
Structural control	medium	large	large
Electronic control	medium	medium	large
Temperature range ¹	4 K – ~1000 K	4 K – ~1000 K	0.4 K - ~500 K
Pressure range ¹	vacuum – ~30 bar	vacuum – ~1 bar	vacuum
Matrix	support, reactants	none	none or support
Number of experimental techniques ²	medium	large	small
DFT Calculations	still difficult	possible	possible
other:	'real' system	model system	model system, quantum size effects

¹ Pressure and temperature might place restrictions on the number of experimental techniques that are available.

² Note that this does not imply that the same techniques can be applied in the study of supported nanoparticles and single crystal surfaces.

1.3 Adsorption of H₂ and CO on Transition Metals

Adsorption of diatomic molecules like H₂ and CO on transition metals is of tremendous importance for several processes and materials, including various catalytic reactions, hydrogen storage materials and metallurgy. In addition, co-adsorption of H₂ and CO is of significant interest due to its relevance to the Fischer-Tropsch process, which is a process to convert mixtures of these two molecules to long chain hydrocarbons.^[29, 30] Co-adsorption of these molecules is furthermore relevant in PrOx (Preferential Oxidation) catalysis. There, the main goal is to selectively oxidize CO in H₂-rich streams to obtain sufficiently pure H₂ streams for fuel cell applications.^[31, 32] As a consequence, adsorption of these molecules on extended metal surfaces and on metal nanoparticles has been studied extensively.^[33-37] Here only a brief introduction is given, more elaborate discussions can be found in the corresponding chapters.

A molecule or atom adsorbed on a metal can be bound in different sites. Possible binding sites are schematically depicted in Figure 1.3. In general, atomic adsorbates (with the exception of the noble gases) have a preference for high coordination sites, while molecularly bound species can also be bound in atop or bridging sites. For instance, molecularly bound CO has been observed in atop, bridge, face, and hollow sites, while atomic carbon, oxygen, and hydrogen atoms are nearly always threefold (or higher) coordinated. Atop bound hydrogen atoms are rarely observed. Adsorbate binding sites can vary with coverage, temperature, pressure, and from one crystallographic plane to another. Examples of element specific adsorption sites for molecularly bound CO and atomic hydrogen are given in Figure 1.4.^[33, 36, 38-54]

The model that is most widely invoked to describe the binding of carbon monoxide on transition metals, is that of Dewar, Chatt, and Duncanson.^[55, 56] In this model, only

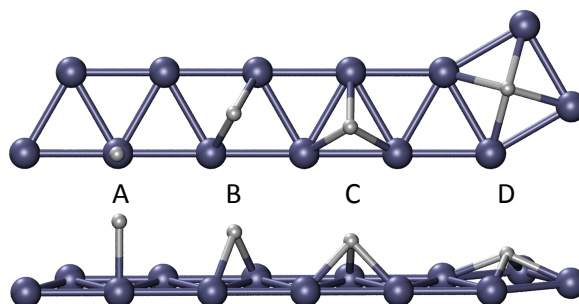


Figure 1.3. Schematic representation of different adsorbate binding sites. The top panel shows a top view, while the bottom panel gives the corresponding side view. There exist several names for the same adsorbate binding site that can be used interchangeably: (A) atop or linearly bound, (B) two-fold coordinated, μ_2 -coordinated, or bridge bound, (C) three-fold coordinated, μ_3 -coordinated, or face bound and (D) four-fold coordinated or μ_4 -coordinated.

Sc	Ti	V	Cr	Mn	Fe	Co	Ni	Cu	Zn
						●	●	●	
Y	Zr	Nb	Mo	Tc	Ru	Rh	Pd	Ag	Cd
					●	●	▲	▲	
Lu	Hf	Ta	W	Re	Os	Ir	Pt	Au	Hg
		●		●		●	●	■	

linearly coordinated hydrogen ● atop bound CO
 bridge bound hydrogen ■ bridge bound CO
 face bound hydrogen ▲ face bound CO
 four-fold coordinated hydrogen ■ Four-fold coordinated CO

Figure 1.4. d-block of the periodic table. Possible adsorption sites of carbon monoxide and atomic hydrogen on several elements are indicated. At room temperature, carbon monoxide binds dissociatively to all elements on the left of the red line, whereas it binds molecularly to the elements on the right of the red line.

the frontier-orbitals of the CO molecule and the metal are considered.[§] A schematic picture of the bonding of CO and H₂ is shown in Figure 1.5. As a CO molecule approaches a metal, a σ bond can be formed by the partial donation of a pair of electrons from the 5 σ orbital of the CO, which is largely localized on the carbon atom, to an orbital of appropriate symmetry on the metal atom. The M–CO bond is stabilized by π -back bonding from filled metal *d*-orbitals into an empty 2 π^* orbital of the CO ligand. This back-donation leads to an increased occupation of the 2 π^* orbital, which is anti-bonding with respect to the C–O bond. The adsorption of CO on a transition metal will therefore result in a significant weakening of the C–O bond. If this back-donation is sufficiently large, the CO molecule can dissociate.

[§] It has recently been shown that next to the frontier orbitals, additional orbitals are required to correctly describe the binding of CO on transition metals.^[57, 58]

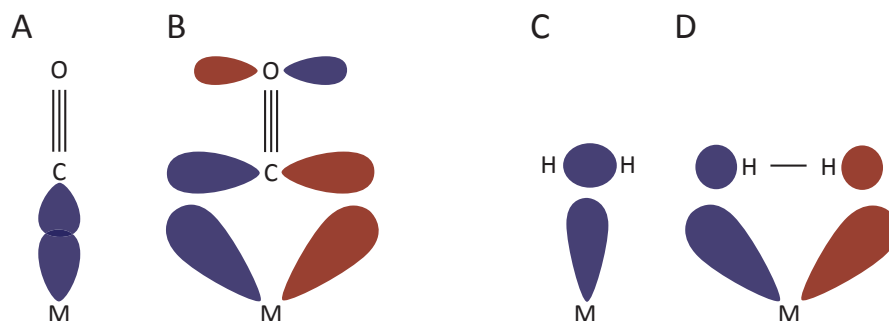


Figure 1.5. Schematic of the Frontier orbital picture of the bonding of CO (A, B) and H_2 (C, D) to a metal atom. In case of CO, a σ bond is formed by hybridization of the occupied 5σ orbital of the CO with a metal orbital of appropriate symmetry (A). The M–CO bond is stabilized by hybridization of an occupied metal d orbital with the anti-bonding $2\pi^*$ orbital of the CO molecule (B). In case of H_2 , a σ bond can be formed by hybridization of the occupied σ orbital of the H_2 molecule and a metal orbital of appropriate symmetry (C). Back-donation from an occupied metal d orbital to the anti-bonding σ^* orbital of H_2 leads to the breaking of the H–H bond over nanoparticles and extended surfaces of transition metals.

Experimentally it has been determined that CO dissociates on all transition metals to the left of the diagonal cobalt-ruthenium-rhenium at room temperature and that it binds molecularly to all metals to the right of this diagonal (see Figure 1.4). At elevated temperatures CO also dissociates on cobalt, nickel and ruthenium and for example, supported metal particles of these elements can be used as catalysts in CO hydrogenation reactions.

The principles of donation and back-donation also play a role in the adsorption of H_2 on transition metals. In contrast to CO, an M– H_2 bond can be formed when the hydrogen molecule approaches the metal with its intra-molecular axis parallel to the surface. A σ bond is formed between the occupied σ molecular orbital of H_2 and a metal orbital of appropriate symmetry. Back-donation from an occupied d -orbital of the metal into the anti-bonding σ^* orbital of the H_2 molecule weakens the H–H bond. On nanoparticles and extended surfaces of transition metals, the amount of back-donation is so large that a H_2 molecule dissociates upon adsorption. In the final state, the hydrogen atoms are nearly always adsorbed in high coordination sites (see Figure 1.4). Molecular H_2 coordinated to a transition metal have been found in certain organometallic complexes,^[59] on edges of certain single crystal planes of Ni on which all adsorption sites for atomic hydrogen are occupied,^[60] and on a Pd (210) surface.^[61]

1.4 Scope and Outline of this Thesis

A significant number of studies have been performed on H₂ and CO adsorption on metal clusters. These studies have provided a wealth of information on, e.g., cluster reactivity, ionization potentials and adsorbate-cluster bond energies. To fully understand the interaction between adsorbates and metal clusters, structural information is required. However, direct structural information on adsorbate binding geometries is scarce and the effects of co-adsorption of both H₂ and CO on metal clusters have remained unexplored.

The aim of the research described in this thesis was to obtain fundamental knowledge on the interaction of H₂ and/or CO with charged transition metal clusters. To this end vibrational spectroscopic studies, complemented with quantum chemical calculations have been performed. It has been shown that this approach can provide direct, size and charge state dependent information on cluster geometries.^[62, 63]

The employed methodology is introduced in chapter 2, together with a description of the experimental setup. In the second part of that chapter, an introduction into the theoretical methods that are used is presented. The research described in this thesis can be divided into three main topics. Chapters 3 and 4 address the adsorption of hydrogen on 3d transition metal clusters. Hydrogen is known to dissociatively chemisorb in high coordination sites on extended surfaces of all 3d transition metals but it is not clear how hydrogen will bind to small metal clusters. Therefore, hydrogen chemisorption on a variety of transition metal clusters was investigated. Particular emphasis was given to hydrogen chemisorption on nickel clusters, as this element plays an important role in hydrogenation catalysis. In chapter 3, the binding of multiple hydrogen molecules on scandium, vanadium, iron, cobalt, and nickel clusters is studied, while in chapter 4 the adsorption of a single hydrogen molecule on nickel clusters is studied.

In the second part of the thesis, the effects of co-adsorption of hydrogen and carbon monoxide on transition metal clusters are studied. Simultaneous adsorption of these two species occurs for instance in CO hydrogenation reactions. Despite its relevance to various catalytic processes, co-adsorption of H₂ and CO on transition metal clusters has remained unexplored. As a case study, we have investigated the effects of co-adsorption on a late (cobalt, chapter 5) and an early (vanadium, chapter 6) transition metal.

The final research topic regards the influence of charge on the binding of CO in saturated carbonyl complexes. Although the charge state/electron density of a particle is of paramount importance for its catalytic performance, there exist only few studies on the effects of charge on the binding geometries of adsorbates on transition metal clusters. In chapter 7, the case of rhodium carbonyl complexes is presented, while in chapter 8 the binding of CO in cobalt and nickel carbonyls is discussed. The thesis ends with a summary and some concluding remarks.

Chapter 2

Infrared Multiple Photon Dissociation Spectroscopy and Theoretical Concepts

2.1 Infrared Multiple Photon Dissociation Spectroscopy

Direct absorption measurements on transition metal cluster complexes in the gas-phase are difficult due to the low particle densities. Alternative, indirect mass spectrometry based techniques to measure vibrational spectra of such species have been developed. IR Multiple Photon Dissociation (IR-MPD) spectroscopy is one of these techniques. The basic idea behind IR-MPD is that the IR absorption spectrum can be reconstructed by recording the photo induced fragmentation yield as a function of photon frequency. For strongly bound complexes like M_nH_m and M_nCO_m , the amount of energy required to break a covalent bond, and hence induce fragmentation, is on the order of 1-6 eV. This implies that for such systems, many IR photons need to be absorbed, hence the name IR-multiple photon dissociation spectroscopy. Below the principles behind IR-MPD spectroscopy will be briefly discussed. More detailed information can be found elsewhere.^[64-66]

All vibrational modes have a certain degree of anharmonicity. Therefore, absorption of many monochromatic IR photons cannot take place in a single vibrational ladder. This is often referred to as the 'anharmonicity bottleneck'.^[67] Anharmonicities also provide a coupling mechanism between the different vibrational modes of a cluster complex. Because of this coupling, the energy of an absorbed photon can be transferred to the heat bath of other vibrational modes. This process is known as internal vibrational redistribution (IVR). As a result of the IVR, the vibrational lifetime is shortened and consequently the absorption lines are broadened. The IVR rate depends on the vibrational density of states and on the internal energy of the complex. At low internal energies IVR is slow and photon absorption can be limited by anharmonicities. As the internal energy of the complex increases by the absorption of photons, the IVR rate increases and rapid sequential absorption of multiple photons on the same transition can take place, leading to an ever-increasing internal energy. In this regime, typical timescales associated with intramolecular relaxation are on the order of 10^{-11} - 10^{-12} s.

In the low-pressure (collision free) environment of the molecular beam, the highly excited complexes can cool by emitting photons, electrons or by fragmentation. In principle, all three processes are possible and which process dominates depends on the internal energy. Radiative cooling is described by the Stefan-Boltzmann law, hence the emission of photons scales as the internal energy to the fourth power. In contrast, the rate constants for electron emission and fragmentation scale exponentially with internal energy. Therefore, at low internal energy radiative cooling will be the dominant relaxation process while at high internal energy, fragmentation or electron emission will dominate. For most molecules and cluster complexes, typical fragmentation barriers are lower than typical ionization potentials and consequently most molecules and clusters fragment rather than ionize. For the systems described in this Ph.D. thesis, fragmentation was observed to be the dominant relaxation process.

To perform IR-MPD studies on transition metal complexes in the gas-phase, the radiation source has to meet two key requirements. The first is that the source has to be tunable over a broad spectral range. In general, this is true for most spectroscopic techniques. Second, the source has to produce radiation with a high fluence on the microsecond time scale. Cluster complexes in a molecular beam typically travel with velocities of several hundred meters per second. With a focal depth on the order of several hundred micrometers to millimeters, the interaction time between the radiation and the complexes is on the order of microseconds. For IR-MPD experiments, where sequential absorption of multiple photons is required, a high fluence on the microsecond time scale is therefore crucial. IR-MPD experiments on gas-phase species were initially performed using line-tunable CO₂ lasers.^[68-70] However, only a limited spectral range (from ~900-1100 cm⁻¹) can be accessed using these lasers. Appropriately designed 'free electron lasers' (FELs) can cover a much broader spectral range (see below) and are currently the source of choice for IR-MPD studies.

Note that the above implies that an IR-MPD spectrum of a compound is not necessarily directly comparable to the linear absorption spectrum of the same compound. In general, absorption peaks in an IR-MPD spectrum are shifted to lower frequencies as compared to the linear absorption spectrum due to anharmonicities. Furthermore, relative intensities cannot be compared directly as the fragmentation yield depends in a highly non-linear way on the laser fluence. Peak intensities can therefore only be compared qualitatively. Nevertheless, it has been shown^[65, 66] that in many cases the differences are quite small and that IR multiple photon absorption spectra provide reliable information on the vibrational modes of the investigated systems. Using the Free Electron Laser for Infrared eXperiments, FELIX, IR multiple photon excitation experiments have been performed on numerous transition metal containing species, including pure^[62, 63, 71-74] and doped metal clusters, metal-CO complexes,^[75-79] metal oxide clusters,^[80-85] and metal carbides.^[86-89]

2.2 Experimental

2.2.1 Free Electron Lasers

All experiments described in this Ph.D. thesis were performed on a molecular beam machine coupled to a beam-line of the 'Free Electron Laser for Infrared eXperiments'^[90], FELIX, which is based at the FOM Institute for Plasma Physics, in Nieuwegein, the Netherlands. An excellent book on FEL physics is available^[91] and only a brief introduction will be given here.

A schematic layout of the central component of an FEL is depicted in Figure 2.1. A pulsed beam of electrons traveling at relativistic velocities is injected into a periodic magnetic structure, called an undulator, which is placed inside an optical cavity. The undulator consists of N pairs of magnets with alternating polarity and periodicity λ_u . The resulting magnetic field is perpendicular to the propagation direction of the electrons. The Lorentz force exerted on the electrons causes them

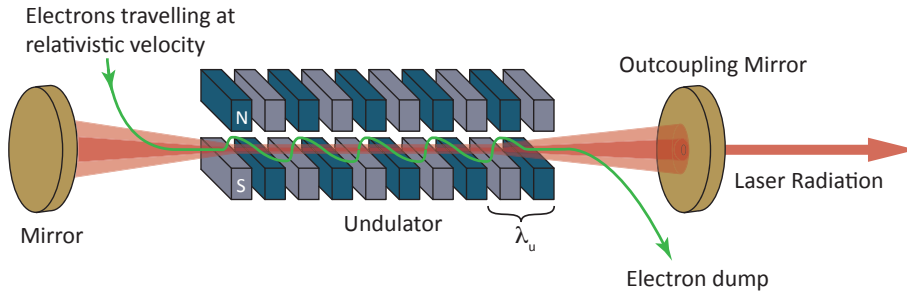


Figure 2.1. Schematic layout of an FEL undulator and optical cavity.

to undergo a sinusoidal wiggling motion while traversing the undulator. At each change in direction the electron emit radiation with a frequency that is given by the ratio of the velocity of the electrons to the length of one period of the path traveled by the electrons. As the photons travel in a straight line at the speed of light while the electrons travel slower in a sinusoidal path, the electrons initially do not emit coherently. The high velocity of the electrons results in a strong Lorentz contraction ($1/\gamma$) and Doppler shift ($1/2\gamma$) of the wavelength of the radiation that is emitted in the forward direction. Assuming that the Lorentz factor is large, the wavelength of the spontaneous emission is given by:

$$\lambda \propto \frac{\lambda_u}{2\gamma^2} (1 + K^2) \quad 2.1$$

The variable K is a dimensionless parameter that depends on the strength of the magnetic field in the undulator. It usually has a value close to 1. For FELIX the electron energy ranges from ~ 15 MeV to ~ 50 MeV, which results in a γ value of 20-100. Combined with an undulator periodicity of 65 mm, this brings the wavelength of the emitted radiation into the micrometer range.

The intensity of the spontaneously emitted radiation is normally low. This is a consequence of the fact that the length of the electron bunch is much larger than the wavelength of the emitted radiation and the electrons therefore do not emit coherently. However, the electrons in an undulator can be made to emit coherently. The electric field of the moving electrons can couple to the radiation field in the optical cavity and cause a net transfer of electron kinetic energy to the radiation field or visa versa, depending on the relative phases of the current and field. This energy transfer causes a velocity modulation. Electrons that are in phase with the radiation field are retarded and electrons that are out of phase are accelerated. The relative changes in velocity result in a longitudinal density modulation of the electrons, which is referred to as 'micro-bunching'. With complete micro bunching all electrons radiate coherently and the radiated power becomes proportional to N^2 and is thus greatly increased with respect to the spontaneously emitted radiation. Typically the output power resulting from stimulated emission is 10^7 - 10^8 times higher than that from spontaneous emission.

The temporal structure of the emitted radiation is determined by the characteristics of the electron beam. The linear radio frequency accelerators in use at the FELIX facility typically generate 7 μs long macro pulses with a repetition rate of up to 10 Hz. Each macro pulse consists of a train of micro pulses, whose duration can be varied from ~ 300 fs to several ps, with a repetition rate of either 25 MHz or 1 GHz. The bandwidth of the micro pulses is near-transform limited. Typical values range from $<0.5\%$ to several percent full width at half maximum of the central wavelength. Macro pulse energies in the 1 GHz mode of operation are 30-100 mJ. The wavelength of the output radiation can be changed by changing the electron kinetic energy or the magnetic field strength in the undulator. FELIX covers the spectral range from 2300 cm^{-1} to 40 cm^{-1} on the fundamental. It is also possible to extend the tuning range to 3700 cm^{-1} by optimizing FELIX to lase on the third harmonic of the radiation.

The temporal structure and fluence of the radiation produced combined with the spectral characteristics, make FELIX a uniquely suitable light source to perform IR-MPD studies on a large variety of (transition) metal clusters, including transition metal hydride and transition metal carbonyl complexes. Typical vibrational frequencies associated with metal hydride and metal carbonyl complexes are shown in Figure 2.2. Two- and three-fold coordinated hydrogen atoms give rise to vibrational modes in the $500\text{-}1500\text{ cm}^{-1}$ range. Metal-dihydrogen stretch vibrations associated with molecularly bound H_2 are located in the narrow range around 700 cm^{-1} , while the corresponding internal H-H stretch vibration lies around 3400 cm^{-1} . The characteristic C=O stretch vibration of CO bound to transition metal compounds is found between 1700 cm^{-1} and 2150 cm^{-1} , depending on binding geometry and the charge state of the metal cluster. The corresponding M-CO vibrational modes lie below 650 cm^{-1} .

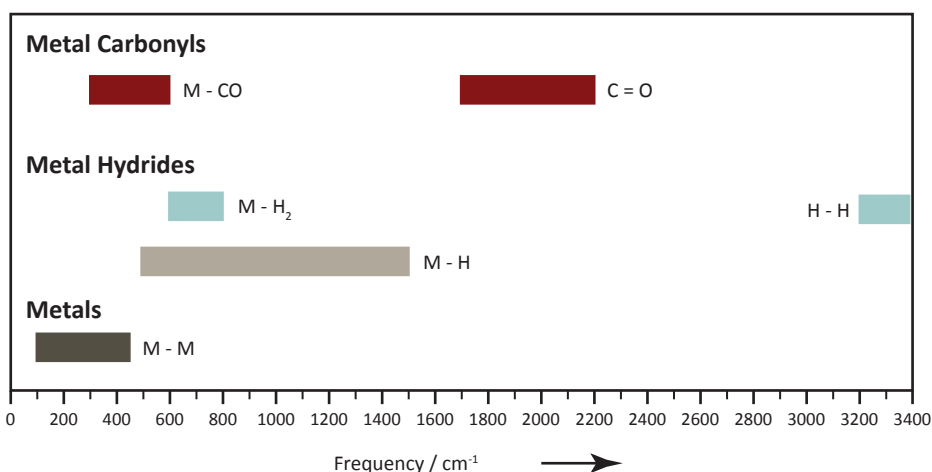


Figure 2.2. Overview of the spectral ranges of fundamental vibrational modes associated with transition metal containing hydride and carbonyl clusters.

2.2.2 The Molecular Beam Machine

A schematic of the molecular beam machine that was used for the experiments described in this Ph.D. thesis is shown in Figure 2.3.^[66, 75] The 2nd harmonic output of an Nd:YAG laser is focused onto a metal target rod, creating a plasma above the surface of the rod. The rod is continuously rotated and translated to expose a fresh spot on the surface. The plasma is quenched by a pulse of He gas delivered by a pulsed valve, resulting in clustering and thermalization of the species in the plasma. Neutral, anionic and cationic clusters are produced in this process. Downstream of the cluster source the clusters enter a flow reactor channel where they can react with a gas of interest that is injected by a second pulsed valve. The extent of complex formation can be controlled by adjusting the gas flow through the second pulsed valve. Upon increasing the partial pressure in the reactor channel, sequential molecules are adsorbed on the clusters. At one point, the complexes do not bind additional molecules when the reactant content is increased further. At this point saturation coverage has been reached. After the reactor channel, the molecular beam is expanded into vacuum and shaped by a skimmer and an aperture. A counter-propagating pulsed IR beam delivered by FELIX is focused on the aperture to ensure that the full cross-section of the molecular beam is exposed to the IR radiation. The FELIX beam is timed in such a way that the cluster beam is irradiated when it is near the focus. When the radiation is resonant with an IR-allowed transition of the cluster complex, sequential absorption of single photons can take place, leading to fragmentation of the complex as described in section 2.1. After passing the aperture, the molecular beam enters the extraction region of a reflectron time-of-flight mass spectrometer. The extraction pulse is timed such that spectra are recorded of a part of the cluster distribution that is exposed to a macro-pulse of IR radiation (lower trace Figure 2.4). The entire setup runs at a frequency of 10 Hz. FELIX runs with a macro pulse repetition rate of 5 Hz. Mass spectra of a reference distribution that is not exposed to IR radiation are recorded on alternate shots (upper trace Figure 2.4) to compensate for long-term fluctuations in cluster intensity. IR-depletion spectra are measured by recording the ratio of the ion intensities as a function of photon frequency. Because detection is mass selective, the vibrational spectra of different cluster complexes can be measured simultaneously.

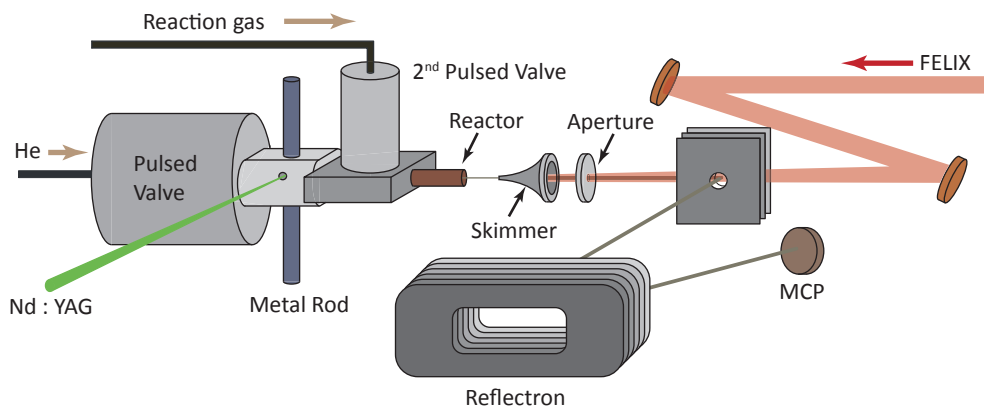


Figure 2.3. Schematic of the molecular beam setup used to perform IR-MPD studies of cluster complexes.

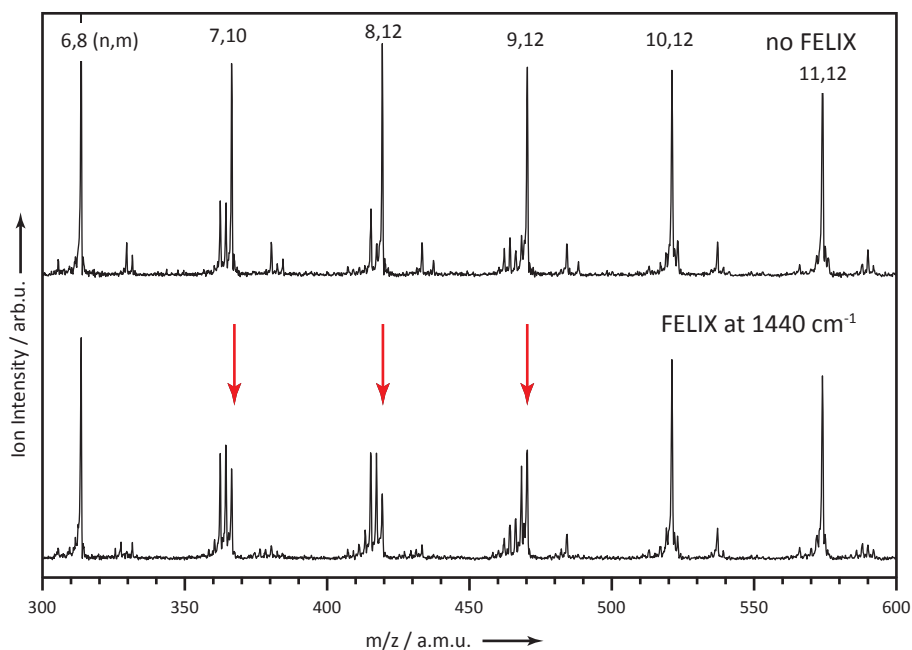


Figure 2.4. Mass spectra of fully hydrogen saturated $V_nH_m^+$ complexes with mass/charge ratios between 300 and 600 a.m.u. The top spectrum shows part of the mass distribution of cluster complexes in the molecular beam where 7,10 indicates the $V_7H_{10}^+$ complex, etc. The lower mass spectrum shows the changed mass distribution upon overlap of the molecular beam with a beam of IR photons with a frequency of 1440 cm^{-1} . The arrows indicate photo-induced fragmentation.

2.3 Theoretical methods

To aid in the interpretation of the results from the spectroscopic studies, the experimental work is complemented by quantum chemical calculations. Primarily cluster complex geometries and the corresponding vibrational spectra are calculated. By comparing the calculated spectra of several isomers with the experimentally measured spectrum, information on complex geometries is obtained. To better understand the theoretical results described in the following chapters, the fundamental principles of electronic structure theory, density functional theory, geometry optimizations and harmonic frequency calculations are briefly discussed.^[92-94] All of the calculation described in this Ph.D. thesis have been performed using the commercially available TURBOMOLE package, except where noted otherwise.^[95]

2.3.1 Basic Principles of Electronic Structure Theory

The basis of quantum mechanics is equation 2.2, which was introduced in 1926 and is known as the time-dependent Schrödinger equation^[96]:

$$\hat{H}(R, r, t)\psi(R, r, t) = -i\hbar \frac{\partial}{\partial t} \psi(R, r, t) \quad 2.2$$

In this equation $\hat{H}(R, r, t)$ is the Hamilton, or energy operator, which depends on the nuclear and electron coordinates (R and r , respectively) and on the time, is the wavefunction that describes the system of interest. The symbol \hbar is Plank's constant divided by 2π . By solving equation 2.2, in principle all information on the system can be obtained. However, no analytic solutions to equation 2.2 are known for systems containing two or more interacting electrons. Hence, for all practical calculations on molecules and clusters, approximate solutions have to be generated.

For many systems of interest, the Hamilton operator does not depend on time. In these cases, equation 2.2 simplifies to the time-independent Schrödinger equation (equation 2.3).

$$\hat{H}(R, r)\psi(R, r) = E\psi(R, r) \quad 2.3$$

where E represents the energy of the system. The non-relativistic Hamiltonian operator for a many body system, like a molecule or cluster, is given by:

$$\hat{H}(R, r) = -\frac{\hbar^2}{2} \sum_A \frac{1}{m_A} \nabla_A^2 - \frac{\hbar^2}{2} \sum_i \frac{1}{m_e} \nabla_i^2 - \frac{1}{4\pi\epsilon_0} \left(\sum_A \sum_i \frac{Z_A e^2}{r_{Ai}} - \sum_i \sum_{j>i} \frac{e^2}{r_{ij}} - \sum_A \sum_{B>A} \frac{Z_A Z_B}{r_{AB}} \right) \quad 2.4$$

where A and B are nuclear indices, i and j electron indices, and m_a and m_e are the nuclear and electron mass, respectively. The symbols e , Z , and r , respectively denote the elementary charge, the nuclear-charge, and the inter-particle distances. The first two terms on the right hand side of equation 2.4 describe the kinetic energy contributions to the total energy due to the nuclei and electrons, respectively. The attractive Coulomb interaction between nuclei and electrons gives rise to the third term. The last two terms account for the repulsive Coulomb interactions between electrons and nuclei, respectively. In equation 2.4 relativistic effects are ignored, i.e. this Hamilton operator does not account for the velocity dependence of the mass of the particles, retardation effects, and spin-orbit coupling.

Solutions of the time-independent Schrödinger equation (equation 2.3) almost always make use of the Born-Oppenheimer approximation.^[97, 98] The justification of this approximation stems from the fact that nuclei move much slower than electrons and hence in first order, the electron motion only depends on the nuclear positions and not their movement. In turn, the nuclei 'see' only a smeared out potential due to the much faster moving electrons. Applying this approximation leads to a separate treatment of the electrons and nuclei:

$$\hat{H}_e(R, r) \psi_n(R, r) = E_e(R) \psi_n(R, r) \quad 2.5 \text{ a}$$

$$\hat{H}_n(R) \psi_n(R) = E_n \psi_n(R) \quad 2.5 \text{ b}$$

In the Born-Oppenheimer picture, the nuclei move on a potential energy surface (PES), $E_e(R)$, which is a solution of the electronic Schrödinger equation (equation 2.5a). Solving the nuclear Schrödinger equation (equation 2.5b), leads to energy levels for molecular vibrations (see section 2.3.4). Although the Born-Oppenheimer approximation leads to approximate energies, the errors that are introduced are typically of the order of the electron/nucleus mass ratio ($\approx 10^{-3}$). Hence, as long as the electron wavefunction, $\psi_n(R, r)$, does not change significantly with respect to small distortions of the nuclear coordinates, the Born-Oppenheimer approximation is a good approximation.

As already outlined above, no analytic solutions of the Schrödinger equation exist for molecules and clusters. However, approximate solutions can be generated using the variational principle, which states that an approximate wave function gives rise to an energy higher than, or equal to the exact energy. By minimizing the energy, a good approximation of the ground state of a system can be obtained.

To be acceptable, the wavefunction has to fulfill certain criteria. One of these is that for protons, neutrons and electrons, which are all fermions, the total electronic wave function must be antisymmetric with respect to the interchange of two electron coordinates. The Pauli exclusion principle^[99], which states that no two particles can be in the exact same state, is a direct consequence of this anti-symmetry requirement. The anti-symmetry requirement can be fulfilled by writing the wave function in the form of a Slater determinant.^[100] In such a determinant the columns are single

electron wave functions, orbitals, and the electron coordinates are given along the rows. For the general case of an N electron system, the Slater determinant is given by:

$$\psi_e = \frac{1}{\sqrt{N!}} \begin{vmatrix} \varphi_1(1) & \varphi_2(1) & \dots & \varphi_N(1) \\ \varphi_1(2) & \varphi_2(2) & \dots & \varphi_N(2) \\ \dots & \dots & \dots & \dots \\ \varphi_1(N) & \dots & \dots & \varphi_N(N) \end{vmatrix} \quad 2.6$$

The combination of a single determinant wave function and the variational principle leads to the Hartree-Fock model.^[101-103] In Hartree-Fock (HF) theory, the electron - electron interactions are treated in an average manner and it is therefore also referred to as a mean field method. In a self-consistent field HF calculation, the energy of the system at hand can be calculated using the Hartree-Fock equations. Starting from a trial wavefunction, the energy can be computed. This wavefunction is then used to obtain a new wavefunction, which is again used to evaluate the energy, etc. This iterative procedure continues until a self-consistent solution is obtained.

By definition, single determinant methods like HF do not account for electron correlation. Improving upon HF by expressing the wavefunction in multiple determinants leads to methods like Configuration Interaction and Coupled Cluster.^[104] However, whereas these methods can provide more accurate results, they are computationally so demanding that they become prohibitively expensive for systems containing multiple transition metal atoms.

In practical calculations, the molecular orbitals are described by a predefined set of functions, the so-called basis set. Any type of function can be used, including plane-waves, exponential functions and Gaussian functions. Plane-wave basis sets are used for systems where periodic boundary conditions can be applied, while Gaussian basis sets are ubiquitous in calculations on finite systems like molecules and clusters. All calculations described in this Ph.D. thesis were performed using Gaussian type basis sets and hence the discussion below applies to this type of basis set. In the limit of an infinite number of basis functions, the molecular orbitals are described exactly. However, the computational cost formally scales as the fourth power of the number of basis functions. In practical calculations, the number of basis functions therefore has to be limited. The smallest set of functions required to contain all the electrons, is referred to as the minimum basis set. For example, a minimum basis set for C consists of two s-functions (1s and 2s) and one set of p-functions (2p_x, 2p_y, and 2p_z). A basis set with double the number of functions is called a Double Zeta (DZ) basis. Equivalently, the Triple Zeta (TZ) and Quadruple Zeta (QZ) basis sets have three and four times the minimum number of function sets required. Because the core electrons do not significantly influence the chemical bonding, only the number of valence orbitals is increased in practical calculations. Such basis sets are called split valence basis sets. In addition to increasing the number

of basis functions of the same type, also polarization functions (P) can be added to a basis set. In general, polarization functions are higher angular momentum functions, required for describing charge polarization effects and electron-electron correlation effects. As an example, s-functions can be polarized by adding p-functions, which in turn can be polarized by d-functions, etc.

2.3.2 Density Functional Theory

As was shown in a landmark paper by Hohenberg and Kohn,^[105] the ground-state electronic energy is determined by the electron density, $\rho(r)$ and that the energy can be expressed as a functional of the electron density. Hence, by knowing $\rho(r)$ all properties of interest can be computed. This forms the basis of a complementary approach to electronic structure theory: Density Functional Theory (DFT). Instead of the many-particle wavefunction, the electron density distribution function is the fundamental variable in DFT. Shortly after the first paper, Kohn and Sham introduced a variational method to minimize the density dependent energy, $E(\rho(r))$,^[106] which can be expressed as:

$$E[\rho] = T_0[\rho] + \int (V_{ext}(r) + V_{ee}(r))\rho(r)dr + E_{xc}[\rho] \quad 2.7$$

In this equation $T_0[\rho]$ is the kinetic energy of a non-interacting electron gas with the same density as the real system, V_{ext} is an external potential, V_{ee} represents the Coulomb repulsion of the electrons and E_{xc} denotes all terms not accounted for by the other terms. These include electron exchange, electron correlation, and corrections to the kinetic energy and Coulomb interaction.

The ‘only’ problem in DFT is that the exact functional describing the exchange-correlation term is unknown. Many different approximate functionals, of different type, exist. The simplest, so-called ‘local’ functionals, which are based on the free electron gas, only depend on the electron density $\rho(r)$. An example is the PWLDA functional.^[107] Of course, the electron distribution in molecules and clusters is spatially inhomogeneous. Generalized gradient corrected functionals account for this effect by making the functional not only dependent on the electron density, $\rho(r)$, but also on the gradient of the electron density, $\nabla\rho(r)$, PBE^[108] and BP86^[109, 110] are examples of gradient corrected functionals. A third class of functionals is the so-called hybrid functionals, which combine generalized gradient functionals with a certain percentage of exact exchange. The widely used B3LYP functional is a hybrid functional.^[111, 112] Unfortunately, there is no guarantee that the accuracy of results obtained from DFT calculations can be increased by using more sophisticated functionals.

All the quantum chemical calculations described in this Ph.D. thesis were performed using density functional theory and either the BP86 or B3LYP parameterization of the exchange-correlation functional.

2.3.3 Geometry Optimization

For molecules and clusters, many different possibilities exist to arrange the constituent atoms. In many cases, especially for clusters, the precise molecular structure is not known from experimental studies. In these cases geometry optimizations can be performed to find minima on the potential energy surface, i.e., stable molecular conformations. The change in the total energy of a system when the constituent atoms are displaced from their equilibrium positions $R_{i,0}$ by R_i can be expressed by a Taylor expansion:

$$E(R) = E(R_0) + \sum_i^{N_{vib}} \left(\frac{\partial E}{\partial R_i} \right) (R_i - R_0) + \sum_i^{N_{vib}} \sum_{j>i}^{N_{vib}} \left(\frac{\partial^2 E}{\partial R_i \partial R_j} \right) (R_i - R_0)(R_j - R_0) + \dots \quad 2.8$$

where N_{vib} is the number of vibrational degrees of freedom. It is convenient to change from the coordinates R_i to normal coordinates, Q_i . There are exactly $3N-6$ normal coordinates for a non-linear polyatomic molecule. Upon applying this transformation, equation 2.8 becomes:

$$E(Q) = E(Q_0) + \sum_i^{N_{vib}} \left(\frac{\partial E}{\partial Q_i} \right) (Q_i - Q_0) + \sum_i^{N_{vib}} \left(\frac{\partial^2 E}{\partial Q_i^2} \right) (Q_i - Q_0)^2 + \dots \quad 2.9$$

During a geometry optimization step, the potential energy surface is sampled with respect to changes in the intermolecular distances. The gradient of the total energy (second term on the right hand side of equation 2.9) can be used to evaluate how the atomic arrangement should change in order to lower the total energy. This procedure is repeated until the gradient vanishes and all second derivatives (third term on the right hand side of equation 2.9) are positive, signifying that an (local) energetic minimum structure has been found. The above algorithm implies that the system under investigation will always relax to the nearest energetic minimum structure. The strength of inter atomic bonds in metal clusters is not strongly dependent on directionality; therefore many geometrical isomers are close in energy. The potential energy surface of metal clusters is rather flat and many different minima exist, all of which can have a different energy. To find the global minimum structure of a complex that consists of several metal atoms, many different geometry optimization runs have to be performed, each starting from different initial starting geometries. However, there is no guarantee that the true ground state structure has been identified after a finite number of calculations.^[113]

2.3.4 Vibrational Frequency Calculations

When a stable structure has been found, the nuclear Schrödinger equation (eq. 2.5b) can be used to calculate the frequencies of all $3N-6$ vibrational modes. For the calculations described in this Ph.D. thesis, it is assumed that the potential energy surface around the energetic minimum is harmonic. The curvature of the PES with respect to the normal modes, $\partial^2 E / \partial Q_i^2$, the Hessian matrix, provides bond force constants, which can be used to calculate harmonic vibrational frequencies using the equation for a harmonic oscillator:

$$\nu_i = \frac{1}{2\pi} \sqrt{\frac{k_i}{\mu_i}} \quad 2.10$$

where ν_i , k_i , and μ_i are the vibrational frequency, bond force constant, and reduced mass associated with normal mode i , respectively.

For a stable structure, i.e. a structure corresponding to an energetic minimum on the PES, all distortions of the structure lead to an increase of the total energy. In this case, by definition, the gradient of the energy vanishes and all second derivatives, and hence all calculated vibrational frequencies, are positive. For an unstable structure, i.e. a structure that does not correspond to an (local) energetic minimum on the PES, distortions are possible that lead to a decrease in energy. The gradient of the energy with respect to these distortions is negative. When performing a vibrational frequency calculation, this gives rise to imaginary frequencies. A vibrational frequency calculation can therefore be used to verify if a stable structure has been identified.

The IR intensity of a vibrational absorption mode, depends on the change in dipole moment induced by the displacement of the atoms associated with that vibration. The single photon absorption cross-section corresponding to a certain transition can be calculated from Fermi's golden rule:

$$\sigma_{i \rightarrow f} = \frac{2\pi}{\hbar} \left| \int \psi_f(Q) \mu(Q) \psi_i(Q) dQ \right|^2 \delta(E_f - E_i) \quad 2.11$$

In this equation, $\mu(Q)$ represents the dipole moment operator and the integral runs over all normal coordinates. The delta function shows that a transition can only take place if the energy of the absorbed photon is equal to the energy difference between the initial- and final- state. By expressing the dipole moment operator as a Taylor expansion and assuming that the PES is harmonic around the energetic minimum, it can than be shown that the single photon absorption cross-section corresponding to the j th normal mode can be written as:

$$\sigma_{i \rightarrow f} \propto \left| \frac{d\mu}{dQ_i} \right|^2 \quad 2.12$$

Therefore, cross-sections corresponding to vibrational modes are, in first order, proportional to the derivative of the dipole moment with respect to the normal modes.

As outlined in section 2.1, IR-MPD spectroscopy is a multiple photon technique, based on recording the depletion of the ion signal as a function of photon frequency. Therefore, the calculated single photon cross-sections cannot be compared to the experimental spectrum directly. A complicating factor in the conversion of single photon cross-sections to depletion spectra is that the number of absorbed photons required to induce fragmentation is unknown. For visual comparison, the single photon absorption cross-sections calculated by the procedure outlined above can be converted to a fraction of undissociated complexes by assuming that absorption of the first photon is rate determining in the IR-MPD process. This assumption is reasonable considering that internal vibrational redistribution of the photon energy becomes much faster with increasing internal energy (see section 2.1). Under this assumption, the calculated single photon cross sections can be converted into a depletion spectrum according to:

$$\frac{I(\nu)}{I_0} = 10^{-\frac{\sigma(\nu)P_{\text{FEL}}(\nu)}{c}} \quad 2.13$$

where $\sigma(\nu)$ is the calculated single photon cross-section at frequency ν , $P_{\text{FEL}}(\nu)$ the output power of the free electron laser at frequency ν . The constant c is introduced to obtain the best possible agreement with experiment.

Adsorption of Multiple H₂ Molecules on 3d Transition Metal Clusters §

Abstract

The adsorption of H₂ on a series of gas-phase transition metal (scandium, vanadium, iron, cobalt, and nickel) clusters containing up to 20 metal atoms is studied using IR-multiple photon dissociation spectroscopy complemented with density functional theory based calculations. Comparison of the experimental and calculated spectra gives information on hydrogen bonding geometries. The adsorption of H₂ is exclusively dissociative on Sc_nO⁺, V_n⁺, Fe_n⁺, and Co_n⁺, while both atomic and molecularly chemisorbed hydrogen is present in Ni_nH_m⁺ complexes. It is shown that hydrogen adsorption geometries depend on the elemental composition as well as on the cluster size and that the adsorption sites are different for clusters and extended surfaces. In contrast to what is observed for extended metal surfaces, where hydrogen has a preference for high coordination sites, hydrogen can be both two- or three-fold coordinated to cationic metal clusters.

§ Adapted from: I. Swart, F.M.F. de Groot, B.M. Weckhuysen, P. Gruene, G. Meijer, and A. Fielicke, *H₂ Adsorption on 3d Transition Metal Clusters: a Combined Infrared Spectroscopy and Density Functional Study*, J. Phys. Chem. A, **112**, 1139 (2008)

3.1 Introduction

The interaction of H₂ with transition metals is of fundamental interest to the fields of hydrogen storage, catalysis, and metallurgy. The adsorption of hydrogen on nickel, cobalt and iron is of considerable importance as these metals are active hydrogenation (nickel), ammonia synthesis (iron), or Fischer-Tropsch (cobalt and iron) catalysts. Under reaction conditions, the surface of catalytically active metals is often covered with hydrogen. By studying H₂ adsorption on small transition metal clusters, fundamental insight can be obtained into elementary steps that take place on catalytically active surfaces.

Hydrogen adsorption on transition metal clusters has been studied extensively and has been summarized in two reviews.^[114, 115] However, structural information on the hydrogen binding sites is relatively scarce. On extended metal surfaces, hydrogen atoms are known to have a preference for high coordination sites. However, it is not at all clear if this is also the case for hydrogen adsorption on transition metal clusters that contain only a few metal atoms. To date, only indirect information on bonding geometries is available from hydrogen uptake measurements. It is generally accepted that H₂ dissociates upon adsorption on transition metal clusters. Experimental evidence in support of this mechanism includes the observation that the ionization potential of metal clusters increases upon adsorption of hydrogen,^[116] the strength of the cluster – hydrogen bond^[117-121] and that the reaction between hydrogen and metal clusters is irreversible at room temperature.^[122] From these and other experiments it has been concluded that hydrogen can be two-, three- or four-fold coordinated to metal clusters, but not linearly.

Upon exposure of the transition metal clusters to H₂, the clusters bind H₂ molecules and form metal hydride complexes. Reactivity studies have demonstrated that the reactivity of different transition metals toward H₂ shows large variations with cluster size. The reactivity of a cluster is found to correlate with the electronic properties, as expressed, for instance, by the HOMO to LUMO excitation energy or by an (effective) ionization potential of the cluster. It has been argued, therefore, that the chemisorption probability depends on the energy barrier caused by Pauli repulsion between H₂ and the metal cluster. For the reaction of niobium clusters with H₂, it has been found that the entrance channel barrier is determined by an avoided crossing with ionic potential surfaces. More generally, the requirement for a charge transfer in the activation of H₂ could account for the dependence of the reaction rate on the ionization potential.^[27, 123, 124] At sufficiently high H₂ concentration, the cluster usually saturates with a well-defined number of H₂ molecules. So far, this element specific saturation behavior for the reaction with hydrogen has been studied, e.g., for vanadium, iron, and cobalt clusters.^[125-127] These saturated complexes can be considered as ideal model systems for the above mentioned highly covered surfaces in hydrogenation reactions. To date, there are no conclusive explanations for the observed saturation stoichiometries, e.g., in terms of cluster structure or H adsorption geometry. A systematic study on hydrogen saturated transition metal clusters that allows for an understanding of the interaction between metal and

hydrogen ligands is thus highly desirable. By performing this study on a series of 3d-transition metals, one can gain insight into the effect of increasing *d*-orbital occupation.

Few studies on scandium clusters containing more than 3 metal atoms have been reported in the literature. The ionization potentials of scandium monoxide clusters, Sc_nO^+ , have been measured^[128] and the magnetic moments of neutral scandium clusters containing between 5 and 20 metal atoms have been determined.^[129] The structures of bare scandium clusters have been calculated using density functional theory (DFT).^[130] However, to the best of our knowledge, no studies on H_2 or D_2 chemisorption on scandium clusters have been performed.

In contrast to this, vanadium clusters have received considerable research interest. The adsorption of H_2 and D_2 has been studied using flow tube and ion trap techniques^[117, 125, 131-134] and the reactivity of vanadium clusters toward H_2 and D_2 has been measured.^[117, 125, 133, 134] The V_n^+ -D bond energies have been measured by studying the kinetic energy dependence of the reaction of cationic vanadium clusters with D_2 . These bond energies have been determined to be between 2 and 3 eV, depending on cluster size. From these and other studies it has been proposed that H_2 and D_2 bind dissociatively to vanadium clusters, which has been confirmed by a combined vibrational spectroscopy and DFT study on hydrogen saturated cationic vanadium clusters.

The reaction of H_2/D_2 with iron clusters has been the subject of several studies as well. The reactivity of iron clusters toward H_2 has been found to depend strongly on the size of the cluster and to correlate with the difference between ionization potential and electron affinity of the clusters.^[135] The Fe_n^+ -D bond energies have been measured for clusters with $n = 2-15$, and vary from 1.4 eV to 2.8 eV.^[119] From magnetic deflection experiments it has been found that the magnetic moment of iron clusters increases upon hydrogen chemisorption.^[136] For Fe_n clusters, it has also been shown that the ionization potential increases upon hydrogen adsorption.^[116] Vibrational spectra of neutral iron hydride complexes have been measured using a tunable CO_2 laser covering the spectral range from 885-1090 cm^{-1} . Several absorption features, ascribed to Fe-H modes, have been observed in this spectral range.^[137] DFT calculations on $\text{Fe}_{13}\text{H}_{14}$ (T_d symmetry) indicate that two- and three-fold coordinated hydrogen atoms result in vibrations in the 820-1500 cm^{-1} range. The vibrational spectrum of FeH_2 in the gas-phase^[138] shows that the anti-symmetric stretch mode has a frequency of 1674 cm^{-1} .

The reaction of H_2/D_2 with cobalt clusters is among the most intensively studied reactions in the field of cluster science. As for iron clusters, the reactivity of cobalt clusters toward H_2/D_2 is strongly size dependent.^[27, 139] The reactivity does not strongly depend on temperature,^[140] indicating that the adsorption of hydrogen on cobalt clusters is a non-activated process. The experimentally determined Co_n^+ -D bond energies do not strongly depend on size (for clusters with $n = 2-16$) and generally increase with increasing cluster size from 2 eV to 2.6 eV. Indirect

information on deuterium binding sites is available from D₂ uptake measurements.^[141] Hydrogen is believed to be two-, three- or four-fold coordinated to cobalt, but never linearly.

As nickel is an effective hydrogenation catalyst, the reaction of H₂/D₂ with nickel clusters has also received considerable interest. Again, the reaction of small nickel clusters with hydrogen depends on the size of the cluster.^[121] Nickel clusters have been found to bind more H₂ molecules than other transition metal clusters,^[142] suggesting that part of the adsorbed hydrogen is bound in a different way to nickel than to other transition metals. The Ni_n⁺-D bond energies^[121] have been found to be similar to the V_n⁺-D, Fe_n⁺-D, and Co_n⁺-D bond energies. The bond strength increases from 2 eV for the trimer to 2.6 eV for a cluster containing 16 nickel atoms. The values for the larger clusters are close to the values obtained for hydrogen adsorption on extended surfaces. The similarity in bond strengths for the different transition metals suggests that the metal d-orbitals do not play an important role in the M-H bond. One can therefore expect that the metal hydrogen vibrations have similar frequencies.

Vibrational spectroscopy, combined with quantum chemical calculations, can provide detailed information on adsorption geometries for cluster complexes.^[75] In this chapter the determination of the size dependent hydrogen adsorption sites, at high (saturation) hydrogen coverage, on Sc_nO⁺, V_n⁺, Fe_n⁺, Co_n⁺, and Ni_n⁺ clusters with $n = 3-20$ is discussed. Vibrational spectra of the transition metal hydride complexes have been obtained using infrared multiple photon dissociation (IR-MPD) spectroscopy. Vibrational spectra have been measured in the range from 500 cm⁻¹ to 1600 cm⁻¹, covering both the M-H stretch, $\nu(\text{M-H})$, and deformation mode, $\delta(\text{M-H})$, regions. Vibrations of the metal cluster core are expected to be below 500 cm⁻¹ (see section 2.2.1).^[62, 63] For the nickel deuteride complexes, the spectral region in which the D-D stretch, $\nu(\text{D-D})$, vibration is expected, has been scanned as well. The high H/Ni ratios reported in the literature would indicate partly molecularly bound H₂ and vibrational spectroscopy can unambiguously resolve how H₂/D₂ is bound to nickel clusters. The experimental work is complemented with density functional theory calculations for complexes containing 4, 5, and 6 metal atoms. Comparison of the experimental and calculated spectra provides information on hydrogen adsorption geometries and bond strengths.

3.2 Experimental

InfraRed Multiple Photon Dissociation (IR-MPD) spectroscopy was used to measure the IR spectra of metal hydride complexes in the range of the M-H stretch and deformation modes (500 - 1500 cm⁻¹). Details of the IR-MPD mechanism and the experimental setup can be found in chapter 2. For the experiments described in this chapter, the H₂ content in the flow reactor channel was chosen such that increasing the H₂ content further did not lead to adsorption of more H₂ molecules, i.e. the clusters described in this chapter are saturated with H₂.

For scandium, vanadium, iron, and cobalt commercially available metal rods have been used as ablation targets. The study of H₂ chemisorption on nickel clusters using mass spectrometry is complicated by the natural isotopic distribution of nickel. Therefore, an isotopically enriched nickel target was used. This target was prepared by electroplating ⁵⁸Ni (>99.8%) onto an Au substrate. An electroplating solution was prepared by dissolving 2.00 g ⁵⁸Ni (Cambridge Isotope Laboratories) in 1.2 mL concentrated HCl, 2.2 mL concentrated H₂SO₄ and 12.0 mL 30% H₂O₂. Subsequently 3 g H₃BO₃ was added and the pH was adjusted to pH = 2 using KOH pellets. The solution was heated to 60 °C under continuous stirring to decompose any excess H₂O₂. After cooling to room temperature, demineralized water was added until the total volume was 60 mL.

A three-electrode setup was used for the plating process, coupled to a potentiostat. An Au cylinder with a length of 2.7 cm and a diameter of 0.57 cm (Schöne Edelmetaal) was used as the working electrode. Custom-made stainless steel extensions could be screwed onto both ends of the Au cylinder (see Figure A1). All stainless steel areas in contact with the plating solution, as well as the bottom of the Au rod, were passivated using Teflon tape. To ensure that the Ni layer grew cylindrically, the Au rod was placed in the middle of a cylindrical Pt mesh with a length of 3.5 cm that was used as the counter electrode. Finally, a Radiometer Analytical red rod reference electrode (ref 201) was used to measure the potential.

Applying a constant current of -1A for 10 s nucleated the growth. Subsequently the current was set to -20 mA to allow the Ni layer to grow. The electroplating was conducted under continuous stirring at a temperature of 60°C. Throughout the deposition demineralized water was added to keep the volume constant. The deposition was stopped after a total of -2000 C had passed through the cell.

3.3 Theoretical Method

The experimental spectra of several metal hydride complexes are complemented with DFT based calculations to obtain structural information. The calculations employ the BP86 parameterization of the exchange correlation functional and a triple zeta valence plus polarization (TZVP) basis set for all atoms.^[143]

The number of structural isomers dramatically increases with increasing cluster size. Because structural information on both bare and hydrogenated metal clusters is scarce, calculations have only been performed on selected metal hydride complexes. The following computational procedure has been applied. First, the geometries of several cluster complexes were optimized for each cluster size. Different metal cluster geometries were used and hydrogen atoms were placed both in two and three fold coordination sites. For every geometric isomer, optimizations have been performed using different spin states. The optimization procedure has been conducted without any symmetry restrictions. After the optimization procedure, the vibrational spectrum was calculated within the harmonic approximation. The calculated single photon absorption cross sections were convoluted with Gaussians with a width of 20 cm⁻¹ and converted into depletion spectra using equation 2.12.

3.4 Results and Discussion

First, the saturation compositions of the metal hydride complexes will be treated. Subsequently the experimental and simulated depletion spectra, as well as the determined metal hydride complex geometries, will be discussed element by element. Finally, a comparison between hydrogen adsorption on clusters of different elements is made.

3.4.1 Complex Composition

Nearly all clusters in the size range under investigation react at room temperature with H₂. Only Fe₃⁺ and Co₃⁺ do not bind any hydrogen. Upon increasing the H₂ pressure in the reactor channel, the metal clusters sequentially bind H₂ molecules until a size specific saturation coverage is reached. For some of the Ni_{*n*}⁺ clusters a product distribution is observed in the mass spectrum even at the highest H₂ content used, indicating that saturation has not yet been reached. For cobalt, a saturation behavior has been observed but upon increasing the H₂ content further, the cluster added additional weaker bound H₂ molecules. Physisorption of molecular hydrogen at temperatures below 150 K has been observed before on neutral iron clusters.^[137] The maximum number of H₂ molecules that could bind under our experimental conditions as a function of element and cluster size, is given in Figure 3.1. As expected, the number of hydrogen molecules depends on the metal and on the size of the cluster; it increases as the clusters become larger and it decreases from scandium to vanadium to iron to cobalt, but then sharply increases for nickel. All metal clusters bind an even number of hydrogen atoms, except for Co₉⁺ that binds 9 hydrogen atoms. In view of the strong (4.52 eV) H-H bond, one would expect to observe only species containing an even number of hydrogen atoms. The Co₉⁺-D bond energy has been reported to be $\sim 2.3 \pm 0.3$ eV and chemisorption is therefore not expected to be exothermic enough to permit the ejection of one hydrogen atom. A possibility could be that this complex is formed via fragmentation of a larger cluster via, e.g., CoH loss.

The scandium clusters produced in our setup always contain one or two oxygen atoms. It has not been possible to produce bare metal clusters. Both Sc_{*n*}O⁺ and Sc_{*n*}O₂⁺ readily reacted with H₂. In many cases, Sc_{*n*}O₂⁺ clusters bind one H₂ molecule less than Sc_{*n*}O⁺ clusters. Clearly, the number of hydrogen atoms that can bind to a certain cluster is larger than the number of identical adsorption sites. Hydrogen must therefore be bound in different adsorption sites. DFT calculations on scandium complexes with 4, 5, and 6 metal atoms, see below, indicate that structures with internal hydrogen atoms are not formed and that all hydrogen atoms are located on the surface of the cluster.

The far-infrared spectra of bare V_{*n*}⁺ clusters compared to calculated vibrational spectra, led to the determination of the structures for small vanadium clusters.^[63] For many of the smaller clusters, there is a direct relation between the number of triangular facets on the bare clusters and the observed hydrogen saturation number.

This strongly suggests that the hydrogen atoms mainly occupy threefold-hollow sites (μ_3 coordination) on the cluster surface. The exceptions are the V_4^+ and V_5^+ clusters, which have a hydrogen saturation stoichiometry of 6 and 8, respectively, but the metal clusters have only 4 and 6 triangular facets, respectively. Therefore, at least some hydrogen has to be linear (μ_1) or two-fold (μ_2) coordinated to these metal clusters. In section 3.4.3, it will be shown that hydrogen is indeed predominantly threefold coordinated to cationic vanadium clusters but a minor number of bridge bound hydrogen atoms can be present.

The composition of the saturated cationic iron-hydride complexes agrees in most cases with previously reported values for neutral iron-hydride complexes.^[135, 137] For Fe_{11}^+ , Fe_{14}^+ , and Fe_{15}^+ the maximum number of H_2 molecules that is found to bind to the cationic cluster is lower than to the corresponding neutral cluster.^[135, 137]

Cationic cobalt clusters containing between 6 and 9 metal atoms are particularly unreactive toward molecular hydrogen.^[27, 120, 122] Only at relatively high H_2 concentrations, H_2 could be adsorbed onto these clusters. Co_9^+ presents a special case, as it is the only metal complex that binds an odd number of hydrogen atoms.

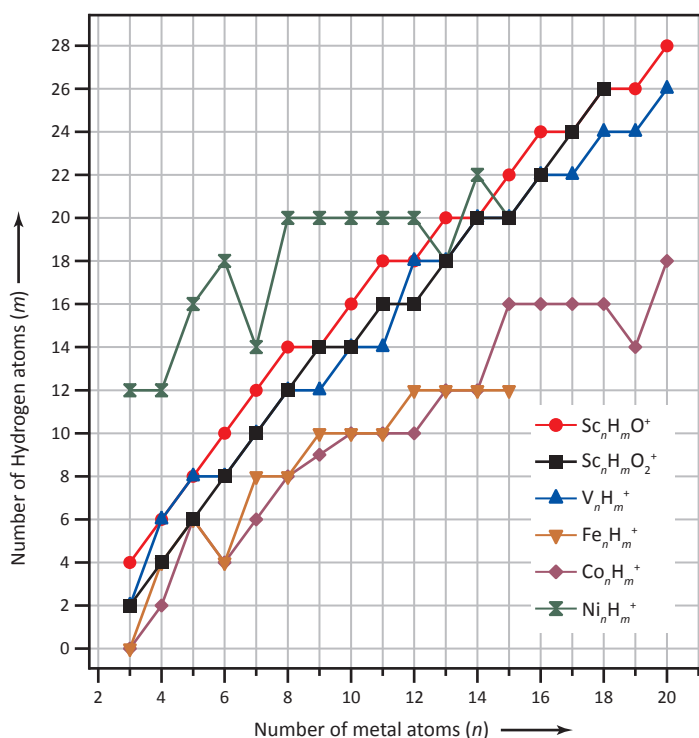


Figure 3.1. Largest number of hydrogen atoms present in $Sc_nH_mO^+$, $Sc_nH_mO_2^+$, $V_nH_m^+$, $Fe_nH_m^+$, $Co_nH_m^+$, and $Ni_nH_m^+$ complexes as a function of cluster size ($n = 3-20$). For several $Ni_nH_m^+$ complexes a distribution was observed but also in this case, the largest value of m is given.

Nickel clusters can bind significantly more H₂ molecules than the other transition metal clusters. The large hydrogen uptake by small Ni_{*n*}⁺ clusters has been reported before,^[142] although the values we report here are even slightly higher. The reason why cationic nickel clusters are so much more reactive than the other transition metal clusters remains an open question. A Ni₄⁺ cluster is predicted to have a (distorted) tetragonal shape,^[144-146] while the Ni₅⁺ cluster is expected to have a trigonal bipyramid structure.^[145-147] These clusters bind 6 and 8 H₂ molecules, respectively. The number of adsorbed hydrogen atoms corresponds to the number of facets plus two times the number of Ni atoms, suggesting that all facets are covered by one hydrogen atom and that additionally each Ni atom binds one H₂ molecule. Quantum chemical calculations support this assignment and will be discussed in section 3.4.6. In addition, the other nickel clusters bind more H atoms than their number of facets and bridge sites. This strongly suggests that also on the larger nickel clusters part of the H₂ is molecularly chemisorbed. It has been shown that hydrogen can be molecularly bound on a hydrogen saturated Ni [510] surface.^[60] For this system, an absorption band due to a D-D stretch vibration was observed at 2306 cm⁻¹. The vibrational spectra of cationic nickel deuteride complexes have been measured in the 2100 cm⁻¹ - 2700 cm⁻¹ range to obtain more information about the hydrogen adsorption geometries.

3.4.2 Scandium

The experimental IR-MPD spectra of Sc_{*n*}H_{*m*}O⁺ (*n* = 3-20) and Sc_{*n*}H_{*m*}O₂⁺ (*n* = 3-18) are given in Figure 3.2. Several absorption features are identified in the 800-1250 cm⁻¹ range. The spectra show complicated band patterns, indicating that these complexes do not have a high degree of symmetry. The most intense absorption band shifts to lower frequency with increasing cluster size. Vibrational spectra of bare cationic vanadium^[62, 63] and cobalt^[148] clusters only show bands below 450 cm⁻¹ and we therefore assign the absorption bands in the 800-1250 cm⁻¹ range to Sc-H vibrations. The spectra of Sc_{*n*}H_{*m*}O⁺ do not change dramatically with cluster size and the spectra of Sc_{*n*}H_{*m*}O⁺ and Sc_{*n*}H_{*m*}O₂⁺ complexes are similar. This suggests that the Sc-H bonds are not significantly influenced by the presence of an additional oxygen atom.

DFT calculations have been performed for hydrogen saturated scandium mono-oxide complexes containing 3-6 metal atoms. The isomers and the corresponding vibrational spectra that are in best agreement with experiment are shown in Figure 3.2. Structures and vibrational spectra of other isomers can be found in appendix A. The spectra of the Sc₃H₄O⁺, Sc₄H₆O⁺, Sc₅H₈O⁺, and Sc₆H₁₀O⁺ complexes are dominated by an intense band centered at ~1100 cm⁻¹. For Sc₅H₈O⁺ and Sc₆H₁₀O⁺, this band has structure, implying the presence of multiple closely spaced bands. The vibrational spectra of Sc₃H₄O⁺ and Sc₄H₆O⁺ exhibit a narrow absorption band at 640 cm⁻¹ that is absent in the spectra of Sc₅H₈O⁺ and Sc₆H₁₀O⁺. For the Sc₅H₈O⁺ and Sc₆H₁₀O⁺, complexes the vibrational spectrum of the lowest energy isomers are

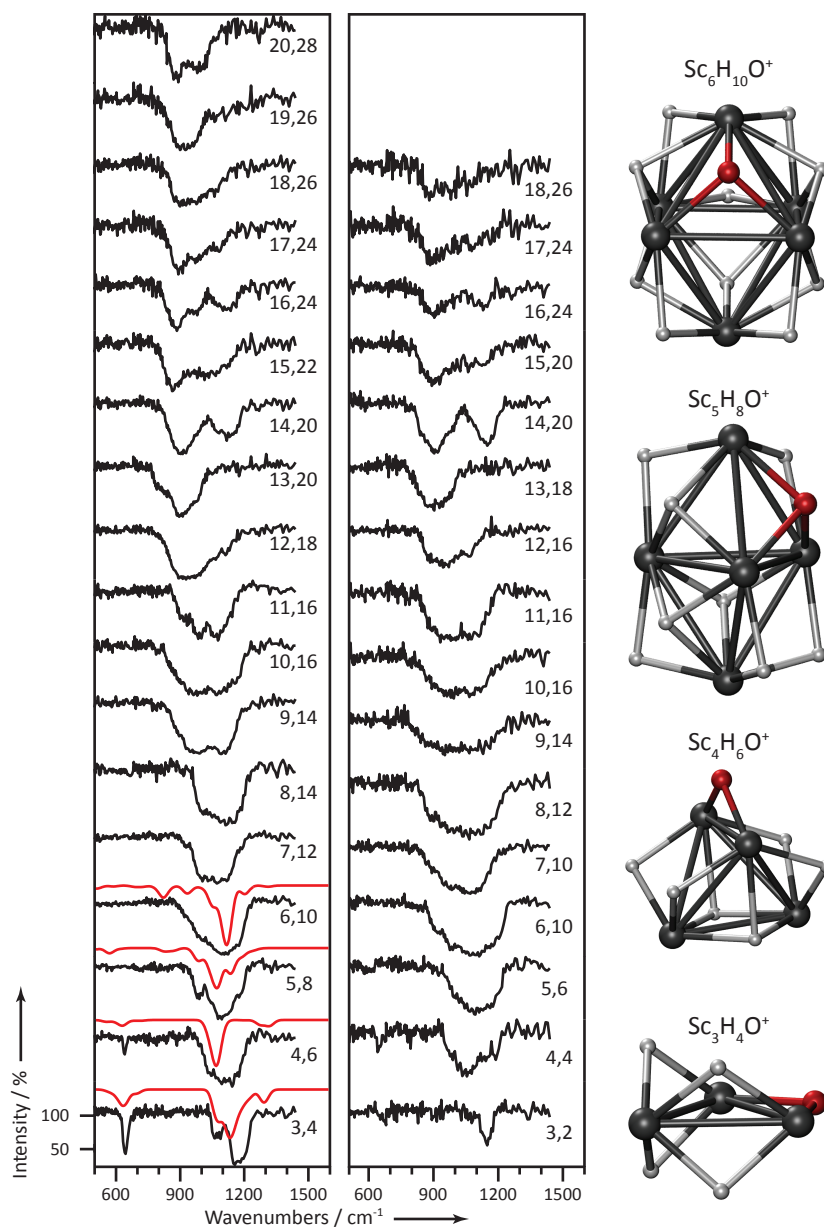


Figure 3.2. IR-MPD spectra (black) of $\text{Sc}_n\text{H}_m\text{O}^+$ (left panel) for $n = 3-20$ and $\text{Sc}_n\text{H}_m\text{O}_2^+$ (right panel) for $n = 3-18$ (bottom to top). The values (n, m) correspond with the number of scandium and hydrogen atoms in the complex respectively. Simulated depletion spectra that are in best agreement with experiment are shown in red together with the corresponding cluster geometries.

found to be in best agreement with the experimentally observed spectra. These complexes have the lowest possible spin state (doublet for Sc₆H₁₀O⁺ and singlet for Sc₅H₈O⁺). In the case of Sc₄H₆O⁺, the experimental spectrum is in best agreement with an isomer that is 0.03 eV higher in energy than the lowest energy isomer. This complex, has the lowest possible spin state (doublet). This is within the expected accuracy of the calculations. In contrast to the complexes with 4, 5, and 6 metal atoms, no single isomer of Sc₃H₄O⁺ identified in the calculations provides good agreement between the experimental and simulated depletion spectrum. The vibrational spectrum of the lowest energy isomer identified in the calculations (Figure 3.2) reproduces the intense absorption bands at ~650 cm⁻¹ and ~1180 cm⁻¹, but this isomer cannot account for the absorption band at ~1070 cm⁻¹. A possible explanation for this discrepancy is that there is more than one isomer present in the molecular beam. An absorption band at ~1070 cm⁻¹ is present in the vibrational spectrum of the isomer shown in Figure 3.2 with a triplet spin state, which is +0.43 eV higher in energy. The simulated spectrum of Sc₃H₄O⁺ shown in Figure 3.2 is a linear combination of the vibrational spectra of the singlet and triplet complexes. Structures and vibrational spectra of other isomers can be found in Appendix A.

The optimized cluster structures of Sc₃H₄O⁺ and Sc₄H₆O⁺ shown in Figure 3.2 have C_{2v} symmetry, while the Sc₅H₈O⁺ and Sc₆H₁₀O⁺ complexes have C₁ symmetry. All hydrogen is bridge (μ₂) bound in Sc₃H₄O⁺ while for the other three complexes a combination of bridge (μ₂) bound and face (μ₃) bound hydrogen atoms is predicted. The three metal atoms of the Sc₃H₄O⁺ complex form a triangle. The oxygen atom is bridge bound in the same plane, while the four hydrogen atoms are bridge bound along the edges of the triangle. The structure of the Sc₄H₆O⁺ complex can be described as a tetrahedron spanned by the scandium atoms with four bridge (μ₂) bound and two face (μ₃) bound hydrogen atoms. The oxygen atom is bridge (μ₂) bonded. The five metal atoms in the Sc₅H₈O⁺ complex span a distorted trigonal bipyramid while the oxygen atom is face (μ₃) bound to the metal cluster. The structure of the Sc₆H₁₀O⁺ complex can be described in similar terms. The six metal atoms form a distorted octahedron to which the oxygen atom is face (μ₃) bound. Isomers with hydrogen atoms inside the metal cage are found to be at least 0.5 eV higher in energy than isomers with only surface bound hydrogen. The vibrational spectrum of tetrahedrally coordinated hydrogen in α-ScH_{0.34} has been measured using neutron scattering. The frequencies of two modes associated with tetrahedrally coordinated hydrogen atoms were reported to be 834 cm⁻¹ and 1189 cm⁻¹, respectively.^[149] None of the complexes in the size range that was investigated shows an absorption band at ~1200 cm⁻¹. This provides another indication that these scandium complexes do not contain any internal hydrogen atoms. Isomers with an internal oxygen atom are even less favorable, being at least 0.7 eV higher in energy than isomers with a surface bound O atom. Such species are therefore not expected to be present in the molecular beam. The calculations indicate that there are many closely spaced vibrations in the 900–1250 cm⁻¹ range. The vibrations are not localized, i.e., they involve the collective motion of several hydrogen atoms and it is not straightforward to assign absorption bands to local modes. The most intense absorption band at ~1100 cm⁻¹ is assigned to

collective stretch vibrations of bridge (μ_2) bonded hydrogen atoms. The absorption band at 640 cm^{-1} observed for $\text{Sc}_3\text{H}_4\text{O}^+$, $\text{Sc}_4\text{H}_6\text{O}^+$, and $\text{Sc}_4\text{H}_4\text{O}_2^+$ is narrow compared to the other bands, suggesting that this band is not due to a Sc-H vibration. The frequency of bridge (μ_2) bonded oxygen to scandium has been reported to be 615 cm^{-1} .^[150] The calculations for $\text{Sc}_3\text{H}_4\text{O}^+$ and $\text{Sc}_4\text{H}_6\text{O}^+$ indeed show that the oxygen atom in isomers, whose vibrational spectrum is in best agreement with the experimental spectrum, is bridge (μ_2) bound. Because of the relatively good agreement between experimental and calculated spectra, the band at 640 cm^{-1} is tentatively assigned to an Sc-O stretch vibration of a bridge (μ_2) bound oxygen atom. The absence of this band in the spectra of $\text{Sc}_5\text{H}_8\text{O}^+$ and $\text{Sc}_6\text{H}_{10}\text{O}^+$ then suggests that the oxygen atom is threefold coordinated to scandium in these two complexes. Indeed, the calculations show that for these complexes the lowest energy isomers have a face (μ_3) bound oxygen atom. A relatively narrow absorption band around 640 cm^{-1} is only observed for $\text{Sc}_4\text{H}_6\text{O}^+$, $\text{Sc}_4\text{H}_4\text{O}_2^+$, and $\text{Sc}_3\text{H}_4\text{O}^+$, implying that in these complexes the oxygen atom is bridge bound, while it is threefold, or higher, coordinated to the other scandium complexes. As pointed out above, the lowest energy isomers of $\text{Sc}_5\text{H}_8\text{O}^+$ and $\text{Sc}_6\text{H}_{10}\text{O}^+$ contain a face (μ_3) bound oxygen atom.

3.4.3 Vanadium

The spectra of the hydrogen saturated vanadium clusters are given in Figure 3.3 for complexes containing between 4 and 20 metal atoms. Several cluster size specific absorption bands associated with V-H vibrations are observed in the $550\text{--}1450\text{ cm}^{-1}$ range. The spectra of most species show complicated band patterns, indicating that the vanadium hydride complexes do not have a high degree of symmetry. The only exception is V_6H_8^+ for which two well-resolved absorption bands are observed, indicating that this complex might have a higher degree of symmetry.

As outlined in section 3.4.1, there is in many cases a correspondence between the number of triangular facets of a cluster and the hydrogen saturation stoichiometry. This strongly suggests that the hydrogen atoms are primarily face bound to the cationic clusters. To test this hypothesis, DFT calculations were performed for hydrogen-saturated clusters with 4-9 vanadium atoms. The isomers and the corresponding vibrational spectra that are in best agreement with experiment are shown in Figure 3.3. Structures and vibrational spectra of other isomers can be found in appendix A. For V_6H_8^+ the lowest energy structure has octahedral symmetry and therefore a relatively simple IR spectrum, in agreement with experiment. The hydrogen atoms bind on top of the facets of the octahedron formed by the vanadium atoms. The band centered at 1275 cm^{-1} can be assigned to a collective anti-symmetric stretch mode of face bound (μ_3) hydrogen atoms. The band observed experimentally at 800 cm^{-1} corresponds to a collective bending mode of threefold coordinated (μ_3) hydrogen atoms. The calculated structures of the other complexes are less symmetric. The vibrations in the $700\text{--}1400\text{ cm}^{-1}$ regime involve collective motion of many different atoms, i.e. the vibrations are not localized and it is not straightforward to assign modes to absorption bands.

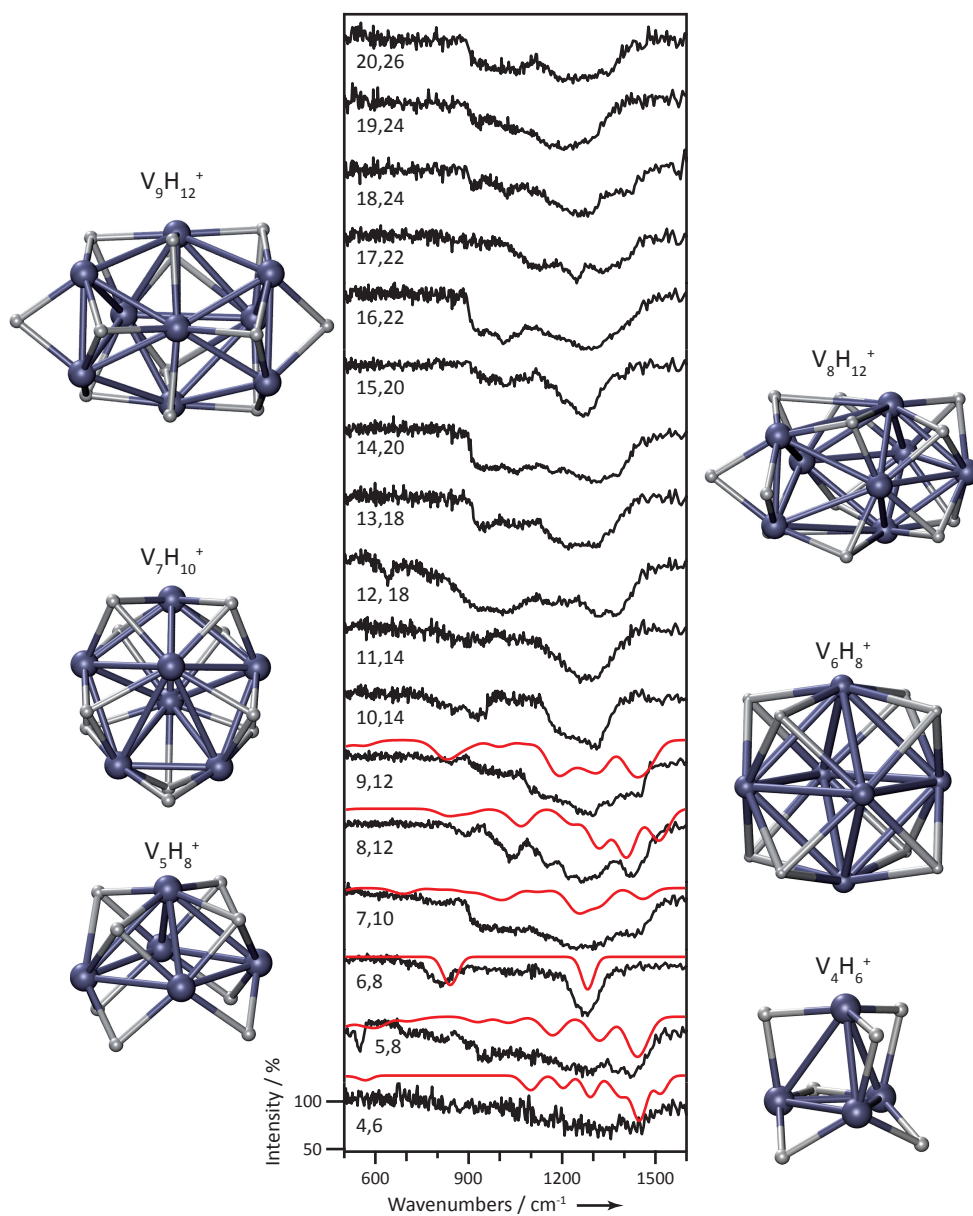


Figure 3.3. IR-MPD spectra of $V_nH_m^+$ complexes for $n = 4-20$ (bottom to top). The values (n, m) correspond to the number of vanadium and hydrogen atoms in the complex respectively. Simulated depletion spectra that are in best agreement with experiment are shown in red together with the corresponding cluster geometries.

Experimentally, many of the cluster complexes show an absorption band around 1450 cm^{-1} . This absorption feature can only be reproduced in the calculations by assuming that some of the hydrogen atoms bind in bridging (μ_2) sites. The calculated structures of V_5H_8^+ , $\text{V}_7\text{H}_{10}^+$, $\text{V}_8\text{H}_{12}^+$ and $\text{V}_9\text{H}_{12}^+$ shown in Figure 3.3 contain at least one hydrogen atom in a bridging site. The vibrational spectra of clusters containing 12, 14, 16–18 vanadium atoms also show an absorption band at $\sim 1400\text{ cm}^{-1}$ and these complexes therefore likely contain some bridge (μ_2) bound hydrogen atoms.

It can therefore be concluded that hydrogen predominantly binds in three fold hollow sites of cationic vanadium clusters, but a minor number of two-fold coordinated hydrogen atoms can be present.

3.4.4 Iron

The experimental IR-MPD spectra of Fe_nH_m^+ complexes with $n = 4-15$ are shown in Figure 3.4. Several cluster size dependent absorption bands are observed in the $700-1500\text{ cm}^{-1}$ range. The vibrational spectra of Fe_4H_4^+ , Fe_5H_6^+ , Fe_6H_4^+ and Fe_8H_8^+ in the $700-1500\text{ cm}^{-1}$ range are similar and consist of two well-resolved bands ($\sim 1200\text{ cm}^{-1}$ and $\sim 1400\text{ cm}^{-1}$). The exact positions and spacing of these bands depend on the particular complex. The similar spectra imply that hydrogen is similarly bound in these four complexes and that these complexes have a relatively high degree of symmetry. The bands observed for the cationic iron hydride complexes are found at higher frequencies than reported earlier for neutral iron-hydride complexes.^[137] Calculations on $\text{Fe}_{13}\text{H}_{14}$ reported in the literature assign these bands to bridge (μ_2) bound hydrogen atoms.^[137] We have performed DFT calculations for Fe_4H_4^+ , Fe_5H_6^+ , and Fe_6H_4^+ . The isomers and the corresponding vibrational spectra that are in best agreement with experiment are shown in Figure 3.4. Structures and vibrational spectra of other isomers can be found in appendix A. Indeed, the optimized complexes, whose vibrational spectra are in best agreement with the experimental spectra, contain only bridge (μ_2) bound hydrogen atoms. The isomers shown are 0.15 eV, 0.14 eV and 0.08 eV higher in energy, respectively than the lowest energy isomer. This is within the expected accuracy of such calculations, especially when considering different spin states. It is known that neutral iron hydride complexes have large magnetic moments.^[136] Our calculations indicate that the cationic iron hydride complexes have a large number of unpaired electrons, 13 for Fe_4H_4^+ , 17 for Fe_5H_6^+ and 19 for Fe_6H_4^+ . In the Fe_4H_4^+ complex, the four iron atoms are arranged in a slightly bend rhombic shape with a hydrogen atom bound to each of the sides of the rhombus. It is interesting to note that for Fe_4H_4^+ and Co_4H_2^+ the calculations indicate that the four metal atoms are arranged in a distorted rhombus, whereas for $\text{Sc}_4\text{H}_6\text{O}^+$ and V_4H_6^+ the metal atoms span a distorted tetrahedron. As observed for the scandium and vanadium complexes with five metal atoms, the five iron atoms of Fe_5H_6^+ span a trigonal bipyramid. The Fe_6H_4^+ complex has D_{4h} symmetry. The six iron atoms are arranged to form an octahedron with the four hydrogen atoms all bridge (μ_2) bound in one plane. The band with the lowest frequency (1200 cm^{-1} for Fe_4H_4^+ , 1210 cm^{-1} for Fe_5H_6^+ , 1130 cm^{-1} for Fe_6H_4^+) is assigned to the collective anti-

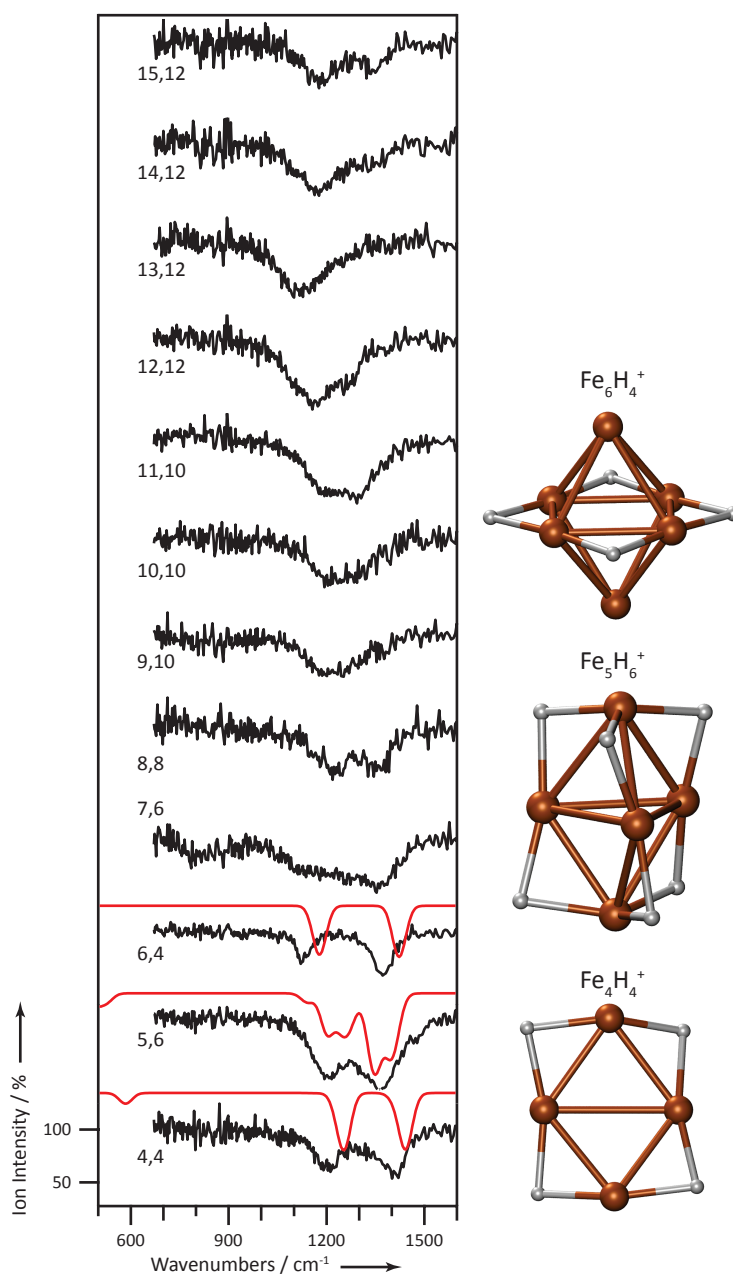


Figure 3.4. IR-MPD spectra of $Fe_nH_m^+$ complexes for $n = 4-15$ (bottom to top). The values (n,m) correspond to the number of iron and hydrogen atoms in the complex respectively.

symmetric bending vibration of the bridge (μ_2) bound hydrogen atoms. The highest frequency band (1400 cm^{-1} for Fe_4H_4^+ , 1360 cm^{-1} for Fe_5H_6^+ , 1370 cm^{-1} for Fe_6H_4^+) is caused by the collective anti-symmetric stretch vibration of the bridge (μ_2) bound hydrogen atoms. Absorption bands at $\sim 1400\text{ cm}^{-1}$, indicative of bridge (μ_2) bound hydrogen atoms, are also present in the vibrational spectra of Fe_7H_6^+ , Fe_8H_8^+ , and $\text{Fe}_{15}\text{H}_{12}^+$. Calculations on isomers of Fe_4H_4^+ , Fe_5H_6^+ , and Fe_6H_4^+ containing face (μ_3) bound hydrogen atoms, see Appendix A, show that the collective stretch vibration of threefold coordinated hydrogen atoms lies in the $1200\text{--}1300\text{ cm}^{-1}$ frequency range. Absorption bands at higher frequencies are thus clear indications for bridge (μ_2) bound hydrogen atoms. Part of the hydrogen is therefore expected to be bridge (μ_2) bound in Fe_7H_6^+ , Fe_8H_8^+ , $\text{Fe}_{14}\text{H}_{12}^+$, and $\text{Fe}_{15}\text{H}_{12}^+$. The presence of face (μ_3) bound hydrogen atoms cannot be excluded. Additional quantum chemical calculations are required to verify how hydrogen is bound in the larger complexes. It is interesting to note the difference between the spectra of $\text{Fe}_{12}\text{H}_{12}^+$ and $\text{Fe}_{13}\text{H}_{12}^+$. Both Fe_{12}^+ and Fe_{13}^+ bind 12 hydrogen atoms but the spectra of the hydride complexes are different. Therefore, part of the hydrogen atoms have to be differently bound, which in turn implies that the metal cluster structure is different. DFT calculations have indeed predicted that the Fe_{13} cluster does has icosahedral symmetry, whereas the Fe_{12} cluster does not.^[151]

It is known from low energy electron diffraction (LEED) studies that H atoms adsorbed on a Fe(110) surface are bound in quasi threefold hollow sites.^[152] As outlined above, at least several of the hydrogen atoms are bridge (μ_2) bonded to cationic iron clusters in the size range under investigation. Apparently the bulk adsorption behavior has not yet been reached for iron clusters containing 15 atoms.

3.4.5 Cobalt

The experimental IR-MPD spectra of H_2 saturated cobalt complexes containing between 4 and 20 cobalt atoms are shown in Figure 3.5. The vibrational spectra of the cobalt hydride complexes change considerably as a function of cluster size. In the vibrational spectra of most complexes, at least two bands are present in the $1050\text{--}1450\text{ cm}^{-1}$ range. The absolute and relative spectral positions depend on the number of metal atoms in the cluster. Vibrational spectra of bare cationic cobalt clusters^[148] only show bands below 450 cm^{-1} and we therefore assign the absorption bands in the $600\text{--}1500\text{ cm}^{-1}$ range to Co-H vibrations.

To determine the hydrogen binding geometries, DFT calculations were performed for Co_4H_2^+ , Co_5H_6^+ , and Co_6H_4^+ . The isomers and the corresponding vibrational spectra that are in best agreement with experiment are shown in Figure 3.5. Structures and vibrational spectra of other isomers can be found in appendix A. The vibrational spectra of the lowest energy isomers of Co_4H_2^+ and Co_6H_4^+ are in good agreement with the experimental spectra of these species. The Co_5H_6^+ isomer, whose vibrational spectrum is in best agreement with experiment, is 0.23 eV higher in energy than the lowest energy isomer identified in the calculations. In case of Co_5H_6^+ , two hydrogen atoms are threefold coordinated to the cobalt cluster, while the

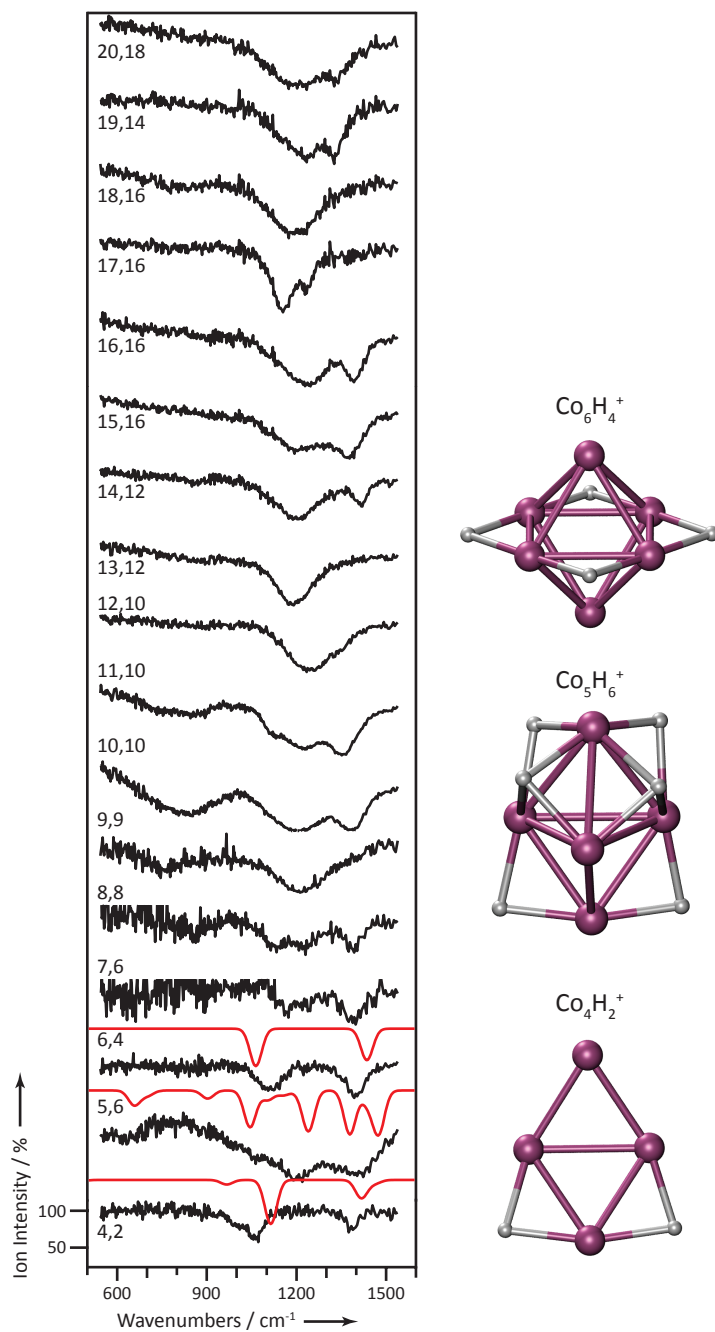


Figure 3.5. IR-MPD spectra of $Co_nH_m^+$ complexes for $n = 4-20$ (bottom to top). The values (n,m) correspond to the number of cobalt and hydrogen atoms in the complex respectively.

other four atoms are bridge (μ_2) bonded. The agreement between the experimental and simulated spectrum of Co_5H_6^+ is not very good and it might be that several isomers are present and/or that the actual structure is different from the one shown in Figure 3.5. The calculations indicate that the Co_6H_4^+ complex consists of an octahedral arrangement of cobalt atoms with all four hydrogen atoms bridge bound in a single plane. The complex is predicted to have 13 unpaired electrons. In the optimized Co_4H_2^+ complex, the metal atoms form a slightly bend elongated rhombus with the two hydrogen atoms bridge (μ_2) bound symmetrically with respect to the long axis of the rhombus. Three bands (1390 cm^{-1} , 1060 cm^{-1} and 1000 cm^{-1}) are observed in the vibrational spectrum of Co_4H_2^+ that are reproduced by the calculations. They can be assigned to collective anti-symmetric stretch, symmetric bending and anti-symmetric bending vibrations of the bridge (μ_2) bound hydrogen atoms, respectively. The optimized geometry of Co_4H_2^+ is similar to the structure of the neutral complex reported in the literature.^[153]

An absorption band with a frequency of $\sim 1400\text{ cm}^{-1}$, indicative of bridge bound hydrogen atoms, is present in the spectra of several of the larger cobalt hydride complexes, implying that part of the hydrogen atoms are bridge (μ_2) bonded in those complexes. On extended cobalt surfaces, hydrogen is known to adsorb in threefold hollow (μ_3) sites.^[154] Vibrational spectra of face bound hydrogen atoms adsorbed on a crystalline cobalt surface^[154] show absorption features around 1150 cm^{-1} . Calculations on isomers of Co_4H_2^+ , Co_5H_4^+ , and Co_6H_4^+ that contain face (μ_3) bound hydrogen atoms show that the stretch vibration of threefold coordinated hydrogen atoms lies in the $1200\text{--}1320\text{ cm}^{-1}$ range for cationic cobalt hydride complexes. Absorption bands in the $1100\text{--}1300\text{ cm}^{-1}$ range are present in the spectra of most cobalt hydride complexes. This strongly suggests that part of the hydrogen atoms are face (μ_3) bound in cobalt hydride complexes that have an absorption band in this range.

Interestingly, the vibrational spectra of $\text{Co}_{16}\text{H}_{16}^+$ and $\text{Co}_{17}\text{H}_{16}^+$ are rather different, suggesting that bulk adsorption behavior is not yet been reached for cobalt clusters with 17 metal atoms. For several complexes (Co_5H_6^+ , Co_8H_8^+ , Co_9H_9^+ , $\text{Co}_{10}\text{H}_{10}^+$, $\text{Co}_{11}\text{H}_{10}^+$, and $\text{Co}_{18}\text{H}_{16}^+$), a broad band is observed at lower frequency. Such a broad band is not present in the vibrational spectra of the hydrogen complexes of the earlier transition metals. Due to the rather poor agreement between the experimental and the calculated spectra of Co_5H_6^+ , no definite assignment of this band can be made.

3.4.6 Nickel

The IR-MPD spectra of Ni_nH_m^+ / Ni_nD_m^+ complexes with $n = 4\text{--}15$ are shown in Figure 3.6. The spectra of the nickel hydride/deuteride complexes are quite different from the spectra of the earlier transition metal hydride complexes. As for the other transition metal hydrides, absorption bands in the $1000\text{--}1500\text{ cm}^{-1}$ range, indicative of dissociatively bound hydrogen, are observed for the Ni_nH_m^+ complexes. Hence, several of the adsorbed hydrogen atoms are bridge and/or face bound to the nickel

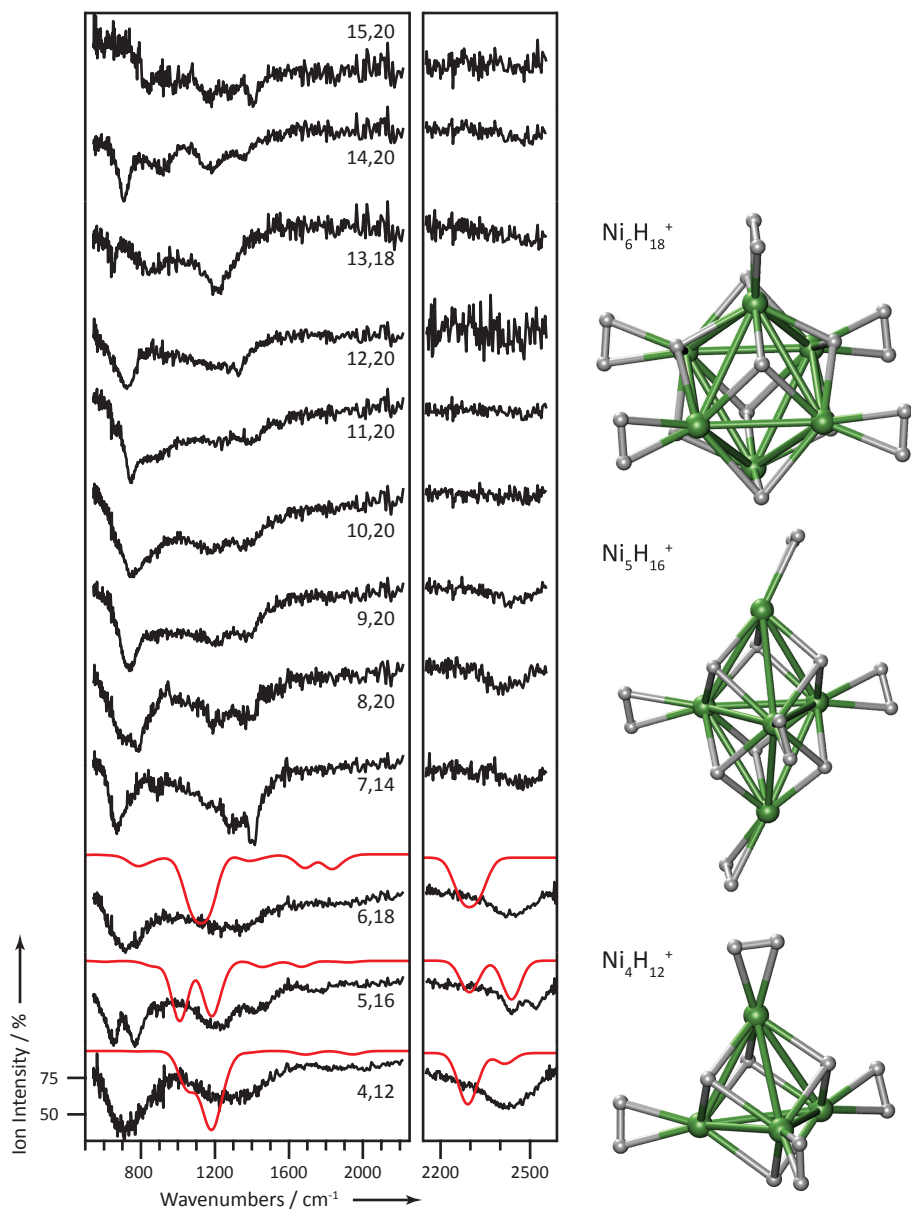


Figure 3.6. IR-MPD spectra of $Ni_nH_m^+$ complexes for $n = 4-15$ (bottom to top). The values (n,m) correspond to the number of nickel and hydrogen atoms in the complex respectively.

clusters. This assignment is supported by DFT calculations (see below). However, absorption bands located in the 2300 cm^{-1} - 2500 cm^{-1} range are observed for nickel deuteride complexes up to $\text{Ni}_9\text{D}_{20}^+$, proving that at least part of the D_2 is molecularly bound in these complexes. This is consistent with the value of the D-D stretch ($\nu(\text{D-D})$) band observed for molecularly bound D_2 on a deuterium saturated Ni [510] surface (2306 cm^{-1}).^[60] The D-D stretch band, $\nu(\text{D-D})$, is shifted considerably to lower frequency compared to the frequency of free D_2 (2941 cm^{-1}). This implies that the D_2 molecules must be chemisorbed to the nickel cluster since physisorbed species only show small frequency shifts.^[155] For $\text{Ni}_5\text{D}_{16}^+$ two relatively narrow bands are observed in the high-frequency range, whereas in the spectra of the other complexes only a single broad absorption is observed. For molecularly bound D_2 on a deuterium saturated Ni [510] surface, the absorption bands were also relatively broad. The spectra of the nickel hydride complexes also exhibit distinctly different features in the low frequency range compared to the other transition metal hydride complexes. A strong absorption band is observed for all nickel hydride complexes at frequencies below 900 cm^{-1} . The presence of these bands provides further evidence that (part of the) hydrogen is differently bound in nickel hydride complexes. They are assigned to the Ni- H_2 stretch ($\nu(\text{Ni-H}_2)$) vibration. DFT calculations support this assignment (see below). The metal-dihydrogen bond can be described by similar concepts used to describe the metal - olefin bond^[59] (see section 1.3).

To determine the hydrogen binding geometries and bond energies, DFT calculations were performed for $\text{Ni}_4\text{H}_{10}^+$, $\text{Ni}_4\text{H}_{12}^+$, $\text{Ni}_5\text{H}_{14}^+$, $\text{Ni}_5\text{H}_{16}^+$, $\text{Ni}_6\text{H}_{16}^+$, and $\text{Ni}_6\text{H}_{18}^+$. The hydrogen binding energy is calculated from $E_b = E_{\text{Ni}_n\text{H}_m^+} - E_{\text{Ni}_n\text{H}_{m-2}^+} - E_{\text{H}_2}$. One finds values of +0.54 eV, +0.56 eV, and +0.46 eV for $\text{Ni}_4\text{H}_{12}^+$, $\text{Ni}_5\text{H}_{16}^+$, and $\text{Ni}_6\text{H}_{18}^+$, respectively. These binding energies for molecular chemisorbed H_2 are in agreement with the experimental data.

The isomers and the corresponding vibrational spectra that are in best agreement with experiment are shown in Figure 3.6. Structures and vibrational spectra of other isomers can be found in appendix A. For the Ni_nH_m^+ and Ni_nD_m^+ complexes, the agreement between the experimental and simulated spectra is reasonable. All the experimentally observed features are reproduced by the calculations. Upon substitution of the hydrogen atoms by deuterium, all modes, except for the Ni - Ni modes, scale down in frequency by a factor close to $\sqrt{2}$ ($\pm 1.2\%$). The calculated frequencies of the $\nu(\text{D-D})$ bands are too low while the calculated frequencies of the $\nu(\text{Ni-H}_2)$ vibrations are too high. This demonstrates that the calculations overestimate the Ni- H_2 bond strength. All nickel complexes have the lowest possible (doublet) spin state. The quenching of the magnetic moment of nickel clusters upon adsorption of hydrogen has also been observed experimentally.^[156] The $\text{Ni}_4\text{H}_{12}^+$ complex can be described as a cluster with a tetrahedral core spanned by the Ni atoms with one hydrogen atom bound to each facet of the tetrahedron and one H_2 molecule bound to each nickel atom. The structures of the $\text{Ni}_5\text{H}_{16}^+$ and $\text{Ni}_6\text{H}_{18}^+$ complex can be described in similar terms where the five nickel atoms in $\text{Ni}_5\text{H}_{16}^+$ span a trigonal bipyramid and the 6 Ni atoms in $\text{Ni}_6\text{H}_{18}^+$ span a tetragonal bipyramid.

As outlined above, the DFT calculations assign the strong absorption band at ~ 750 cm⁻¹ to a $\nu(\text{Ni-H}_2)$ vibration. Such an absorption band is observed for all Ni_nH_m^+ complexes with $n = 4-14$. However, the disappearance of the other tell-tale feature of molecularly chemisorbed H₂, the $\nu(\text{D-D})$ band, for clusters with 10 or more nickel atoms could indicate that only atomically bound hydrogen is present for the bigger complexes. Other possible reasons for this discrepancy include a shift of the D-D stretch vibration to higher/lower frequency or that the D-D stretch vibrations have only little IR intensity. If the intramolecular axis of H₂ molecularly chemisorbed on an extended surface is parallel to that surface, the H-H stretch vibration will only have little intensity due to the induced dipole in the metal. Because a Ni-H₂ stretch vibration band is present in the spectra of all nickel hydride complexes (except for $\text{Ni}_{15}\text{H}_{20}^+$), it is most likely that part of the hydrogen is molecularly bound in these complexes. The absence of bands due to D-D stretch vibrations than implies that part of the electrons in the nickel hydride complexes with more than 10 nickel atoms are delocalized. It has indeed been shown that the cluster charge is delocalized over the surface of the cluster.^[76] However, a combination of a theoretical and more detailed spectroscopic study is needed to identify the reason for the absence of a D-D stretch absorption band for the nickel hydride complexes with more than 10 nickel atoms.

3.4.7 Comparison of Hydrogen Binding Geometries

It is instructive to compare the vibrational spectra of different metal hydride complexes and the hydrogen bonding geometries on different metals. The IR-MPD spectra of metal hydride (M_nH_m^+) complexes with $n = 4-6$ (for which computational results are available) are shown in Figure 3.7 (black) along with simulated depletion spectra of isomers (red) that are in best agreement with the experimental spectra. The corresponding cluster geometries are shown in Figure 3.8.

There are significant differences between complexes of a different element but of the same size. It is interesting to note that the stretch vibration of hydrogen atoms bridge (μ_2) bound to vanadium, iron, and cobalt clusters gives rise to an absorption band around ~ 1400 cm⁻¹. However, the vibrational frequency of bridge (μ_2) bound hydrogen to scandium is significantly lower than that of hydrogen bridge (μ_2) bound to vanadium, iron or cobalt. This indicates that the $\text{Sc}_n\text{O}^+-\text{H}$ bond is significantly different from the V_n^+-H , Fe_n^+-H , and Co_n^+-H bonds. In addition, the vibrational frequencies of face (μ_3) bound hydrogen to vanadium, cobalt, and nickel clusters are rather similar, suggesting that the bond strengths are rather similar. Indeed, the V_n^+-D , Fe_n^+-D , Co_n^+-D , and Ni_n^+-D bond dissociation energies are remarkably similar.^[117, 119-121] Unfortunately, no quantitative information is available on $\text{Sc}_n\text{O}^+-\text{D}$ bond dissociation energies.

Interestingly, the vibrational spectrum of Fe_6H_4^+ is similar to the spectrum of Co_6H_4^+ suggesting that the hydrogen is similarly bound in these two complexes. The bands observed for Co_6H_4^+ (1110 cm⁻¹ and 1400 cm⁻¹) are shifted slightly compared to Fe_6H_4^+ (1130 cm⁻¹ and 1370 cm⁻¹). The spectrum of Co_4H_2^+ also resembles the

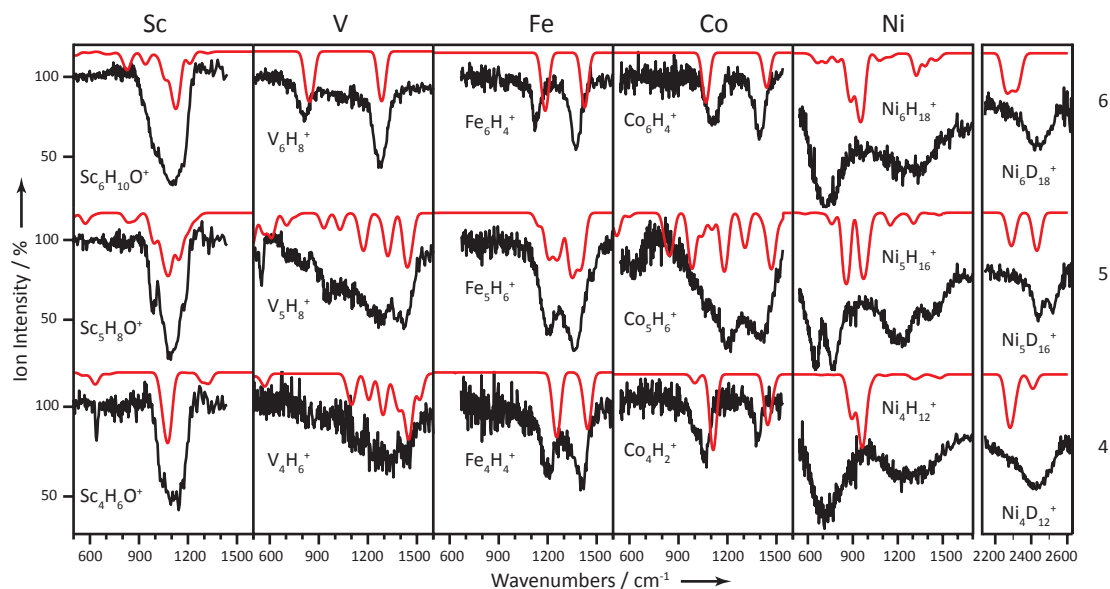


Figure 3.7. Experimental (black) and simulated (red) IR depletion spectra of hydrogen saturated $\text{Sc}_n\text{H}_m\text{O}^+$, V_nH_m^+ , Fe_nH_m^+ , Co_nH_m^+ , Ni_nH_m^+ , and Ni_nD_m^+ complexes for $n = 4, 5,$ and 6 (bottom to top).

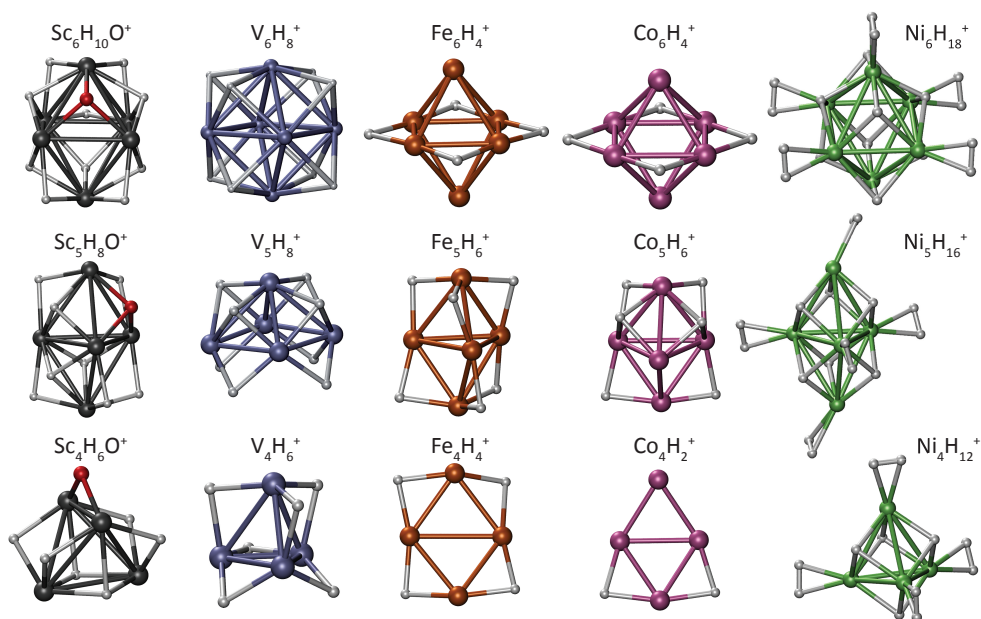


Figure 3.8. Optimized cluster geometries of $\text{Sc}_n\text{H}_m\text{O}^+$, V_nH_m^+ , Fe_nH_m^+ , Co_nH_m^+ , and Ni_nH_m^+ (left to right) complexes for $n = 4\text{--}6$ selected based on the comparison of experimental and calculated IR spectra.

spectrum of Fe₄H₄⁺ except for the clear shoulder observed at 1000 cm⁻¹ for Co₄H₂⁺. These complexes indeed have similar geometries, as shown in Figure 3.8. The metal atoms in Fe₄H₄⁺ and Co₄H₂⁺ are arranged in a distorted rhombus (quasi planar) while the metal atoms in Sc₄H₆O⁺, V₄H₆⁺ and Ni₄H₁₂⁺ form a distorted tetragon.

A compilation of the vibrational frequencies for similarly bound hydrogen species bound to the different metals investigated in this study is given in Table 3.1.

Table 3.1. Experimental vibrational frequencies (cm⁻¹) and their assignments for the Sc_nH_mO⁺, V_nH_m⁺, Fe_nH_m⁺, Co_nH_m⁺, and Ni_nH_m⁺ complexes.

Mode	Sc	V	Fe	Co	Ni
ν(M-H ₂)					650 – 760
ν(D-D)					2420 – 2515
ν(M-μ ₂ H)	1100 - 1110	1420 - 1430	1350 - 1400	1385 - 1400	
ν(M-μ ₃ H)	*	1270 - 1280		1150 - 1230	1210 - 1270
δ(M-μ ₂ H)	*	*	1130 - 1220	1030 – 1110	
δ(M-μ ₃ H)	*	810		*	*

* No clearly resolved band in the experimental spectra.

3.5 Conclusions

The vibrational spectra of a series of transition metal hydride complexes reported here represent a direct probe of atomic and molecular hydrogen binding to cationic metal clusters. Several element and size dependent absorption features are identified. Nickel clusters show distinctly different behavior compared to the other transition metals that were studied. Nickel clusters bind much more hydrogen and a significant part of the adsorbed hydrogen is molecularly chemisorbed. Density functional theory calculations on hydrogen saturated Sc_nH_mO⁺, V_nH_m⁺, Fe_nH_m⁺, Co_nH_m⁺, and Ni_nH_m⁺ complexes generally provide good agreement with experimental measurements. In contrast to what is observed for extended metal surfaces, where hydrogen has a preference for high coordination sites, hydrogen bound to transition metal clusters of scandium, vanadium, iron, and cobalt can be bound in both bridge and face sites. For hydrogen-saturated nickel clusters, no indications for bridge bound hydrogen atoms were found. All hydrogen atoms are bound to the surface of the metal cluster, structures with hydrogen located inside the metal cluster are found to be much higher in energy. A clear transition from molecular to bulk like behavior has not been observed in the size range that was studied.

Adsorption of a Single H₂ Molecule on Nickel Clusters §

Abstract

The reaction of a single H₂ molecule with small cationic nickel clusters in the gas-phase was investigated. The vibrational spectra indicate that the first H₂ molecule that binds to the highly reactive Ni₅⁺ and Ni₆⁺ clusters dissociates upon adsorption. In contrast, it is found that a H₂ molecule can bind molecularly on the relatively unreactive Ni₄⁺ cluster. This complex with molecularly bound H₂ can be considered a structural model for a precursor state to H₂ dissociation.

§ Adapted from: I. Swart, P. Gruene, A. Fielicke, G. Meijer, B.M. Weckhuysen, and F.M.F. de Groot, *Molecular Adsorption of H₂ on Small Cationic Nickel Clusters*, Phys. Chem. Chem. Phys. **in press** (2008)

4.1 Introduction

Adsorption of H₂ on extended transition metal surfaces is nearly always dissociative, i.e. the H-H bond is broken and two individual H atoms are present on the surface or in the bulk of the material. This is also the case for H₂ adsorption on Ni surfaces.^[33, 157, 158] The dissociation of H₂ on Ni is direct, i.e. it does not proceed via a molecular precursor state.^[33, 159] H₂ molecules can only bind molecularly on the step sites of a Ni(510) surface if this surface is fully saturated with H atoms.^[60, 160] Small Ni particles do not necessarily exhibit the same behavior as extended surfaces. Consequently, the reaction of gas-phase Ni clusters with H₂ has been the subject of many studies.^[121, 141, 147, 156, 161-163] However, detailed information on H binding sites on small Ni particles is scarce. In agreement with what is observed for extended Ni surfaces, H₂ can bind molecularly on hydrogen saturated Ni clusters (see chapter 3).^[164] It is not clear if H₂ molecules bind molecularly to nickel clusters only once all sites for dissociative adsorption are blocked, or if already the first H₂ molecule can bind molecularly.

In this chapter, the reaction of a single H₂ molecule with Ni_{*n*}⁺ clusters (*n*=4-6) is studied. It will be shown that the first H₂ molecule can bind molecularly on the relatively unreactive Ni₄⁺ cluster, but that it binds exclusively dissociatively on the highly reactive Ni₅⁺ and Ni₆⁺ clusters.

4.2 Experimental

InfraRed Multiple Photon Dissociation (IR-MPD) spectroscopy was used to measure the IR spectra of metal hydride complexes in the range of the M-H stretch and deformation modes, as well as in the range of the H-H stretch region. Deuterium was used to probe the high-frequency range because the D-D stretch vibration is located in a spectral range that is easier accessible with FELIX. Details of the IR-MPD mechanism and the experimental setup can be found in chapter 2. For the experiments described in this chapter, the H₂ content in the flow reactor channel was chosen such that only complexes with a single H₂ molecule were present in the molecular beam. Because Ni₄⁺ is much less reactive than Ni₅⁺ and Ni₆⁺, different conditions had to be used to measure the vibrational spectra of these three complexes.

To prevent congestion of the mass-spectra due to the isotopic distribution of Ni, an isotopically enriched nickel target was used. This target was prepared by electroplating ⁵⁸Ni (>99.8%) onto an Au substrate. An electroplating solution was prepared by dissolving 2.00 g ⁵⁸Ni (Cambridge Isotope Laboratories) in 1.2 mL concentrated HCl, 2.2 mL concentrated H₂SO₄ and 12.0 mL 30% H₂O₂. Subsequently 3 g H₃BO₃ was added and the pH was adjusted to pH = 2 using KOH pellets. The solution was heated to 60 °C under continuous stirring to decompose any excess H₂O₂. After cooling to room temperature, demineralized water was added until the total volume was 60 mL. A three-electrode setup was used for the plating process, coupled to a potentiostat. An Au cylinder with a length of 2.7 cm and a diameter of 0.57 cm (Schöne Edelmetaal) was used as the working electrode. Custom-made

stainless steel extensions could be screwed onto both ends of the Au cylinder (see Figure A1). All stainless steel areas in contact with the plating solution, as well as the bottom of the Au rod, were passivated using Teflon tape. To ensure that the Ni layer grew cylindrically, the Au rod was placed in the middle of a cylindrical Pt mesh with a length of 3.5 cm that was used as the counter electrode. Finally, a Radiometer Analytical red rod reference electrode (ref 201) was used to measure the potential.

Applying a constant current of -1A for 10 s nucleated the growth. Subsequently the current was set to -20 mA to allow the Ni layer to grow. The electroplating was conducted under continuously stirring at a temperature of 60°C. Throughout the deposition demineralized water was added to keep the volume constant. The deposition was stopped after a total of -2000 C had passed through the cell.

4.3 Theoretical Method

The experimental spectra of the complexes with 4, 5, and 6 metal atoms are complemented with DFT based calculations to obtain structural information. The calculations employ the BP86 parameterization of the exchange correlation functional and a triple zeta valence plus two sets of polarization (TZVPP) basis set for all atoms.^[143]

The following computational procedure has been applied. First, the geometries of several cluster complexes were optimized for each cluster size. Initial complex geometries were generated based on bare metal structures proposed in the literature.^[145, 147] Geometries of nickel hydride complexes were created with molecularly and dissociatively bound hydrogen. In case of isomers with dissociatively coordinated hydrogen, the atoms were placed both in two and three fold coordination sites. For every geometric isomer, optimizations were performed using different spin states. It is known the adsorption of H₂ decreases the total magnetic moment of Ni_{*n*} clusters.^[156] The optimization procedure has been conducted without any symmetry restrictions. After the optimization procedure, the vibrational spectrum was calculated within the harmonic approximation. The calculated single photon absorption cross sections were convoluted with Gaussians with a width of 20 cm⁻¹ and converted into depletion spectra using equation 2.12.

4.4 Results and Discussion

In Figure 4.1A, three mass spectra, measured at different H₂ partial pressures in the reactor, are shown. Upon introduction of H₂ in the flow tube reactor, the formation of metal hydride complexes is observed. Due to the presence of a small amount of water in the cluster apparatus, the molecular beam of nickel hydride clusters is contaminated with a small amount of nickel-water complexes. A clear dependence of the reactivity toward H₂ on cluster size is observed. At low hydrogen content, Ni₅⁺ and Ni₆⁺ already bind H₂, but no Ni₄H₂⁺ is found. The Ni₄H₂⁺ complex can only be formed by increasing the hydrogen content in the reactor further. At those pressures,

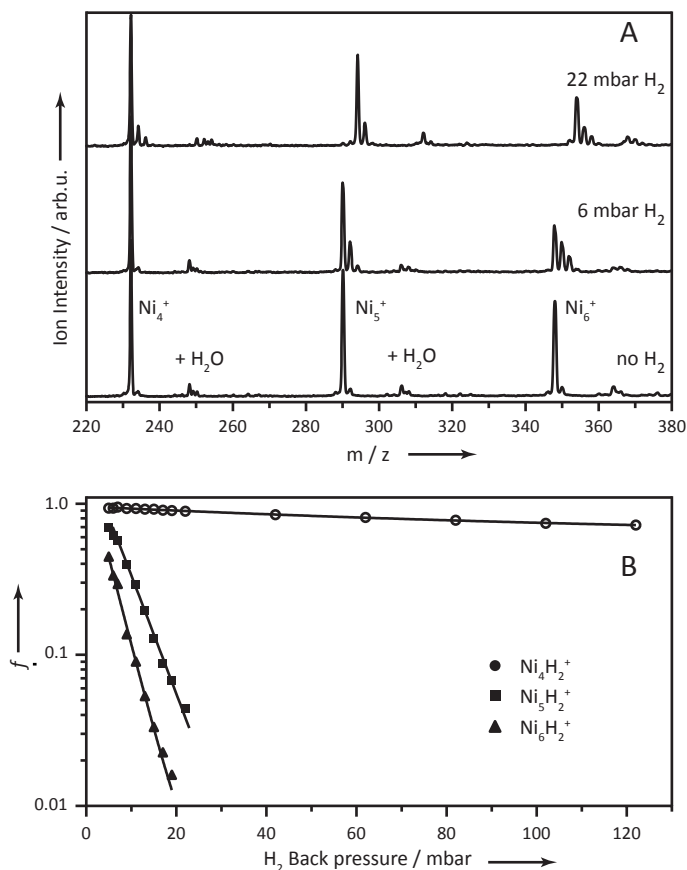


Figure 4.1. A) Mass spectra taken at various H₂ concentrations in the reactor, using backpressures ranging from no H₂ (bottom) to 22 mbar (top). Several peaks due to nickel water complexes are present in the spectrum. B) Semi-logarithmic plot of the fraction of un-reacted Ni clusters, f , versus the H₂ backpressure.

Ni₅⁺ and Ni₆⁺ already bind multiple H₂ molecules. The differences in reactivity can be quantified by assuming that the addition of the first H₂ molecule is irreversible and rate determining in the process of adsorption of multiple H₂ molecules.^[162] Since the molecular H₂ in the reactor is present in excess, the depletion of the bare nickel clusters should then follow pseudo-first-order kinetics:

$$-\ln(f) = k [\text{H}_2] \tau \quad 4.1$$

where f is the fraction of bare Ni clusters remaining at a certain H₂ concentration, k the rate constant for the adsorption of the first H₂ molecule, [H₂] the concentration of H₂ in the reactor, and τ the interaction time. Assuming that the hydrogen partial

pressure in the reactor channel is proportional to the backpressure of H₂ in the pulsed valve, a semi-logarithmic plot of the logarithm of the fraction of bare Ni clusters remaining at a certain H₂ concentration, f , versus the backpressure should give a straight line with a slope proportional to the rate constant. Such a plot is shown in Figure 4.1B. The good fit of the experimental data to the pseudo-first-order model indicates that the simple kinetic scheme outlined above is a reasonable approximation. Under the assumption that the reaction time is similar for all cluster sizes, the relative reactivity of Ni₄⁺, Ni₅⁺, and Ni₆⁺ toward H₂ scales as 1:65:85. This differs significantly from the ratio of the rate constants for the formation of Ni₅D₂⁺ and Ni₆D₂⁺ measured under single collision conditions (0.15 10⁻¹⁰ cm³s⁻¹ and 2.3 10⁻¹⁰ cm³s⁻¹, respectively).^[121] These differences can be understood by a rapid stabilization of the complex via collisional thermalization in the reaction channel, which is missing under single collision conditions.

Consistent with the high reactivity of Ni₅⁺ and Ni₆⁺, collision induced dissociation experiments have found no significant barriers for the formation of Ni₅D₂⁺ and Ni₆D₂⁺. Ni₄D₂⁺ is not stable after formation under single collision conditions.^[121] Barriers to the formation of M_{*n*}D₂ complexes have been found for cobalt and iron clusters of certain size.^[119, 120, 135, 140] It is possible that these barriers lead to a stabilization of a precursor state to dissociation in which the hydrogen is molecularly coordinated. However, such a state has never been directly observed experimentally.

To probe how hydrogen is bound in Ni₄H₂⁺, Ni₅H₂⁺, and Ni₆H₂⁺, the vibrational spectra of these complexes were recorded under conditions such that only complexes with a single H₂ molecule were present in the molecular beam. Because Ni₄⁺ is much less reactive than Ni₅⁺ and Ni₆⁺, different conditions had to be used to measure the vibrational spectra of these three complexes. The experimental vibrational spectra of Ni_{*n*}H₂⁺/Ni_{*n*}D₂⁺ ($n = 4-6$) complexes are shown in black in Figure 4.2. For the complexes with 5 and 6 Ni atoms, intense absorption bands are observed in the 1000-1500 cm⁻¹ range, implying that the H is predominantly dissociatively bound in bridging or face sites.^[164] For the Ni₄D₂⁺ complex, a band located at 2460 cm⁻¹ is observed, proving that there is at least one isomer present in which the D₂ molecule is molecularly bound. The frequency of the D-D stretch band is shifted considerably to lower frequency compared to the frequency of free D₂ (2941 cm⁻¹). This implies that the molecularly bound D₂ molecules must be chemisorbed since physisorbed species only show small frequency shifts.^[155] A strong absorption band at 680 cm⁻¹ is observed in the spectrum of Ni₄H₂⁺, but not in the spectra of Ni₅H₂⁺ and Ni₆H₂⁺, which again points to a different binding of the hydrogen in Ni₄H₂⁺ compared to Ni₅H₂⁺ and Ni₆H₂⁺. Based on the findings for saturated Ni_{*n*}H_{*m*}⁺ complexes (chapter 3), this band can be assigned to the Ni-(H₂) stretch vibration, $\nu(\text{Ni}-(\text{H}_2))$. Comparison of the IR-MPD spectrum with simulated spectra supports this assignment. The molecular adsorption of H₂ on Ni₄⁺ is remarkable as sites for dissociatively bound H atoms are available and that the dissociative chemisorption of H₂ on nickel surfaces does not proceed via a molecular precursor state.

To obtain information on adsorption geometries and bond energies, DFT calculations were performed. Species with molecular or dissociatively bound H

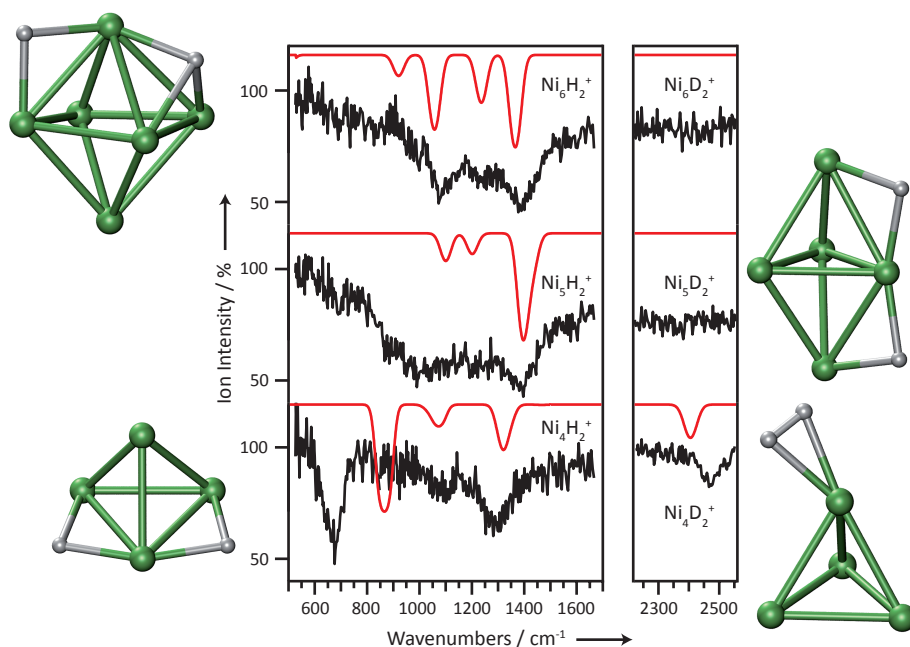


Figure 4.2. Experimental (black) and simulated (red) spectra of Ni₄H₂⁺, Ni₅H₂⁺ and Ni₆H₂⁺ (bottom to top). The corresponding geometries are shown next to the spectra. The simulated spectrum of Ni₄H₂⁺ is a linear combination with a ratio of 4:1 of the spectra of the two isomer with molecular H and dissociated H respectively.

are found to be (local) energetic minima. Upon substitution of H by D, all modes, except the Ni–Ni modes, scale down in frequency by a factor close to $\sqrt{2}$ ($\pm 1.2\%$). The energy differences between isomers are small, typically $\Delta E < 0.2$ eV, which is within the expected accuracy of the calculations. Hence, a ground state geometry cannot be assigned based on energetic considerations alone. Simulated vibrational spectra that provide reasonable agreement with the experimental spectra are shown in Figure 4.2 (red) together with the corresponding optimized cluster geometries. Note that the actual structures can be different from the ones shown in Figure 4.2. For Ni₄H₂⁺, two isomers are required to account for all the absorption features observed in the experimental spectrum (see below). Relative energies, geometries, and vibrational spectra of other isomers of Ni₄H₂⁺, Ni₅H₂⁺, and Ni₆H₂⁺ can be found in Figures 4.3, 4.4 and 4.5, respectively. In agreement with experiment, the hydrogen atoms are dissociatively bound in the isomers of Ni₅H₂⁺ and Ni₆H₂⁺ whose vibrational spectra are in best agreement with the experimental spectra. Complexes with molecularly bound H₂ are at least 0.4 eV higher in energy. In contrast, for Ni₄H₂⁺, the lowest energy isomer identified in the calculations is the complex with molecularly bound H₂. The binding energy of the H₂ molecule is calculated to be 0.5 eV. The calculated frequency of $\nu(\text{D-D})$ is too low compared to experiment, while the calculated frequency of $\nu(\text{Ni}-(\text{H}_2))$ is too high. Both of these observations

imply that the calculations overestimate the Ni - H₂ bond strength. This was also observed for the saturated nickel-hydride complexes (see paragraph 3.4.6). In the experimental spectrum of Ni₄H₂⁺ there is a weak absorption band at ~1090 cm⁻¹, for which the complex with molecular hydrogen cannot account. It is likely that this band is due to the presence of a second, less abundant isomer in which the hydrogen is dissociatively bound. Indeed, the calculations show that there are at least two isomers that have an absorption band around 1090 cm⁻¹ and which are iso-energetic (within the accuracy of the calculations, $\Delta E = 0.1$ eV) with the complex containing molecularly bound H₂. Hence, it is likely that at least two isomers of Ni₄H₂⁺, one with molecularly bound and one with dissociatively bound hydrogen, coexist in the molecular beam. The structures of the complex with molecularly bound hydrogen and of a nearly iso-energetic isomer with dissociatively bound hydrogen are shown in Figure 4.2, together with a simulated vibrational spectrum that is a linear combination with a 4:1 ratio (isomer with molecular H versus the isomer with dissociated H) of the spectra of the two individual isomers (Figure 4.3).

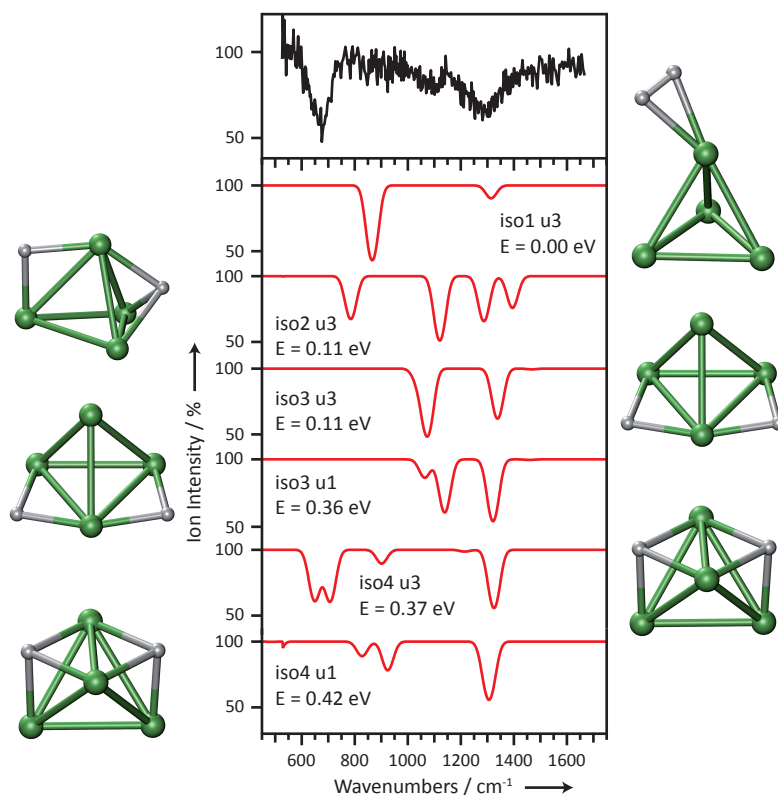


Figure 4.3. Experimental (black) and simulated (red) vibrational spectra of Ni₄H₂⁺ complexes in the 450-1750 cm⁻¹ range. Relative energies of the isomers are given in eV. The letter 'u' denotes the number of unpaired electrons. The corresponding cluster structures are shown next to the spectra.

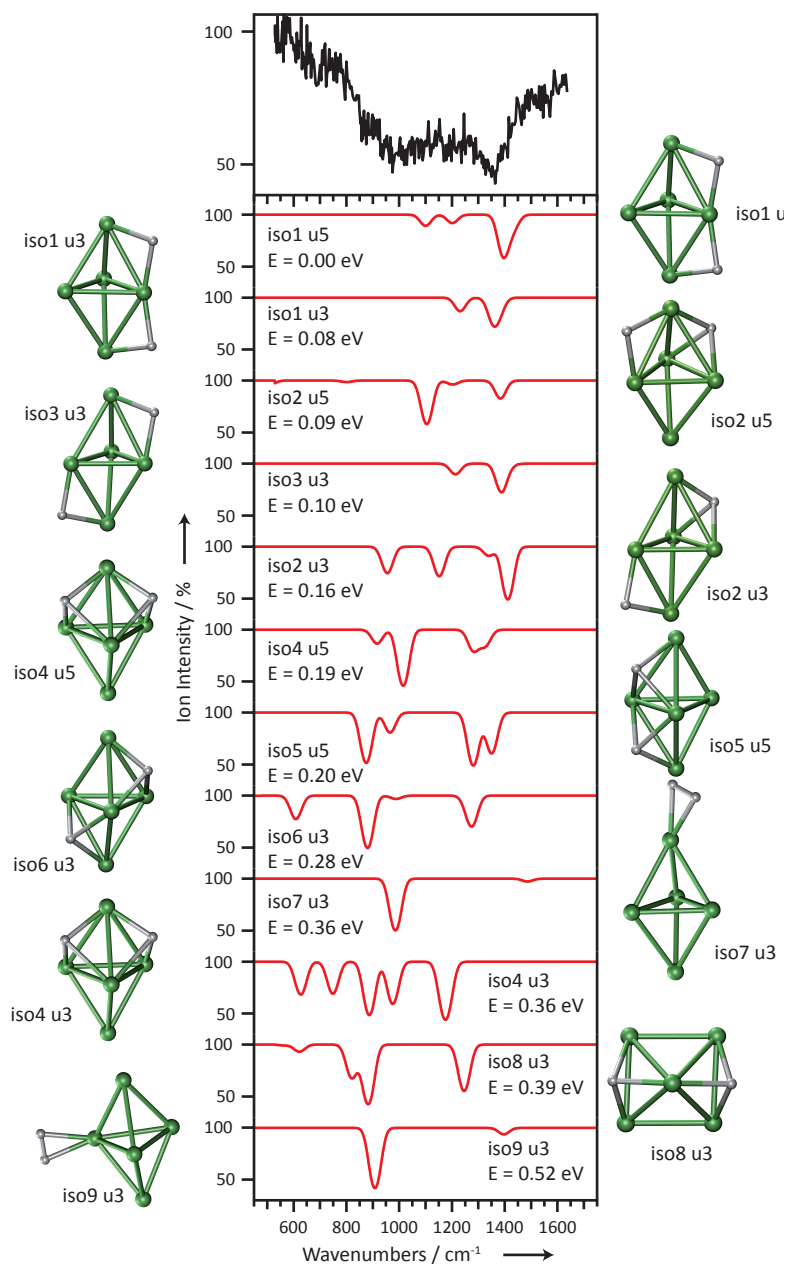


Figure 4.4. Experimental (black) and simulated (red) vibrational spectra of Ni₅H₂⁺ complexes in the 450-1750 cm⁻¹ range. Relative energies of the isomers are given in eV. The letter 'u' denotes the number of unpaired electrons. The corresponding cluster structures are shown next to the spectra.

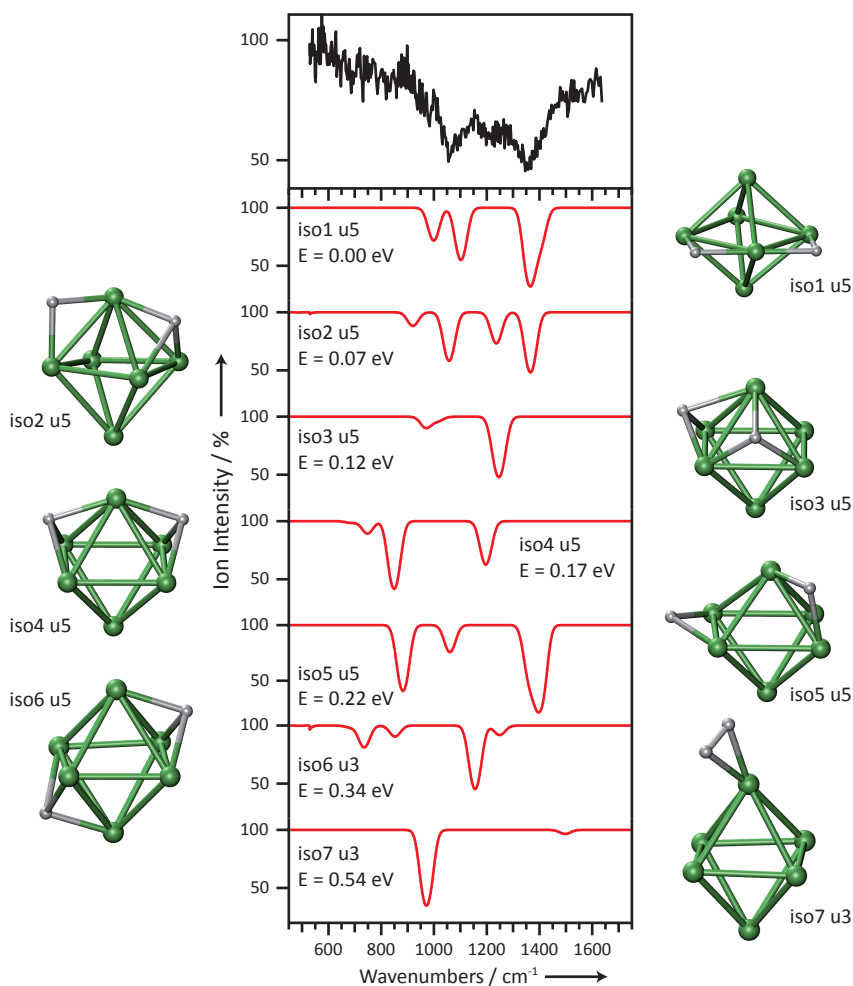


Figure 4.5. Experimental (black) and simulated (red) vibrational spectra of Ni_6H_2^+ complexes in the 450-1750 cm^{-1} range. Relative energies of the isomers are given in eV. The letter 'u' denotes the number of unpaired electrons. The corresponding cluster structures are shown next to the spectra.

It is interesting to speculate about the reason why two isomers of Ni_4H_2^+ co-exist in the molecular beam. In Figure 4.6, two schematic one-dimensional potential energy curves for the interaction of a single H_2 molecule with a metal (cluster) are shown. In general, (Figure 4.6 A), when a H_2 molecule approaches a transition metal, it will first experience a weak Van-der-Waals attraction. Typical energies associated with these interactions are below 0.1 eV and H_2 can be physisorbed at sufficiently low temperatures^[165] (not indicated). When the H_2 molecule moves closer to the metal surface, the orbitals of H_2 hybridize with metal d -orbitals to reduce the Pauli repulsion between the filled molecular orbital of the H_2 molecule and the electrons of the

metal. This leads to the formation of a chemical bond between the H₂ molecule and the metal, i.e. the H₂ molecule becomes molecularly bound. Depending on the extent of the hybridization, the crossing between the potential wells corresponding to dissociative and molecular chemisorption can either be above or below zero energy. If the crossing occurs below zero energy (dashed line Figure 4.6 A), the hybridization leads to dissociation of the H₂ molecule and subsequent atomic adsorption. This is the typical behavior of H₂ adsorption on extended transition metal surfaces. For Ni₅⁺ and Ni₆⁺, it has been shown that D₂ adsorption is a non-activated process.^[121] Furthermore, we find that H₂ adsorbs dissociatively on Ni₅⁺ and Ni₆⁺. This suggests that H₂ adsorption on these clusters follows the same path as H₂ adsorption on extended Ni surfaces. If the crossing occurs at positive energies (dotted line Figure 4.6 A), an activation barrier to dissociation is present and the complex can become 'trapped' in a state where the H₂ molecule is molecularly chemisorbed. This might be the case for the Ni₄H₂⁺ complex. The presence of two isomers of Ni₄H₂⁺ can be explained from the fact that at finite temperatures the clusters will have an internal

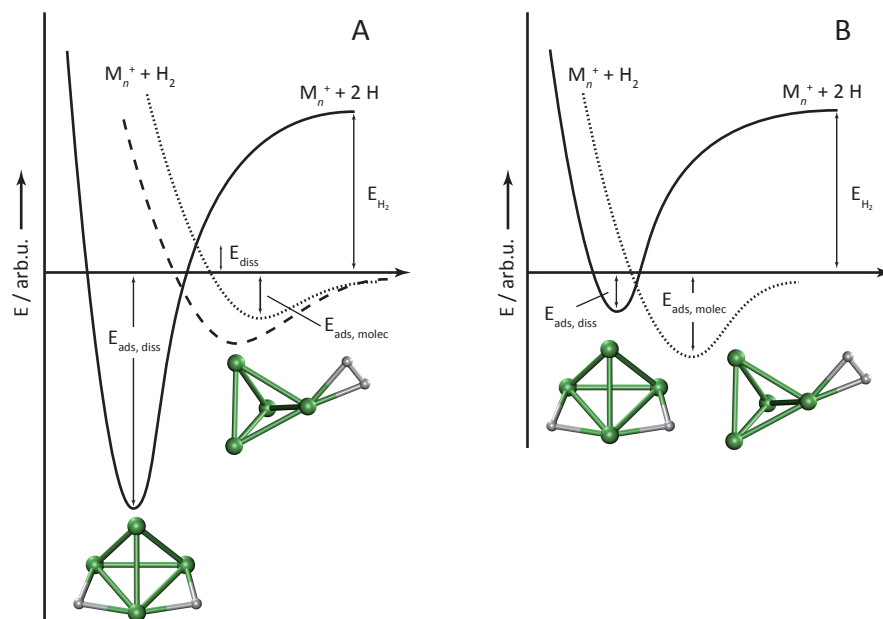


Figure 4.6. Two schematic one-dimensional potential energy diagrams for the interaction of a single H₂ molecule with a metal cluster. The solid lines give the potential energy of a metal cluster interacting with two single H atoms. The dotted and dashed lines represent the potential energy for the interaction between a metal cluster and a H₂ molecule. **A.** Conventional diagram. H₂ is dissociatively bound in the global minimum structure. The dissociation of H₂ can be an activated or a non-activated process (crossing of dotted–solid and dashed–solid lines respectively). If an activation barrier is present (crossing at positive energy), species with molecularly bound H₂ can become 'trapped' in the local energetic minimum. **B.** Alternative energy diagram for Ni₄H₂⁺ if the isomer with molecularly coordinated H₂ is the global minimum structure. Both schemes can account for the two isomers of Ni₄H₂⁺.

energy distribution described by the Boltzmann factor. For some of the clusters, the internal energy will be large enough to surmount the activation barrier, leading to complexes with dissociatively bound H, whereas others remain trapped in the local energetic minimum.

Up to now it is assumed that species with dissociatively coordinated H correspond to the global energetic minimum structure (which is the case for hydrogen adsorbed on extended metal surfaces). However, for small metal clusters the complex with molecularly chemisorbed H₂ could correspond to the global energetic minimum (Figure 4.6 B). Complexes with dissociatively bound H then correspond to local energetic minima. At 0 K the H₂ molecule will be molecularly bound in all complexes. At finite temperatures there will be a Boltzmann distribution between complexes with dissociatively and molecularly coordinated hydrogen, thus explaining the co-existence of the two complexes in the molecular beam.

Both schematic energy diagrams shown in Figure 4.6 can account for the co-existence of the two isomers of Ni₄H₂⁺. In principle, the potential energy surface for the interaction of H₂ with Ni₄⁺ can be calculated using quantum mechanical methods, allowing for a decisive assignment of the reaction path. As outlined above, the DFT based calculations find that the complex with molecular coordinated H has a lower energy than isomers with dissociatively bound H when the BP86 parameterization of the exchange-correlation is used. However, the differences in energy are small ($\Delta E = 0.1$ eV). This implies that for Ni₄H₂⁺ DFT based calculations cannot be used to reliably construct a potential energy diagram as given in Figure 4.6. Possibly, higher-level computational methods such as multi-reference-configuration-interaction or coupled-cluster perform significantly better for this complex. From the experimental side, temperature dependent vibrational spectroscopy studies might be able to provide additional information on the potential energy landscape of the Ni₄H₂⁺ complex.

4.5 Conclusions

It is demonstrated that a H₂ molecule can bind molecularly on Ni₄⁺ but that it binds exclusively dissociatively on Ni₅⁺ and Ni₆⁺. Furthermore, the adsorption behavior correlates with the relative reactivity of the metal clusters toward H₂. This correlation implies that the dissociative chemisorption of H₂ on Ni₄⁺ is an indirect process; for other small nickel clusters low barriers might exist as well. In that case, the rate-determining step is the conversion of the molecular precursor state to the final state where the hydrogen is dissociatively bound. The Ni₄H₂⁺ isomer with molecular bound H₂ could be considered a model for a precursor state to dissociation.

Effects of Co-adsorption of H₂ and CO on Cobalt Clusters §

Abstract

The effect of co-adsorption of hydrogen on the binding of carbon monoxide to cobalt clusters is studied by recording infrared multiple photon dissociation spectra of Co_nH_mCO⁺ clusters as a function of hydrogen coverage. It is found that co-adsorption of H₂ leads to an increase in the C–O bond strength of adsorbed carbon monoxide, as evidenced by an increase of the C–O stretch vibration. Qualitatively, the adsorbed hydrogen reduces the electron density of the metal particle that is available for back-donation to the carbon monoxide, hence leading to the observed increase in the C–O bond strength. To obtain quantitative information, a model describing the charge and size dependence of CO adsorbed on late transition metal clusters is extended to incorporate the effect of co-adsorption of H₂. Each adsorbed hydrogen atom is found to reduce the electron density available for back-donation by an amount depending on the cluster size.

§ Adapted from: I. Swart, A. Fielicke, D.M. Rayner, G. Meijer, B.M. Weckhuysen, and F.M.F. de Groot, *Controlling the Bonding of CO on Cobalt Clusters by Coadsorption of H₂*, *Angew. Chem. Int. Ed.*, **46**, 5317 (2007)

5.1 Introduction

Reactions of small molecules with transition metal particles have attracted considerable interest over the past decades since they can provide a conceptual framework for applications such as heterogeneous catalysis and hydrogen storage.^[156, 166-168] Especially the reaction of H₂ and CO with supported iron and cobalt particles has been widely studied due to its relevance to the Fischer-Tropsch process in which a mixture of H₂ and CO is converted into long chain hydrocarbons. In this process, the breaking of the strong C–O bond is an important step. Upon adsorption of CO on a transition metal, the electron density in orbitals that are antibonding with respect to the C–O bond is increased by transfer of electron density from the metal, ultimately leading to the weakening, or activation, of the C–O bond. This activation and therefore the reactivity of CO toward hydrogenation sensitively depend on adsorption geometry and on the electron density of the metal particle. Consequently, vibrational spectroscopy of CO adsorbed on metal particles can be used to characterize binding sites and to probe the electron density of the metal particle.

The reactions of CO and H₂ with cobalt clusters in the gas-phase have been studied, but no investigations regarding the co-adsorption of both molecules have been reported. Furthermore, detailed information on adsorbate binding sites and metal cluster electron densities is scarce. This kind of information is essential when trying to obtain fundamental insight into the elementary steps of adsorption processes. Recently, InfraRed Multiple Photon Dissociation (IR-MPD) spectroscopy was used to characterize the size and charge dependence of the C–O stretch vibration, $\nu(\text{CO})$, of cobalt mono-carbonyl complexes in the gas-phase.^[76] The main findings are as follows. Carbon monoxide binds exclusively to one atom in cobalt clusters (atop bound CO) and the C–O bond strength strongly depends on the charge state and the size of the cluster to which the CO molecule is bound. The dominating factor in the behavior of $\nu(\text{CO})$ is the availability of electron density for back-donation from the metal to the anti-bonding $2\pi^*$ orbital of CO. Electrostatic effects play a significant but minor role. For charged clusters, the evolution of $\nu(\text{CO})$ as a function of size is related to the dilution of charge density at the binding site. For details on the hydrogen chemisorption on cobalt clusters, the reader is referred to chapter 3.

In contrast to the adsorption of either H₂ or CO, no studies are available on the effects of co-adsorption of these two molecules. This is the topic of this chapter. IR-MPD spectroscopy is used to study the effect of adsorbed hydrogen on the binding of CO to cationic cobalt clusters. By combining these results with the available information on cobalt mono-carbonyl complexes, and cobalt-hydride clusters, fundamental insight into the effects of co-adsorption of H₂ and CO is obtained.

5.2 Experimental

IR-MPD spectroscopy was used to measure the vibrational spectra of (hydrogenated) mono-carbonyl complexes in the range of the C–O stretch vibration ($1600 - 2200 \text{ cm}^{-1}$) and in the range of the M–H stretch and deformation modes ($900 - 1500 \text{ cm}^{-1}$). Details of the IR-MPD mechanism and the experimental setup can be found in chapter 2. Monocarbonyl complexes with varying hydrogen coverages were generated by adjusting the H_2/CO ratio and the opening time of the second pulsed valve.

5.3 Results and Discussion

The IR-MPD spectra of $\text{Co}_{11}\text{H}_m\text{CO}^+$, with $m = 0, 2, 4, 10,$ and 12 (bottom to top) are shown in Figure 5.1.A. No absorption bands were detected in the $1600 - 1950 \text{ cm}^{-1}$ region, indicating that CO is exclusively atop (μ^1) bound to hydrogen covered Co_n^+ clusters. This has been found earlier for CO adsorption on bare Co_n^+ clusters.^[76] H_2

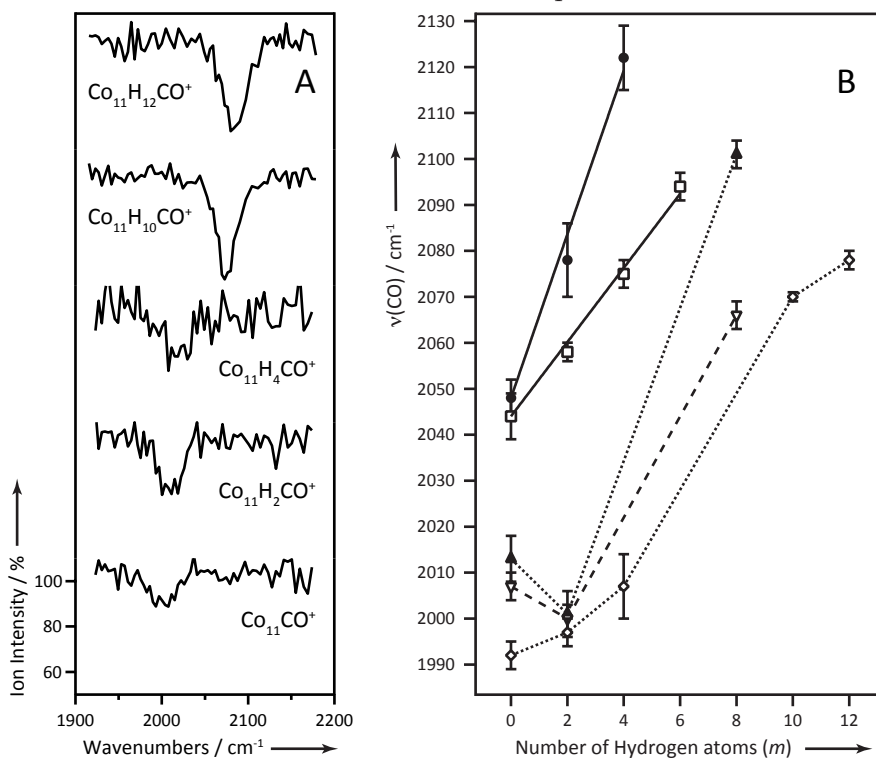


Figure 5.1. A) IR-MPD spectra of $\text{Co}_{11}\text{H}_m\text{CO}^+$ complexes with 0,2,4,10 and 12 co-adsorbed hydrogen atoms in the range of the C–O stretch vibration. B) Frequency of the C–O stretch vibration of mono-carbonyl complexes as a function of the number of co-adsorbed hydrogen atoms for complexes containing 4(\bullet), 5(\square), 7(\blacktriangle), 9(∇), and 11(\diamond) cobalt atoms. The solid lines give fits of the data to equation 5.3. The dashed lines indicate trends.

Table 5.1. Values of $\nu(\text{CO})$ for cobalt mono-carbonyl (Co_nCO^+) and hydrogen saturated mono-carbonyl ($\text{Co}_n\text{H}_m\text{CO}^+$) complexes for $n = 4-20$. The error bars correspond to two times the standard deviation given by the fitting procedure.

n	m	$\text{Co}_n\text{H}_m\text{CO}^+$ (cm^{-1})	n	m	$\text{Co}_n\text{H}_m\text{CO}^+$ (cm^{-1})
4	0	2048 ± 5	11	0	1992 ± 3
	2	2078 ± 8		2	1997 ± 3
	4	2122 ± 7		4	2007 ± 7
5	0	2044 ± 5		10	2070 ± 1
	2	2058 ± 2		12	2078 ± 2
	4	2075 ± 3	12	0	1985 ± 4
	6	2094 ± 3		12	2081 ± 2
6	0	2030 ± 7	13	0	1987 ± 3
	2	2042 ± 3		14	2079 ± 3
	6	2094 ± 3	14	0	1978 ± 3
7	0	2013 ± 5		14	2077 ± 2
	2	2001 ± 5	15	0	1974 ± 3
	8	2101 ± 3		14	2078 ± 4
8	0	2006 ± 5	16	0	1975 ± 2
	2	1999 ± 6		16	2015 ± 5
	8	2099 ± 2	17	0	1974 ± 2
9	0	2007 ± 3		16	2063 ± 2
	2	2000 ± 3	18	0	1970 ± 3
	8	2066 ± 3		16	2024 ± 5
10	0	1999 ± 5	19	0	1970 ± 3
	2	2006 ± 4		14	2028 ± 2
	10	2088 ± 2	20	0	1967 ± 3
				20	2066 ± 4

adsorbs dissociatively on cationic Co clusters.^[120] In Figure 5.1.B the value of $\nu(\text{CO})$ is plotted as a function of the number of co-adsorbed hydrogen atoms for complexes containing 4, 5, 7, 9, and 11 Co atoms. Upon increasing H₂ coverage, the C–O stretch frequency shifts to higher energy. This behavior was observed for all cluster sizes studied, except for Co_7^+ , Co_8^+ and Co_9^+ for which a decrease of $\nu(\text{CO})$ upon adsorption of the first H₂ molecule was observed. The C–O stretch vibration of the hydrogen-saturated complexes ($\text{Co}_7\text{H}_8\text{CO}^+$, $\text{Co}_8\text{H}_8\text{CO}^+$ and $\text{Co}_9\text{H}_8\text{CO}^+$) was again higher than the value of the corresponding mono-carbonyl complex. The initial decrease of $\nu(\text{CO})$ correlates with a particular low reactivity of these clusters toward hydrogen.^[169] For the small clusters, the shift of $\nu(\text{CO})$ is linear with hydrogen coverage and the slope decreases as the clusters become larger. Larger clusters readily react with H₂ and it

was experimentally not possible to measure $\nu(\text{CO})$ at intermediate hydrogen coverage for these clusters. The experimentally determined values of $\nu(\text{CO})$ for $\text{Co}_n\text{H}_m\text{CO}^+$ complexes with $n = 4\text{--}20$, are given in Table 5.1. These values are determined from a least squares fitting procedure of the experimental spectra with a Gaussian function.

In organometallic chemistry the classical picture of bonding between a transition metal atom and a CO molecule consists of donation of electron density from the 5σ orbital of CO to the metal and back-donation of electron density from the metal d -orbitals to the $2\pi^*$ orbital of the CO molecule.^[55, 56, 170] This $2\pi^*$ orbital is anti-bonding with respect to the C-O bond. The frequency of the C-O stretching vibration is directly related to the strength of the C-O bond and therefore also to the population of the $2\pi^*$ orbital. Upon adsorption of CO on a bare transition metal, the C-O bond usually becomes weaker due to the increased population of the anti-bonding $2\pi^*$ orbital, which is reflected in a shift of $\nu(\text{CO})$ to lower frequencies compared to its gas-phase value. As can be seen in Figure 5.1.B, the co-adsorption of H_2 molecules generally leads to an increase in C-O bond strength.

Qualitatively, upon adsorption of H_2 on Co_nCO^+ complexes some electrons of the metal cluster become localized in Co-H bonds, making them unavailable for back-donation to the $2\pi^*$ orbital of CO.^[171, 172] Upon co-adsorption of H_2 , the population of the $2\pi^*$ orbital will therefore be reduced, which leads to a higher C-O stretching frequency. This assumption has been used earlier to explain the shift in $\nu(\text{CO})$ for CO bound to hydrogen covered Ni and Co particles on surfaces.^[173, 174]

By using the recently measured charge dependence of $\nu(\text{CO})$ in cobalt cluster mono-carbonyl complexes,^[76] it is possible to estimate the amount of charge transferred into the Co-H bonds. For example, one finds for $\text{Co}_{11}\text{CO}^{+/0/-}$ values for $\nu(\text{CO})$ of 1992, 1943 and 1868 cm^{-1} , respectively, resulting in a shift of $\sim 62\text{ cm}^{-1}/z$ where ze is the charge on the cluster (e the elementary charge). This can be compared to the dependence of $\nu(\text{CO})$ on the number of co-adsorbed hydrogen atoms (m), as shown in Figure 5.1.b, which gives for $\text{Co}_{11}\text{H}_m\text{CO}^+$ an average shift of $\sim 8\text{ cm}^{-1}$ per hydrogen atom. Binding of a single hydrogen atom therefore has, on average, the same effect as adding $8/62 = 0.13$ of a single positive charge to the cluster.

More generally we can extend the quantitative model^[76] for the charge dependence of $\nu(\text{CO})$ in late transition metal carbonyl clusters to present a global picture of charge transfer in $\text{Co}_n(\text{CO})\text{H}_m^+$ complexes. The model incorporates the electrostatic interaction between the charge of the cluster and the CO dipole and the effect of donation of electron density from the metal to the $2\pi^*$ orbital of CO. The cluster size plays a role due to delocalization of charge over the cluster surface. The validity of this assumption has been shown before.^{[76][175]}

The effect of co-adsorption of H_2 can be incorporated in the model by introduction of an additional term in the expression that describes the population of the $2\pi^*$ orbital, $P(2\pi)$ of the CO molecule. The extended equation reads:

$$P(2\pi) = P(2\pi)_\infty - \frac{\gamma z}{n_s} - \frac{\gamma \sum_i^{n_s} \delta_i}{n_s} \quad 5.1$$

The first term on the right hand side of equation 5.1, $P(2\pi)_{z,r}$, represents the population of the $2\pi^*$ orbital of a CO molecule adsorbed on a cluster of infinite size. The second term describes the change in this number due to the charge ($z\ e$) of the cluster that is distributed over all surface atoms and is inversely proportional to the number of surface atoms, n_s , with a proportionality constant γ . Localization of electron density in the i th Co-H bond is postulated to have the same effect as increasing the charge of the Co_nCO^+ complex by $\delta_i\ e$. We allow δ to depend on i to include possible variation in Co-H bonding with coverage. Following through as described in ref. 9 one then obtains the following expression for $\nu(\text{CO})$:

$$\nu(\text{CO}) = \nu(\text{CO})_0 + \frac{\gamma^* \sum_i^{n_H} \delta_i}{n_s} \quad 5.2$$

with $\nu(\text{CO})_0 = \nu_\infty + \Delta\nu_{ES} + \gamma^* z/n_s$ the frequency for the specific cluster size without H, and $\gamma^* = \nu_\infty \beta \gamma / (2F_\infty)$. Here ν_∞ is the extrapolated value of $\nu(\text{CO})$ for CO adsorbed on an infinite cluster (with C-O stretch force constant F_∞), $\Delta\nu_{ES}$ is the shift due to the electrostatic effect and β a proportionality constant relating the population of the $2\pi^*$ orbital to the C-O stretching force constant.

If the effects of the subsequently added hydrogen ligands on $P(2\pi)$ are identical, δ_i will have the same value for each co-adsorbed hydrogen atom. This appears to be the case for small clusters with n up to 6 where $\nu(\text{CO})$ shifts linearly with the number of co-adsorbed hydrogen atoms. In this case, equation 5.2 can be simplified to the form:

$$\nu(\text{CO}) = \nu(\text{CO})_0 + \frac{\gamma^* n_H \delta}{n_s} \quad 5.3$$

where $\gamma^* \delta/n_s$ is the shift induced per adsorbed hydrogen atom and can be evaluated from the slope of the plot of $\nu(\text{CO})$ against n_H . The solid lines in Figure 5.1.B indicate fits of the data to equation 5.3. For the larger clusters, there are too few points to establish with certainty that the linear relationship continues to hold, but one can proceed using the shift measured for the saturated complexes to evaluate an average value of δ directly from equation 5.3 using the values of $\nu(\text{CO})_0$ and γ^*/n_s as reported in the literature.^[76] With our measurements the amount of electron transfer to co-adsorbed hydrogen can be quantified. The values of δ for clusters with 4-20 metal atoms are given in Figure 5.2. Values of δ range from 0.09 to 0.25 electrons per hydrogen atom depending on cluster size. There is no obvious correlation of this size dependence with what is known about the geometric or electronic structure of Co_n^+ clusters. The observed linear relationship of $\nu(\text{CO})$ with hydrogen atom coverage demonstrates that CO is not influencing charge transfer between the cluster and hydrogen ligands to any appreciable extent. Therefore, CO can be used as a probe for the electron density within the cluster complex, at least for the $\text{Co}_n(\text{CO})\text{H}_2^+$ complexes.

Equation 5.3 predicts that as long as the ratio n_H/n_s is significant, a shift in $\nu(\text{CO})$ will be observed. This implies that a shift in $\nu(\text{CO})$ should be observed even for CO

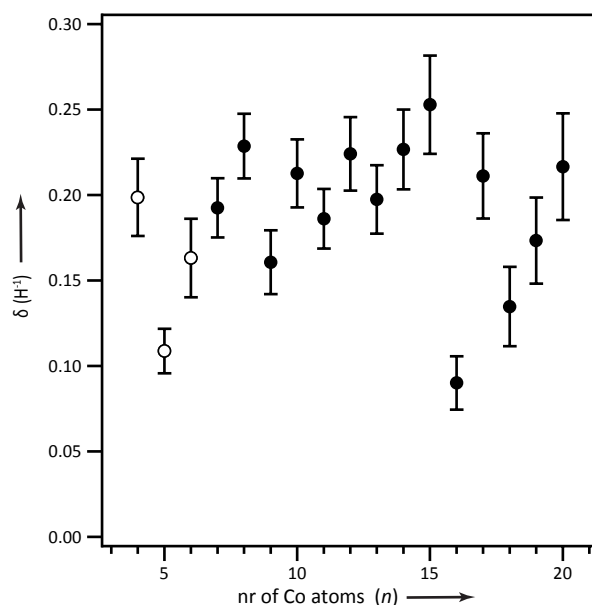


Figure 5.2. Averaged values of δ for Co_n^+ clusters ($n = 4 - 20$). Open symbols indicate values obtained from a fit of the data to equation 5.3, solid symbols indicate that only values of the mono-carbonyl and hydrogen saturated complexes have been used.

adsorbed on bigger particles if they are sufficiently covered with hydrogen. Indeed, a shift of $\nu(\text{CO})$ to higher frequency was observed for co-adsorption of CO and H_2 on $\text{Ru}/\text{Al}_2\text{O}_3$, Co/SiO_2 and on Ni surfaces,^[174, 176-181] for which it has also been found in DFT calculations.^[182]

This treatment ignores the observation that for $\text{Co}_7(\text{CO})\text{H}_2^+$, $\text{Co}_8(\text{CO})\text{H}_2^+$ and $\text{Co}_9(\text{CO})\text{H}_2^+$ an initial red shift in $\nu(\text{CO})$ is observed. Following the charge localization arguments outlined above, this implies that for these complexes more electron density is available on the metal compared to the mono-carbonyl complexes for donation into the $2\pi^*$ orbital of CO. The behavior exhibited by most of the complexes establishes that hydrogen atoms bound as hydrides increase $\nu(\text{CO})$, leading to the conclusion that hydrogen might be bound differently in the three exceptional cases. A possible explanation is that H_2 is molecularly bound in $\text{Co}_7(\text{CO})\text{H}_2^+$, $\text{Co}_8(\text{CO})\text{H}_2^+$, and $\text{Co}_9(\text{CO})\text{H}_2^+$. As demonstrated in chapter 4, a single H_2 molecule can be molecularly bound to a bare metal cluster and that this adsorption behavior can correlate with a low reactivity toward H_2 . Furthermore, molecular and dissociatively bound H_2 are known to co-exist on a Pd(210) surface with a hydrogen surface coverage below saturation.^[61] Non-classical hydrides, where H_2 binds molecularly are also known in organometallic chemistry.^[59] The bonding is characterized as a 3-centre, 2 electron σ interaction involving donation of charge from the H_2 to the metal centre. Indeed, molecularly bound H_2 on Pd(210) leads to a decrease of the surface work function.^[61] H_2 binding molecularly in $\text{Co}_7(\text{CO})\text{H}_2^+$, $\text{Co}_8(\text{CO})\text{H}_2^+$ and $\text{Co}_9(\text{CO})\text{H}_2^+$ can therefore be

expected to lower $\nu(\text{CO})$ as is observed. As shown in chapter 4, a single H₂ molecule can bind molecularly to a Ni₄⁺ cluster. However, given the prevailing consensus that H₂ binds dissociatively to transition metal clusters, this proposal is somewhat remarkable and warrants further study. The averaged values of δ for Co₇⁺, Co₈⁺ and Co₉⁺ obtained from the saturated complexes are similar to the values of the other sizes, suggesting that at hydrogen saturation all hydrogen is present in the form of hydrides.

5.4 Conclusions

In summary, it has been shown that the 3d electron density available for back-donation to an adsorbate can be controlled by co-adsorption of H₂ molecules. Each co-adsorbed hydrogen atom reduces the amount of electron density available for back-donation on average by 0.09 – 0.25 of an electron depending on cluster size. From a catalysis point of view, the co-adsorption of H₂ and CO on cobalt particles leads to a deactivation of CO toward dissociation. If there is to be a reaction of H₂ with CO on the cluster surface at higher temperatures, it is predicted that low H₂ coverage clusters will show the highest reactivity. The observed relationship between $\nu(\text{CO})$ with hydrogen atom coverage demonstrates that, at least for Co_{*n*}(CO) H₂⁺ complexes, CO is a suitable probe for the electron density. These results point to how the concepts of donation and back-donation developed in organic-metallic chemistry extrapolate to larger systems like clusters or even extended surfaces.

Effects of Co-adsorption of H₂ and CO on Vanadium Clusters §

Abstract

Structural information on hydrogen covered vanadium clusters, containing between 5 and 20 atoms, and their complexes with CO has been obtained with infrared multiple photon dissociation spectroscopy. The experimental work is complemented with density functional theory based calculations for the V₅ to V₉ cluster sizes. The non-dissociative or dissociative binding of CO on the metal clusters is detected by the presence or absence of the $\nu(\text{CO})$ stretching band in the infrared spectra. It is found that the CO molecule dissociates on bare vanadium clusters, while it adsorbs intact on all saturated hydrogen covered V₅₋₂₀⁺ clusters, with the distinctive exception of V₅⁺, V₉⁺, V₁₁⁺ and V₁₉⁺. It is shown that dissociative chemisorption is prevented when H atoms block the potential binding sites of the C and O atoms. Co-adsorption of H₂ does not have a significant electronic influence on the binding of CO to V_nH_m⁺ clusters, in contrast to co-adsorption of H₂ and CO on Co_n⁺ clusters.

§ Adapted from: I. Swart, A. Fielicke, B. Redlich, G. Meijer, B.M. Weckhuysen and F.M.F. de Groot, *Hydrogen-Induced Transition from Dissociative to Molecular Chemisorption of CO on Vanadium Clusters*, J. Am. Chem. Soc., **129**, 2516 (2007)

6.1 Introduction

The interaction of transition metal clusters in the gas-phase with CO and H₂ can provide information relevant to the Fischer-Tropsch synthesis, i.e. the reaction of CO with H₂ over supported metal nanoparticles to form long-chain hydrocarbons.^[29, 183] Using the interaction of a surface with an adsorbate as a starting point, one finds that, at room temperature, all metals to the left of the diagonal Co-Ru-Re in the periodic table dissociate CO.^[184] At elevated temperatures Co, Ru and Ni also dissociate CO and, for example, supported Ru, Co and Fe nanoparticles are used in the Fischer-Tropsch process.

The reaction of gas-phase clusters of the late transition metals Co, Ni, Rh, and Au with CO has been studied using IR spectroscopy at room temperature and, in analogy with supported nanoparticles and metal surfaces, non-dissociative chemisorption has been observed (also see chapters 6, 7, and 8).^[76, 78] In contrast it has been shown by a combined spectroscopy / Density Functional Theory (DFT) study that CO is dissociatively chemisorbed on small clusters of the early transition metal Nb.^[185] On neutral and charged vanadium clusters the adsorption of H₂, D₂ and CO has been studied using flow tube and ion trap techniques.^[117, 125, 131-134, 186, 187] From these and other studies it has been found that individual H₂ and CO molecules chemisorb dissociatively on clusters of the early transition metals V and Nb.^[122, 125, 131-133, 185, 186] The hydrogen binding geometries on cationic vanadium clusters has been extensively discussed in chapter 3.

In this chapter, the effects of co-adsorption of H₂ and CO on cationic vanadium clusters are discussed. Infrared Multiple Photon Dissociation (IR-MPD) spectroscopy is used to measure vibrational spectra of hydrogen saturated cationic vanadium clusters (V_{*n*}H_{*m*}⁺) and their complexes with CO (V_{*n*}H_{*m*}CO⁺) containing up to 20 vanadium atoms. The spectral range covered in the experiment includes the range of the C-O stretch vibration (1600-2200 cm⁻¹) and of the V-H stretch and deformation modes (700-1500 cm⁻¹). The experimental work is complemented with DFT calculations to obtain information on the geometry and chemical bonding in the saturated vanadium hydrides and the mono-carbonyl vanadium hydride complexes.

6.2 Experimental

IR-MPD spectroscopy was used to measure the IR spectra of (hydrogenated) mono-carbonyl complexes in the range of the C-O stretch vibration (1600 - 2200 cm⁻¹) and in the range of the V-H stretch and deformation modes (900 - 1500 cm⁻¹). Details of the IR-MPD mechanism and the experimental setup can be found in chapter 2. Hydrogen saturated monocarbonyl complexes were generated by using a H₂/CO ratio of 1000 and adjusting the gas flow through the valve.

6.3 Theoretical Method

The experimental spectra of several $V_nH_m^+$ and $V_nH_mCO^+$ complexes were complemented with DFT based calculations to obtain structural information. The calculations employed the BP86 parameterization of the exchange correlation functional and a triple zeta valence plus polarization (TZVP) basis set for all atoms, as implemented in the TURBOMOLE package.^[143]

The number of structural isomers dramatically increases with increasing cluster size. Because the number of structural isomer rapidly increases with cluster size, calculations have only been performed on complexes with less than 10 metal atoms. The following computational procedure was used. As a starting point for the calculations, the geometries of the bare vanadium clusters as identified by a combined theoretical/IR-MPD study^[63] were used and hydrogen atoms were placed in three fold hollow (μ_3) sites. For the mono-carbonyl complexes, CO molecules were coordinated to different metal atoms. For V_9^+ complexes, an additional similar metal cluster geometry was used that is degenerate in energy.^[63] First, the geometries of several cluster complexes were optimized for each cluster size. For every geometric isomer, optimizations were performed using different spin states. The optimization procedure was conducted without any symmetry restrictions. After the optimization procedure, the vibrational spectrum was calculated within the harmonic approximation. The calculated single photon absorption cross sections were convoluted with Gaussians with a width of 20 cm^{-1} and converted into depletion spectra using equation 2.12.

Charge density difference plots were created using the StoBe-deMon code.^[188] For these calculations also the BP86 exchange-correlation functional was used. For C and O, a TZVP basis set was used, while the basis set for V was of double-zeta quality (including a diffuse d).

6.4 Results and Discussion

Reactions of cationic vanadium clusters with molecular hydrogen lead to successive addition of H_2 molecules to the cluster until a cluster size specific coverage is reached (see chapter 3). Upon mixing 0.1% CO with the H_2 , also saturated vanadium hydrides on which a single CO molecule was absorbed, were produced. The IR-MPD spectra of $V_nH_m^+$ and $V_nH_mCO^+$ complexes are shown in Figure 6.1 for the size range for $n = 5-20$. Several absorption bands are identified between 700 and 1500 cm^{-1} . For the vanadium hydride complexes, no bands are observed at higher frequencies. The observed absorption bands are not in all cases fully resolved. $V_6H_8^+$ is the only complex in the size range ($n = 5-20$) studied that shows two well-resolved bands, implying a highly symmetric structure. Other clusters seem to have a less symmetric structure. IR-MPD spectra of bare vanadium clusters show exclusively modes below 450 cm^{-1} and the absorption bands in the $700 - 1500\text{ cm}^{-1}$ range are consequently assigned to V-H stretch and deformation vibrations.^[62, 63]

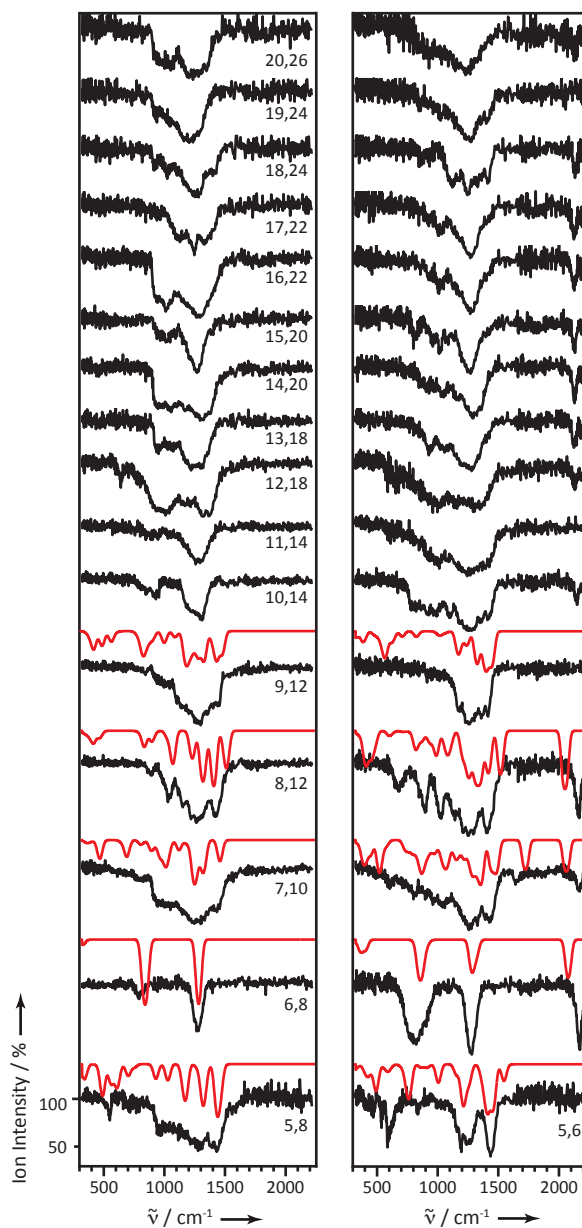


Figure 6.1. IR-MPD spectra (black) of fully saturated $V_nH_m^+$ (left panel) and the corresponding $V_nH_mCO^+$ complexes for $n = 5-20$ (right panel, bottom to top). Values of n and m for the fully saturated clusters are denoted as n,m in the graph. The spectra depicted in red are calculated IR spectra for the structures shown in Figure 6.2. The calculated spectrum of $V_7H_{10}CO^+$ is a linear combination of the two isomers depicted.

The far-infrared spectra of bare V_n^+ clusters compared to calculated IR spectra, led to the determination of the structures for small vanadium clusters.^[63] For many of the smaller clusters, there is a direct relation between the number of triangular facets on the bare clusters and the observed hydrogen saturation number. This strongly suggests that the hydrogen atoms mainly occupy threefold-hollow sites (μ_3 coordination) on the cluster surface. The only exception is the V_5^+ cluster, which has a hydrogen saturation stoichiometry of 8 but the metal cluster has 6 triangular facets. Therefore, at least some hydrogen has to be linear (μ_1) or two-fold (μ_2) coordinated to the metal cluster. Comparison of IR-MPD spectra and calculated vibrational spectra supports this assignment and will be discussed below.

The reaction of vanadium clusters with hydrogen in the presence of a small amount of CO (0.1%) yields mainly saturated vanadium cluster hydrides and, to a small fraction, their complexes with single CO molecules. Although H_2 and CO may compete in the reaction with the clusters, the high excess of H_2 relative to CO leads in most cases to the initial formation of the hydrogen saturated complexes like in the absence of CO. This indicates that the CO reacts mainly with pre-formed hydrogen covered clusters. The IR-MPD spectra of the complexes of cationic vanadium cluster hydrides with CO ($V_nH_mCO^+$) are shown in the right panel of Figure 6.1 for $n = 5-20$. The spectra of the $V_nH_mCO^+$ complexes in many cases resemble the spectra of the corresponding hydride complexes in the 700-1700 cm^{-1} range. Significant changes in this range are found in the spectra of the mono-carbonyl complexes with 5, 10, 11, 16, 17, 18, and 19 vanadium atoms. The hydrogen saturation stoichiometry of a V_5^+ cluster decreased from 8 to 6 in the presence of CO, indicating competitive adsorption of CO and H_2 . The spectra of CO adsorbed on vanadium clusters without hydrogen adsorption show no detectable absorption features in the range of the $\nu(CO)$ stretching vibration (1650-2200 cm^{-1}), indicating that CO is dissociatively chemisorbed on all bare vanadium clusters. In contrast, for most of the $V_nH_mCO^+$ complexes a band corresponding to the C-O stretching vibration of atop (μ_1) bound CO between 2120 and 2170 cm^{-1} is observed (see Figure 6.3). The presence of a $\nu(CO)$ band implies that it is possible to molecularly chemisorb CO on cationic vanadium clusters by co-adsorbing hydrogen molecules. On hydrogen covered cationic vanadium clusters containing 5, 9, 11 and 19 vanadium atoms no $\nu(CO)$ stretching band was observed, indicating dissociative chemisorption of CO on these cluster sizes.

To probe the origin of the size dependent stabilization of CO on hydrogen covered vanadium clusters with respect to the behavior on the bare metal clusters and to obtain information on the binding geometries of the adsorbed species, density functional theory (DFT) based calculations were performed on $V_nH_m^+$ and $V_nH_mCO^+$ complexes for $n = 5-9$.^[95, 189, 190] The ground state structures of several geometric isomers in different spin states have been optimized for every cluster complex. Note that in this process only a small portion of the configurational space is probed and it is possible that the actual structures are different from the structures shown in Figure 6.2. Structures and vibrational spectra of other isomers of $V_nH_m^+$ and $V_nH_mCO^+$ can be found in Appendices A and B, respectively. In many cases, several different

structures are close in energy and theory might not be accurate enough to correctly predict the most stable complex. Moreover, for kinetic reasons, the experiment may favor metastable species. The IR spectra are sensitive to the geometry and the electronic state of the cluster complex and the energy differences between low energy isomers are typically on the order of 0.1-1 eV. In case a structure could not be assigned based on energetic considerations alone, a structure was assigned based on the comparison of the calculated and experimental spectra. These selected structures correspond, in most cases, with the lowest energy isomers found in the calculations. The exceptions are V₅H₆CO⁺ and V₇H₁₀⁺ for which the calculations indicate that the lowest energy isomers have a triplet spin state. However, the experimental spectra is in better agreement with isomers with a singlet spin state that are only 0.12 eV and 0.20 eV higher in energy, respectively. This is close to the expected accuracy of the calculations. Typically the energy difference between spin states is small, less than 0.2 eV, and it is therefore not possible to assign a particular spin state to a cluster based on energetic considerations alone. The calculated cross-sections were converted to simulated depletion spectra as discussed in chapter 2, to allow for a direct comparison with the experimental spectra. The calculated spectra, folded with a Gaussian peak shape of 20 cm⁻¹ width, that are in best agreement with the experimental data are shown in Figure 6.1 directly above the experimental IR-MPD spectra. No frequency scaling is applied. The intensity of the calculated CO stretching peak in Figure 6.1 has been scaled to 50 % of the calculated value for ease of comparison. This intensity scaling accounts for the considerable lower IR laser intensity used in the dissociation experiments in the range of the ν(CO) vibration (15 mJ/pulse at 2200 cm⁻¹ vs. typically 60 mJ/pulse in the range from 600-1500 cm⁻¹). The intensity ratios between different peaks may be different in the calculated and experimental spectra due to the fact that the calculations give single photon cross sections, while IR-MPD is a multiple photon process.

The optimized cluster geometries as found from the calculations are shown in Figure 6.2. For the V_{*n*}H_{*m*}⁺ complexes, the vibrational spectra and structures of isomers whose vibrational spectra are in best agreement with the experimental spectra have been discussed in Chapter 3.4.3. The main conclusion for the vanadium hydrides is that hydrogen predominantly binds in three fold hollow sites, but that a minor number of two-fold coordinated hydrogen atoms can be present.

The calculations find that CO is dissociatively chemisorbed in V₅H₆CO⁺, in agreement with the competitive adsorption of CO and H₂ and the absence of detectable absorption features in the range of the ν(CO) stretching vibration (1650-2200 cm⁻¹). For V₆H₈CO⁺, all three fold hollow sites are occupied with hydrogen atoms and CO is molecularly chemisorbed to one metal atom. Its experimental IR spectrum is relatively simple, due to the high symmetry of the complex, and well reproduced by the calculations. For V₇H₁₀CO⁺ it was not possible to fully deplete the ion intensity by exciting the CO stretch mode at ~ 2160 cm⁻¹ when using full laser power, which is an indication for the presence of isomers. Moreover, it is the only cluster complex whose IR-MPD spectrum exhibits a weak absorption at 1650 cm⁻¹. For all other cluster complexes, the highest observed

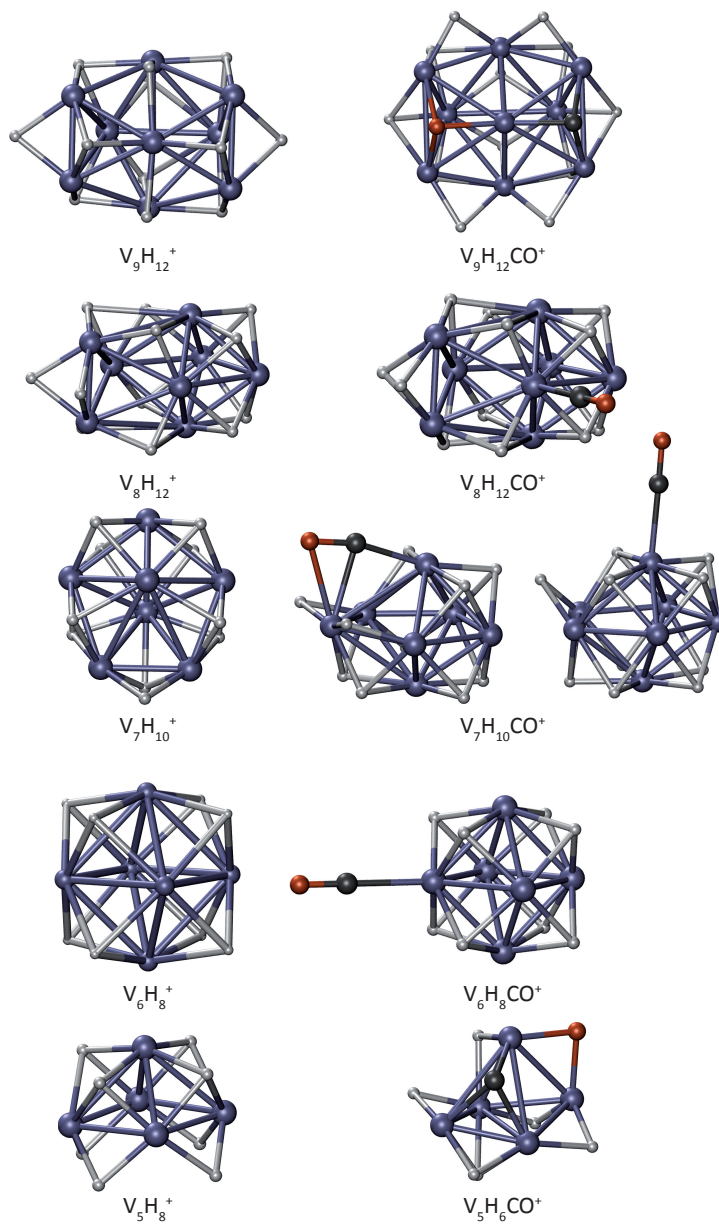


Figure 6.2. Geometric structures of isomers of saturated $V_nH_m^+$ (left) and $V_nH_mCO^+$ complexes (right) for $n = 5-9$ selected based on the comparison of experimental and calculated IR spectra.

V-H absorption band is around 1450 cm⁻¹. In the calculations, this feature can be accounted for by a CO molecule that is bridged bonded to this cluster in a tilted configuration (η^2 coordinated). The energy difference between configurations with atop and η^2 bound CO is only ~0.2 eV and it is likely that both isomers coexist in the molecular beam. Together with the experimental evidence, this proves that at least two different isomers of V₇H₁₀CO⁺ contribute to the spectrum shown in Figure 6.1. Structures with three-fold coordinated CO were found to be unstable and can therefore not be the origin of the band observed experimentally at 1650 cm⁻¹.

The geometry with the tilted bridge (η^2) bonded CO molecule could resemble a precursor state to dissociation that is stabilized by the co-adsorbed hydrogen atoms. In fact, structures similar to the complex with the η^2 bound CO molecule have been observed experimentally for CO adsorbed on Fe(100), Fe(001) and Cr(110).^[191-194] At the low temperatures employed in these experiments the precursor state for dissociation is stabilized. Tilted bridge (η^2) bound CO molecules have also been predicted to play an important role in the dissociation of CO on transition metals.^[195, 196]

For V₈H₁₂CO⁺, good agreement between the calculated and the experimental IR spectrum is obtained for a structure where ten hydrogen atoms bind in three fold hollow sites while two hydrogen atoms are bridge bonded. The band pattern that is observed experimentally is also reproduced by the calculations. CO is molecularly chemisorbed to one of the vanadium atoms. For V₉H₁₂CO⁺ no absorption band in the range of the CO stretch vibration was observed, indicating dissociative chemisorption of CO. Bare V₉⁺ has 14 three-fold hollow sites,^[63] while the highest hydrogen saturation number that could be achieved under our experimental conditions was 12. As can be seen from the calculated geometry of V₉H₁₂⁺ (Figure 6.2), 2 hydrogen atoms are coordinated in a convex site spanned by 4 vanadium atoms, effectively blocking 2 three fold hollow sites. The adsorption energy of an additional hydrogen molecule is not enough to cause a rearrangement of the V₉H₁₂⁺ cluster. Upon adsorption of CO, the hydrogen ligands can undergo a rearrangement, as is indicated by the calculated cluster geometries, and CO adsorbs dissociatively. Complexes with dissociated CO will always be lower in energy due to the formation of strong V-O and V-C bonds. In the case of V₉H₁₂CO⁺, our calculations indicate that geometries with molecular chemisorbed CO are more than 1.75 eV (170 kJ/mol) higher in energy than geometries with dissociatively chemisorbed CO. This implies that in the absence of energetic barriers, CO will be dissociatively chemisorbed in V₉H₁₂CO⁺.

The mechanism of CO dissociation is thought to involve tilted precursor states.^[196] If the surface is completely covered with hydrogen, these tilted precursor states cannot form, nor are there sites available for the C and O atom, leading to molecular instead of to dissociative chemisorption. Only for vanadium clusters where the hydrogen saturation stoichiometry matches the number of triangular facets (clusters with 6, 7, and 8 vanadium atoms) a $\nu(\text{CO})$ stretch vibration is observed.

Clusters with 5, 9, 11 and 19 V atoms do not show a band in the range of the $\nu(\text{CO})$ stretch vibration. For V₅H_{*m*}⁺, the saturation stoichiometry (*m*) is 8. However, in the

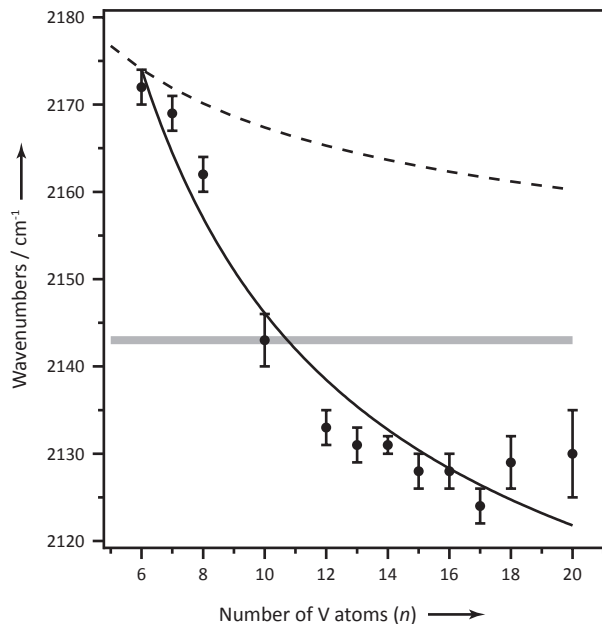


Figure 6.3. Frequency of the $\nu(\text{CO})$ vibration for $\text{V}_n\text{H}_m\text{CO}^+$ clusters as a function of cluster size. The dashed line gives the contribution of the electrostatic effect to the size evolution of $\nu(\text{CO})$ while the solid line represents a fit to equation 6.1. The gray line marks the value of $\nu(\text{CO})$ for gas-phase CO.

presence of CO, the maximum number of H atoms that can bind to the cluster is only 6, indicating competitive adsorption of CO and H_2 . In case of $\text{V}_9\text{H}_{12}\text{CO}^+$, CO does dissociate because the surface is not completely covered with hydrogen (14 sites available and only 12 are occupied by hydrogen atoms). For $\text{V}_{11}\text{H}_m^+$, the saturation stoichiometry (m) is 14 and the bare vanadium cluster has 17 triangular facets.^[63] The exact structure of the bare V_{19}^+ cluster is not known and it is therefore not possible to relate the number of triangular facets with the hydrogen saturation stoichiometry. For these cluster sizes, on which CO is dissociatively chemisorbed, not all available sites are blocked with hydrogen.

In Figure 6.3, the frequency of the C–O stretch vibration is plotted as a function of cluster size. The value of $\nu(\text{CO})$ decreases from 2173 cm^{-1} for $\text{V}_6\text{H}_8\text{CO}^+$ to 2130 cm^{-1} for $\text{V}_{20}\text{H}_{26}\text{CO}^+$. The behavior of $\nu(\text{CO})$ as a function of cluster size is similar to what is observed for CO adsorbed on bare cationic Co, Ni, and Rh clusters.^[75, 76] For those systems, the experimental trends could be reproduced by equation 6.1.

$$\nu(\text{CO}) = \nu_s + \frac{1395}{(r_V n^{1/3} + r_C + \frac{1}{2} r_{\text{C-O}})^2} + \frac{\gamma'}{1.29 n^{0.875}} \quad 6.1$$

Here, n is the number of metal atoms in the cluster, ν_s represents the value of $\nu(\text{CO})$ for CO adsorbed on a single crystal surface, r_V , r_C , and $r_{\text{C-O}}$ are the radii of a V, C, and

O atom, respectively, and γ' is a proportionality constant. The electric field of the charged cluster interacts with the CO dipole and leads to a strengthening of the C–O bond. This is accounted for by the second term. The final term describes the change in the population of the $2\pi^*$ orbital due to the charge at the CO binding site.^[76] A rigorous derivation of equation 6.1 can be found in ref.^[76] The size evolution of $\nu(\text{CO})$ observed for CO adsorbed on $V_nH_m^+$ clusters can also be reproduced by equation 6.1 (black line in Figure 6.3). The model shows that the dominating factor in the behavior of $\nu(\text{CO})$ is the availability of electron density for back-donation from the metal to the anti-bonding $2\pi^*$ orbital of CO. Electrostatic effects (dashed line in Figure 6.3) play a significant but minor role.

As shown in chapter 5, co-adsorption of H has a significant electronic influence on the binding of carbon monoxide on Co_n^+ clusters. For that system the co-adsorption of H leads to a reduction of the amount of electron density available for back-donation, resulting in an increase of $\nu(\text{CO})$. The similarity of the size dependence of $\nu(\text{CO})$ for CO adsorbed on $V_nH_m^+$ and on bare Co, Ni, and Rh clusters, suggests that the co-adsorbed H atoms do not significantly influence the CO binding in $V_nH_m\text{CO}^+$ complexes in another way than structurally stabilizing the CO against dissociation. To investigate if co-adsorbed H atoms have an electronic effect on the binding of CO on V_n^+ clusters, charge density difference (CDD) plots were constructed for CO adsorbed on bare and hydrogenated V_6^+ and V_8^+ . These plots, shown in Figure 6.4, demonstrate how the electron density rearranges in the plane containing the CO molecule and the V atom to which it is coordinated upon adsorption of a CO molecule. If H atoms influence the binding of CO, the differences should emerge in the CDD plots of for $V_n\text{CO}^+$ and $V_nH_m\text{CO}^+$. CDD plots are constructed by subtracting the electron density of the fragments from the electron density of the entire complex, e.g. $\rho(V_6H_8\text{CO}^+) - \rho(V_6H_8^+) - \rho(\text{CO})$. For complexes containing H, the optimized geometries as shown in Figure 6.2 were used, while for the corresponding V_n^+ and $V_n\text{CO}^+$ clusters the same geometry minus the H atoms was used. All calculations were performed for clusters with the lowest possible number of unpaired electrons. For $V_6H_8^+$, $V_8H_{12}^+$, $V_6H_8\text{CO}^+$, and $V_8H_{12}\text{CO}^+$ good agreement with the experimental IR-MPD spectrum is obtained for clusters with one unpaired electron, which are the lowest energy isomers identified in the calculations. The V_6^+ and V_8^+ clusters are also predicted to have one unpaired electron in the electronic ground state.^[63, 197, 198] The calculations indicate that the spin state of the V_6^+ and V_8^+ clusters do not change upon adsorption of CO.

For CO adsorption on both bare and hydrogenated clusters there is a loss of charge in σ -orbitals and an increase of charge in the π system, consistent with the classical picture of donation and back-donation. For both the hexamer and the octamer, the electron density in the π system increases somewhat more in case of CO adsorption on the bare cluster compared to adsorption on a hydrogen-saturated cluster. Hence, co-adsorption of H slightly reduces the amount of electron density in the π system. Additionally, the frequency of the C–O stretch vibration was calculated for all four complexes. For $V_6\text{CO}^+$ and $V_6H_8\text{CO}^+$, values of 2085 cm⁻¹ and 2088 cm⁻¹ are found, consistent with the similar CDD plots. The frequency of the C–O stretch vibration

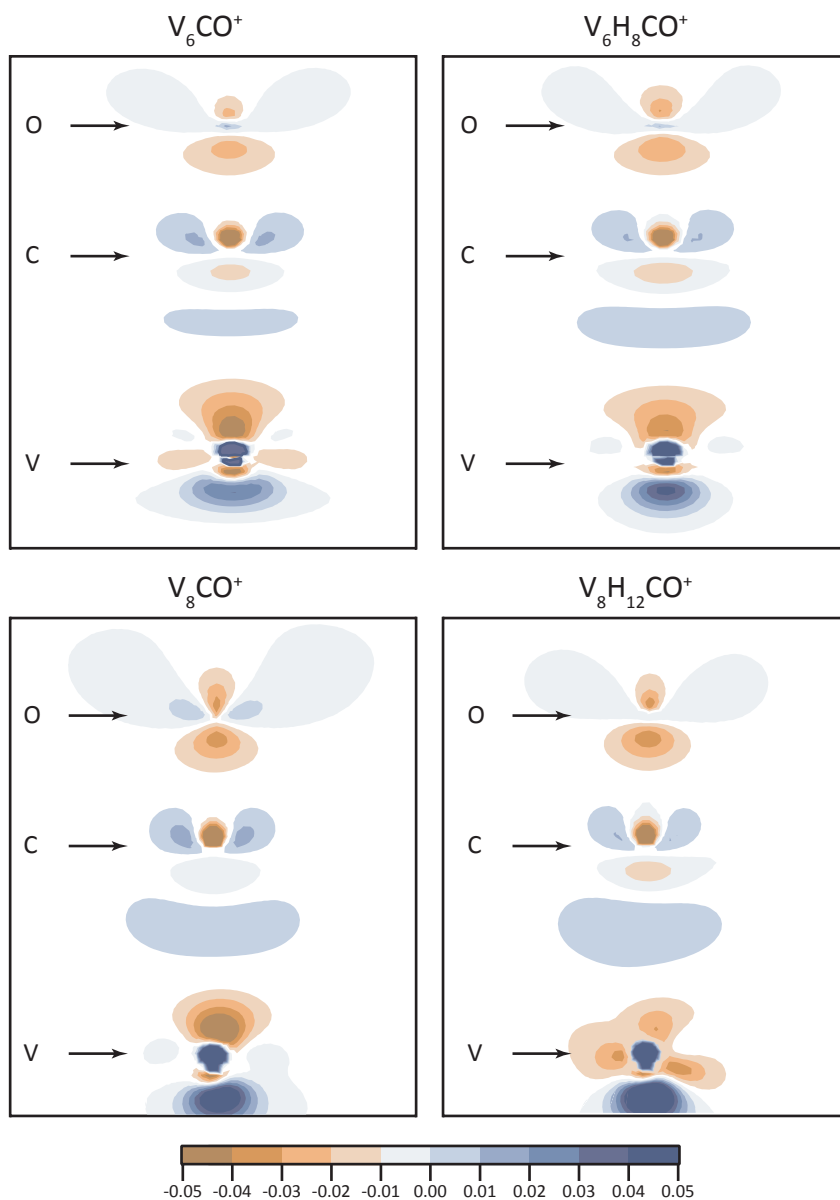


Figure 6.4. Charge density difference plots, $\rho(V_nH_mCO^+) - \rho(V_nH_m^+) - \rho(CO)$, for CO adsorption on V_6^+ (top left), $V_6H_8^+$ (top right), V_8^+ (bottom left), and $V_8H_{12}^+$ (bottom right). Regions of electron loss are shown in brown, while regions where the electron density increases are shown in blue. The plot is for a plane containing the CO molecule as well as the V atom to which it is bound.

is calculated to be 2050 cm⁻¹ for V₈CO⁺ and 2060 cm⁻¹ for V₈H₁₂CO⁺, i.e. $\nu(\text{CO})$ shifts to higher frequency with 0.8 cm⁻¹ per adsorbed H atom. This is much smaller than the shift of 12 cm⁻¹ per H atom observed experimentally for the Co₈⁺ cluster.

It is interesting to speculate as to why co-adsorption of H₂ has a much stronger electronic influence in case of a late transition metal (Co) compared to an early transition metal (V). For VCO and CoCO deposited in solid Ne, values of $\nu(\text{CO})$ of 1931 cm⁻¹ and 1974 cm⁻¹ are found, respectively.^[199, 200] As expected, there is more back-donation by a V atom than by a Co atom. It has been shown that both 4s–4s and 3d–3d interactions contribute significantly to V_n⁺–V and Co_n⁺–Co bonding.^[117, 120] As a V atom has only 3 d-electrons, compared to the 7 d-electrons of Co, it might be that in case of V_n⁺ clusters the majority of these electrons is involved in M–M bonding, making them unavailable for back-donation. If this is the case, co-adsorption of H₂ on V_n⁺ will have a much smaller effect compared to co-adsorption on Co_n⁺. A much smaller degree of back-donation is also consistent with the higher values of $\nu(\text{CO})$ observed for V_nH_mCO⁺ complexes compared to those found for Co_nCO⁺ clusters.

6.5 Conclusions

The saturation behavior in the reaction of vanadium cluster cations with hydrogen has been explained by a covering of the cluster surface with H atoms that are predominantly bound in μ_3 configuration on triangular facets of the metal cluster. Completely hydrogen covered vanadium cluster cations bind co-adsorbed CO molecules non-dissociatively, whereas in cases that the number of adsorbed hydrogen atoms is smaller than the number of triangular facets, the absence of a characteristic $\nu(\text{CO})$ band indicates dissociation of co-adsorbed CO molecules.

It is furthermore shown that the adsorbed H atoms have only a small electronic effect on the binding of CO, in contrast to what is observed for co-adsorption of H₂ and CO on Co_n⁺ clusters.

It can therefore be concluded that the stabilization of CO against thermodynamically favorable dissociative chemisorption is a structural effect. There have to be at least two vacant three-fold hollow sites on the cluster to accommodate the C and O atoms to enable dissociation of CO. If all such sites are passivated with H atoms, a CO molecule can only bind molecularly.

These results show that the interaction of CO molecules with vanadium clusters can be controlled by co-adsorption of hydrogen molecules. The findings presented in this chapter show how the reactivity of a metal cluster can be modified by structural effects. This aids the atomistic understanding of the influence of hydrogen co-adsorption on reactivity.

On the Effect of Charge on the Binding of CO in Rhodium Carbonyls: From Bridging to Terminal CO §

Abstract

The structures of cationic rhodium carbonyl cluster compounds containing 1 to 6 Rh atoms are established by infrared multiple photon dissociation spectroscopy and density functional theory calculations. Comparison with the neutral analogues reveals that ionization of the neutral compounds destabilizes bridge bound CO ligands in $\text{Rh}_2(\text{CO})_8$ and $\text{Rh}_4(\text{CO})_{12}$, leading to cationic complexes with only terminally bound CO. The destabilization is associated with removal of charge from an orbital that is bonding with respect to bridge-bound CO.

§ Adapted from I. Swart, F.M.F. de Groot, B.M. Weckhuysen, D.M. Rayner, G. Meijer, and A. Fielicke, *The Effect of Charge on the CO Binding in Rhodium Carbonyls: from Bridging to Terminal CO*. J. Am. Chem. Soc., **130**, 2126 (2008)

7.1 Introduction

Changing the electron density of a catalyst can have a profound influence on its selectivity and activity. For this reason, electronic promoter materials are often added to a catalyst to tailor the electron density of the active particle and to obtain optimal performance.^[201] Despite the widespread use of electronic promoters, the mechanisms responsible for the observed effect(s) are often poorly understood. For CO oxidation over a Pt or Rh catalyst, the activity increases with electron density.^[9, 202] In contrast, the hydrogenation of CO over Co and Rh based catalysts is more active and more selective upon reducing the electron density of the metal particles.^[11, 203] This change in electron density also leads to a decrease in the ratio of bridge to linear bound CO but the mechanism behind this destabilization of bridge bound CO is unknown.^[11, 204]

In this chapter, the issue of charge-induced changes in the binding of CO to metal centers is discussed by focusing on rhodium carbonyls as models. Due to its catalytic versatility, Rh based catalysts have been used for both the hydrogenation and oxidation of CO.^[205] The structures of the neutral saturated carbonyl complexes containing 2, 4 and 6 Rh atoms are known.^[206-209] The cluster geometries are shown in Figure 7.1. The Rh dimer binds 8 CO molecules, 2 of which are bridge bound. The complex has C_{2v} symmetry. The Rh tetramer binds 12 CO ligands in such a way that the cluster has C_{3v} symmetry. The complex consists of a tetrahedral core of Rh atoms with 9 terminally bound CO molecules and three μ_2 coordinated ligands. The Rh hexamer binds 16 carbonyls ligands and forms a cluster with T_d symmetry. Four of the CO molecules are face bound to the metal core, while the remaining ligands are terminally bound.

In contrast, little is known about the charged complexes. The structures of the cationic rhodium carbonyls are established by infrared multiple photon dissociation (IR-MPD) spectroscopy, combined with Density Functional Theory (DFT) calculations. By comparing the structures of the cationic species with structures of the corresponding neutral complexes, information regarding the effect of charge on the binding geometry of CO is obtained.

7.2 Theoretical Method

The experimental spectra are complemented with DFT calculations to obtain information on cluster geometries and electronic structure.^[95] The calculations employed the B3LYP parameterization of the exchange correlation functional and a triple zeta valence plus polarization (TZVP) basis set for all atoms (def-TZVP) set as implemented in TURBOMOLE vers.5.9.1. For Rh an effective core potential was used. The valence shell consisted of the 4s, 4p, 4d and 5s electrons.

The following computational procedure has been applied. First, the geometries of several structural isomers were optimized for each cluster size. All calculations were done for the lowest possible spin state. After the optimization procedure, the vibrational spectrum was calculated within the harmonic approximation. The

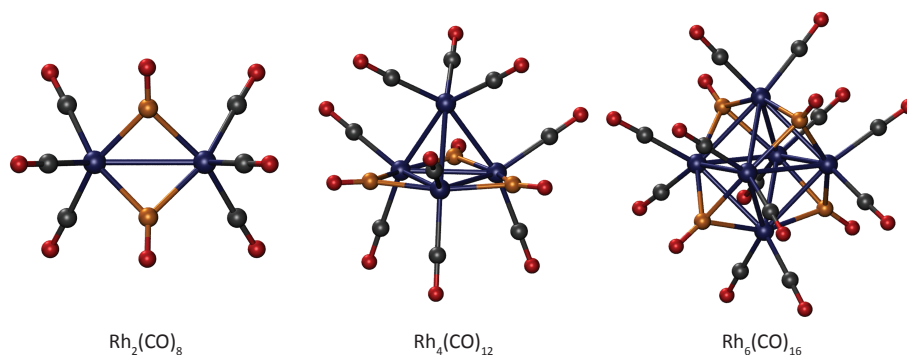


Figure 7.1. Geometries of $\text{Rh}_2(\text{CO})_8$, $\text{Rh}_4(\text{CO})_{12}$, and $\text{Rh}_6(\text{CO})_{16}$. Rh atoms are shown in blue, O atoms in red, C atoms of linearly coordinated CO are depicted in gray, while C atoms of bridge and face bound CO are shown in yellow.

calculated single photon absorption cross sections were convoluted with Gaussians with a width of 10 cm^{-1} and converted into depletion spectra using equation 2.12. A scaling factor of 0.96 was used for the frequency in the range of the C–O stretch vibration.

Charge density difference plots were created using the StoBe-deMon code.^[188] For these calculations, the exchange functional by Becke^[109] and the correlation functional of Perdew^[110] were used. For C and O, a TZVP basis set was used, while the basis set for Rh was of double-zeta quality (including a diffuse d).

7.3 Results and Discussion

Upon introduction of CO in the reactor channel, the Rh_n^+ clusters bind multiple CO molecules. The pressure in the reactor channel was increased until the resulting molecular beam distribution did not change anymore, i.e., when the clusters were saturated with carbon monoxide.^[210] The saturation numbers, and the total number of cluster valence electrons (CVEs) for clusters with 1–6 metal atoms, are given in Table 7.1. The saturation numbers of the cationic rhodium dimer, tetramer and hexamer are the same as those of the corresponding neutral clusters. Homoleptic rhodium carbonyl complexes with 3 and 5 metal atoms have not been identified before. An odd number of cluster valence electrons implies that the cluster valence orbitals cannot accept another two electrons from an additional CO molecule, e.g. 85 CVEs corresponds to 86 CVEs for a closed shell species. Electron counting rules (see section 8.1) can be used to predict the structures of small metal clusters but they do not provide much information about the binding of the carbonyl ligands.

The experimental IR-MPD spectra in the C–O stretching region and the Rh–C stretch and deformation region for complexes with 1–6 metal atoms are shown in Figure 7.2. Terminally bound CO ligands are present for all complexes (absorption bands between $2060\text{--}2100 \text{ cm}^{-1}$) but bridging ($\mu_2\text{-CO}$) and/or face capping ($\mu_3\text{-CO}$)

Table 7.1. Saturation numbers and number of cluster valence electrons (CVEs) for $\text{Rh}_n(\text{CO})_m^+$. Also the cluster structures that are predicted by electron counting rules are given.

<i>n</i>	<i>m</i>	CVEs	Predicted structure
1	5	18	-
2	8	33	dimer
3	9	44	no prediction. rule breaking?
4	12*	59	tetrahedron
5	14	72	trigonal bipyramid
6	16	85	multiple possibilities

* Upon increasing the CO content further, $\text{Rh}_4(\text{CO})_{13}^+$ and $\text{Rh}_4(\text{CO})_{14}^+$ could be formed.

carbonyls (absorption bands between 1750-1900 cm^{-1}) are only present for $\text{Rh}_5(\text{CO})_{14}^+$ and $\text{Rh}_6(\text{CO})_{16}^+$. When repeating the experiments at 20 times the IR fluence, the spectra exhibit saturation and broadening of the band(s) due to terminally bound CO, but no new absorptions are observed. This confirms that noise does not mask transitions with low oscillator strength. Furthermore, the saturation of the depletion via the band(s) due to atop bound CO confirms that other isomers, insensitive to IR-MPD due to strongly bound CO, are not present in significant quantities. The DFT calculations confirm this assignment and also predict that vibrational modes associated with bridge bound CO in isomers of complexes with 2-4 metal atoms have significant IR intensities, which should be observed experimentally.

The cluster structures and the calculated spectra that are in best agreement with experiment are shown together with the IR-MPD spectra in Figure 7.2. Structures and vibrational spectra of other isomers are given in Appendix C. The calculated and experimental spectra are in good agreement in both the C–O stretching range, $\nu(\text{CO})$, and in the Rh–C stretch and deformation region, $\nu/\delta(\text{RhC})$. Only for $\text{Rh}_4(\text{CO})_{12}^+$ a discrepancy is found (see below). The lowest energy isomers identified by the calculations are also the ones whose vibrational spectra are in best agreement with the experimental data.

The $\text{Rh}(\text{CO})_5^+$ complex, which obeys the 18-electron rule, has D_{3h} symmetry. All carbonyl ligands are terminally bound in the $\text{Rh}_2(\text{CO})_8^+$ complex in such a way that the complex has D_{2d} symmetry. The structure of $\text{Rh}_3(\text{CO})_9^+$ (D_3 symmetry) consists of a triangle of metal atoms and three CO molecules are atop bound to each rhodium atom. Two of the three carbonyl ligands are tilted toward the neighboring rhodium atoms, while the third lies in the plane spanned by the rhodium atoms. Regular electron counting rules indicate that if all nine carbonyl ligands contribute the normal two electrons, each Rh atom in $\text{Rh}_3(\text{CO})_9^+$ has 17 VEs. There are three possible explanations to account for the deviation from the 18e rule: 1) the complex contains Rh=Rh double bonds, 2) the tilted carbonyl ligands donate more than two electrons, or 3) it is sterically impossible for an additional CO molecule to bind to $\text{Rh}_3(\text{CO})_9^+$. The calculated Rh–Rh distances provide a measure of the metal–metal bonding in

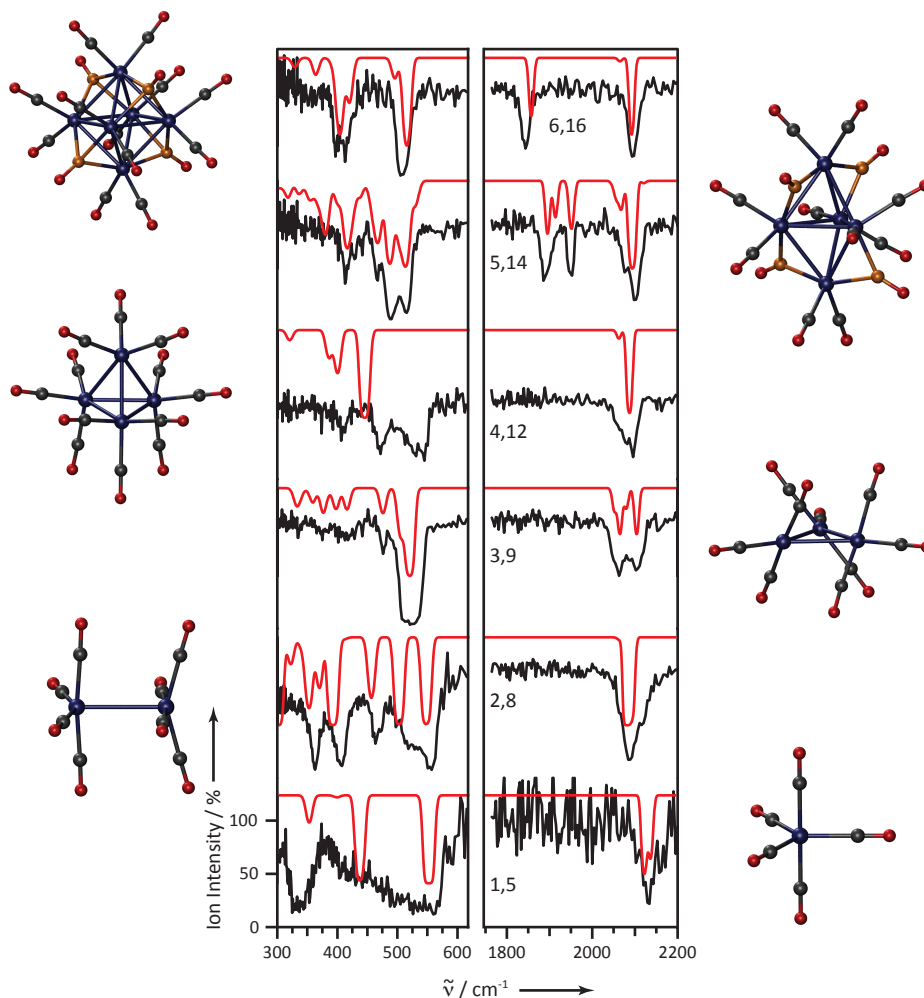


Figure 7.2. Experimental (black) and simulated (red) vibrational spectra of $\text{Rh}_n(\text{CO})_m^+$ complexes. The values n, m indicate the number of Rh atoms and CO molecules respectively. The simulated depletion spectra are based on the calculated single photon absorption spectra. Atoms are coded by color as in Figure 7.1.

these complexes. Although the reported vibrational spectra do not directly probe the Rh-Rh bonding, the good agreement between the calculated and experimental spectra gives confidence in the computed structures. The Rh-Rh bond lengths in $\text{Rh}_3(\text{CO})_9^+$ are calculated to be 2.87 Å, not shorter than in other complexes (2.73-2.90 Å). The $\text{Rh}_2(\text{CO})_8^+$ complex is an exception with a calculated Rh-Rh bond length of 3.19 Å. This implies that Rh=Rh double bonds are not present in $\text{Rh}_3(\text{CO})_9^+$. Highly unsymmetrical bridging carbonyl ligands that donate more than two electrons

have been reported for vanadium, chromium and iron carbonyl complexes.^[211-213] However, the $\angle\text{CO-M-M}$ in these clusters is much smaller than what is observed for the $\text{Rh}_3(\text{CO})_9^+$ complex, suggesting that it is unlikely that the tilted CO ligands donate more than 2 electrons. It has been shown that geometrical factors can play an important role in the determination of CO saturation coverages.^[214, 215] Therefore, it is most likely that the Rh trimer cannot bind more than 9 CO molecules due to steric reasons.

The $\text{Rh}_4(\text{CO})_{12}^+$ complex has 59 CVEs, corresponding to 60 CVEs for a closed shell complex. Electron counting rules predict that the 4 metal atoms span a tetrahedron in a complex with 60 CVEs. The isomer whose vibrational spectrum is in best agreement with the experimental spectrum has only terminally bound carbonyl ligands. However, an absorption band is observed in the experimental spectrum at $\sim 530\text{ cm}^{-1}$, which is missing in the simulated spectrum. A possible explanation for this discrepancy is that the complex is distorted from the high symmetry structure (T_d) shown in Figure 7.2 or that a second isomer is present in the molecular beam. Because of the discrepancy, it is not possible to unambiguously assign a cluster structure. However, from the experimental spectra it is clear that the $\text{Rh}_4(\text{CO})_{12}^+$ complex contains only terminally coordinated carbonyl groups. As the CO content in the reactor is increased further, $\text{Rh}_4(\text{CO})_{13}^+$ and $\text{Rh}_4(\text{CO})_{14}^+$ are formed. The vibrational spectra in the range of the C–O stretch vibration of these complexes are shown in Figure 7.3, together with the spectrum of $\text{Rh}_4(\text{CO})_{12}^+$. The absorption bands observed for $\text{Rh}_4(\text{CO})_{13}^+$ and $\text{Rh}_4(\text{CO})_{14}^+$ at $\sim 1920\text{ cm}^{-1}$ and $\sim 1880\text{ cm}^{-1}$, respectively,

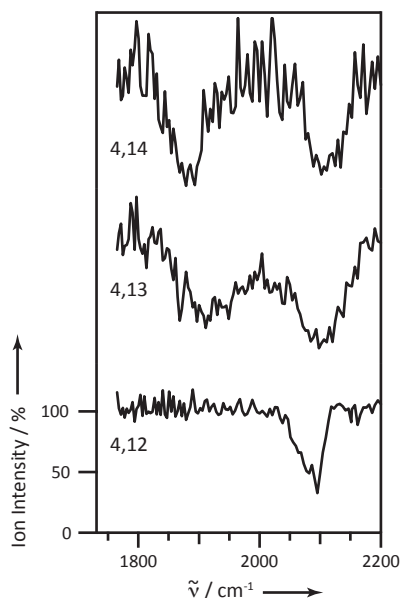


Figure 7.3. Vibrational spectra in the $\nu(\text{CO})$ range of $\text{Rh}_4(\text{CO})_{12}^+$, $\text{Rh}_4(\text{CO})_{13}^+$, and $\text{Rh}_4(\text{CO})_{14}^+$ complexes (bottom to top).

demonstrate that these complexes contain bridge bound carbonyl ligands. It might be that the additional CO ligand(s) adsorb in bridging positions, but it is also possible that the additional CO ligands induce a structural rearrangement.^[215] Calculations are needed to determine the structures of the $\text{Rh}_4(\text{CO})_{13}^+$ and $\text{Rh}_4(\text{CO})_{14}^+$ complexes.

The structure of $\text{Rh}_5(\text{CO})_{14}^+$ (C_1 symmetry) can be described as a trigonal-bipyramid of metal atoms with two bridge bound CO molecules and two ligands bound in quasi three-fold hollow sites. The remaining carbonyls are terminally bound (two CO molecules per rhodium atom). The structure of $\text{Rh}_6(\text{CO})_{16}^+$ is the same as that of the corresponding neutral complex. It contains four μ_3 -coordinated carbonyl ligands on alternating facets and the 12 remaining carbonyls are terminally bound, giving the complex T_d symmetry. Apparently, the structure of the complex is not significantly affected by a Jahn-Teller distortion.

In Figure 7.4, the vibrational spectra of the neutral (taken from ref.^[209]) and cationic species in the range of the C–O stretch vibration are compared. It is immediately clear that cationic and neutral $\text{Rh}_2(\text{CO})_8$ and $\text{Rh}_4(\text{CO})_{12}$ have different structures. The neutral complexes have two and three bridge bound carbonyl ligands, respectively,^[206, 209] whereas all CO molecules are terminally bound in $\text{Rh}_2(\text{CO})_8^+$ and $\text{Rh}_4(\text{CO})_{12}^+$.

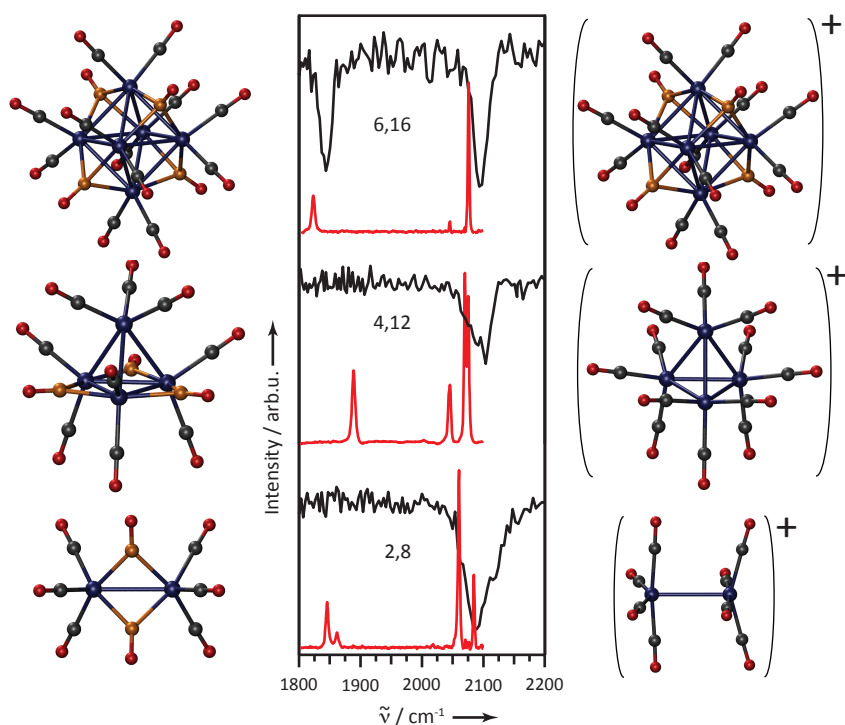


Figure 7.4. Experimental vibrational spectra of $\text{Rh}_2(\text{CO})_8^{+/0}$, $\text{Rh}_4(\text{CO})_{12}^{+/0}$ and $\text{Rh}_6(\text{CO})_{16}^{+/0}$ (cations: black, neutrals: red, bottom to top) in the $\nu(\text{CO})$ range. Structures for the neutral complexes are shown on the left and for the cations on the right. Atoms are coded by color as in Figure 7.1.

Removing an electron from the neutral complexes thus leads to a destabilization of the bridge bound carbonyl ligands. In contrast, $\text{Rh}_6(\text{CO})_{16}$ does not undergo a structural rearrangement. The metal cores of the cations retain the structure of the neutral compounds.

DFT calculations were performed for neutral complexes and for cations in the structure of the neutral clusters to compare the electronic structures. The calculations identify the correct ground state isomers of the neutral complexes. For $\text{Rh}_2(\text{CO})_8$, the neutral complex with only terminally bound CO molecules is just 0.09 eV higher in energy. The calculations show that the highest occupied molecular orbital (HOMO) of the complex with the bridging carbonyls is doubly occupied and can be thought of as a combination of rhodium d-orbitals with anti-bonding $2\pi^*$ orbitals of the bridging CO ligands (see Figure 7.5 A). In terms of the frontier orbital picture, this is the orbital that is involved in the back-donation of M–CO binding. The HOMO is bonding with respect to the Rh– μ_2 -CO bonds. Ionization removes an electron from this orbital. Mulliken overlap population analysis shows that the electron density in a single Rh– μ_2 -CO bond is reduced by 12% upon removing one electron from the neutral cluster. Figure 7.5 B shows the changes in electron density upon removal of an electron from the neutral Rh dimer in the plane containing a bridge bound CO ligand and the two Rh atoms. The electron density in the region associated with the Rh– μ_2 -CO bond clearly decreases when ionizing the neutral compound. The $\text{Rh}_2(\text{CO})_8^+$ complex is unstable in the structure of the neutral. It is a transition state that is +0.65 eV higher in energy than the isomer with only terminally bound CO. Consequently, the complex will undergo a charge induced structural rearrangement, resulting in the complex with only terminally bound CO. In this cluster, the Rh–Rh bond is longer than in the neutral molecule (3.188 Å vs. 2.826 Å). If the geometry of the cationic cluster is optimized, starting from the geometry of the neutral molecule and forcing the complex to retain the bridge bound CO ligands, the Rh–Rh bond decreases from 2.826 Å to 2.733 Å. This is consistent with the larger electron density of the cation in the Rh–Rh bond region (Figure 7.5 B). The destabilization of the bridge bound CO ligands is unlikely to be due to an increase in Rh–Rh bond length.

Calculations on neutral $\text{Rh}_4(\text{CO})_{12}$ show that the HOMO of this molecule has A_1 symmetry and that it is non-bonding with respect to the bridge bound CO molecules. However, there are two degenerate states with E symmetry that have only slightly lower energy than the HOMO ($\Delta E = 0.06$ eV) and which are involved in the binding of the μ_2 -coordinated CO molecules. Calculations on the cationic complex show that ionization from one of the orbitals with E symmetry is more favorable than ionization from the HOMO. Mulliken overlap population analysis shows that the electron density between the rhodium atoms and the bridging CO ligands is reduced by 38%. This is visualized in the charge density difference plot of the plane containing the three Rh atoms of the basal plane, as well as all three μ_2 -coordinated CO molecules, shown in Figure 7.5 D. The electron density in the Rh– μ_2 -CO bond regions decreases upon removing an electron. This weakens the Rh– μ_2 -CO bonds, eventually leading to a complex with only terminally bound CO.

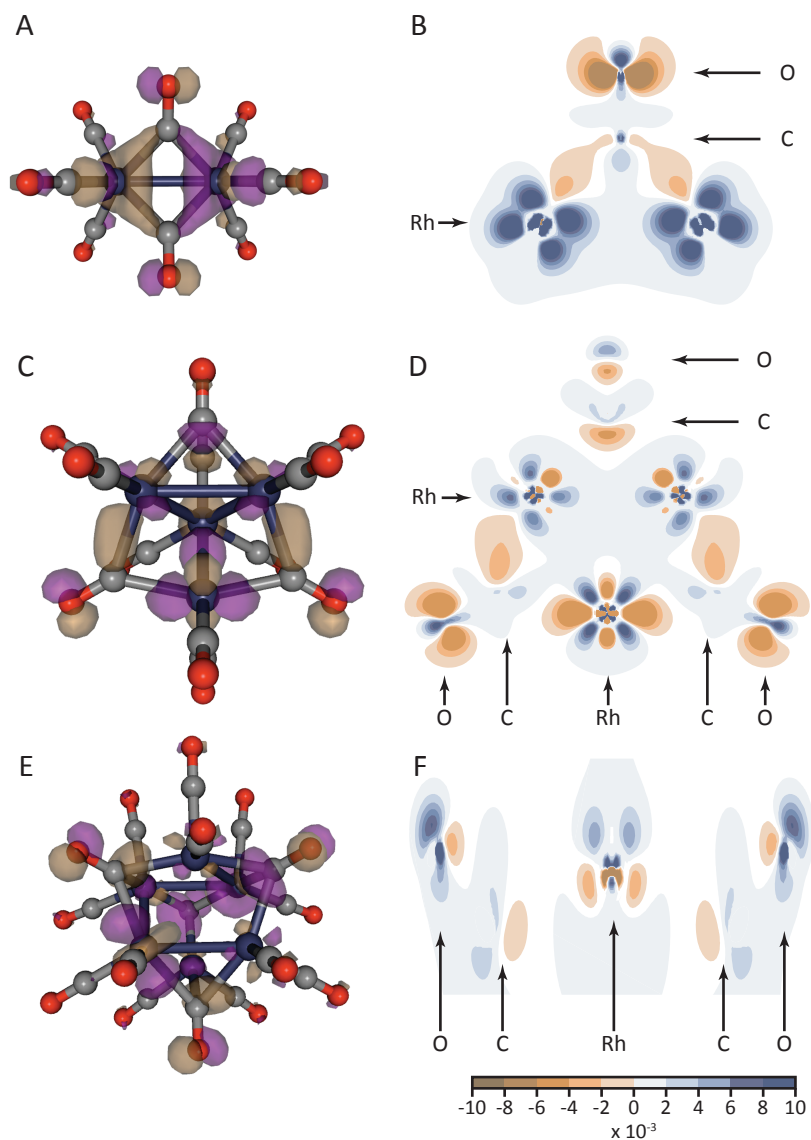


Figure 7.5. The Highest Occupied Molecular Orbital (HOMO) of $\text{Rh}_2(\text{CO})_8$ and $\text{Rh}_6(\text{CO})_{16}$ and the HOMO-1 orbital of $\text{Rh}_4(\text{CO})_{12}$ are shown in A, E, and C respectively. The brown and purple regions correspond to the different phases of the wavefunction. Charge density difference (CDD) plots, $\rho(\text{Rh}_n(\text{CO})_m^+) - \rho(\text{Rh}_n(\text{CO})_m)$, are shown in B, D, and F. For the Rh dimer, the CDD plot was created for the plane containing the two Rh atoms as well as a bridge bound CO ligand. In panel D the CDD is given for the plane containing the three basal Rh atoms and all three μ_2 -coordinated CO molecules of $\text{Rh}_4(\text{CO})_{12}^{+/0}$. For $\text{Rh}_6(\text{CO})_{16}$, the CDD plane spans two face bound CO ligands as well as the Rh atom to which both carbonyls are bound. Regions of electron loss are indicated in brown and regions of electron increase in blue.

As shown by the experimental and calculated vibrational spectra, the highly symmetric $\text{Rh}_6(\text{CO})_{16}$ complex (T_d symmetry) does not undergo structural rearrangement upon removal of an electron. The HOMO of $\text{Rh}_6(\text{CO})_{16}$ is involved in the binding of the face-capping CO molecules. It has t_2 symmetry and is fully occupied, i.e., there are 6 electrons in 3 equivalent orbitals. This results in a stable complex. Removing one electron from the HOMO reduces the electron density between the rhodium atoms and the μ_3 -coordinated carbonyl ligands by only 4% and hence the complex does not undergo reorganization. In Figure 7.5F, a charge density difference plot is shown for the plane containing two face-capping CO molecules and the Rh atom to which both carbonyls are bonded. The electron density in the region of the Rh- μ_3 -coordinated CO decreases upon ionization but the effect is much smaller than for $\text{Rh}_2(\text{CO})_8$ and $\text{Rh}_4(\text{CO})_{12}$.

7.4 Conclusions

Saturated cationic rhodium carbonyl complexes $\text{Rh}_n(\text{CO})_m^+$ ($n = 1-6$) have been characterized by a combined vibrational spectroscopy and density functional theory study. The saturation compositions of all clusters, except Rh_3^+ , can be rationalized using electron-counting schemes. In case of the Rh_3^+ cluster, a saturation limit of 11 carbonyl ligands is predicted, whereas experimentally a value of only 9 CO molecules was found for Rh_3^+ . It is argued that this discrepancy is most likely due to steric reasons. The Rh_2^+ , Rh_4^+ , and Rh_6^+ clusters bind the same number of CO ligands as the corresponding clusters. This allows a comparison of the structures and vibrational spectra to be made. From this comparison it becomes apparent that bridge bound CO ligands are selectively destabilized when an electron is removed from a neutral Rh carbonyl cluster. The destabilization comes about because an electron is removed from an orbital that is involved in the binding of the μ_2 -coordinated carbonyl ligands. These results provide a possible explanation for effects of promoter materials that are observed for CO bonding on transition metal hydrogenation catalysts.

A Vibrational Spectroscopic and Density Functional Theory Investigation of Cationic Cobalt- and Nickel-Carbonyl Clusters in the Gas-Phase

Abstract

Cationic cobalt and nickel carbonyl clusters containing 1-6 metal atoms were produced in the gas-phase and characterized by recording vibrational spectra in the C–O stretch and the M–C stretch and deformation range. The maximum number of CO molecules that can bind to Co_n^+ and Ni_n^+ cluster was determined. The experimental spectra are complemented with density functional theory calculations for the complexes with 1, 2, and 3 metal atoms. Terminally bound CO ligands are present for all complexes. The C–O stretch vibration of these ligands systematically shifts to lower energy with increasing cluster size. In case of $\text{Co}_n(\text{CO})_m^+$ complexes, bridge- and/or face-bound carbonyl ligands were present for species with $n \geq 2$, while for $\text{Ni}_n(\text{CO})_m^+$ clusters such bonding motifs are present for complexes with $n \geq 4$. The complex compositions are related to structures by using electron-counting schemes. For the $\text{Co}_3(\text{CO})_{10}^+$ complex, which electron counting rules predict to be unsaturated, the calculations find that one Co–Co bond is much shorter than the other two M–M bonds, suggesting that a Co=Co double bond is present. The saturation numbers of the cationic cobalt dimer, tetramer and hexamer are the same as those of the corresponding neutral clusters that can be prepared by standard organometallic chemistry methods. This allows evaluating the influence of charge on the binding of the CO molecules. It is found that the removal of an electron from $\text{Co}_2(\text{CO})_8$ and $\text{Co}_4(\text{CO})_{12}$ leads to distortions of the bridge bound carbonyl ligands.

8.1 Introduction

Since the first transition metal carbonyl, $\text{Ni}(\text{CO})_4$, was synthesized in 1890^[216], the synthesis, characterization, and reactivities of these complexes have been the subject of numerous studies. As a result, there currently exists a rich variety of CO containing compounds, underlining the importance of CO as a ligand in organometallic chemistry. Carbonyl compounds find use as catalysts and as precursor molecules in organic chemistry. They have also been used as structural models for chemisorption on extended metal surfaces.

The structures of metal carbonyl complexes have been rationalized by using electron-counting schemes, the simplest of which is the 18-electron rule. These electron-counting rules are based on the assumption that the stability of a complex is directly related to the completeness of the valence electronic shell. The correlations between geometrical structure and the number of CVEs have been justified by calculations.^[217,218] By filling all 9 of its valence orbitals, a transition metal atom obtains the electronic configuration of the next highest noble gas. The metal atom donates its valence electrons, while each adsorbed CO molecule contributes two electrons. Hence, $\text{Ni}(\text{CO})_4$ has 18 cluster valence electrons (CVEs) and can be considered a closed shell complex. This rule also makes it easy to understand why $\text{Co}(\text{CO})_4$, which has only 17 CVEs, is readily reduced to $\text{Co}(\text{CO})_4^-$. For small transition metal clusters, i.e. with 5 or less metal atoms, predictions regarding metal cluster structures can be made using the Effective Atomic Number (EAN) rule, which is an extension of the 18-electron rule. The EAN rule assumes that all M-M bonds are two-center/two-electron bonds. The number of predicted M-M bonds is given by: $z = (18n - k)/2$, where n is the number of metal atoms and k the number of CVEs. For most complexes with six and more metal atoms, more M-M bonds are observed than are predicted by the EAN rule. An alternative, non-localized electron counting scheme is required to rationalize the structures of these metal carbonyl complexes. The non-localized electron counting schemes developed for borane (boron-hydrogen) and carboborane (boron-carbon) clusters have been adapted for transition metal clusters. In Polyhedral Skeleton Electron Pair Theory (PSEPT)^[205], a close-packed, *closo*, cluster with u vertices is held together by $u+1$ electron pairs. The increasingly more open structures, *nido*, *arachno*, and *hypho* are held together by $u+2$, $u+3$, and $u+4$ electron pairs, respectively. In PSEPT, the number of electron pairs involved in M-M bonding is given by: $S = (k - 12n)/2$. Here, k is the number of valence electrons and the value 12 comes from the assumption that each metal atom uses 3 orbitals for M-M bonding and 6 orbitals for ligand binding and to accommodate non-bonding electrons. Common cluster structures and the corresponding CVE counts are given in Figure 8.1.^[205]

In case of anionic and cationic complexes, the CVE count has to be corrected for the charge state of the cluster. Certain complexes have an odd number of CVEs. The implication is that the cluster valence orbitals cannot accept another two electrons from an additional CO molecule, e.g. 59 CVEs corresponds to 60 CVEs for a closed shell species.

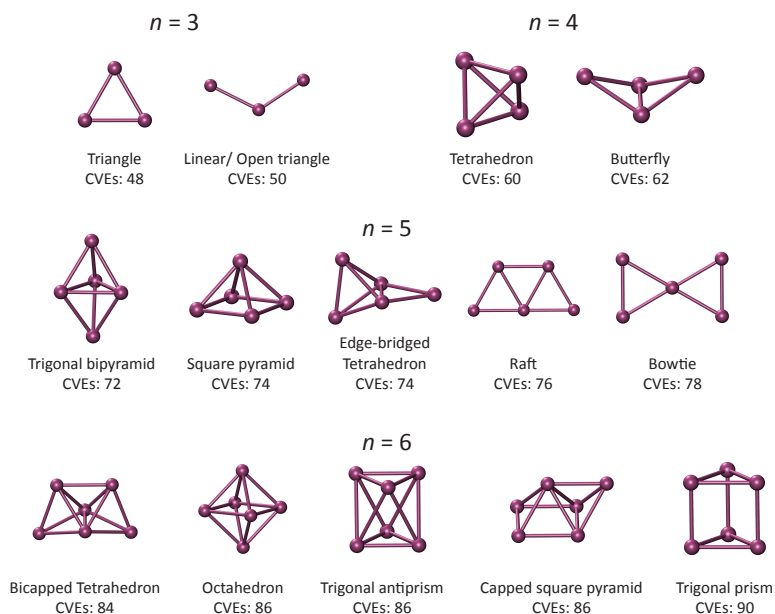


Figure 8.1. Common cluster structures and their cluster valence electron count.

By studying a neutral complex and the corresponding charged species, it is possible to investigate the charge dependence of the binding of a ligand. However, the first stable homoleptic cationic carbonyl complexes, $M(\text{CO})_6^+$, with $M = \text{Mn}, \text{Tc}, \text{Re}$, were not synthesized until 71 years after the discovery of $\text{Ni}(\text{CO})_4$.^[219] Several other homoleptic transition metal carbonyl cations were isolated by conjugating it with a weakly coordinating anion.^[220-222] However, no homoleptic cationic carbonyl clusters containing more than two metal atoms have been synthesized by using such methods. It is of significant interest to study how the bonding of ligands depends on the size and charge-state of the metal cluster to which it is adsorbed. With the advent of matrix-isolation and molecular beam based techniques, it became possible to study charged, saturated and unsaturated transition metal carbonyl complexes with more than one metal atom. Another significant advantage of molecular beam based techniques is that the species under investigation are not coordinated by atoms or other molecules. Hence, it is possible to obtain information that is free of matrix effects. This opens up the possibility to study the size- and charge- dependent binding of adsorbates.

The adsorption of multiple CO molecules on Co_n^+ clusters has been investigated by measuring relative reaction rate constants and by determining the maximum number of carbonyl ligands that could bind to Co_n^+ clusters as function of cluster size.^[223] The sequential bond dissociation energies of this complex have been determined from collision induced dissociation experiments.^[224] Recently, a stable salt of $\text{Co}(\text{CO})_5^+$ with the anion $(\text{CF}_3)_3\text{BF}^-$ was prepared.^[225, 226] The first molecular beam study into the

binding of CO on cationic Ni clusters appeared more than two decades ago.^[210] The maximum number of CO molecules that could bind to such clusters was determined and metal cluster structures were proposed^[227] by using electron counting rules.^[205] Later on, it has been argued that the CO saturation coverage of larger neutral Ni clusters is almost completely determined by geometrical constraints imposed by the size of the metal cluster and the Van der Waals size of the carbonyl ligand.^[215]

Although electron-counting rules have proven to be quite useful in predicting the structure of the metal cluster core, the predicted structures are by no means definitive and should be regarded as a framework to interpret the experimental results. Furthermore, electron-counting rules do not provide much insight on adsorbate binding geometries. Detailed information on carbonyl adsorption geometries can only be obtained from spectroscopic and theoretical methods. Currently, such knowledge is only available for anionic Fe carbonyl clusters^[228] and cationic Rh carbonyl complexes. The latter is discussed in chapter 7.

In this chapter, a combined IR multiple photon dissociation (IR-MPD) spectroscopy and density functional theory (DFT) study into the binding of CO on Co_n^+ and Ni_n^+ clusters is presented. The vibrational spectra of $\text{Co}_n(\text{CO})_m^+$ and $\text{Ni}_n(\text{CO})_m^+$ complexes ($n = 1-6$) were recorded in the range of the C–O stretch vibration, $\nu(\text{CO})$, and in the M–C stretch and deformation range, $\nu\delta(\text{MC})$. The experimental work is complemented with DFT calculations for the complexes with 1, 2, and 3 metal atoms. Where available, the structures of the cationic complexes are compared with those of the corresponding neutral compounds.

8.2 Theoretical Method

The experimental spectra are complemented with DFT calculations to obtain information on complex geometries as well as on the electronic structure of the complexes. The calculations employed the B3LYP parameterization of the exchange-correlation functional and a triple zeta valence plus polarization (TZVP) basis set for all atoms (def2-TZVP), as implemented in TURBOMOLE version 5.9.1.^[95]

The following computational procedure has been applied. First, the geometries of several structural isomers were optimized for each cluster size. All calculations were done for the lowest possible spin state. After the optimization procedure, the vibrational spectrum was calculated within the harmonic approximation. The calculated single photon absorption cross sections were convoluted with Gaussians with a width of 8 cm^{-1} and converted into depletion spectra using equation 2.12. A scaling factor of 0.96 was used for the frequency in the range of the C–O stretch vibration.

Charge density difference plots were created using the StoBe-deMon code.^[188] For these calculations, the exchange functional by Becke^[109] and the correlation functional of Perdew^[110] were used. For C and O, a TZVP basis set was used, while the basis set for Co and Ni was of double-zeta quality (including a diffuse d).

8.3 Results and Discussion

First, the complex compositions of results cationic Co and Ni carbonyls complexes that are formed in the molecular beam are discussed. Subsequently, the results from the combined vibrational spectroscopy and DFT study will be presented. Where applicable, a comparison with the *4d* analog of the Co carbonyls, the $\text{Rh}_n(\text{CO})_m^+$ complexes, is made.

8.3.1 Complex Compositions

Upon introduction of CO in the reactor channel, the Co_n^+ and Ni_n^+ clusters in the molecular beam bind multiple CO molecules. The CO content in the reactor channel was increased until a cluster size dependent saturation limit was reached.^[210] For Ni_n^+ clusters, carbonyl complexes are not only formed by successive addition of CO molecules but also by fragmentation.^[210] The maximum number of carbonyl ligands, m , that could bind to Co_n^+ and Ni_n^+ clusters is given in Table 8.1. The values of the corresponding anionic and neutral clusters, as reported in the literature,^[205, 214, 215, 229-233] are also listed, together with the total number of cluster valence electrons (CVEs).

The maximum number of CO molecules that can bind to a metal cluster of a certain size strongly depends on the charge state of the cluster. In general, a cationic species binds an equal number, or more, CO molecules than the neutral cluster, which in turn binds an equal amount, or more, than the corresponding anionic complex. The only exception is the Ni pentamer, whose anion binds one CO molecule more than the corresponding neutral cluster. As a result, the Ni_5^- cluster has 75 CVEs compared to 72 for the corresponding neutral complex. Electron counting rules predict that the metal cluster core will be different for these complexes. This might be intrinsic to the structures of $\text{Ni}_5^{-/0}$, however, it is also possible that the structure of the metal cluster changes due to adsorption of CO.^[215]

The saturation limits observed for Co_n^+ clusters agree with those reported in the literature.^[223] The only exception is Co_5^+ for which in this study a saturation limit of 15 molecules is found, whereas a value of 14 ligands was reported previously. The Co_n^+ clusters bind the same number of CO ligands as the corresponding Rh_n^+ clusters, except for the trimer and pentamer, where Rh_3^+ and Rh_5^+ bind 9 and 14 CO molecules, respectively, compared to 10 and 15 for Co_3^+ and Co_5^+ . The cationic Co dimer, tetramer, and hexamer bind the same number of CO molecules as the corresponding neutral clusters that can be prepared using standard metal-organic chemistry techniques.

The $\text{Co}(\text{CO})_5^+$ complex has 18 valence electrons, and can be regarded as a closed shell structure. The Co dimer binds 8 CO molecules and the complex has a total of 33 valence electrons. Electron counting rules predict that a trigonal trimer carbonyl complex has 48 CVEs, implying a saturation limit of 11 CO molecules for Co_3^+ . However, a maximum of 10 CO ligands is found to bind on Co_3^+ , giving the complex 46 CVEs. One possible explanation for this discrepancy is that this

Table 8.1. Saturation limits of anionic, neutral and cationic cobalt and nickel clusters and the corresponding cluster valence electron (CVE) counts.

$\text{Co}_n(\text{CO})_m^-$ [231-233]			$\text{Co}_n(\text{CO})_m$ [205]		$\text{Co}_n(\text{CO})_m^+$	
<i>n</i>	<i>m</i>	CVEs	<i>m</i>	CVEs	<i>m</i>	CVEs
1	4	18	4	17	5	18
2	7	33	8	34	8	33
3	10	48	Not known		10	46
4	12	61	12	60	12	59
5	13	72	Not known		15	74
6	15	85	16	86	16	85

$\text{Ni}_n(\text{CO})_m^-$ [229, 230]			$\text{Ni}_n(\text{CO})_m$ [214, 215]		$\text{Ni}_n(\text{CO})_m^+$	
<i>n</i>	<i>m</i>	CVEs	<i>m</i>	CVEs	<i>m</i>	CVEs
1	3	17	4	18	4	17
2	Not known		7	34	7	33
3	6	43	9	48	9	47
4	9	59	10	60	11	61
5	12	75	11	72	12	73
6	12	85	13	86	13	85

complex contains a double bond. As discussed in chapter 7, electron-counting rules also predict a wrong saturation stoichiometry for Rh_3^+ . In case of Co_4^+ , a saturation limit of 12 ligands is found, which is the same as for the neutral tetramer. The $\text{Co}_4(\text{CO})_{12}^+$ complex has 59 CVEs, corresponding to 60 CVEs for a closed shell structure and the 4 metal atoms are predicted to span a tetrahedron. A saturation limit of 15 CO molecules for Co_5^+ gives the complex 74 CVEs, which would imply that the 5 Co atoms are arranged in a square based pyramid. A CVE count of 85 for $\text{Co}_6(\text{CO})_{16}^+$ can correspond to several structures of the bare metal cluster. The 6 Co atoms in Co_6H_4^+ form an octahedron (see chapter 3). The neutral Co_6 cluster also binds 16 CO molecules, and this complex has an octahedral core of metal atoms. Hence, it is likely that also in $\text{Co}_6(\text{CO})_{16}^+$ the metal atoms span an octahedron.

The saturation numbers of Ni_5^+ and Ni_6^+ are the same as reported previously for thermalized Ni_n^+ clusters.^[234] In that study, a saturation value of 10 carbonyl ligands was reported for Ni_4^+ , whereas here a value of 11 molecules is found. The saturation numbers found for thermalized Ni_2^+ , Ni_3^+ , and Ni_4^+ deviate from values reported for non-thermalized Ni clusters.^[210] For those clusters, the dimer, trimer and tetramer could bind 9, 8, and 10 CO molecules, respectively.

The $\text{Ni}(\text{CO})_4^+$ complex has 17 CVEs, corresponding to 18 CVEs for a closed shell complex. The Ni_2^+ cluster binds 7 CO molecules, giving the complex 33 CVEs. The 9 carbonyl ligands bound to Ni_3^+ result in a CVE count of 47 for the $\text{Ni}_3(\text{CO})_9^+$ complex. Electron counting rules predict 3 Ni-Ni bonds for the 48 CVE closed shell complex,

suggesting the Ni atoms form a triangle. A saturation limit of 11 CO molecules for Ni_4^+ brings the total number of valence electrons to 61, which implies that the 4 metal atoms are arranged in a butterfly like structure. The Ni pentamer binds 12 carbonyl ligands and the metal cluster core is predicted to be a square pyramid. A CVE count of 85 for the $\text{Ni}_6(\text{CO})_{13}^+$ complex can correspond to several different arrangements of Ni atoms. The structure of the $\text{Ni}_6(\text{CO})_{12}^-$ complex, which also has 85 CVEs, is known and can be described as a consisting of two identical $\text{Ni}_3(\text{CO})_6$ subunits, which are rotated by 60° . The 6 metal atoms span a trigonal antiprism.^[235] In contrast, as discussed in chapter 3, the 6 Ni atoms in $\text{Ni}_6\text{H}_{18}^+$ are predicted to form an octahedron.

8.3.2 Vibrational Spectroscopy and DFT results

To obtain information on the binding geometry of the CO ligands, IR-MPD spectra were recorded in the range of the C–O stretch vibration ($1750\text{--}2200\text{ cm}^{-1}$) and in the M–C stretch and deformation region ($300\text{--}600\text{ cm}^{-1}$). The IR-MPD spectra of $\text{Co}_n(\text{CO})_m^+$ and $\text{Ni}_n(\text{CO})_m^+$ complexes with 1–6 metal atoms are shown in Figure 8.2 and Figure 8.3, respectively. When recording IR-MPD spectra using the full FELIX laser fluence, the spectra of several complexes exhibit saturation in the low frequency range, i.e. the ion intensity is fully depleted. This can obscure the number of absorption bands and their relative intensities. Upon reducing the laser fluence to 50%, the spectra do not exhibit saturation anymore. For several complexes, not all peaks present in the spectra recorded at 100% laser fluence are present in the spectra recorded at 50% laser fluence. In those cases, spectra recorded at both 100% (black lines) and 50% (grey) laser power are shown.

For both $\text{Co}_n(\text{CO})_m^+$ and $\text{Ni}_n(\text{CO})_m^+$ complexes, terminally bound CO ligands are present for all complexes (absorption bands between $2000\text{--}2100\text{ cm}^{-1}$). Bridging ($\mu_2\text{-CO}$) and/or face capping ($\mu_3\text{-CO}$) carbonyls (absorption bands between $1750\text{--}2000\text{ cm}^{-1}$) are present for the Co complexes with 2–5 metal atoms, while such bonding motifs are only present for $\text{Ni}_4(\text{CO})_{11}^+$, $\text{Ni}_5(\text{CO})_{12}^+$, and $\text{Ni}_6(\text{CO})_{13}^+$. Face capping CO ligands are probably also present for $\text{Co}_6(\text{CO})_{16}^+$ (absorption band at $\sim 1820\text{ cm}^{-1}$), but due to the relatively poor signal to noise ratio this cannot be determined unambiguously. For $\text{Co}_4(\text{CO})_{12}^+$, two different absorption bands due to bridge and/or face bound CO are present. This suggests that two differently bound carbonyl ligands exist in this complex.

The absorption bands in the $2000\text{--}2100\text{ cm}^{-1}$ range observed for $\text{Ni}_2(\text{CO})_7^+$ and $\text{Ni}_3(\text{CO})_9^+$ are assigned to asymmetrically bridge bound CO molecules. This assignment is confirmed by DFT calculations, as discussed below.

For both Ni and Co carbonyls, the spectral position of the highest energy absorption band, which is due to atop bound CO, systematically shifts to lower wavenumbers with increasing cluster size, as illustrated by Figure 8.4. This was also observed for the value of $\nu(\text{CO})$ in case of Co_nCO^+ , Ni_nCO^+ , and Rh_nCO^+ clusters, whereas a shift to higher wavenumbers was observed for $\text{Fe}_n(\text{CO})_m^-$ complexes.^[76, 228] In case of the complexes with a single CO molecule, this behavior can be attributed to the dilution

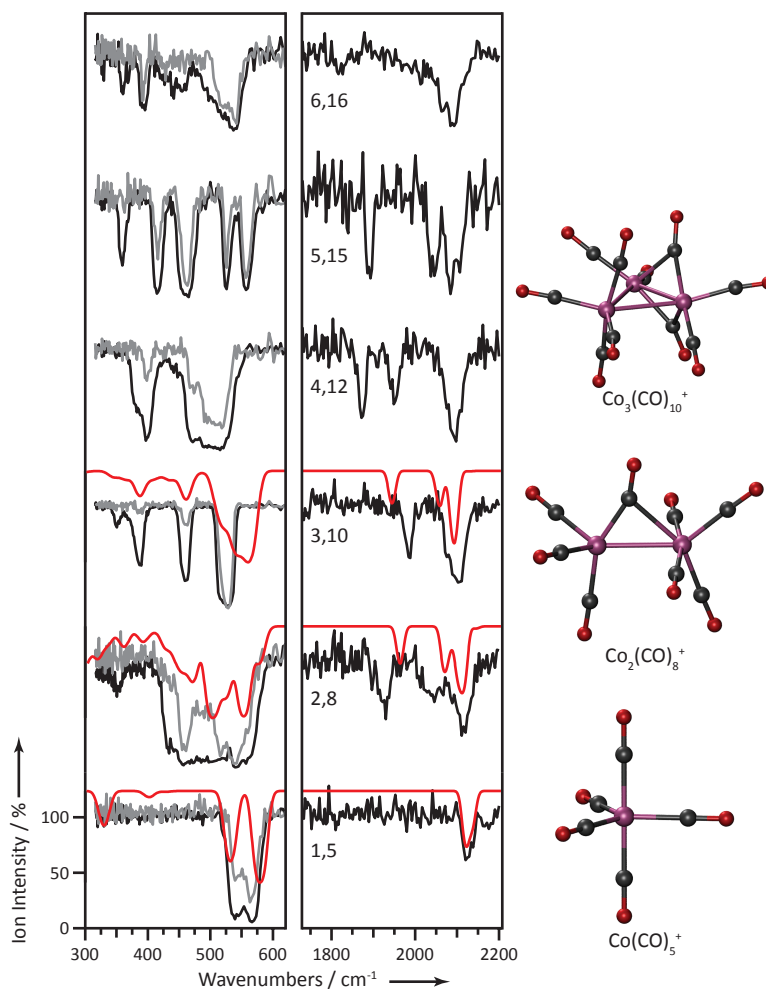


Figure 8.2. Experimental (black) and simulated (red) vibrational spectra of $\text{Co}_n(\text{CO})_m^+$ complexes. The values n,m indicate the number of metal atoms and CO ligands respectively. The grey lines correspond to spectra recorded at half the IR laser fluence used to record the black spectra. The optimized complex geometries are shown next to the spectra. Co atoms are depicted in pink, C atoms in dark grey and O atoms in red.

of the cluster charge with increasing cluster size.^[76] However, next to the charge dilution, additional factors can play a role for complexes with more than one adsorbed CO molecule. First, as all carbonyl groups compete for the available electron density of the metal atom, the amount of back-donation, and hence the spectral position of the observed absorption band, will depend on the number of CO ligands bound

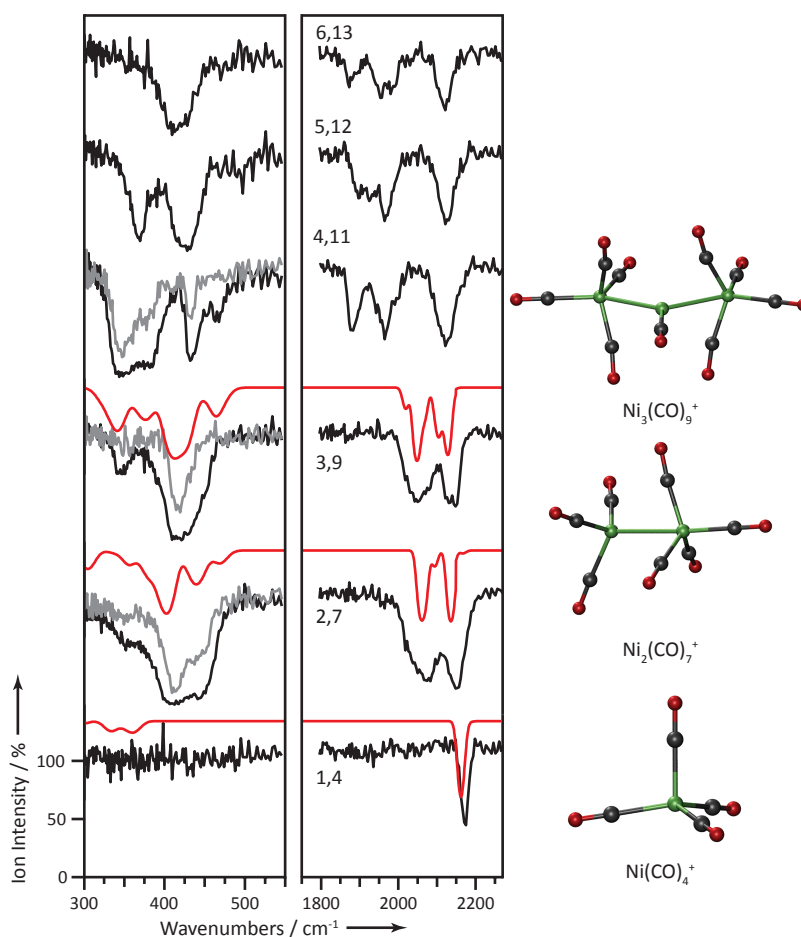


Figure 8.3. Experimental (black) and simulated (red) vibrational spectra of $\text{Ni}_n(\text{CO})_m^+$ complexes. The values n, m indicate the number of metal atoms and CO ligands respectively. The grey lines correspond to spectra recorded at half the IR laser fluence used to record the black spectra. The optimized complex geometries are shown next to the spectra. Ni atoms are depicted in green, C atoms in dark grey and O atoms in red.

to that atom.^[199] This number depends on cluster size. For example, each Co atom binds on average 3 CO ligands in $\text{Co}_5(\text{CO})_{15}^+$, while it binds 5 carbonyls in $\text{Co}(\text{CO})_5^+$. Furthermore, interactions between CO molecules might influence the value of $\nu(\text{CO})$.

To obtain more insight into the bonding of CO on Co_n^+ and Ni_n^+ clusters, DFT calculations were performed for clusters with 1, 2, and 3 metal atoms. The complex geometries and calculated vibrational spectra that are in best agreement with the experimental spectra are shown together with the IR-MPD spectra in Figure 8.2 and

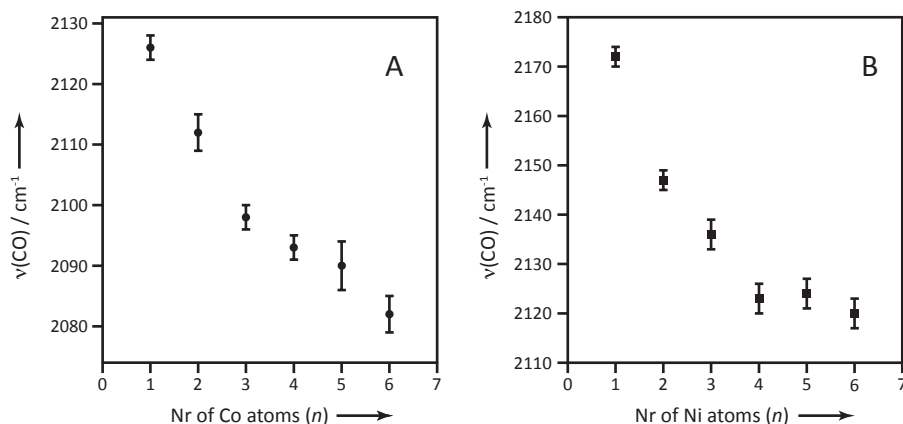


Figure 8.4. Frequency of the $\nu(\text{CO})$ vibration of atop bound CO in $\text{Co}_n(\text{CO})_m^+$ (A) and $\text{Ni}_n(\text{CO})_m^+$ complexes (B) as a function of cluster size. Peak positions were determined by fitting the highest energy peak observed in the experimental spectra with a Gaussian function. The error bars represent two times the standard deviation (2σ) of the fit.

Figure 8.3 for $\text{Co}_n(\text{CO})_m^+$ and $\text{Ni}_n(\text{CO})_m^+$, respectively. Structures and vibrational spectra of other isomers are given in Appendix C. The calculated and experimental spectra are in reasonable agreement in both the C–O stretch and M–C stretch and deformation region. Because not all possible geometric isomers have been calculated, it might be that the actual structures are different from the ones shown in Figures 8.2 and 8.3.

Experimentally, only a single absorption band at 2172 cm^{-1} is observed for $\text{Ni}(\text{CO})_4^+$. This value is in excellent agreement with the matrix isolation value of 2176 cm^{-1} .^[230] The vibrational spectrum of the lowest energy isomer of $\text{Ni}(\text{CO})_4^+$ reproduces the experimental spectrum. The $\text{Ni}(\text{CO})_4^+$ complex has C_{3v} symmetry and hence is distorted with respect to the T_d symmetric structure of the neutral complex. Experimentally, no absorption bands due to Ni–C stretch and deformation modes are found. The calculations predict that these modes have a low IR intensity. The lowest energy isomer of $\text{Ni}_2(\text{CO})_7^+$ contains only terminally bound carbonyl ligands. Three of these are tilted toward the second Ni atom and could also be regarded as highly asymmetrically bridge bound CO molecules. These tilted atop bound carbonyls are responsible for the absorption band observed experimentally at $\sim 2080\text{ cm}^{-1}$. The absorption bands in the low frequency range are also accurately reproduced by the calculations. An absorption band due to asymmetrically bridge bound CO ligands is also present in the spectrum of $\text{Ni}_3(\text{CO})_9^+$. Indeed, the calculations find that for this complex 5 CO molecules are terminally bound, and 4 ligands are highly asymmetrically bridge bound. Interestingly, 4 CO ligands are coordinated to each of the terminal Ni atoms, while only a single CO molecule is bound to the middle Ni atom. The metal cluster core of this complex can be described as an open triangle

and has two Ni-Ni bonds. This is in contrast to the 3 Ni-Ni bonds predicted for $\text{Ni}_3(\text{CO})_9^+$ by the EAN rule. An open triangular structure of the metal cluster core of $\text{Ni}_3(\text{CO})_9$ has been proposed before.^[215]

The $\text{Co}(\text{CO})_5^+$ complex, which obeys the 18 electron rule, can be described as a trigonal bipyramid and has D_{3h} symmetry. The single absorption band observed experimentally at 2126 cm^{-1} is predicted to consist of two peaks, split by 16 cm^{-1} . It was not possible to resolve the doublet structure of the peak due to the spectral bandwidth of FELIX. This value is in excellent agreement with the value of 2121 cm^{-1} found for the salt $\text{Co}_5(\text{CO})_5^+[(\text{CF}_3)_3\text{BF}]^-$.^[225] The two strong absorption bands at $\sim 540\text{ cm}^{-1}$ and $\sim 565\text{ cm}^{-1}$ are accurately reproduced by the calculations. The lowest energy isomer of $\text{Co}_2(\text{CO})_8^+$ has only terminally bound CO ligands. However, an absorption band due to a bridge bound CO ligand is observed in the experimental spectrum at 1930 cm^{-1} . Hence, an isomer with at least one two-fold coordinated CO ligand must be present in the molecular beam. One of the isomers of neutral $\text{Co}_2(\text{CO})_8$ has two bridge bound CO ligands, see Figure 8.5. However, the calculations indicate that the cation is unstable in such a geometry. A stable isomer with a single asymmetric bridge bound CO ligand is only 0.01 eV higher in energy than the lowest energy isomer. This energy difference is smaller than the accuracy of the calculations. The vibrational spectrum of this isomer provides reasonable agreement with the experimental spectrum in both the high- and low-frequency range. The calculated value of the C–O stretch vibration due to the bridge bound CO ligand is too high compared to the experimental value. In case of $\text{Co}_3(\text{CO})_{10}^+$, peaks due to terminal and bridge bound CO ligands are found in the high-frequency range. In the low frequency range, 4 well resolved absorption bands are observed. The lowest energy isomer identified in the calculations is also the one whose vibrational spectrum is in best agreement with the experimental spectrum. The complex has 8 terminally bound CO molecules, while 2 carbonyls are bridge bound on the same edge of the triangle spanned by the Co atoms. The Co–Co bond that is doubly bridged by carbonyl ligands is much shorter than the other two Co–Co bonds: 2.45 \AA versus 2.78 \AA . It is also much shorter than the bond lengths found for $\text{Co}_2(\text{CO})_8^+$ (see appendix C). The value of 2.45 \AA is close to the value of 2.36 \AA reported for several organometallic complexes with Co=Co double bonds.^[236, 237] Hence, it is likely that the $\text{Co}_3(\text{CO})_{10}^+$ contains a Co=Co double bond. A double bond would also give the complex a total of 48 CVEs, in agreement with predictions from electron counting schemes. Multiple M–M bonds have been proposed to account for the saturation stoichiometries of unsaturated metal carbonyl complexes.^[212, 213, 238, 239]

In Figure 8.5 the spectra of saturated neutral- (taken from the literature^[240-242]) and cationic cobalt carbonyls with 2, 4, and 6 metal atoms are shown. The structures of the neutral compounds are also given in Figure 8.5. In case of $\text{Co}_2(\text{CO})_8$, three different isomers co-exist.^[240] One of the isomers of $\text{Co}_2(\text{CO})_8$ has two symmetric bridge bound CO ligands, while the carbonyl moieties are all terminally bound in the other complexes. As has been shown above, in case of the cationic dimer, one asymmetric carbonyl ligand is present. From the vibrational spectra it is immediately clear that part of the CO ligands in $\text{Co}_4(\text{CO})_{12}^+$ must be differently bound compared

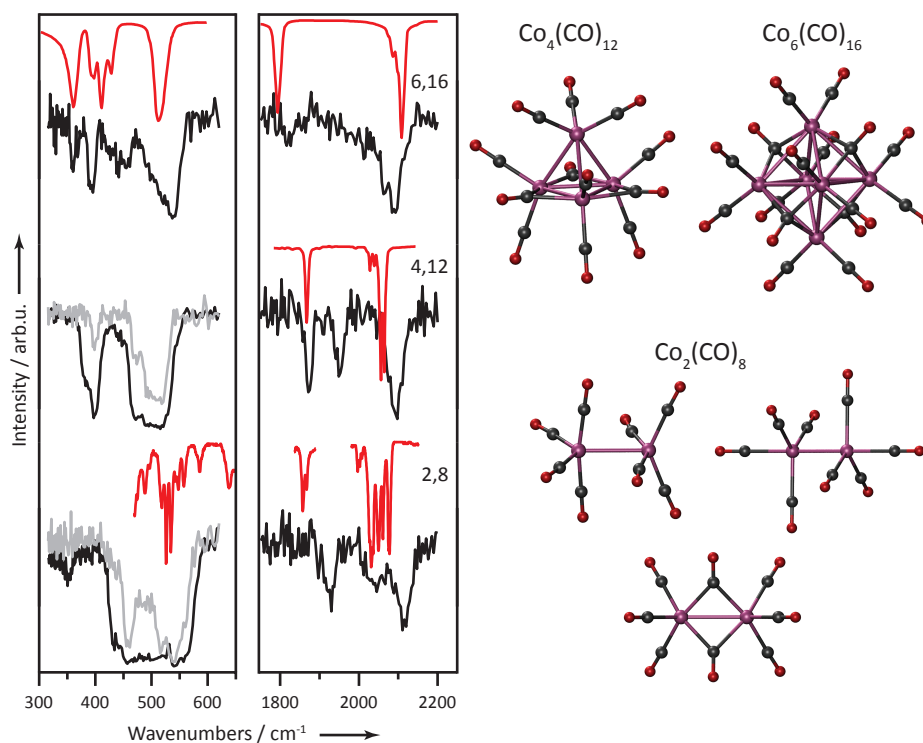


Figure 8.5. Experimental vibrational spectra of $\text{Co}_2(\text{CO})_8^{0/+}$, $\text{Co}_4(\text{CO})_{12}^{0/+}$, and $\text{Co}_6(\text{CO})_{16}^{0/+}$ (cations: black, neutrals: red). The structures of the neutral complexes are shown next to the spectra. Three isomers of $\text{Co}_2(\text{CO})_8$ are known to co-exist.

to the neutral complex. Hence, it can be concluded that removal of an electron from $\text{Co}_2(\text{CO})_8$ and $\text{Co}_4(\text{CO})_{12}$ leads to a distortion of the bridge bound carbonyl groups. As discussed in chapter 7, a charge induced destabilization of bridge bound CO ligands is also observed for $\text{Rh}_2(\text{CO})_8$ and $\text{Rh}_4(\text{CO})_{12}$. In those cases, the selective destabilization resulted from a reduction in the electron density of the regions associated with the $\text{Rh}-\mu_2\text{-CO}$ bonds. The vibrational spectrum of $\text{Co}_6(\text{CO})_{16}^+$ is similar to the spectrum of the neutral compound, suggesting that also the structures of the cationic and neutral complexes are similar. This was also observed for $\text{Rh}_6(\text{CO})_{16}^{+/0}$.

To investigate the origin of the destabilization of the bridge bound CO ligands, charge density difference (CDD) plots were constructed using the optimized geometry of the neutral complex. The plots are shown in Figure 8.6 and depict how the electron density, ρ , in a plane changes when an electron is removed from the cluster, i.e. the plots give $\rho(\text{Co}_n(\text{CO})_m^+) - \rho(\text{Co}_n(\text{CO})_m)$. In case of $\text{Co}_2(\text{CO})_8$, the changes in electron density are given for the plane containing the two Co atoms and one

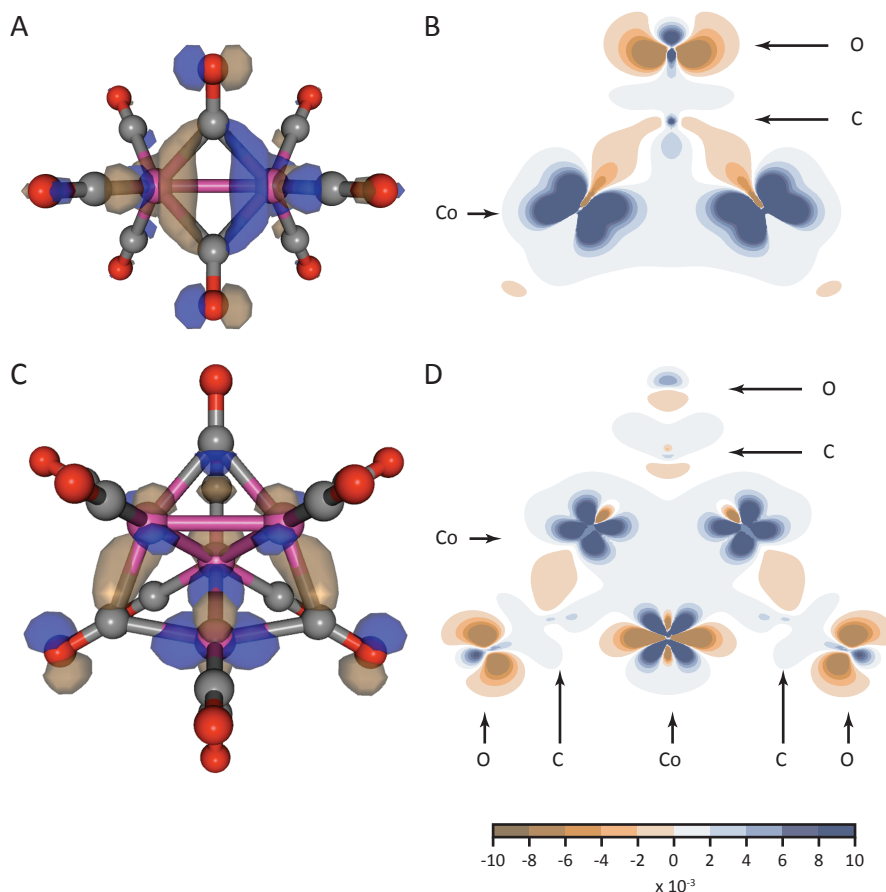


Figure 8.6. The Highest Occupied Molecular Orbitals (HOMOs) of $\text{Co}_2(\text{CO})_8$ and $\text{Co}_4(\text{CO})_{12}$ are shown in A and C respectively. The brown and blue regions correspond to the different phases of the wavefunction. Charge density difference plots, $\rho(\text{Co}_n(\text{CO})_m^+) - \rho(\text{Co}_n(\text{CO})_m)$, for the dimer and tetramer are given in B and D, respectively. In case of the dimer a plane containing the two Co atoms as well as one bridge bound CO ligand is used, while for $\text{Co}_4(\text{CO})_{12}$ the CDD is given for the basal plane with 3 metal atoms. Regions of increased electron density are shown in blue, while regions corresponding to electron density depletion are shown in brown.

bridge bound CO ligand. For $\text{Co}_4(\text{CO})_{12}$, the CDD is plotted for the basal plane of the complex that is spanned by 3 Co atoms. The three bridge bound CO ligands are located slightly above this plane.

The highest occupied molecular orbital (HOMO) of $\text{Co}_2(\text{CO})_8$ is involved in the bonding of the bridge bound CO ligands and can be thought of as a combination of the $2\pi^*$ orbitals of the bridge bound carbonyl ligands and Co d -orbitals. Ionizing the neutral compound corresponds to the removal of an electron from this orbital

and consequently leads to a destabilization of the bridge bound CO ligands. Indeed, as shown in Figure 8.6B, the electron density in the region associated with the Co- μ_2 -CO bond decreases when removing an electron from the neutral cluster. Mulliken overlap population analysis shows that the electron density in a single Co- μ_2 -CO bond is reduced by 2%. A similar story holds for Co₄(CO)₁₂. The HOMO of the complex (Figure 8.6C) is involved in the binding of the bridge bound carbonyl ligands. Hence, removing one electron from this orbital will weaken the Co- μ_2 -CO bonds. The CDD plot (Figure 8.6D) demonstrates that the electron density between the Co atoms of the basal plane and the bridge bound CO molecules decreases upon ionizing the neutral complex. Mulliken overlap population analysis finds that the electron density decreases by 14%. This reduction is likely to result in distortions of the bridge bound carbonyl ligands, resulting in different vibrational spectra for Co₄(CO)₁₂ and Co₄(CO)₁₂⁺.

Similar effects were found for Rh carbonyl compounds. However, Rh₂(CO)₈⁺ and Rh₄(CO)₁₂⁺ do not contain bridge bound CO molecules, while the corresponding Co complexes have at least one bridge bound carbonyl ligand. In case of the Rh carbonyls, a much larger reduction of the electron density in the regions associated with bridge bound CO was found, see chapter 7. In this respect, it is interesting that Co₄(CO)₁₂ and Rh₄(CO)₁₂ both have three bridge bound CO molecules, while all CO ligands are terminally bound in the 5d analog Ir₄(CO)₁₂.^[243, 244]

8.4 Conclusions

A series of saturated cationic cobalt and nickel carbonyl complexes, containing up to 6 metal atoms have been characterized by recording vibrational spectra in the range of the C-O stretch vibration and in the range of the M-C stretch and deformation modes. The experimental spectra are complemented with DFT calculations for the complexes with 1, 2, and 3 metal atoms. Terminally bound CO molecules are present for all complexes investigated. The C-O stretch vibration of atop bound CO ligands systematically shifts to lower energy with increasing cluster size. The possible reasons for this behavior are discussed. Bridge and/or face capping carbonyl ligands are present for all Co_n(CO)_m⁺ complexes with $n \geq 2$, while for Ni_n(CO)_m⁺ such bonding motifs are only observed for clusters with $n \geq 4$. However, asymmetrically bridge bound CO ligands are present in Ni₂(CO)₇⁺ and Ni₃(CO)₉⁺. The complex compositions are related to structures by using electron-counting schemes. For Co₃⁺ electron counting schemes predict a saturation limit of 11 CO molecules, whereas experimentally a value of 10 CO ligands is found. This discrepancy can be accounted for by the presence of a Co=Co double bond. In case of cobalt carbonyls, the saturation limits of the cationic dimer, tetramer, and hexamer are the same as those of the corresponding neutral species. It is shown that the bonding geometries of the bridge bound carbonyl ligands in the cationic dimer and tetramer are different from those in the neutral species. These distortions of the bridge bound CO molecules are due to removal of an electron from an orbital that is involved in the bonding of the two-fold coordinated carbonyl ligands.

Summary and Concluding Remarks

The aim of the research described in this Ph.D. thesis, was to obtain fundamental knowledge on the adsorption of H₂ and CO on transition metal particles. In this context, the adsorption of the individual H₂ and CO molecules on a series of transition metals clusters in the gas-phase was investigated as well as effects associated with the co-adsorption of H₂ and CO by focusing on an early and a late transition metal as case studies. Below a summary of the scientific work described in this Ph.D. thesis is given, followed by perspectives for future research.

Summary

In the first results chapter, **chapter 3**, a study into the adsorption of multiple H₂ molecules on a series of 3d transition metals clusters is presented. The maximum number of H₂ molecules that can bind to a metal cluster, i.e. the saturation number, is determined as a function of particle size. To obtain information of adsorption geometries, vibrational spectra of the metal hydride complexes were recorded and compared to spectra of optimized cluster geometries determined by Density Functional Theory (DFT) calculations. From the spectra it is concluded that hydrogen is exclusively present in the form of hydrogen atoms in Sc_nOH_m⁺, V_nH_m⁺, Fe_nH_m⁺, and Co_nH_m⁺ clusters. In contrast, part of the hydrogen in Ni_nH_m⁺ complexes is present as H₂ molecules. In other words, both dissociatively and molecularly coordinated hydrogen is present in these Ni complexes.

An important question than is: Does the first H₂ molecule already bind molecularly to Ni_n⁺ clusters, or does the H₂ only bind molecularly after all sites for H atoms are occupied? This question lies at the heart of **chapter 4** in which the adsorption of a single H₂ molecule on Ni_n⁺ clusters is investigated. It is shown that the first H₂ molecule to adsorb on the highly reactive Ni₅⁺ and Ni₆⁺ binds dissociatively, while it binds molecularly on the less reactive Ni₄⁺ cluster. The complex with the molecularly coordinated H₂ can be regarded a structural model for a precursor state to dissociation.

In **chapters 5 and 6**, effects associated with the co-adsorption of H₂ and CO are investigated by focusing on an early (vanadium) and a late (cobalt) transition metal as case studies. Carbon monoxide binds molecularly to the late transition metals, including cobalt. The experiments demonstrate that for CO adsorbed on Co_n⁺ clusters, co-adsorption of H₂ alters the C–O bond strength. In most cases, the C–O bond becomes stronger with increasing hydrogen coverage of the metal particle. A quantitative model describing the dependence of the C–O bond strength on the size and charge of a metal cluster is extended to incorporate the effect of co-adsorption of H₂. As shown in chapter 3, hydrogen dissociates into atoms upon adsorption on Co_n⁺ clusters. This results in a transfer of electron density into Co–H bonds, and hence to a reduction of the electron density that is available for back-donation into the anti-bonding 2π* orbital of the CO. A decrease of the population of this

orbital results in an increase of the C–O bond strength. Hence, co-adsorption of H₂ has a similar effect as a (partial) ionization of the metal cluster. By comparing the magnitude of these effects, it can be inferred that each co-adsorbed hydrogen atom reduces the electron density by 0.09–0.25 of a single charge, depending on the size of the metal cluster. It is concluded that co-adsorbed hydrogen has a profound electronic influence on the binding of CO on Co_{*n*}⁺ clusters.

Carbon monoxide dissociates upon adsorption on extended surfaces of early transition metals like vanadium. It is found that CO also dissociates on V_{*n*}⁺ clusters. However, if all sites for atomic carbon and oxygen are occupied by hydrogen atoms, CO is stabilized against dissociation and it binds molecularly. In contrast to what is observed for cobalt, DFT calculations suggest that the co-adsorbed hydrogen atoms do not have a significant electronic effect on the binding of CO on vanadium. The stabilization of CO against dissociation on vanadium hydride clusters is predominantly a structural effect.

A study into the binding of multiple CO molecules on rhodium, cobalt, and nickel clusters is presented in **chapters 7 and 8**. The structures of saturated cationic rhodium carbonyl complexes containing up to six metal atoms are obtained from a combined experimental and theoretical investigation. Comparing the structures of the Rh cations with those of the corresponding neutral compounds, reveals that ionization of the neutral species leads to a destabilization of the bridge bound CO ligands. The cationic complexes contain only terminally bound CO molecules. The destabilization is associated with the removal of an electron from an orbital that is bonding with respect to the bridge-bound carbonyl groups.

Cationic cobalt and nickel carbonyl clusters are characterized by measuring the maximum number of CO molecules that can bind to a cluster of a certain size and by recording vibrational spectra. The experimental work is complemented with DFT calculations on complexes with one, two, and three metal atoms. The complex compositions are related to structures by using electron-counting schemes. These schemes and DFT calculations suggest that a Co=Co double bond is present in the Co₃(CO)₁₀⁺ complex. For nickel carbonyls it is found that bridge bound CO molecules are only present for complexes with 4 or more metal atoms. Such bonding motifs are present for all cationic cobalt carbonyls with more than one metal atom. This is in contrast to what was observed for rhodium carbonyl complexes. However, the bonding geometries of the two-fold coordinated CO molecules in Co_{*n*}(CO)_{*m*}⁺ complexes are distorted with respect to those in the neutral compounds. This distortion is due to a reduction of the electron density in regions associated with Co–μ₂–CO bonds. The fact that bridge bound carbonyl ligands are still present for cationic cobalt carbonyls, but not for rhodium carbonyls, can be explained by the smaller reduction of the electron density in case of the cobalt carbonyls.

Perspectives for Future Research

The studies described in this Ph.D. thesis show that cluster studies can provide detailed information on CO and H₂ binding geometries and how these are affected by the size and charge of the metal particle, as well as on co-adsorption effects. The obtained information is relevant for several catalytic processes, including the Fischer-Tropsch synthesis and the selective oxidation of CO.

Several directions for future research can be identified. The first direction concerns the extension to other catalytically relevant clusters and molecules. For example, it would be of significant interest to study the adsorption of H₂ and CO on iron carbide clusters, which are proposed to be the active phase in iron based Fischer-Tropsch catalysts. Of course, it is also possible to investigate systems that are relevant for other catalytic reactions entirely. Within the framework of automotive exhaust gas catalysis, it would be of significant interest to investigate the (co-) adsorption of CO and NO_x species on rhodium and platinum clusters. Another example would be to study the adsorption of SO_x or hydrocarbons on vanadium oxide clusters as model systems for vanadium oxide based oxidation catalysts. Several studies in this direction have already been published in the literature.

Many catalytic reactions, including the Fischer-Tropsch reaction, take place at high temperatures, typically of several hundred degrees Celsius. Hence, an interesting direction of research would be to extend the current studies by carrying out temperature dependent experiments. Such studies would narrow the gap between the model system and the actual catalyst. Temperature dependent IR multiple photon dissociation (IR-MPD) spectroscopy experiments have become feasible using a molecular beam machine that has recently been installed at the FELIX facility of the FOM-Institute for Plasma Physics, in Nieuwegein, the Netherlands.

In the experiments described in this Ph.D. thesis, no indications for reactions between co-adsorbed molecules on the metal clusters were found. However, reactions might take place at higher temperatures. In this context it is noteworthy that the co-adsorption of H₂ and CO on cobalt clusters leads to an increased C–O bond strength, as discussed in chapter 5. Hence, it is predicted that clusters with low hydrogen coverage will show the highest reactivity towards the breaking of the C–O bond.

As outlined in chapter 4, a H₂ molecule can bind molecularly to Ni₄⁺ clusters. A temperature dependent study on the Ni₄H₂⁺ system would allow for a determination of the depth of the potential-well associated with molecularly chemisorbed H₂. Furthermore, such studies can be used to determine if a single H₂ molecule can also bind molecularly to nickel clusters other than the tetramer.

A third direction of research would be to use additional experimental techniques that can provide information complementary to the structural data provided by IR-MPD spectroscopy. As knowledge of the electronic state of the system, next to structural information, is often required to obtain a complete understanding of the system under investigation, especially techniques such as molecular beam

deflection methods, photoelectron detachment spectroscopy, and X-ray absorption spectroscopy are of interest. These methods also provide insight into the correlation effects in the electronic states of the metal cluster complexes. Experimentally obtained knowledge on the electronic state of a cluster complex can furthermore be helpful in the theoretical treatment of the system, particularly when working with late transition metals like iron and cobalt that have a large number of unpaired electrons. Hence, these techniques can be used to obtain more insight into the systems studied in this Ph.D. thesis.

The cobalt hydrogen system is one example where photoelectron spectroscopy is able to provide more insight. As argued in chapter 5, electron density is localized in Co-H bonds upon the dissociative adsorption of H₂ on Co clusters. The orbitals involved in the binding of hydrogen are located below the highest occupied molecular orbital of the metal cluster. As a hydrogen atom has only one electron, vacant states are created below the Fermi level. As these states are filled with electrons, the Fermi level shifts down in the 3*d* band. This shift of the Fermi level with hydrogen coverage should be observable with photoelectron detachment spectroscopy.

Finally, it is possible to deposit mass-selected transition metal clusters that are produced in the gas-phase, on different support materials. These systems are more related to the actual catalyst and hence narrow the materials gap that exists between model systems and industrially used catalysts. Furthermore, by comparing deposited clusters with the corresponding gas-phases species, fundamental information regarding metal-support effects can be obtained.

Samenvatting

De moleculen waterstof (H_2) en koolstofmonoxide (CO) spelen een grote rol in verschillende katalytische processen. Een voorbeeld is de Fischer-Tropsch synthese waarin op kleine metaaldeeltjes geadsorbeerde H_2 en CO moleculen reageren tot koolwaterstoffen. Deze koolwaterstoffen kunnen vervolgens onder andere gebruikt worden als brandstof. Het doel van het onderzoek dat beschreven wordt in dit proefschrift, is het verkrijgen van fundamentele kennis over de adsorptie van H_2 en CO moleculen op kleine metaaldeeltjes. Hiertoe is zowel de adsorptie van de individuele moleculen, als ook de co-adsorptie van H_2 en CO op verschillende metaaldeeltjes in de gasfase onderzocht met behulp van vibratiespectroscopie en kwantummechanische berekeningen.

In **hoofdstuk 3** staat beschreven hoe meerdere H_2 moleculen adsorberen op een reeks van verschillende kleine metaaldeeltjes (scandium, vanadium, ijzer, kobalt en nikkel). Het maximale aantal moleculen dat kan adsorberen op een metaaldeeltje, het zogenaamde verzadigingsgetal, is bepaald als functie van het aantal metaal atomen in het deeltje. Waterstof moleculen (H_2) vallen uit elkaar in waterstof atomen (H) tijdens de adsorptie op grote scandium, vanadium, ijzer, kobalt en nikkel oppervlakken. Dit wordt dissociatieve adsorptie genoemd. Om informatie te verkrijgen over hoe de waterstof is gebonden aan kleine metaaldeeltjes, zijn vibratiespectra gemeten. Ook zijn de vibratiespectra van verschillende geometrische isomeren berekend met dichtheids functionaal theorie. Door de experimentele en gesimuleerde spectra te vergelijken, zijn de bindings geometriën van het waterstof bepaald. Het blijkt dat de H_2 moleculen dissociatief adsorberen op scandium, vanadium, ijzer en kobalt deeltjes. Daarentegen blijkt dat slechts een deel van de waterstof moleculen dissociatief adsorbeert op kleine nikkel deeltjes en dat een ander deel intact adsorbeert (moleculaire adsorptie).

Een belangrijke vraag is dan: Hoe bindt het eerste H_2 molecuul op kleine nikkel deeltjes? Met andere woorden: Valt het eerste H_2 molecuul uit elkaar of niet? Deze vraag wordt beantwoord in **hoofdstuk 4**. Het blijkt dat het antwoord op deze vraag afhankelijk is van het aantal metaal atomen in het deeltje. Het eerste H_2 molecuul dat adsorbeert op nikkel deeltjes met 5 en 6 atomen (Ni_5 en Ni_6) valt uit elkaar, terwijl het molecuul adsorbeert op een deeltje met 4 nikkel atomen (Ni_4). Bovendien wordt aangetoond dat het adsorptiegedrag van het eerste waterstof molecuul (dissociatief of molecuulair) correleert met de activiteit (hoe snel de deeltjes reageren) van de metaaldeeltjes: Ni_5 en Ni_6 reageren snel en binden H_2 dissociatief, terwijl Ni_4 minder snel reageert en het H_2 molecuul intact bindt.

In de **hoofdstukken 5 en 6** worden de effecten die op kunnen treden tijdens de co-adsorptie van H_2 en CO bestudeerd. Als voorbeeld zijn co-adsorptie effecten voor vanadium (V) en kobalt (Co) bestudeerd. Het is bekend dat CO molecuulair

adsorbeert op kobalt deeltjes. De C–O binding van een geadsorbeerd CO molecuul is zwakker dan dat van een vrij CO molecuul. Dit wordt veroorzaakt doordat het metaal elektrondichtheid overdraagt aan het geadsorbeerde CO molecuul: hoe meer er overgedragen wordt, des te zwakker wordt de C–O binding. De beschreven experimenten tonen aan dat de C–O binding in de meeste gevallen sterker wordt door de co-adsorptie van H₂. Een kwantitatief model dat de deeltjesgrootte- en ladings- afhankelijkheid van de C–O binding van CO geadsorbeerd op metalen beschrijft, is uitgebreid zodat ook het effect van co-adsorptie van waterstof kwantitatief beschreven kan worden. Zoals aangetoond in hoofdstuk 3, valt H₂ op kleine kobalt deeltjes uit elkaar in H atomen. Hierbij worden Co–H bindingen gevormd. De elektronendichtheid die hiermee gemoeid is, komt voornamelijk uit het kobalt en kan derhalve niet meer overgedragen worden aan het ook geadsorbeerde CO molecuul. De vorming van Co–H bindingen resulteert dus in een afname van de elektrondichtheid die overgedragen wordt aan CO, en derhalve in een toename van de C–O bindingssterkte. Co-adsorptie van waterstof heeft dus een vergelijkbaar effect als een (gedeeltelijke) ionisatie van het metaaldeeltje. Door het vergelijken van beide effecten is bepaald hoeveel elektrondichtheid elk waterstof atoom ‘wegneemt’ van het metaaldeeltje. Dit varieert van 0.09 tot 0.25 elektron per waterstof atoom, afhankelijk van de deeltjesgrootte. Uit het bovenstaande blijkt duidelijk dat (co-) adsorptie van waterstof een grote invloed heeft op de elektronische structuur van kleine kobalt deeltjes.

Koolstofmonoxide dissocieert op grote vanadium oppervlakken. De experimenten tonen aan dat een CO molecuul ook uit elkaar valt in een koolstof (C) en een zuurstof atoom (O) tijdens de adsorptie op kleine vanadium clusters. Wanneer echter alle mogelijke bindingssites voor C en O atomen bezet zijn met H atomen, blijkt dat het CO molecuul niet meer kan dissociëren. Ook in geval van vanadium worden V–H bindingen gevormd. Echter, in tegenstelling tot kobalt, suggereren kwantummechanische berekeningen dat de co-adsorptie van waterstof geen grote invloed heeft op de sterkte van de C–O binding van op vanadium geadsorbeerd CO. De moleculaire adsorptie van CO is dus voornamelijk een structuur effect.

Een onderzoek naar de adsorptie van meerdere CO moleculen op rhodium, kobalt en nikkel deeltjes wordt beschreven in de **hoofdstukken 7 en 8**. De structuren van enkelvoudig positief geladen rhodium-carbonyl complexen met 1 tot 6 metaal atomen zijn bepaald door middel van een gecombineerde experimentele en theoretische studie. Door de structuren van de positief geladen complexen te vergelijken met die van de bekende neutrale complexen, kon informatie over de effecten van ionisatie worden verkregen. Het blijkt dat ionisatie van de neutrale verbindingen leidt tot een selectieve destabilisatie van CO moleculen die aan twee rhodium atomen gebonden zijn. Kwantummechanische berekeningen laten zien dat deze destabilisatie het gevolg is van een afname van de elektrondichtheid in de gebieden tussen de rhodium atomen en de tweevoudig gecoördineerde CO moleculen.

Voor kobalt en nikkel clusters is het maximum aantal CO moleculen dat kan adsorberen bepaald als functie van de deeltjesgrootte. Met behulp van elektronen-

telschema's kunnen op basis van de verzadigingsgetallen voorspellingen gedaan worden over mogelijke deeltjes structuren. Ook zijn vibratiespectra gemeten voor de complexen met 1 tot 6 metaal atomen en zijn er kwantummechanische berekeningen uitgevoerd voor complexen met 1, 2 en 3 metaal atomen. Zowel de elektronen-telschema's als de kwantummechanische berekeningen suggereren dat een dubbele Co=Co binding aanwezig is in het complex met 3 kobalt atomen. De vibratiespectra laten zien dat CO moleculen die gebonden zijn aan twee metaal atomen in het geval van nickel-carbonylen voorkomen bij complexen met 4 of meer metaal atomen, terwijl tweevoudig gecoördineerde CO moleculen aanwezig zijn voor alle kobalt complexen met meer dan 1 metaal atoom. Echter, de bindingsgeometrie van deze CO moleculen in de enkelvoudig positief geladen complexen is anders dan die in de neutrale verbindingen. Deze verstoring wordt veroorzaakt doordat de elektrondichtheid in de gebieden tussen de metaal atomen en de tweevoudig gecoördineerde CO moleculen afneemt door ionisatie. De afname voor kobalt-carbonylen is echter kleiner dan voor rhodium-carbonylen. Dit kan verklaren waarom er wel tweevoudig gecoördineerd CO wordt gevonden voor kobalt-carbonylen maar niet voor rhodium-carbonylen.

Bibliography

- [1] J. J. Berzelius, *Jahresberichte*, **15**, 237 (1835).
- [2] E. M. Melhado, in *Encyclopædia Britannica*, **2007**.
- [3] R. A. van Santen, P. W. N. M. van Leeuwen, J. A. Moulijn, B. A. Averill, (Editors), *Catalysis: An Integrated Approach*, Elsevier Science, Amsterdam, **1999**.
- [4] B. Yoon, H. Hakkinen, U. Landman, A. S. Worz, J.-M. Antonietti, S. Abbet, K. Judai, U. Heiz, *Science*, **307**, 403 (2005).
- [5] H. Häkkinen, S. Abbet, A. Sanchez, U. Heiz, U. Landman, *Angew. Chem. Int. Ed.*, **42**, 1297 (2003).
- [6] M. Date, H. Imai, S. Tsubota, M. Haruta, *Catal. Today*, **122**, 222 (2007).
- [7] H. H. Kung, M. C. Kung, C. K. Costello, *J. Catal.*, **216**, 425 (2003).
- [8] B. Hvolbæk, T. V. W. Janssens, B. S. Clausen, H. Falsig, C. H. Christensen, J. K. Norskov, *Nano Today*, **2**, 14 (2007).
- [9] T. Visser, T. A. Nijhuis, A. M. J. van der Eerden, K. Jenken, Y. Ji, W. Bras, S. Nikitenko, Y. Ikeda, M. Lepage, B. M. Weckhuysen, *J. Phys. Chem. B*, **109**, 3822 (2005).
- [10] C. Fontaine-Gautrelet, J.-M. Krafft, G. Djega-Mariadassou, C. Thomas, *J. Catal.*, **247**, 34 (2007).
- [11] F. Morales, E. de Smit, F. M. F. de Groot, T. Visser, B. M. Weckhuysen, *J. Catal.*, **246**, 91 (2007).
- [12] F. Morales, F. M. F. de Groot, P. Glatzel, E. Kleimenov, H. Bluhm, M. Hävecker, A. Knop-Gericke, B. M. Weckhuysen, *J. Phys. Chem. B*, **41**, 16201 (2004).
- [13] G. R. Sheffer, T. S. King, *J. Catal.*, **115**, 376 (1989).
- [14] J. M. Driessen, E. K. Poels, J. P. Hindermann, V. Ponec, *J. Catal.*, **82**, 26 (1983).
- [15] R. J. Davis, *Science*, **301**, 926 (2003).
- [16] Q. Fu, H. Saltsburg, M. Flytzani-Stephanopoulos, *Science*, **301**, 935 (2003).
- [17] G. Ertl, S. B. Lee, M. Weiss, *Surf. Sci.*, **114**, 527 (1982).
- [18] G. J. Hutchings, F. King, I. P. Okoye, M. B. Padley, C. H. Rochester, *J. Catal.*, **148**, 453 (1994).
- [19] G. J. Hutchings, *Catal. Lett.*, **75**, 1 (2001).
- [20] J. E. Bailie, H. A. Abdullah, J. A. Anderson, C. H. Rochester, N. V. Richardson, N. Hodge, J. G. Zhang, A. Burrows, C. J. Kiely, G. J. Hutchings, *Phys. Chem. Chem. Phys.*, **3**, 4113 (2001).
- [21] I. Langmuir, *Trans. Faraday Soc.*, **17**, 607 (1922).
- [22] G. Ertl, *Angew. Chem. Int. Ed.*, **47**, 3524 (2008).
- [23] H. Over, Y. D. Kim, A. P. Seitsonen, S. Wendt, E. Lundgren, M. Schmid, P. Varga, A. Morgante, G. Ertl, *Science*, **287**, 1474 (2000).

- [24] G. L. Bezemer, J. H. Bitter, H. Kuipers, H. Oosterbeek, J. E. Holewijn, X. D. Xu, F. Kapteijn, A. J. van Dillen, K. P. de Jong, *J. Am. Chem. Soc.*, **128**, 3956 (2006).
- [25] P. Schnabel, M. P. Irion, K. G. Weil, *J. Phys. Chem.*, **95**, 9688 (1991).
- [26] P. Schnabel, K. G. Weil, M. P. Irion, *Angew. Chem. Int. Ed.*, **31**, 636 (1992).
- [27] J. Conceição, R. T. Laaksonen, L.-S. Wang, T. Guo, P. Nordlander, R. E. Smalley, *Phys. Rev. B*, **51**, 4668 (1995).
- [28] Z. Xu, F. S. Xiao, S. K. Purnell, O. Alexeev, S. Kawi, S. E. Deutsch, B. C. Gates, *Nature*, **372**, 346 (1994).
- [29] M. E. Dry, *App. Catal. A: General*, **138**, 319 (1996).
- [30] M. E. Dry, *App. Catal. A: General*, **276**, 1 (2004).
- [31] R. K. Ahluwalia, Q. Zhang, D. J. Chmielewski, K. C. Lauzze, M. A. Inbody, *Catal. Today*, **99**, 271 (2005).
- [32] R. M. Navarro, M. A. Pena, J. L. G. Fierro, *Chem. Rev.*, **107**, 3952 (2007).
- [33] K. Christmann, *Surf. Sci. Rep.*, **9**, 1 (1988).
- [34] S.-S. Sung, R. Hoffmann, *J. Am. Chem. Soc.*, **107**, 578 (1985).
- [35] J. K. Norskov, *Rep. Prog. Phys.*, **53**, 1253 (1990).
- [36] J. C. Campuzano, in *The Chemical Physics of Solid Surfaces and Heterogeneous Catalysis, Vol. 3* (Eds.: D. A. King, D. P. Woodruff), Elsevier, Amsterdam, **1990**.
- [37] J. W. Davenport, P. J. Estrup, in *The Chemical Physics of Solid Surfaces and Heterogeneous Catalysis, Vol. 3* (Eds.: D. A. King, D. P. Woodruff), Elsevier, Amsterdam, **1990**.
- [38] D. Lerch, A. Klein, A. Schmidt, S. Muller, L. Hammer, K. Heinz, M. Weinert, *Phys. Rev. B*, **73** (2006).
- [39] A. Eichler, J. Hafner, G. Kresse, *J. Phys.-Condens. Mat.*, **8**, 7659 (1996).
- [40] C. Popa, W. K. Offermans, R. A. van Santen, A. P. J. Jansen, *Phys. Rev. B*, **74**, 155428 (2006).
- [41] E. Vesselli, A. Baraldi, F. Bondino, G. Comelli, M. Peressi, R. Rosei, *Phys. Rev. B*, **70** (2004).
- [42] J. Kua, L. J. Lauhon, W. Ho, W. A. Goddard, *J. Chem. Phys.*, **115**, 0 (2001).
- [43] G. Lee, E. W. Plummer, *Surf. Sci.*, **498**, 229 (2002).
- [44] J. L. Nie, H. Y. Xiao, X. T. Zu, *Chem. Phys.*, **321**, 48 (2006).
- [45] C. J. Hagedorn, M. J. Weiss, W. H. Weinberg, *Phys. Rev. B*, **60**, 14016 (1999).
- [46] J. A. Prybyla, P. J. Estrup, S. C. Ying, Y. J. Chabal, S. B. Christman, *Phys. Rev. Lett.*, **58**, 1877 (1987).
- [47] A. M. Baro, W. Erley, *Surf. Sci.*, **112**, L759 (1981).
- [48] C. Y. Fan, K. Jacobi, *Surf. Sci.*, **482**, 21 (2001).
- [49] U. Muschiol, J. Lenz, E. Schwarz, K. Christmann, *Surf. Sci.*, **331-333**, 127 (1995).
- [50] R. Doll, L. Hammer, K. Heinz, K. Bedurftig, U. Muschiol, K. Christmann, A. P. Seitonen, H. Bludau, H. Over, *J. Chem. Phys.*, **108**, 8671 (1998).
- [51] H. Yamazaki, K. Sakamoto, A. Fujii, T. Kamisawa, *Surf. Sci.*, **563**, 41 (2004).
- [52] Y. T. Wong, R. Hoffmann, *J. Phys. Chem.*, **95**, 859 (1991).

- [53] A. Föhlisch, M. Nyberg, J. Hasselstrom, O. Karis, L. G. M. Pettersson, A. Nilsson, *Phys. Rev. Lett.*, **85**, 3309 (2000).
- [54] A. Beutler, E. Lundgren, R. Nyholm, J. N. Andersen, B. J. Setlik, D. Heskett, *Surf. Sci.*, **396**, 117 (1998).
- [55] M. J. S. Dewar, *Bull. Soc. Chim. Fr.*, **18**, C71 (1951).
- [56] J. Chatt, L. A. Duncanson, *J. Chem. Soc.*, 2939 (1953).
- [57] M. Nyberg, A. Föhlisch, L. Triguero, A. Bassan, A. Nilsson, L. G. M. Pettersson, *J. Mol. Struct.-Theochem.*, **762**, 123 (2006).
- [58] A. Nilsson, L. G. M. Pettersson, J. K. Nørskov, *Chemical Bonding at Surfaces and Interfaces*, Elsevier, Amsterdam, **2008**.
- [59] G. J. Kubas, *J. Organomet. Chem.*, **635**, 37 (2001).
- [60] A. S. Mårtensson, C. Nyberg, S. Andersson, *Phys. Rev. Lett.*, **57**, 2045 (1986).
- [61] P. K. Schmidt, K. Christmann, G. Kresse, J. r. Hafner, M. Lischka, A. Grofl, *Phys. Rev. Lett.*, **87**, 096103 (2001).
- [62] A. Fielicke, A. Kirilyuk, C. Ratsch, J. Behler, M. Scheffler, G. von Helden, G. Meijer, *Phys. Rev. Lett.*, **93**, 023401 (2004).
- [63] C. Ratsch, A. Fielicke, A. Kirilyuk, J. Behler, G. von Helden, G. Meijer, M. Scheffler, *J. Chem. Phys.*, **122**, 124302 (2005).
- [64] K. K. Lehmann, G. Scoles, B. H. Pate, *Ann. Rev. Phys. Chem.*, **45**, 241 (1994).
- [65] J. Oomens, B. G. Sartakov, G. Meijer, G. von Helden, *Int. J. Mass Spectrom.*, **254**, 1 (2006).
- [66] G. von Helden, D. van Heijnsbergen, G. Meijer, *J. Phys Chem. A*, **107**, 1671 (2003).
- [67] J. I. Steinfeld, *An Introduction to Modern Molecular Spectroscopy*, 2nd ed., MIT Press, Cambridge, MA, **1986**.
- [68] U. Buck, *J. Phys. Chem.*, **98**, 5190 (1994).
- [69] T. J. Selegue, N. Moe, J. A. Draves, J. M. Lisy, *J. Chem. Phys.*, **96**, 7268 (1992).
- [70] D. M. Rayner, L. Lian, K. Athanassenas, B. A. Collings, R. Fournier, S. A. Mitchell, P. A. Hackett, *Surf. Rev. Lett.*, **3**, 649 (1996).
- [71] A. Fielicke, I. Rabin, G. Meijer, *J. Phys Chem. A*, **110**, 8060 (2006).
- [72] A. Fielicke, G. von Helden, G. Meijer, *Eur. Phys. J. D*, **34**, 83 (2005).
- [73] P. Gruene, A. Fielicke, G. Meijer, *J. Chem. Phys.*, **127**, 234307 (2007).
- [74] A. Fielicke, C. Ratsch, G. von Helden, G. Meijer, *J. Chem. Phys.*, **127**, 234306 (2007).
- [75] A. Fielicke, G. von Helden, G. Meijer, D. B. Pedersen, B. Simard, D. M. Rayner, *J. Phys. Chem. B*, **108**, 14591 (2004).
- [76] A. Fielicke, G. von Helden, G. Meijer, D. B. Pedersen, B. Simard, D. M. Rayner, *J. Chem. Phys.*, **124**, 194305 (2006).
- [77] A. Fielicke, G. von Helden, G. Meijer, B. Simard, S. Dénommée, D. M. Rayner, *J. Am. Chem. Soc.*, **125**, 11184 (2003).
- [78] A. Fielicke, G. von Helden, G. Meijer, D. B. Pedersen, B. Simard, D. M. Rayner, *J. Am. Chem. Soc.*, **127**, 8416 (2005).
- [79] A. Fielicke, G. von Helden, G. Meijer, B. Simard, D. M. Rayner, *J. Phys. Chem. B*, **109**, 23935 (2005).

- [80] K. R. Asmis, G. Santambrogio, M. Brummer, J. Sauer, *Angew. Chem. Int. Ed.*, **44**, 3122 (2005).
- [81] A. Fielicke, G. Meijer, G. von Helden, *Eur. Phys. J. D*, **24**, 69 (2003).
- [82] A. Fielicke, G. Meijer, G. von Helden, *J. Am. Chem. Soc.*, **125**, 3659 (2003).
- [83] A. Fielicke, R. Mitric, G. Meijer, V. Bonacic-Koutecky, G. von Helden, *J. Am. Chem. Soc.*, **125**, 15716 (2003).
- [84] D. van Heijnsbergen, G. von Helden, G. Meijer, M. A. Duncan, *J. Chem. Phys.*, **116**, 2400 (2002).
- [85] D. van Heijnsbergen, K. Demyk, M. A. Duncan, G. Meijer, G. von Helden, *Phys. Chem. Chem. Phys.*, **5**, 2515 (2003).
- [86] G. von Helden, A. G. G. M. Tielens, D. van Heijnsbergen, M. A. Duncan, S. Hony, L. B. F. M. Waters, G. Meijer, *Science*, **288**, 313 (2000).
- [87] D. van Heijnsbergen, M. A. Duncan, G. Meijer, G. von Helden, *Chem. Phys. Lett.*, **349**, 220 (2001).
- [88] D. van Heijnsbergen, A. Fielicke, G. Meijer, G. von Helden, *Phys. Rev. Lett.*, **89**, 013401 (2002).
- [89] D. van Heijnsbergen, G. von Helden, M. A. Duncan, A. J. A. van Roij, G. Meijer, *Phys. Rev. Lett.*, **83**, 4983 (1999).
- [90] D. Oepts, A. F. G. van der Meer, P. W. van Amersfoort, *Infrared Phys. Techn.*, **36**, 297 (1995).
- [91] H. P. Freund, T. M. Antonsen, *Principles of Free-electron Lasers*, 2nd ed., Chapman & Hall, London, **1996**.
- [92] F. Jensen, *Introduction to Computational Chemistry*, John Wiley & Sons, Chichester, **1999**.
- [93] E. Bright Wilson Jr., J. C. Decius, P. C. Cross, *Molecular Vibrations, The Theory of Infrared and Raman Vibrational Spectra*, Dover Publications Inc, New York, **1980**.
- [94] D. A. McQuarrie, J. D. Simon, *Physical Chemistry, a Molecular Approach*, University Science Books, Sausalito, California, **1997**.
- [95] R. Ahlrichs, M. Bär, M. Häser, H. Horn, C. Kölmel, *Chem. Phys. Lett.*, **162**, 165 (1989).
- [96] E. Schrödinger, *Phys. Rev.*, **28**, 1049 (1926).
- [97] M. Born, R. Oppenheimer, *Annalen der Physik*, **20**, 457 (1927).
- [98] C. Eckart, *Phys. Rev.*, **46**, 383 (1934).
- [99] W. Pauli, *Z. Phys.*, **31**, 765 (1925).
- [100] J. C. Slater, *Phys. Rev.*, **34**, 1293 (1929).
- [101] D. R. Hartree, *Proc. Cambridge Phil. Soc.*, **24**, 89 (1928).
- [102] D. R. Hartree, *Proc. Cambridge Phil. Soc.*, **24**, 111 (1928).
- [103] V. A. Fock, *Z. Phys.*, **61**, 126 (1930).
- [104] A. Szabo, N. S. Ostlund, *Modern Quantum Chemistry: Introduction to Advanced Electronic Structure Theory*, Dover Publications, **1996**.
- [105] P. Hohenberg, W. Kohn, *Phys. Rev.*, **136**, B864 (1964).
- [106] W. Kohn, L. J. Sham, *Phys. Rev.*, **140**, A1133 (1965).
- [107] J. P. Perdew, Y. Wang, *Phys. Rev. B*, **45**, 13244 (1992).

- [108] J. P. Perdew, K. Burke, M. Ernzerhof, *Phys. Rev. Lett.*, **77**, 3865 (1996).
- [109] A. D. Becke, *Phys. Rev. A*, **38**, 3098 (1988).
- [110] J. P. Perdew, *Phys. Rev. B*, **33**, 8822 (1986).
- [111] A. D. Becke, *J. Chem. Phys.*, **107**, 8554 (1997).
- [112] C. Lee, W. Yang, R. G. Parr, *Phys. Rev. B*, **37**, 785 (1988).
- [113] B. Hartke, *Angew. Chem. Int. Ed.*, **41**, 1468 (2002).
- [114] M. B. Knickelbein, *Ann. Rev. Phys. Chem.*, **50**, 79 (1999).
- [115] P. B. Armentrout, *Ann. Rev. Phys. Chem.*, **52**, 423 (2001).
- [116] M. R. Zakin, D. M. Cox, R. L. Whetten, D. J. Trevor, A. Kaldor, *Chem. Phys. Lett.*, **135**, 223 (1987).
- [117] R. Liyanage, J. Conceição, P. B. Armentrout, *J. Chem. Phys.*, **116**, 936 (2002).
- [118] J. Conceição, R. Liyanage, P. B. Armentrout, *Chem. Phys.*, **262**, 115 (2000).
- [119] J. Conceição, S. K. Loh, L. Lian, P. B. Armentrout, *J. Chem. Phys.*, **104**, 3976 (1996).
- [120] F. Liu, P. B. Armentrout, *J. Chem. Phys.*, **122**, 194320 (2005).
- [121] F. Liu, R. Liyanage, P. B. Armentrout, *J. Chem. Phys.*, **117**, 132 (2002).
- [122] M. E. Geusic, M. D. Morse, R. E. Smalley, *J. Chem. Phys.*, **82**, 590 (1985).
- [123] R. L. Whetten, D. M. Cox, D. J. Trevor, A. Kaldor, *Phys. Rev. Lett.*, **54**, 1494 (1985).
- [124] A. Bérces, A. Bérces, P. A. Hackett, L. Lian, S. A. Mitchell, D. M. Rayner, *J. Chem. Phys.*, **108**, 5476 (1998).
- [125] G. Dietrich, K. Dasgupta, S. Kuznetsov, K. Lutzenkirchen, L. Schweikhard, J. Ziegler, *Int. J. Mass Spectrom.*, **157-158**, 319 (1996).
- [126] M. D. Morse, M. E. Geusic, J. R. Heath, R. E. Smalley, *J. Chem. Phys.*, **83**, 2293 (1985).
- [127] E. K. Parks, K. Liu, S. C. Richtsmeier, L. G. Pobo, S. J. Riley, *J. Chem. Phys.*, **82**, 5470 (1985).
- [128] S. Yang, M. B. Knickelbein, *Z. Phys. D Atom Mol. Cl.*, **31**, 203 (1994).
- [129] M. B. Knickelbein, *Phys. Rev. B*, **71**, 184442 (2005).
- [130] H. K. Yuan, H. Chen, A. S. Ahmed, J. F. Zhang, *Phys. Rev. B*, **74**, 144434 (2006).
- [131] G. Dietrich, K. Dasgupta, K. Lützenkirchen, L. Schweikhard, J. Ziegler, *Chem. Phys. Lett.*, **252**, 141 (1996).
- [132] Y. M. Hamrick, M. D. Morse, *J. Phys. Chem.*, **93**, 6494 (1989).
- [133] L. Holmgren, A. Rosén, *J. Chem. Phys.*, **110**, 2629 (1999).
- [134] M. R. Zakin, D. M. Cox, R. Brickman, A. Kaldor, *J. Phys. Chem.*, **93**, 6823 (1989).
- [135] S. C. Richtsmeier, E. K. Parks, K. Liu, L. G. Pobo, S. J. Riley, *J. Chem. Phys.*, **82**, 3659 (1985).
- [136] M. B. Knickelbein, *Chem. Phys. Lett.*, **353**, 221 (2002).
- [137] M. B. Knickelbein, G. M. Koretsky, K. A. Jackson, M. R. Pederson, Z. Hajnal, *J. Chem. Phys.*, **109**, 10692 (1998).
- [138] H. Korsgen, P. Murtz, K. Lipus, W. Urban, J. P. Towle, J. M. Brown, *J. Chem.*

- Phys.*, **104**, 4859 (1996).
- [139] J. Ho, L. Zhu, E. K. Parks, S. J. Riley, *Z. Phys. D Atom Mol. Cl.*, **26**, 331 (1993).
- [140] J. Ho, L. Zhu, E. K. Parks, S. J. Riley, *J. Chem. Phys.*, **99**, 140 (1993).
- [141] E. K. Parks, G. C. Nieman, S. J. Riley, *Surf. Sci.*, **355**, 127 (1996).
- [142] D. M. Cox, P. Fayet, R. Brickman, M. Y. Hahn, A. Kaldor, *Catal. Lett.*, **4**, 271 (1990).
- [143] A. Schafer, C. Huber, R. Ahlrichs, *J. Chem. Phys.*, **100**, 5829 (1994).
- [144] C. Ashman, S. N. Khanna, M. R. Pederson, *Chem. Phys. Lett.*, **368**, 257 (2003).
- [145] M. Castro, C. Jamorski, D. R. Salahub, *Chem. Phys. Lett.*, **271**, 133 (1997).
- [146] V. G. Grigoryan, M. Springborg, *Phys. Rev. B*, **70**, 205415 (2004).
- [147] E. K. Parks, L. Zhu, J. Ho, S. J. Riley, *J. Chem. Phys.*, **100**, 7206 (1994).
- [148] P. Gruene, A. Fielicke, G. Meijer, *unpublished results*
- [149] T. J. Udovic, J. J. Rush, N. F. Berk, I. S. Anderson, *Phys. Rev. B*, **45**, 12573 (1992).
- [150] L. Jiang, Q. Xu, *J. Phys Chem. A*, **110**, 5636 (2006).
- [151] C. Köhler, G. Seifert, T. Frauenheim, *Chem. Phys.*, **309**, 23 (2005).
- [152] W. Moritz, R. Imbühl, R. J. Behm, G. Ertl, T. Matsushima, *J. Chem. Phys.*, **83**, 1959 (1985).
- [153] N. O. Jones, M. R. Beltran, S. N. Khanna, T. Baruah, M. R. Pederson, *Phys. Rev. B*, **70**, 165406 (2004).
- [154] K. H. Ernst, E. Schwarz, K. Christmann, *J. Chem. Phys.*, **101**, 5388 (1994).
- [155] S. Andersson, J. Harris, *Phys. Rev. Lett.*, **48**, 545 (1982).
- [156] M. B. Knickelbein, *J. Chem. Phys.*, **116**, 9703 (2002).
- [157] G. Kresse, J. Hafner, *Surf. Sci.*, **459**, 287 (2000).
- [158] G. Kresse, *Phys. Rev. B*, **62**, 8295 (2000).
- [159] H. J. Robota, W. Vielhaber, M. C. Lin, J. Segner, G. Ertl, *Surf. Sci.*, **155**, 101 (1985).
- [160] C. Nyberg, K. Svensson, A. S. Martensson, S. Andersson, *J. Electron. Spectros. Relat. Phenom.*, **64-5**, 51 (1993).
- [161] L. Zhu, J. Ho, E. K. Parks, S. J. Riley, *J. Chem. Phys.*, **98**, 2798 (1993).
- [162] W. F. Hoffman, E. K. Parks, G. C. Nieman, L. G. Pobo, S. J. Riley, *Z. Phys. D Atom Mol. Cl.*, **7**, 83 (1987).
- [163] E. K. Parks, G. C. Nieman, S. J. Riley, *J. Chem. Phys.*, **115**, 4125 (2001).
- [164] I. Swart, F. M. F. de Groot, B. M. Weckhuysen, P. Gruene, G. Meijer, A. Fielicke, *J. Phys. Chem. A*, **112**, 1139 (2008).
- [165] L. Zhu, J. Ho, E. K. Parks, S. J. Riley, *Z. Phys. D Atom Mol. Cl.*, **V26**, 313 (1993).
- [166] A. T. Bell, *Science*, **299**, 1688 (2003).
- [167] R. W. P. Wagemans, J. H. van Lenthe, P. E. de Jongh, A. J. van Dillen, K. P. de Jong, *J. Am. Chem. Soc.*, **127**, 16675 (2005).
- [168] W. Wernsdorfer, R. Sessoli, *Science*, **284**, 133 (1999).
- [169] A. Nakajima, T. Kishi, Y. Sone, S. Nonose, K. Kaya, *Z. Phys. D Atom Mol. Cl.*, **19**, 385 (1991).

- [170] G. Blyholder, *J. Phys. Chem.*, **68**, 2772 (1964).
- [171] H. Smithson, C. A. Marianetti, D. Morgan, A. van der Ven, A. Predith, G. Ceder, *Phys. Rev. B*, **66**, 144107 (2002).
- [172] J. A. Platts, *J. Mol. Struct.- Theochem.*, **545**, 111 (2001).
- [173] M. Primet, N. Sheppard, *J. Catal.*, **41**, 258 (1976).
- [174] M. J. Heal, E. C. Leisegang, R. G. Torrington, *J. Catal.*, **51**, 314 (1978).
- [175] Note that this does not require the clusters to be metallic but only that charge is delocalized.
- [176] S. Z. Todorova, G. B. Kadinov, *Res. Chem. Intermediat.*, **28**, 291 (2002).
- [177] G. E. Mitchell, J. L. Gland, J. M. White, *Surf. Sci.*, **131**, 167 (1983).
- [178] V. L. Kuznetsov, M. N. Aleksandrov, L. N. Bulgakova, *J. Mol. Catal.*, **55**, 146 (1989).
- [179] G. Rangelov, U. Bischler, N. Memmel, E. Bertel, V. Dose, M. Pabst, N. Rosch, *Surf. Sci.*, **273**, 61 (1992).
- [180] N. D. S. Canning, M. A. Chesters, *Surf. Sci.*, **175**, L811 (1986).
- [181] J. G. Love, S. Haq, D. A. King, *J. Chem. Phys.*, **97**, 8789 (1992).
- [182] L. Xu, H. Y. Mao, X. T. Zu, *Chem. Phys.*, **323**, 334 (2006).
- [183] P. L. Hansen, J. B. Wagner, S. Helveg, J. R. Rostrup-Nielsen, B. S. Clausen, H. Topsøe, *Science*, **295**, 2053 (2002).
- [184] G. Broden, T. N. Rhodin, C. Brucker, *Surf. Sci.*, **59**, 593 (1976).
- [185] D. B. Pedersen, D. M. Rayner, B. Simard, M. A. Addicoat, M. A. Buntine, G. F. Metha, A. Fielicke, *J. Phys Chem. A*, **108**, 964 (2004).
- [186] D. M. Cox, K. C. Reichmann, D. J. Trevor, A. Kaldor, *J. Chem. Phys.*, **88**, 111 (1987).
- [187] I. Balteanu, U. Achatz, O. P. Balaj, B. S. Fox, M. K. Beyer, V. E. Bondybey, *Int. J. Mass Spectrom.*, **229**, 61 (2003).
- [188] StoBe-deMon version 2.2 (2006), K. Hermann, L. G. M. Pettersson, M. E. Casida, C. Daul, A. Goursot, A. Koester, E. Proynov, A. St-Amant, D. R. Salahub, Contributing authors, V. Carravetta, H. Duarte, C. Friedrich, N. Godbout, J. Guan, C. Jamorski, M. Leboeuf, M. Leetmaa, M. Nyberg, S. Patchkovskii, L. Pedocchi, F. Sim, L. Triguero, A. Vela
- [189] K. Eichkorn, O. Treutler, H. Oehm, M. Haeser, R. Ahlrichs, *Chem. Phys. Lett.*, **240**, 283 (1995).
- [190] K. Eichkorn, F. Weigend, O. Treutler, R. Ahlrichs, *Theor. Chem. Acc.*, **97**, 119 (1997).
- [191] C. Benndorf, B. Kruger, F. Thieme, *Surf. Sci.*, **163**, L675 (1985).
- [192] D. W. Moon, S. Cameron, F. Zaera, W. Eberhardt, R. Carr, S. L. Bernasek, J. L. Gland, D. J. Dwyer, *Surf. Sci.*, **180**, L123 (1987).
- [193] R. S. Saiki, G. S. Herman, M. Yamada, J. Ostwalder, C. S. Fadley, *Phys. Rev. Lett.*, **63**, 283 (1989).
- [194] N. D. Shinn, T. E. Madey, *J. Chem. Phys.*, **83**, 5928 (1985).
- [195] A. C. Pavao, M. M. Soto, W. A. Lester, S. K. Lie, B. L. Hammond, C. A. Taft, *Phys. Rev. B*, **50**, 1868 (1994).
- [196] A. C. Pavao, T. C. F. Guimaraes, S. K. Lie, C. A. Taft, W. A. Lester, *J. Mol.*

- Struc.- Theochem.*, **458**, 99 (1999).
- [197] X. Y. Wu, A. K. Ray, *J. Chem. Phys.*, **110**, 2437 (1999).
- [198] S. Li, M. M. G. Alemany, J. R. Chelikowsky, *J. Chem. Phys.*, **121**, 5893 (2004).
- [199] M. Zhou, L. Andrews, *J. Phys. Chem. A*, **103**, 7773 (1999).
- [200] M. F. Zhou, L. Andrews, *J. Phys. Chem. A*, **103**, 5259 (1999).
- [201] G. Ertl, H. Knözinger, J. Weitkamp, Eds., *Handbook of Heterogeneous Catalysis*, Wiley-VCH, Weinheim, **1997**.
- [202] M. Lepage, T. Visser, F. Soulimani, A. M. Beale, A. Iglesias-Juez, A. M. J. van der Eerden, B. M. Weckhuysen, *J. Phys. Chem. C*, **in press** (2008).
- [203] T. Koerts, R. A. van Santen, *J. Catal.*, **134**, 13 (1992).
- [204] T. Beutel, O. S. Alekseev, Y. A. Ryndin, V. A. Likholobov, H. Knozinger, *J. Catal.*, **169**, 132 (1997).
- [205] P. J. Dyson, J. S. McIndoe, *Transition Metal Carbonyl Cluster Chemistry*, Gordon and Breach Science Publishers, Amsterdam, **2000**.
- [206] C. H. Wei, *Inorg. Chem.*, **8**, 2384 (1969).
- [207] E. R. Corey, L. F. Dahl, W. Beck, *J. Am. Chem. Soc.*, **85**, 1202 (1963).
- [208] B. T. Heaton, C. Jacob, I. S. Podkorytov, S. P. Tunik, *Inorg. Chim. Acta*, **359**, 3557 (2006).
- [209] A. D. Allian, Y. Z. Wang, M. Saeys, G. M. Kuramshina, M. Garland, *Vib. Spectrosc.*, **41**, 101 (2006).
- [210] P. Fayet, M. J. McGlinchey, L. H. Wöste, *J. Am. Chem. Soc.*, **109**, 1733 (1987).
- [211] Z. H. Liu, Q. Li, Y. M. Xie, R. B. King, H. F. Schaefer, *Inorg. Chem.*, **46**, 1803 (2007).
- [212] S. Li, N. A. Richardson, Y. M. Xie, R. B. King, H. F. Schaefer, *Faraday Discuss.*, **124**, 315 (2003).
- [213] Y. Xie, H. F. Schaefer, R. B. King, *J. Am. Chem. Soc.*, **122**, 8746 (2000).
- [214] E. K. Parks, K. P. Kerns, S. J. Riley, *J. Chem. Phys.*, **112**, 3384 (2000).
- [215] K. P. Kerns, E. K. Parks, S. J. Riley, *J. Chem. Phys.*, **112**, 3394 (2000).
- [216] L. Mond, C. Langer, F. Quincke, *J. Chem. Soc. Trans*, **57**, 749 (1890).
- [217] J. W. Lauher, *J. Am. Chem. Soc.*, **100**, 5305 (1978).
- [218] J. W. Lauher, *J. Am. Chem. Soc.*, **101**, 2604 (1979).
- [219] T. K. W. Hieber, *Angew. Chem.*, **73**, 580 (1961).
- [220] P. K. Hurlburt, O. P. Anderson, S. H. Strauss, *J. Am. Chem. Soc.*, **113**, 6277 (1991).
- [221] P. K. Hurlburt, J. J. Rack, J. S. Luck, S. F. Dec, J. D. Webb, O. P. Anderson, S. H. Strauss, *J. Am. Chem. Soc.*, **116**, 10003 (1994).
- [222] A. J. Lupinetti, M. D. Havighurst, S. M. Miller, O. P. Anderson, S. H. Strauss, *J. Am. Chem. Soc.*, **121**, 11920 (1999).
- [223] B. C. Guo, K. P. Kerns, A. W. Castleman, *J. Chem. Phys.*, **96**, 8177 (1992).
- [224] S. Goebel, C. L. Haynes, F. A. Khan, P. B. Armentrout, *J. Am. Chem. Soc.*, **117**, 6994 (1995).
- [225] E. Bernhardt, M. Finze, H. Willner, C. W. Lehmann, F. Aubke, *Angew. Chem. Int. Ed.*, **42**, 2077 (2003).
- [226] E. Bernhardt, M. Finze, H. Willner, C. W. Lehmann, F. Aubke, *Chem-Eur. J.*,

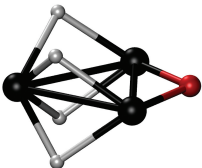
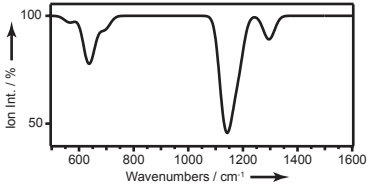

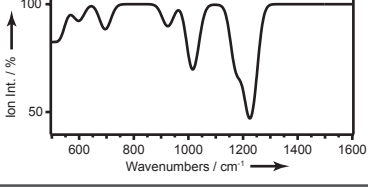
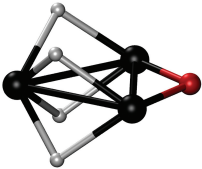
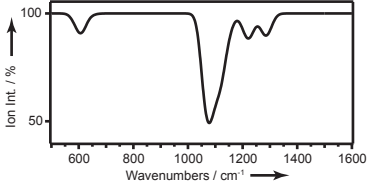
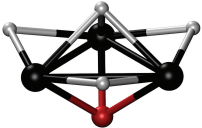
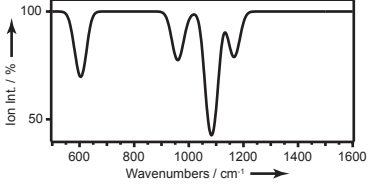
- 12**, 8276 (2006).
- [227] D. M. P. Mingos, D. J. Wales, *J. Am. Chem. Soc.*, **112**, 930 (1990).
- [228] D. T. Moore, J. Oomens, J. R. Eyler, G. Meijer, G. von Helden, D. P. Ridge, *J. Am. Chem. Soc.*, **126**, 14726 (2004).
- [229] P. A. Hintz, K. M. Ervin, *J. Chem. Phys.*, **100**, 5715 (1994).
- [230] B. Liang, M. Zhou, L. Andrews, *J. Phys. Chem. A*, **104**, 3905 (2000).
- [231] W. Hieber, W. Beck, G. Braun, *Angew. Chem.*, **72**, 795 (1960).
- [232] E. Kapiloff, K. M. Ervin, *J. Phys. Chem. A*, **101**, 8460 (1997).
- [233] V. Mahadevan, Y. D. Y. L. Getzler, G. W. Coates, *Angew. Chem. Int. Ed.*, **41**, 2781 (2002).
- [234] S. Vajda, S. Wolf, T. Leisner, U. Busolt, L. H. Woste, D. J. Wales, *J. Chem. Phys.*, **107**, 3492 (1997).
- [235] J. C. Calabrese, L. F. Dahl, A. Cavalieri, P. Chini, G. Longoni, S. Martinengo, *J. Am. Chem. Soc.*, **96**, 2616 (1974).
- [236] A. D. Harley, R. R. Whittle, G. L. Geoffroy, *Organometallics*, **2**, 60 (1983).
- [237] P. Dapporto, S. Midollini, L. Sacconi, *Inorg. Chem.*, **14**, 1643 (1975).
- [238] H. Y. Wang, Y. M. Xie, R. B. King, H. F. Schaefer, *J. Am. Chem. Soc.*, **128**, 11376 (2006).
- [239] I. S. Ignatyev, H. F. Schaefer, R. B. King, S. T. Brown, *J. Am. Chem. Soc.*, **122**, 1989 (2000).
- [240] R. L. Sweany, T. L. Brown, *Inorg. Chem.*, **16**, 415 (1977).
- [241] G. Bor, *Spectrochim. Acta*, **19**, 1209 (1963).
- [242] F. Cariati, V. Valenti, P. Barone, *Gazz. Chim. Ital.*, **99**, 1327 (1969).
- [243] M. R. Churchill, J. P. Hutchinson, *Inorg. Chem.*, **17**, 3528 (1978).
- [244] Roberto Della Pergola, L. Garlaschelli, S. Martinengo, S. Sherlock, W. Gladfelter, in *Inorganic Syntheses* (Ed.: J. A. Robert), **2007**, pp. 245.


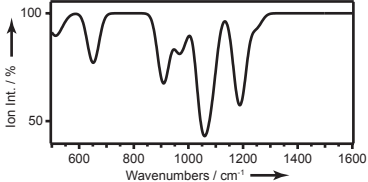
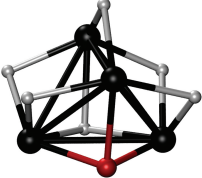
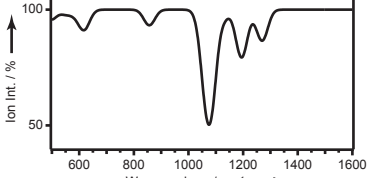
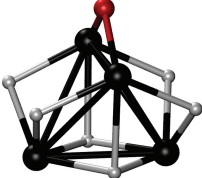
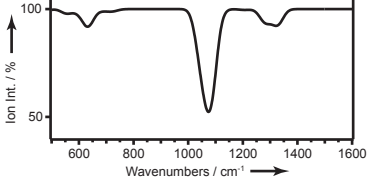
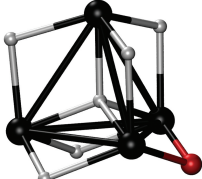
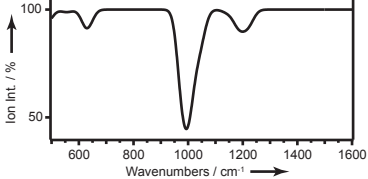
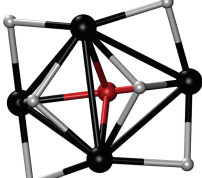
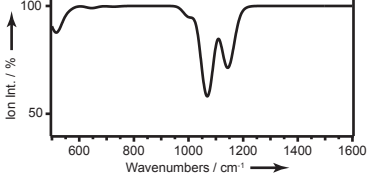

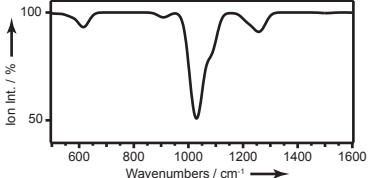
Appendix A

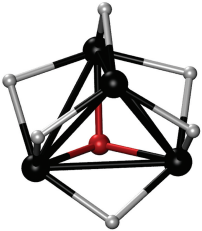
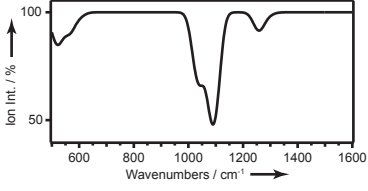
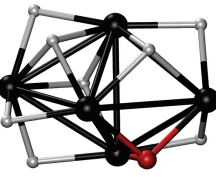
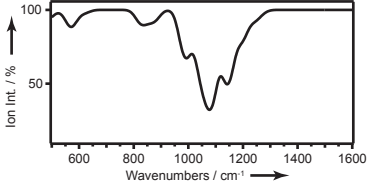

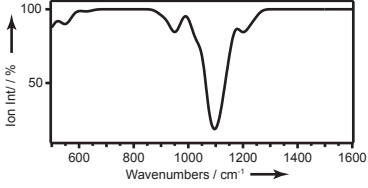

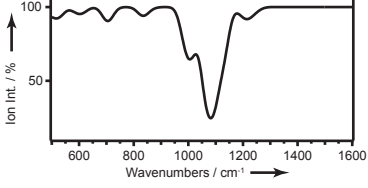
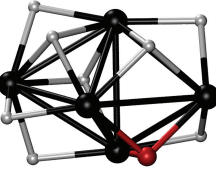
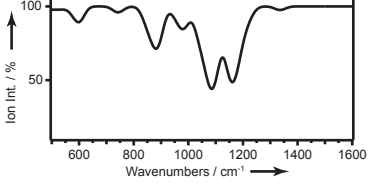
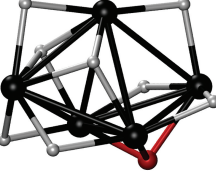
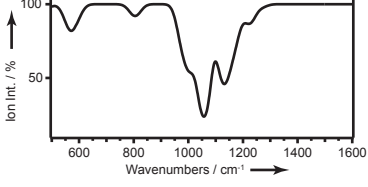
Optimized geometries, relative energies and vibrational spectra of $\text{Sc}_n\text{H}_m\text{O}^+$, V_nH_m^+ , Fe_nH_m^+ , Co_nH_m^+ , and Ni_nH_m^+ complexes.

The tables A1 to A5, give the optimized geometries, relative energies, and simulated vibrational spectra of several isomers of $\text{Sc}_n\text{H}_m\text{O}^+$, V_nH_m^+ , Fe_nH_m^+ , Co_nH_m^+ , and Ni_nH_m^+ , respectively. The calculations were performed using the BP86 parametrization of the exchange-correlation functional and a TZVP basis set for all atoms, as implemented in the TURBOMOLE package. The letter 'u' denotes the number of unpaired electrons and the symmetry label tolerance was 10^{-2} Å. For details, see chapter 3.

Table A.1. Optimized structures, energies and vibrational spectra of several isomers of $\text{Sc}_n\text{H}_m\text{O}^+$ with $n = 3-6$.

Species	Structure	Symmetry	ΔE (eV)	Spectrum
$\text{Sc}_3\text{H}_4\text{O}^+$ iso 1 u=0		C_{2v}	0.00	
$\text{Sc}_3\text{H}_4\text{O}^+$ iso 2 u=2		C_s	+0.39	
$\text{Sc}_3\text{H}_4\text{O}^+$ iso 1 u=2		C_{2v}	+0.43	
$\text{Sc}_3\text{H}_4\text{O}^+$ iso 3 u=2		C_{3v}	+0.48	

Species	Structure	Symmetry	ΔE (eV)	Spectrum
$\text{Sc}_3\text{H}_4\text{O}^+$ iso 4 u=2		C_1	+0.50	
$\text{Sc}_4\text{H}_6\text{O}^+$				
$\text{Sc}_4\text{H}_6\text{O}^+$ iso 1 u = 1		C_s	0.00	
$\text{Sc}_4\text{H}_6\text{O}^+$ iso 2 u = 1		C_{2v}	+0.03	
$\text{Sc}_4\text{H}_6\text{O}^+$ iso 3 u = 3		C_{2v}	+0.63	
$\text{Sc}_4\text{H}_6\text{O}^+$ iso 4 u = 3		C_{2v}	+0.65	
$\text{Sc}_4\text{H}_6\text{O}^+$ iso 3 u = 1		C_1	+0.67	

Species	Structure	Symmetry	ΔE (eV)	Spectrum
$\text{Sc}_4\text{H}_6\text{O}^+$ iso 5 u = 3		C_{3v}	+0.78	
$\text{Sc}_5\text{H}_8\text{O}^+$				
$\text{Sc}_5\text{H}_8\text{O}^+$ iso 1 u = 0		C_1	0.00	
$\text{Sc}_5\text{H}_8\text{O}^+$ iso 2 u = 0		C_s	+0.11	
$\text{Sc}_5\text{H}_8\text{O}^+$ iso 2 u = 2		C_s	+0.35	
$\text{Sc}_5\text{H}_8\text{O}^+$ iso 1 u = 2		C_1	+0.44	
$\text{Sc}_5\text{H}_8\text{O}^+$ iso 3 u = 2		C_{4v}	+0.46	

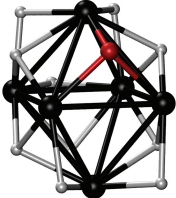
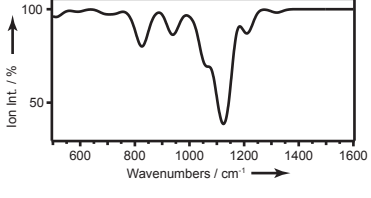
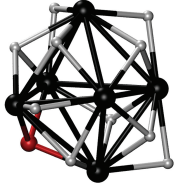
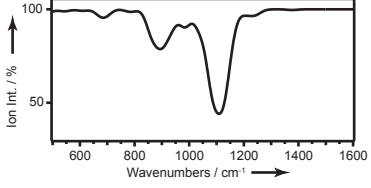

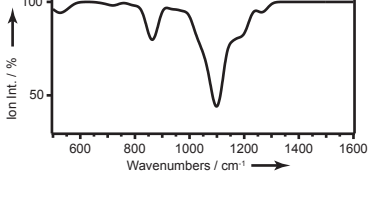
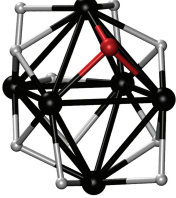
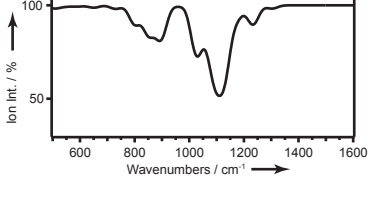

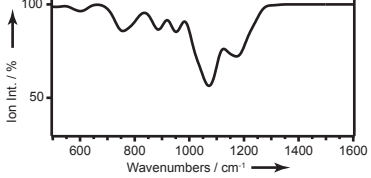
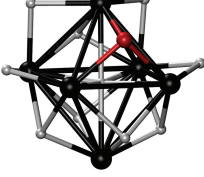
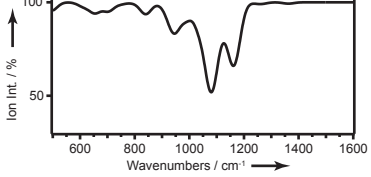
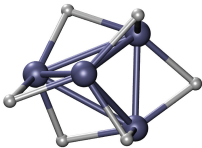
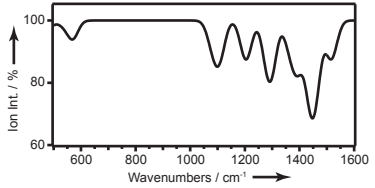
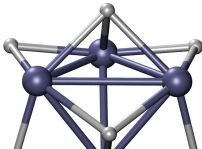
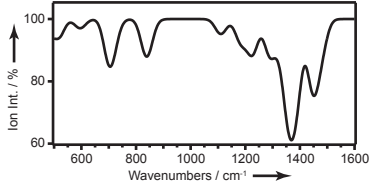
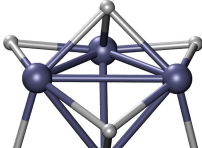
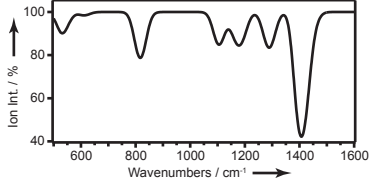
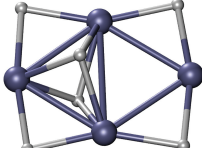
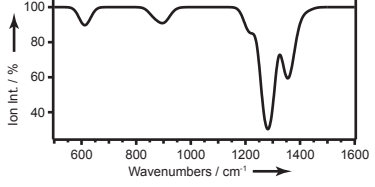
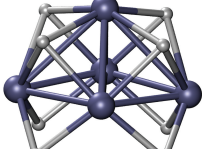
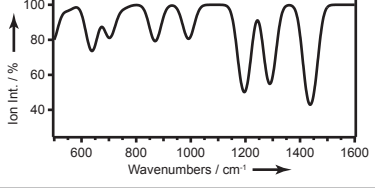
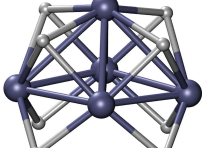
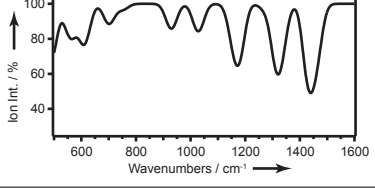
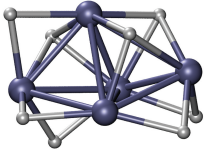
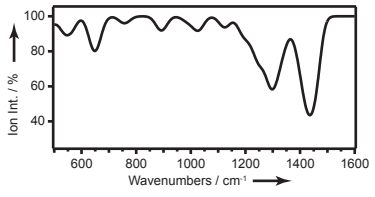
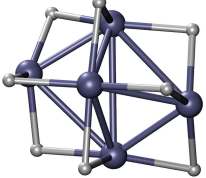
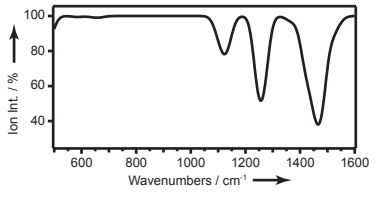
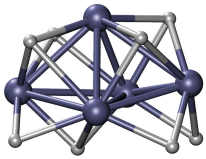
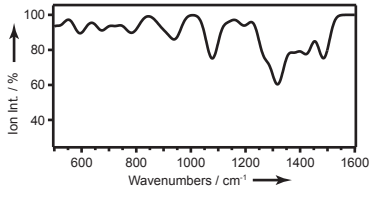
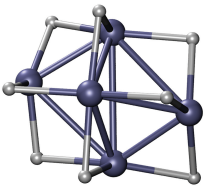
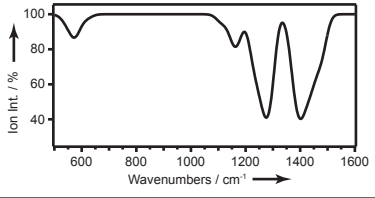
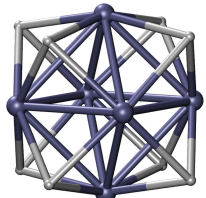
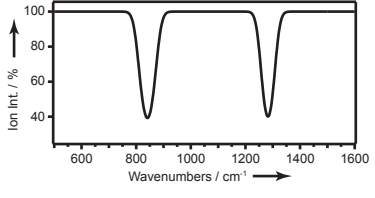
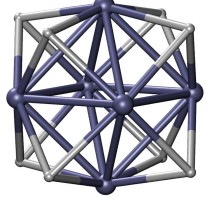
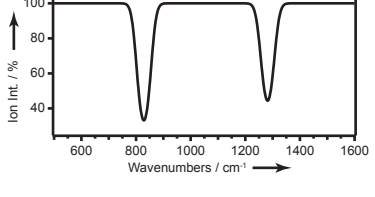
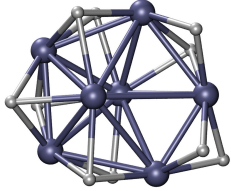
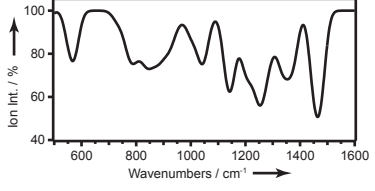
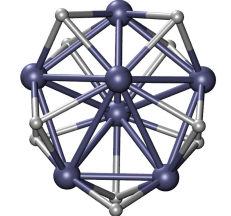
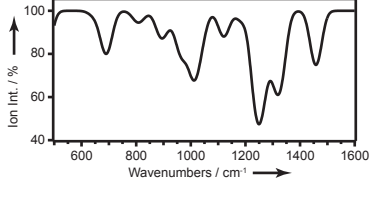
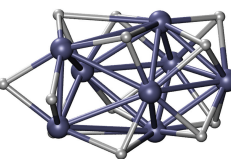
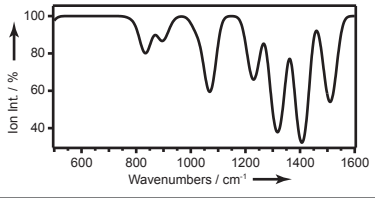
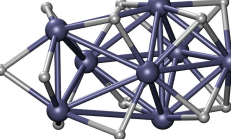
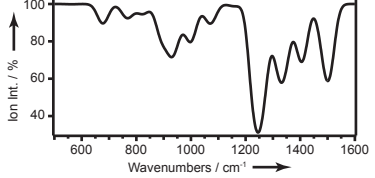
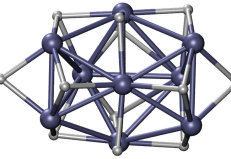
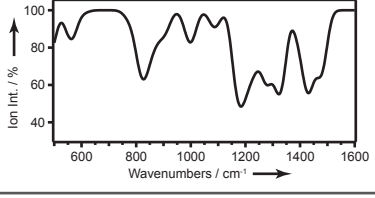
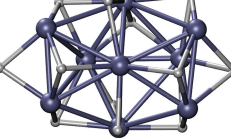
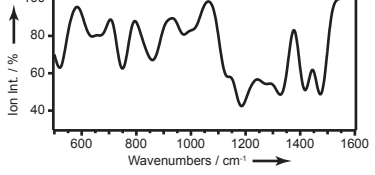
Species	Structure	Symmetry	ΔE (eV)	Spectrum
$Sc_6H_{10}O^+$				
$Sc_6H_{10}O^+$ iso 1 $u = 1$		C_1	0.00	
$Sc_6H_{10}O^+$ iso 2 $u = 1$		C_1	+0.03	
$Sc_6H_{10}O^+$ iso 3 $u = 3$		C_1	+0.08	
$Sc_6H_{10}O^+$ iso 1 $u = 3$		C_1	+0.26	
$Sc_6H_{10}O^+$ iso 4 $u = 1$		C_1	+0.39	
$Sc_6H_{10}O^+$ iso 5 $u = 1$		C_1	+0.49	

Table A.2. Optimized structures, energies and vibrational spectra of several isomers of $V_nH_m^+$ with $n = 4-9$.

Species	Structure	Symmetry	ΔE (eV)	Spectrum
$V_4H_6^+$ iso 1 $u = 1$		C_1	0.00	
$V_4H_6^+$ iso 2 $u = 1$		C_s	+0.45	
$V_4H_6^+$ iso 3 $u = 3$		C_s	+0.45	
$V_4H_6^+$ iso 4 $u = 1$		C_s	+1.31	
$V_5H_8^+$				
$V_5H_8^+$ iso 1 $u = 2$		C_{2v}	0.00	
$V_5H_8^+$ iso 1 $u = 0$		C_{2v}	0.00	

Species	Structure	Symmetry	ΔE (eV)	Spectrum
$V_5H_8^+$ iso 2 $u = 2$		C_1	+0.01	
$V_5H_8^+$ iso 3 $u = 0$		C_2	+0.03	
$V_5H_8^+$ iso 4 $u = 2$		C_1	+0.09	
$V_5H_8^+$ iso 3 $u = 2$		C_1	+0.25	
$V_6H_8^+$				
$V_6H_8^+$ iso1 $u = 1$		D_{4h}	0.00	
$V_6H_8^+$ iso1 $u = 3$		O_h	+0.11	

Species	Structure	Symmetry	ΔE (eV)	Spectrum
$V_7H_{10}^+$				
$V_7H_{10}^+$ iso1 u = 2		C_1	0.00	
$V_7H_{10}^+$ iso1 u = 0		C_1	+0.20	
$V_8H_{12}^+$				
$V_8H_{12}^+$ iso1 u = 1		C_1	0.00	
$V_8H_{12}^+$ iso1 u = 3		C_1	+0.50	
$V_9H_{12}^+$				
$V_9H_{12}^+$ iso1 u = 0		C_1	0.00	
$V_9H_{12}^+$ iso1 u = 2		C_1	+0.17	

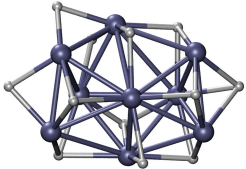
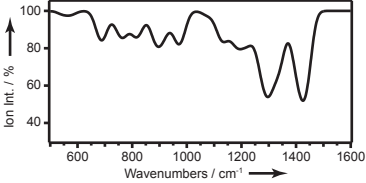
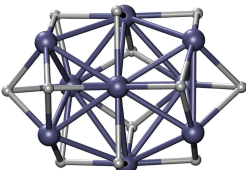
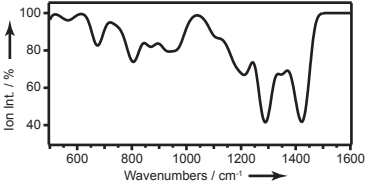
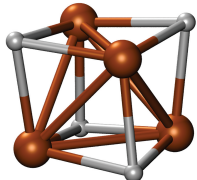
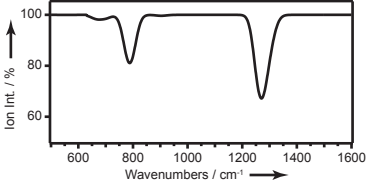
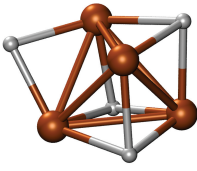
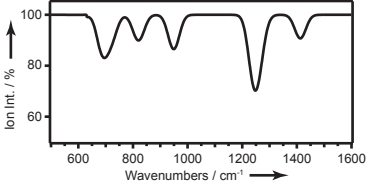
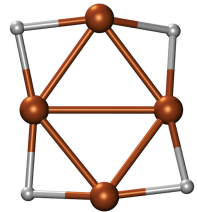
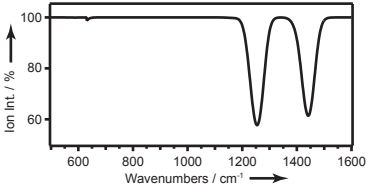
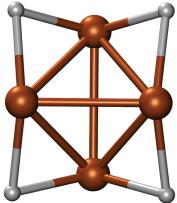
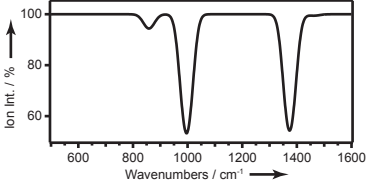
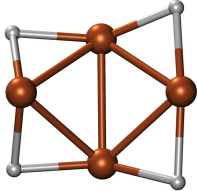
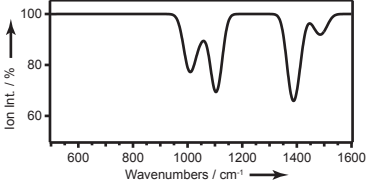
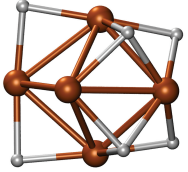
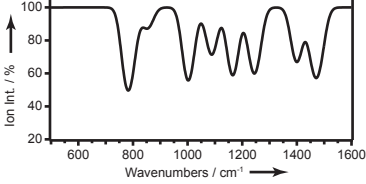
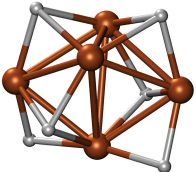
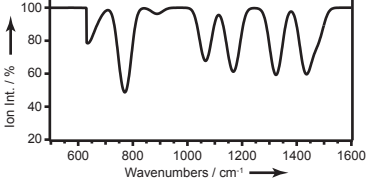
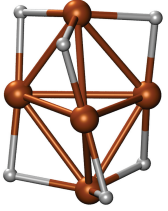
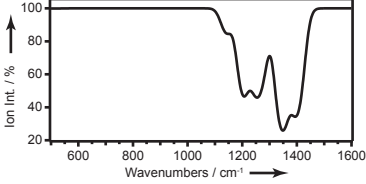
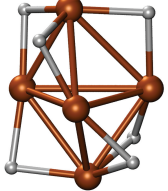
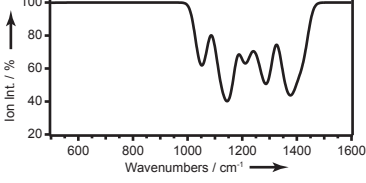
Species	Structure	Symmetry	ΔE (eV)	Spectrum
$V_9H_{12}^+$ iso2 $u = 2$		C_1	+0.18	
$V_9H_{12}^+$ iso2 $u = 0$		C_1	+0.40	

Table A.3. Optimized structures, energies and vibrational spectra of several isomers of $Fe_nH_m^+$ with $n = 4, 5$ and 6 .

Species	Structure	Symmetry	ΔE (eV)	Spectrum
$Fe_4H_4^+$ iso 1 $u = 13$		C_1	0.00	
$Fe_4H_4^+$ iso 2 $u = 13$		C_1	+0.02	
$Fe_4H_4^+$ iso 3 $u = 13$		C_1	+0.15	

Species	Structure	Symmetry	ΔE (eV)	Spectrum
Fe ₄ H ₄ ⁺ iso 4 u = 11		C ₁	+0.64	
Fe ₄ H ₄ ⁺ iso 5 u = 11		C ₁	+0.81	
Fe₅H₆⁺				
Fe ₅ H ₆ ⁺ iso 1 u = 15		C _s	0.00	
Fe ₅ H ₆ ⁺ iso 2 u = 15		C ₁	+0.13	
Fe ₅ H ₆ ⁺ iso 3 u = 17		C ₁	+0.14	
Fe ₅ H ₆ ⁺ iso 4 u = 17		C ₁	+0.18	

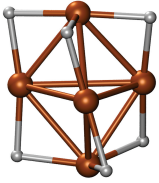
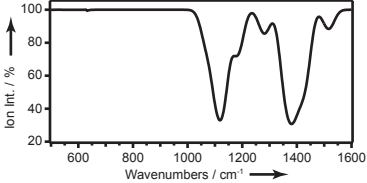
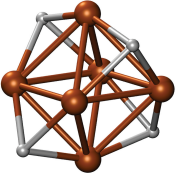
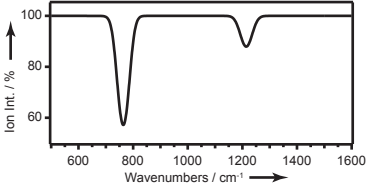
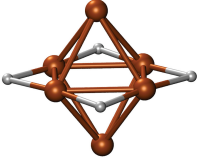
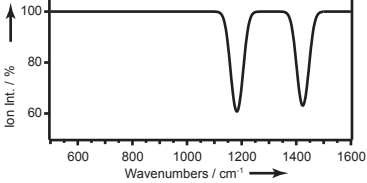
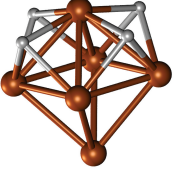
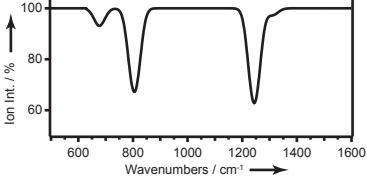
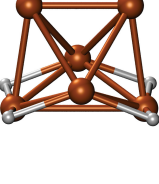
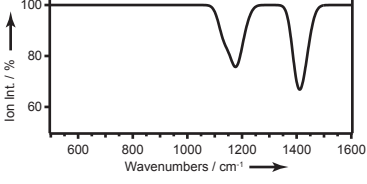
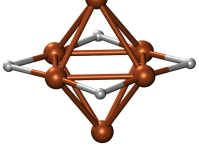
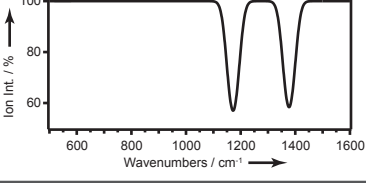
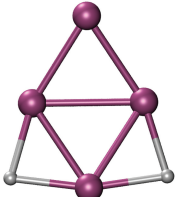
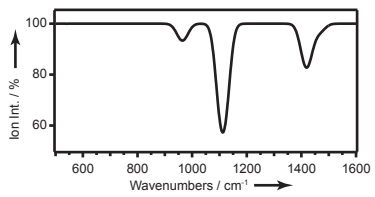
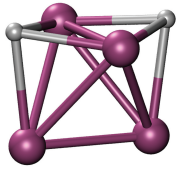
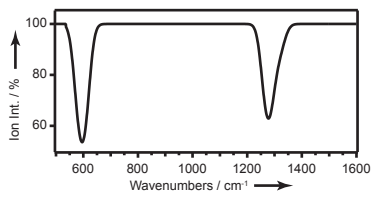
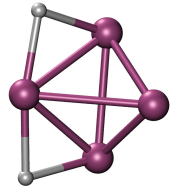
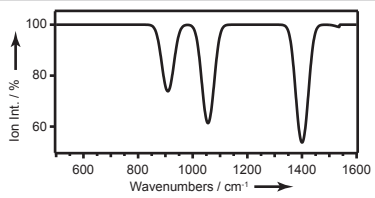
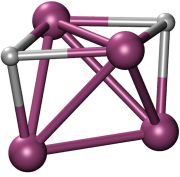
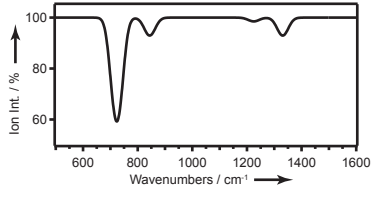
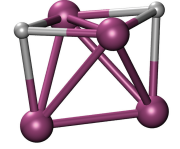
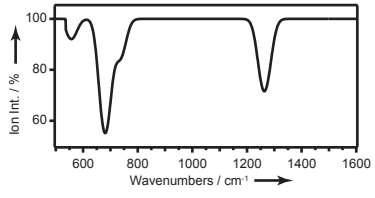
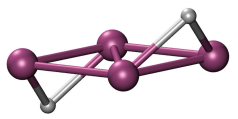
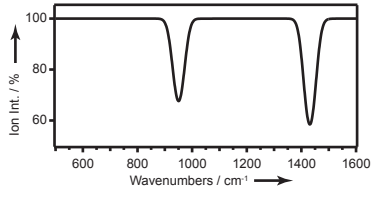
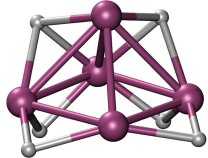
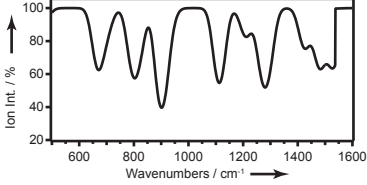
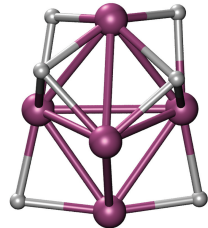
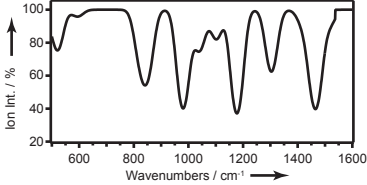
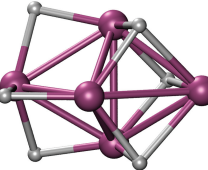
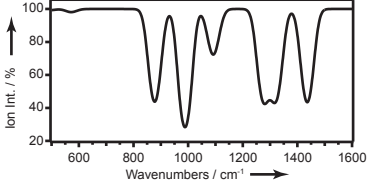
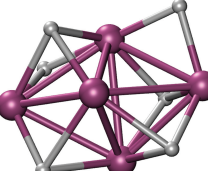
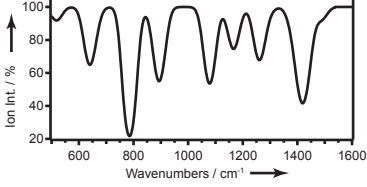
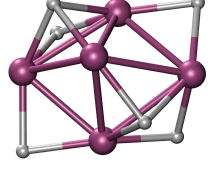
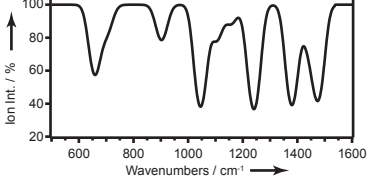
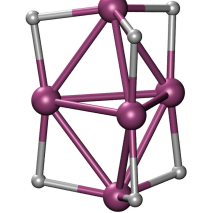
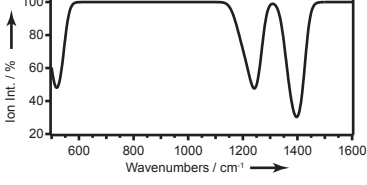
Species	Structure	Symmetry	ΔE (eV)	Spectrum
Fe_5H_6^+ iso 3 u = 15		C_1	+0.28	
Fe_6H_4^+				
Fe_6H_4^+ iso 1 u = 17		T_d	0.00	
Fe_6H_4^+ iso 2 u = 19		C_i	+0.08	
Fe_6H_4^+ iso 3 u = 17		C_{4v}	+0.36	
Fe_6H_4^+ iso 4 u = 19		C_2	+0.43	
Fe_6H_4^+ iso 2 u = 17		D_{2d}	+0.44	

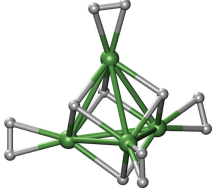
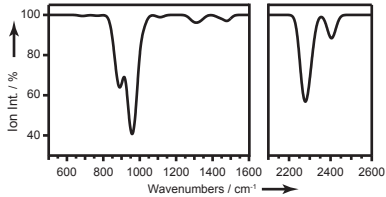
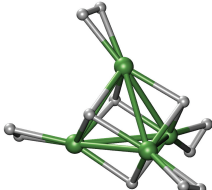
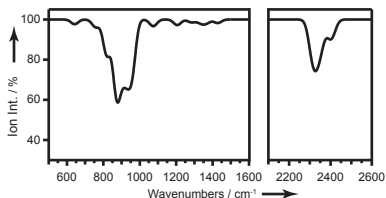
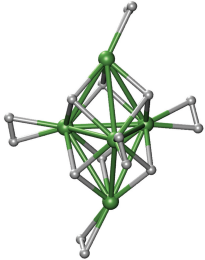
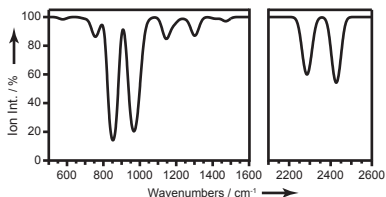
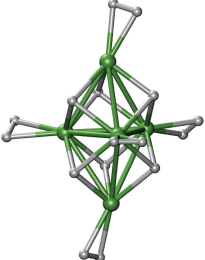
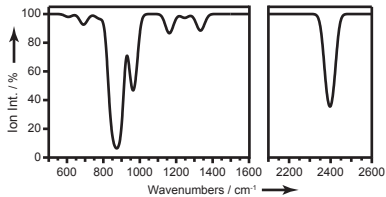
Table A.4. Optimized structures, energies and vibrational spectra of several isomers of Co_nH_m^+ with $n = 4, 5$ and 6.

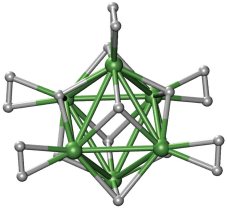
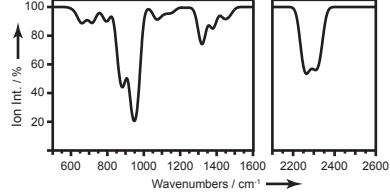
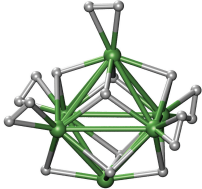
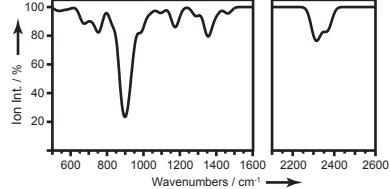
Species	Structure	Symmetry	ΔE (eV)	Spectrum
Co_4H_2^+ iso 1 $u = 9$		C_s	0.00	
Co_4H_2^+ iso 2 $u = 9$		C_1	+0.24	
Co_4H_2^+ iso 3 $u = 7$		C_1	+0.33	
Co_4H_2^+ iso 2 $u = 7$		C_1	+0.36	
Co_4H_2^+ iso 2 $u = 5$		C_1	+0.54	
Co_4H_2^+ iso 4 $u = 9$		C_1	+0.80	

Species	Structure	Symmetry	ΔE (eV)	Spectrum
Co_5H_6^+				
Co_5H_6^+ iso 1 $u = 10$		C_1	0.00	
Co_5H_6^+ iso 2 $u = 10$		C_1	+0.04	
Co_5H_6^+ iso 3 $u = 8$		C_{3v}	+0.13	
Co_5H_6^+ iso 4 $u = 10$		C_1	+0.19	
Co_5H_6^+ iso 5 $u = 10$		C_2	+0.23	
Co_5H_6^+ iso 6 $u = 12$		C_2	+0.26	

Species	Structure	Symmetry	ΔE (eV)	Spectrum
Co_5H_6^+ iso 3 u = 12		C_1	+0.31	
Co_6H_4^+				
Co_6H_4^+ iso 1 u = 13		C_{2h}	0.00	
Co_6H_4^+ iso 2 u = 13		C_1	+0.07	
Co_6H_4^+ iso 3 u = 11		C_1	+0.16	
Co_6H_4^+ iso 4 u = 11			+0.32	
Co_6H_4^+ iso 5 u = 11			+0.45	

Table A.5. Optimized structures, energies and vibrational spectra of several isomers of Ni_nH_m^+ with $n = 4, 5$ and 6.

Species	Structure	Symmetry	ΔE (eV)	Spectrum
$\text{Ni}_4\text{H}_{12}^+$ iso1 u = 1		C_1	0.00	
$\text{Ni}_4\text{H}_{12}^+$ iso1 u = 3		C_1	+0.37	
$\text{Ni}_5\text{H}_{16}^+$				
$\text{Ni}_5\text{H}_{16}^+$ iso1 u = 1		C_1	0.00	
$\text{Ni}_5\text{H}_{16}^+$ iso1 u = 3		C_1	+0.18	

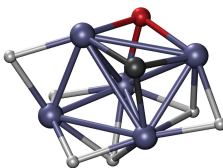
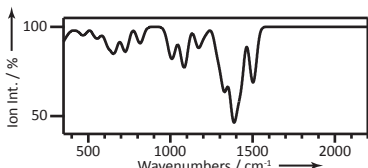
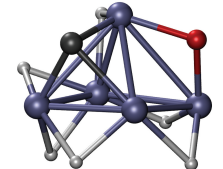
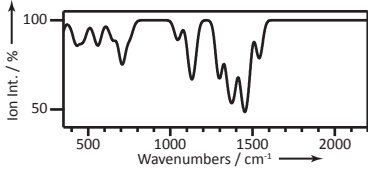
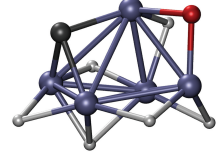
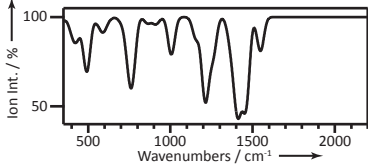
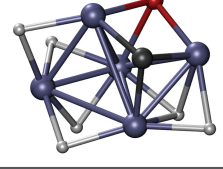
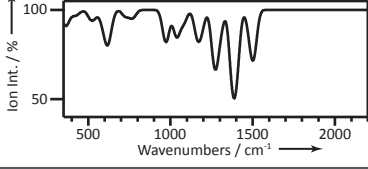
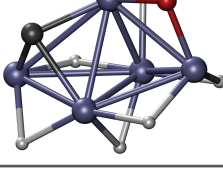
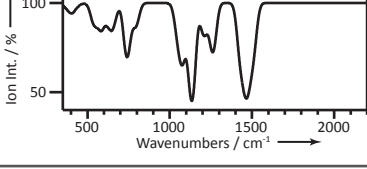
Species	Structure	Symmetry	ΔE (eV)	Spectrum
$\text{Ni}_6\text{H}_{18}^+$				
$\text{Ni}_6\text{H}_{18}^+$ iso1 u = 1		C_1	0.00	
$\text{Ni}_6\text{H}_{18}^+$ iso1 u = 3		C_1	+0.22	

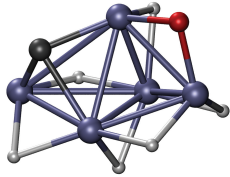
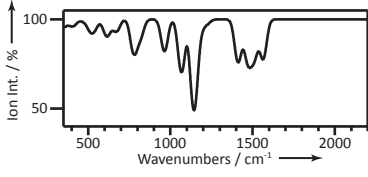
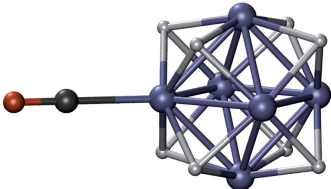
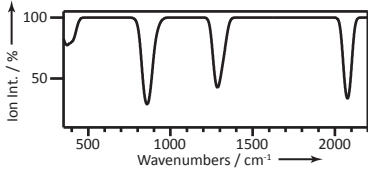
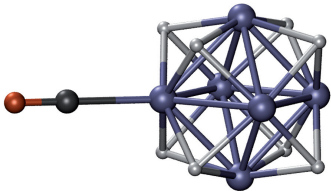
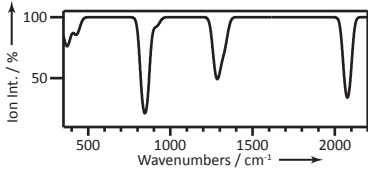
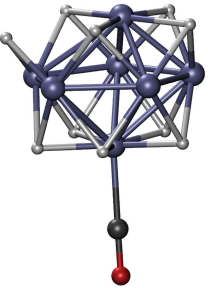
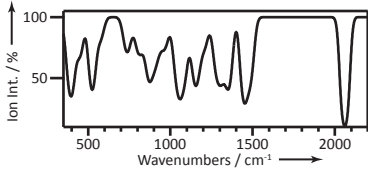
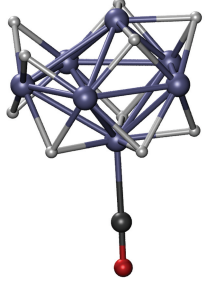
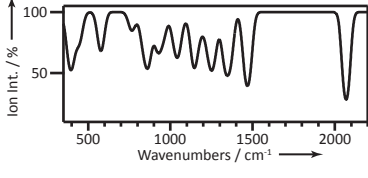
Appendix B

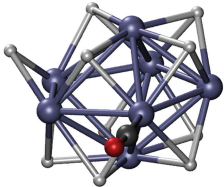
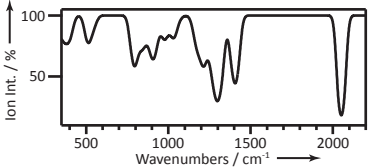
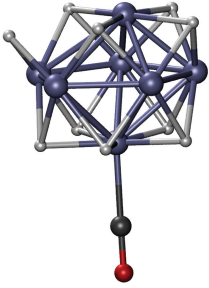
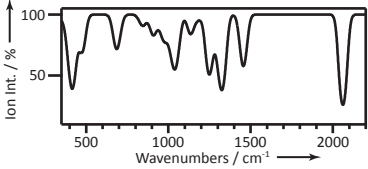
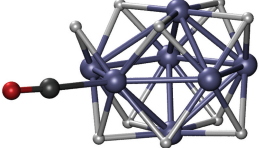
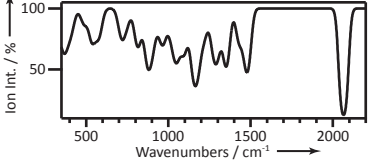
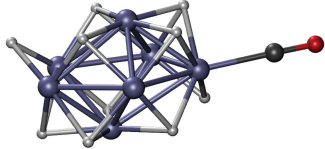
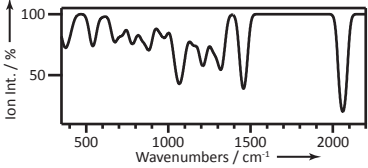
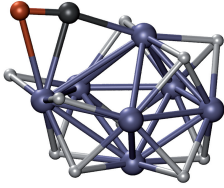
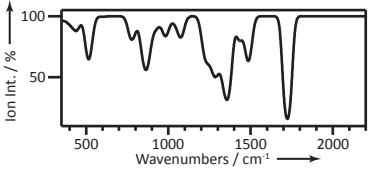
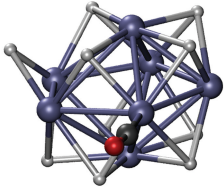
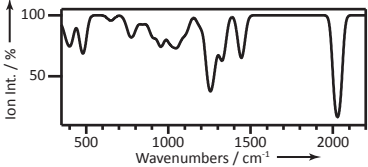
Optimized geometries, relative energies and vibrational spectra of $V_nH_mCO^+$ Complexes

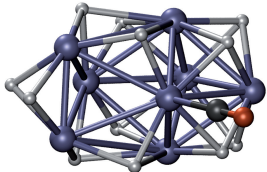
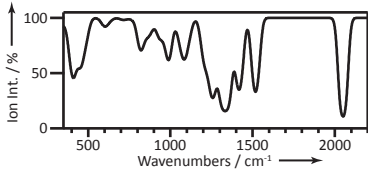
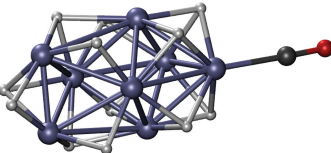
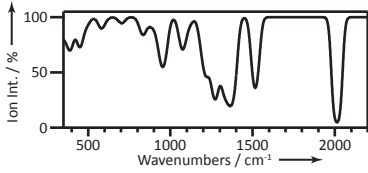
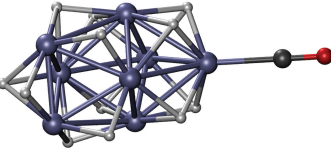
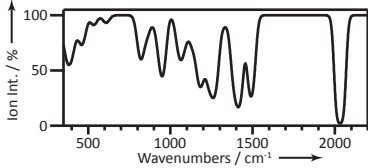
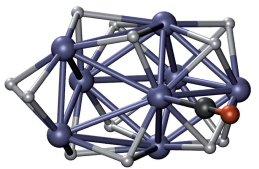
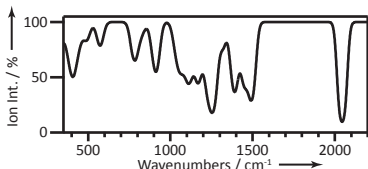
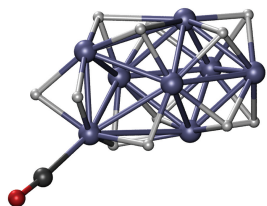
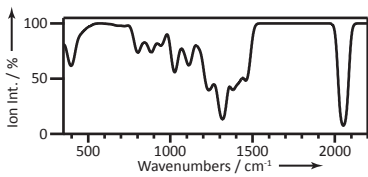
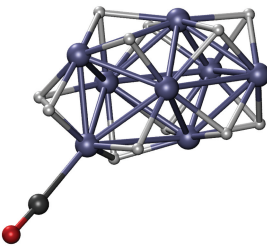
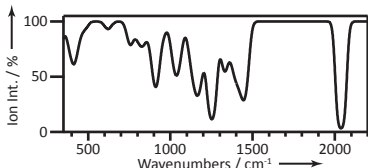
In table B1, the optimized geometries, relative energies, and simulated vibrational spectra of several isomers of $V_nH_mCO^+$ complexes are given. The calculations were performed using the BP86 parametrization of the exchange-correlation functional and a TZVP basis set for all atoms, as implemented in the TURBOMOLE package. The letter 'u' denotes the number of unpaired electrons. For details, see chapter 6.

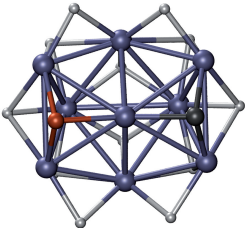
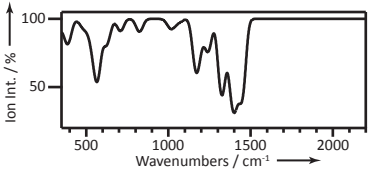
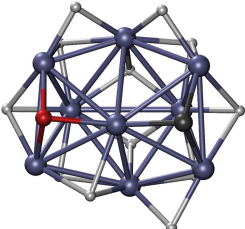
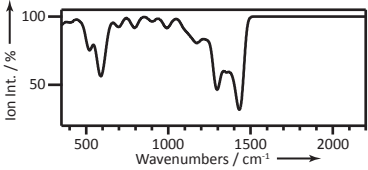
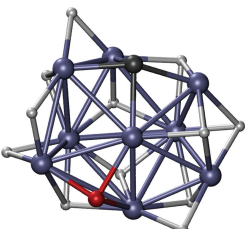
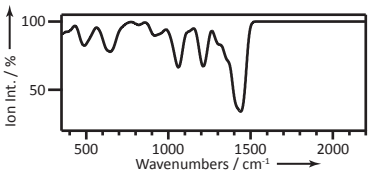
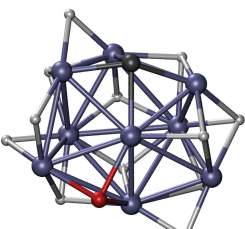
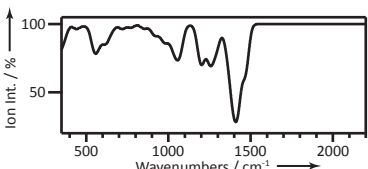
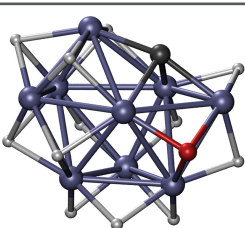
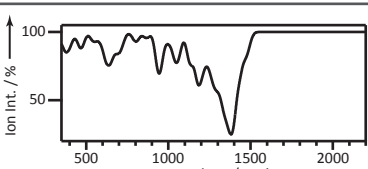
Table B.1. Optimized structures, energies and vibrational spectra of several isomers of $V_nH_mCO^+$ with $n = 5-9$.

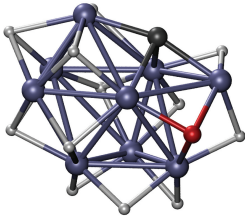
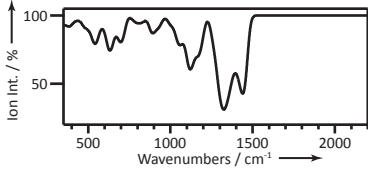
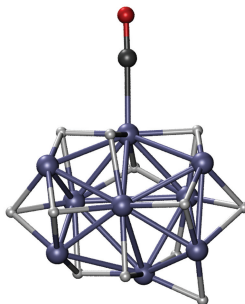
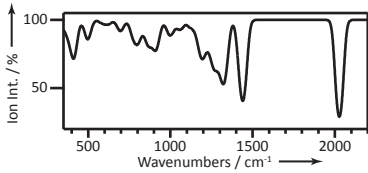
Species	Structure	ΔE (eV)	Spectrum
$V_5H_6CO^+$ iso 1 u 2		0.00	
$V_5H_6CO^+$ iso 2 u 0		+0.05	
$V_5H_6CO^+$ iso 3 u 0		+0.12	
$V_5H_6CO^+$ iso 4 u 0		+0.14	
$V_5H_6CO^+$ iso 5 u 2		+0.25	

Species	Structure	ΔE (eV)	Spectrum
$V_5H_6CO^+$ iso 5 u 0		+0.35	
$V_6H_8CO^+$			
$V_6H_8CO^+$ u 1		0.00	
$V_6H_8CO^+$ u 3		+0.11	
$V_7H_{10}CO^+$			
$V_7H_{10}CO^+$ iso 1 u 2		0.00	
$V_7H_{10}CO^+$ iso 2 u 2		+0.01	

Species	Structure	ΔE (eV)	Spectrum
$V_7H_{10}CO^+$ iso 3 u 2		+0.01	
$V_7H_{10}CO^+$ iso 4 u 0		+0.10	
$V_7H_{10}CO^+$ iso 5 u 2		+0.13	
$V_7H_{10}CO^+$ iso 6 u 2		+0.14	
$V_7H_{10}CO^+$ iso 7 u 0		+0.21	
$V_7H_{10}CO^+$ iso 3 u 0		+0.23	

Species	Structure	ΔE (eV)	Spectrum
$V_8H_{12}CO^+$			
$V_8H_{12}CO^+$ iso 1 u 1		0.00	
$V_8H_{12}CO^+$ iso 2 u 1		+0.09	
$V_8H_{12}CO^+$ iso 3 u 3		+0.11	
$V_8H_{12}CO^+$ iso 1 u 3		+0.17	
$V_8H_{12}CO^+$ iso 4 u 1		+0.24	
$V_8H_{12}CO^+$ iso 6 u 3		+0.32	

Species	Structure	ΔE (eV)	Spectrum
$V_9H_{12}CO^+$			
$V_9H_{12}CO^+$ iso 1 u 0		0.00	
$V_9H_{12}CO^+$ iso 2 u 2		+0.27	
$V_9H_{12}CO^+$ iso 3 u 0		+0.29	
$V_9H_{12}CO^+$ iso 3 u 2		+0.36	
$V_9H_{12}CO^+$ iso 4 u 0		+0.40	

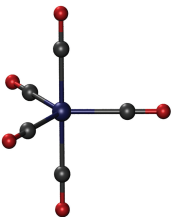
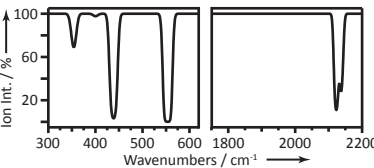
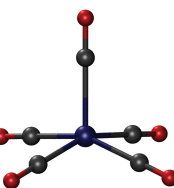
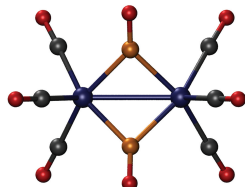
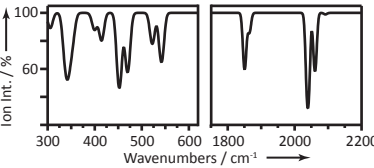
Species	Structure	ΔE (eV)	Spectrum
$V_9H_{12}CO^+$ iso 4 u 2		+0.55	
$V_9H_{12}CO^+$ iso 5 u 0		+1.74	

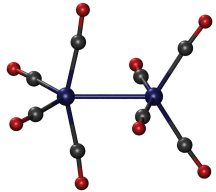
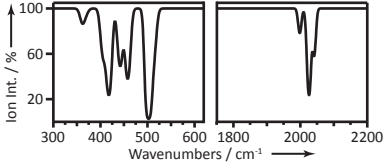
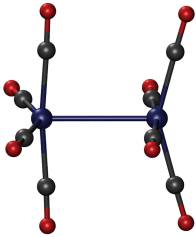
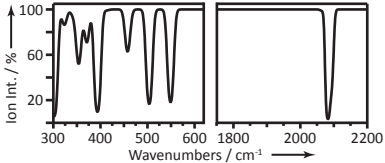
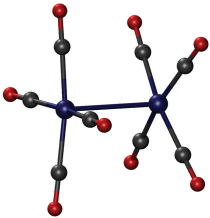
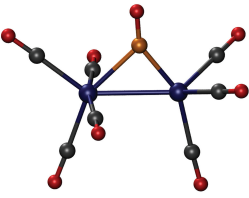
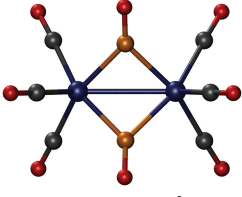
Appendix C

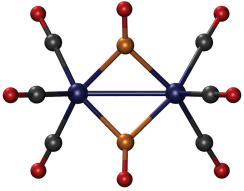
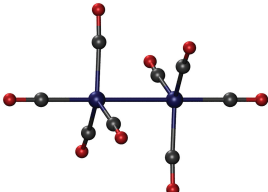
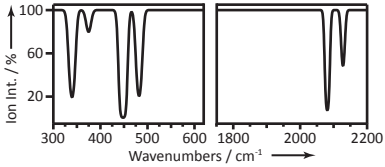
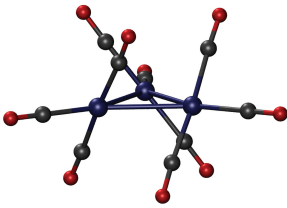
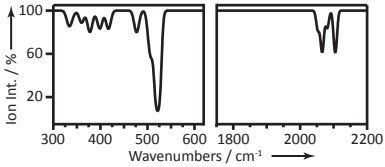
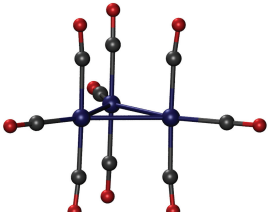
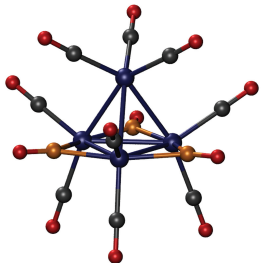
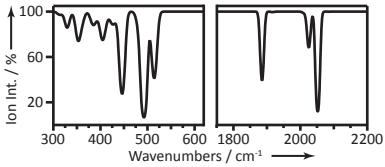
Optimized geometries, relative energies and vibrational spectra of late transition metal (Rh, Co and Ni) carbonyl complexes.

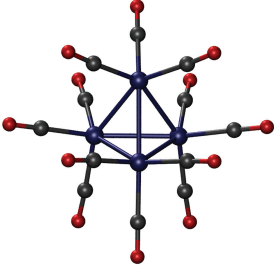
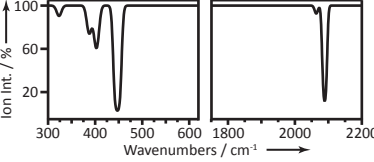
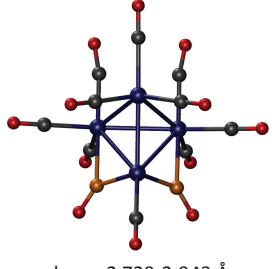
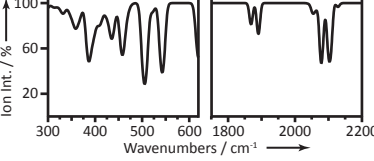
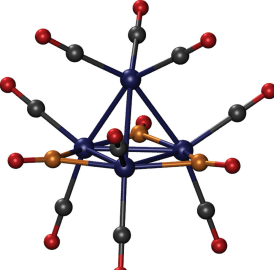
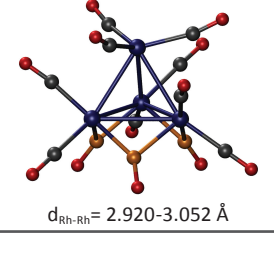
The tables C1 to C3, give the optimized geometries, relative energies, and simulated vibrational spectra of several isomers of $\text{Rh}_n(\text{CO})_m^+$, $\text{Co}_n(\text{CO})_m^+$, and $\text{Ni}_n(\text{CO})_m^+$, respectively. The calculations were performed using the B3LYP parametrization of the exchange-correlation functional and a TZVP basis set for all atoms as implemented in the TURBOMOLE package. For Rh an effective core potential was used with a valence shell that consisted of the 4s, 4p, 4d, and 5s electrons. For details, see chapters 7 and 8.

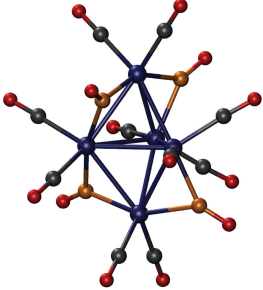
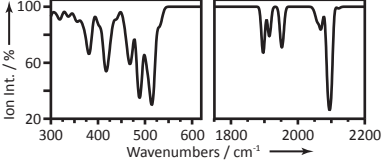
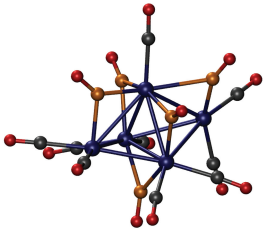
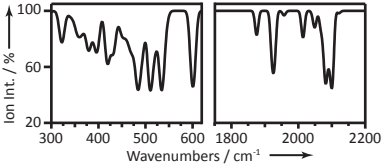
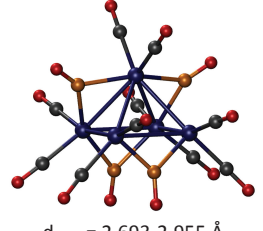
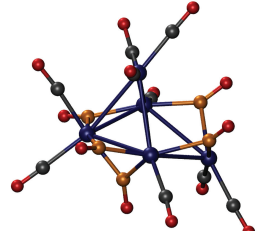
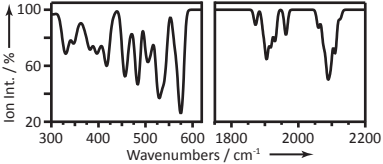
Table C.1. Structures, relative energies, and simulated vibrational spectra of $\text{Rh}_n(\text{CO})_m^{+/0}$ isomers, with $n = 1-6$

Species	Structure	Symmetry	ΔE (eV)	Spectrum
$\text{Rh}(\text{CO})_5^+$ iso 1		D_{3h}	0.00	
$\text{Rh}(\text{CO})_5^+$ iso 2		C_{4v}	+0.01	Not Stable
$\text{Rh}_2(\text{CO})_8$				
$\text{Rh}_2(\text{CO})_8$ iso 1	 $d_{\text{Rh-Rh}} = 2.826 \text{ \AA}$	C_{2v}	0.00	

Species	Structure	Symmetry	ΔE (eV)	Spectrum
Rh ₂ (CO) ₈ iso 2	 $d_{\text{Rh-Rh}} = 2.901 \text{ \AA}$	D_{2d}	+0.09	
Rh₂(CO)₈⁺				
Rh ₂ (CO) ₈ ⁺ iso 1	 $d_{\text{Rh-Rh}} = 3.188 \text{ \AA}$	D_{2d}	0.00	
Rh ₂ (CO) ₈ ⁺ iso 2	 $d_{\text{Rh-Rh}} = 3.218 \text{ \AA}$	D_{4d}	+0.04	Not Stable
Rh ₂ (CO) ₈ ⁺ iso 3	 $d_{\text{Rh-Rh}} = 2.829 \text{ \AA}$	C_s	+0.20	Not Stable
Rh ₂ (CO) ₈ ⁺ iso 4	 $d_{\text{Rh-Rh}} = 2.733 \text{ \AA}$	C_{2v}	+0.31	Not Stable

Species	Structure	Symmetry	ΔE (eV)	Spectrum
$\text{Rh}_2(\text{CO})_8^+$ Cation struc of the neutral.	 $d_{\text{Rh-Rh}} = 2.826 \text{ \AA}$	C_{2v}	+0.65	Not Stable
$\text{Rh}_2(\text{CO})_8^+$ iso 5	 $d_{\text{Rh-Rh}} = 2.786 \text{ \AA}$	D_{3d}	+1.62	
$\text{Rh}_3(\text{CO})_9^+$				
$\text{Rh}_3(\text{CO})_9^+$ iso 1	 $d_{\text{Rh-Rh}} = 2.868 \text{ \AA}$	D_3	0.00	
$\text{Rh}_3(\text{CO})_9^+$ iso 2	 $d_{\text{Rh-Rh}} = 2.971 \text{ \AA}$	D_{3h}	+0.58	Not Stable
$\text{Rh}_4(\text{CO})_{12}$				
$\text{Rh}_4(\text{CO})_{12}$	 $d_{\text{Rh-Rh}} = 2.740\text{-}2.810 \text{ \AA}$	C_{3v}	0.00	

Species	Structure	Symmetry	ΔE (eV)	Spectrum
$\text{Rh}_4(\text{CO})_{12}^+$				
$\text{Rh}_4(\text{CO})_{12}^+$ iso 1	 <p>$d_{\text{Rh-Rh}} = 2.710 \text{ \AA}$</p>	T_d	0.00	
$\text{Rh}_4(\text{CO})_{12}^+$ iso 2	 <p>$d_{\text{Rh-Rh}} = 2.729\text{-}2.943 \text{ \AA}$</p>	C_1	+0.02	
$\text{Rh}_4(\text{CO})_{12}$ cation in structure of the neutral	 <p>$d_{\text{Rh-Rh}} = 2.740\text{-}2.810 \text{ \AA}$</p>	C_{3v}	+0.11	Not Stable
$\text{Rh}_4(\text{CO})_{12}^+$ iso 3	 <p>$d_{\text{Rh-Rh}} = 2.920\text{-}3.052 \text{ \AA}$</p>	C_3	+0.14	Not Stable

Species	Structure	Symmetry	ΔE (eV)	Spectrum
$\text{Rh}_5(\text{CO})_{14}^+$				
$\text{Rh}_5(\text{CO})_{14}^+$ iso 1	 $d_{\text{Rh-Rh}} = 2.729\text{-}2.898 \text{ \AA}$	C_1	0.00	
$\text{Rh}_5(\text{CO})_{14}^+$ iso 2	 $d_{\text{Rh-Rh}} = 2.770\text{-}2.995 \text{ \AA}$	C_1	+0.39	
$\text{Rh}_5(\text{CO})_{14}^+$ iso 3	 $d_{\text{Rh-Rh}} = 2.693\text{-}2.955 \text{ \AA}$	C_s	+0.44	Not Stable
$\text{Rh}_5(\text{CO})_{14}^+$ iso 4	 $d_{\text{Rh-Rh}} = 2.721\text{-}3.144 \text{ \AA}$	C_1	+0.74	

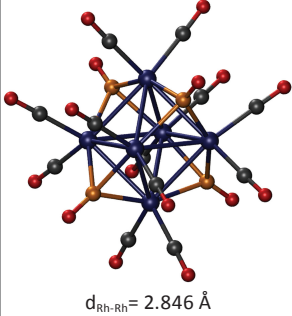
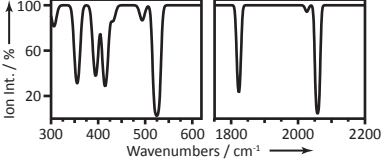
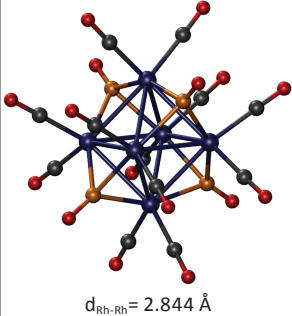
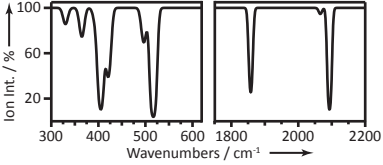
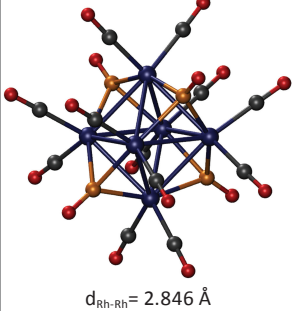
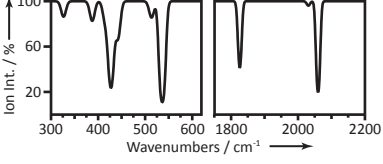
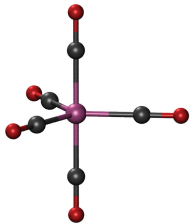
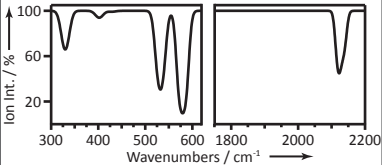
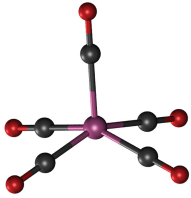
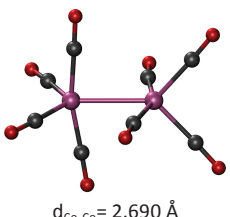
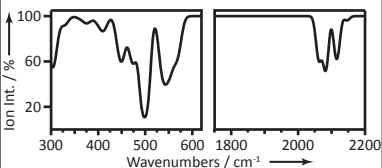
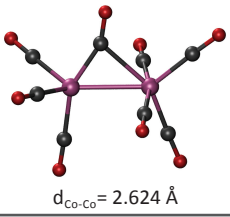
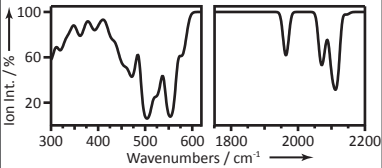
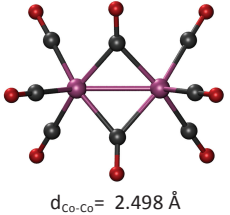
Species	Structure	Symmetry	ΔE (eV)	Spectrum
Rh₆(CO)₁₆				
Rh ₆ (CO) ₁₆	 <p>$d_{\text{Rh-Rh}} = 2.846 \text{ \AA}$</p>	T_d		
Rh₆(CO)₁₆⁺				
Rh ₆ (CO) ₁₆ ⁺ iso 1	 <p>$d_{\text{Rh-Rh}} = 2.844 \text{ \AA}$</p>	T_d	0.00	
Rh ₆ (CO) ₁₆ ⁺ Cation in structure of the neutral	 <p>$d_{\text{Rh-Rh}} = 2.846 \text{ \AA}$</p>	T_d	+0.10	

Table C.2. Structures, relative energies, and simulated vibrational spectra of $\text{Co}_n(\text{CO})_m^+$ isomers, with $n = 1-3$

Species	Structure	Symmetry	ΔE (eV)	Spectrum
$\text{Co}(\text{CO})_5^+$ iso 1		D_{3h}	0.00	
$\text{Co}(\text{CO})_5^+$ iso 2		C_{4v}	+0.08	Not Stable
$\text{Co}_2(\text{CO})_8^+$				
$\text{Co}_2(\text{CO})_8^+$ iso 1	 $d_{\text{Co-Co}} = 2.690 \text{ \AA}$	C_1	0.00	
$\text{Co}_2(\text{CO})_8^+$ iso 2	 $d_{\text{Co-Co}} = 2.624 \text{ \AA}$	C_1	+0.01	
$\text{Co}_2(\text{CO})_8^+$ iso 3	 $d_{\text{Co-Co}} = 2.498 \text{ \AA}$	C_{2v}	+0.36	Not Stable

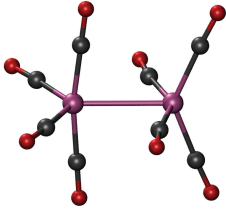
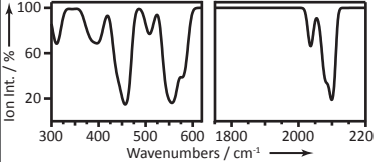
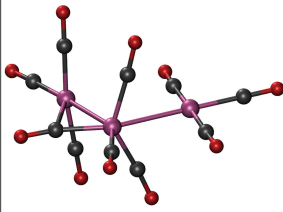
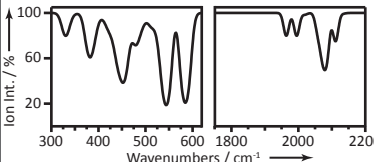
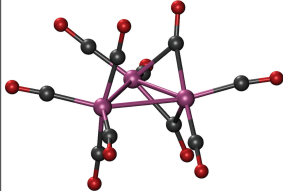
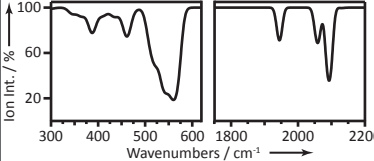
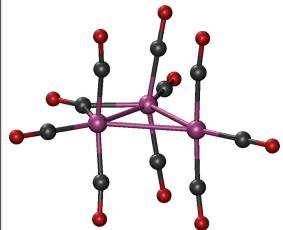
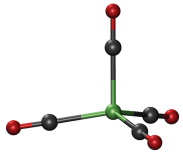
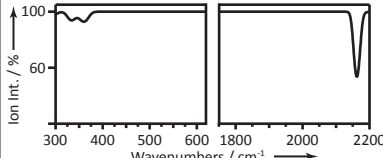
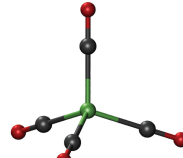
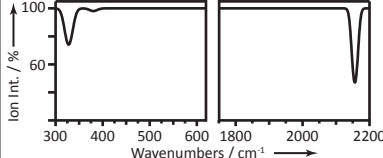
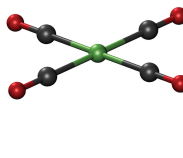
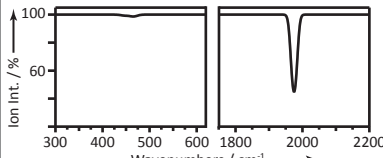
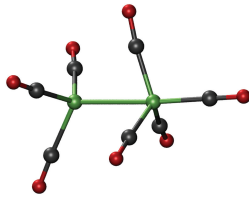
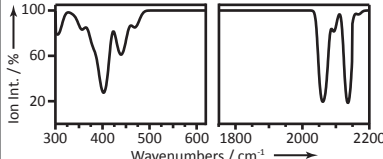
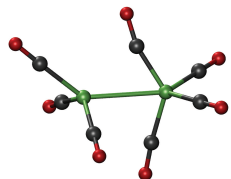
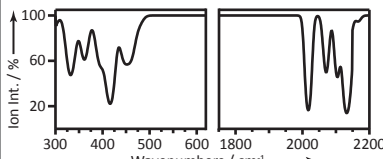
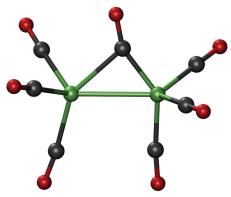
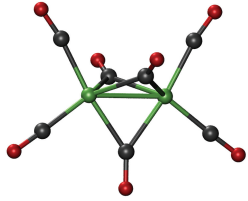
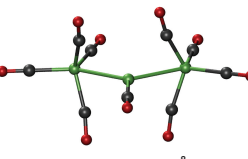
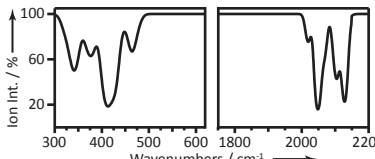
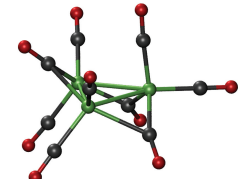
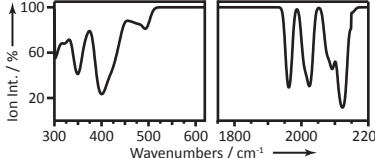
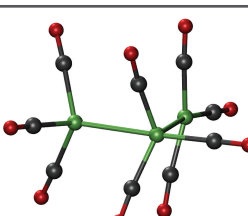
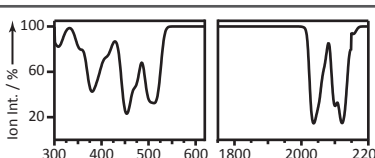
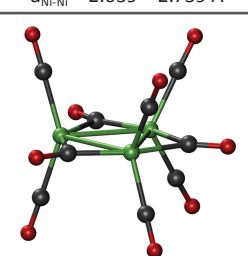
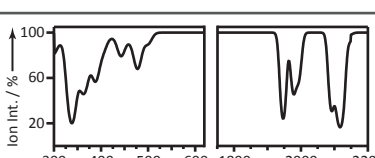
Species	Structure	Symmetry	ΔE (eV)	Spectrum
$\text{Co}_2(\text{CO})_8^+$ iso 4	 <p>$d_{\text{Co-Co}} = 2.829 \text{ \AA}$</p>	C_1	+0.50	
$\text{Co}_3(\text{CO})_{10}^+$				
$\text{Co}_3(\text{CO})_{10}^+$ iso 1	 <p>$d_{\text{Co-Co}} = 2.621\text{-}2.738 \text{ \AA}$</p>	C_1	0.00	
$\text{Co}_3(\text{CO})_{10}^+$ iso 2	 <p>$d_{\text{Co-Co}} = 2.453\text{-}2.789 \text{ \AA}$</p>	C_1	+0.01	
$\text{Co}_3(\text{CO})_{10}^+$ iso 3	 <p>$d_{\text{Co-Co}} = 2.577\text{-}3.096 \text{ \AA}$</p>	C_{2v}	+0.63	Not Stable

Table C.3. Structures, relative energies, and simulated vibrational spectra of $\text{Ni}_n(\text{CO})_m^+$ isomers, with $n = 1-3$

Species	Structure	Symmetry	ΔE (eV)	Spectrum
$\text{Ni}(\text{CO})_4^+$ iso 1		C_{3v}	0.00	
$\text{Ni}(\text{CO})_4^+$ iso 2		T_d	+1.40	
$\text{Ni}(\text{CO})_4^+$ iso 3		D_{4h}	+3.04	
$\text{Ni}_2(\text{CO})_7^+$				
$\text{Ni}_2(\text{CO})_7^+$ iso 1	 $d_{\text{Ni-Ni}} = 2.693 \text{ \AA}$	C_1	0.00	
$\text{Ni}_2(\text{CO})_7^+$ iso 2	 $d_{\text{Ni-Ni}} = 2.776 \text{ \AA}$	C_1	+0.01	
$\text{Ni}_2(\text{CO})_7^+$ iso 3	 $d_{\text{Ni-Ni}} = 2.663 \text{ \AA}$	C_1	+0.11	Not Stable

Species	Structure	Symmetry	ΔE (eV)	Spectrum
$\text{Ni}_2(\text{CO})_7^+$ iso 4	 $d_{\text{Ni-Ni}} = 2.494 \text{ \AA}$	C_{2v}	+1.38	Not Stable
$\text{Ni}_3(\text{CO})_9^+$				
$\text{Ni}_3(\text{CO})_9^+$ iso 1	 $d_{\text{Ni-Ni}} = 2.538 \text{ \AA}$	C_1	0.00	
$\text{Ni}_3(\text{CO})_9^+$ iso 2	 $d_{\text{Ni-Ni}} = 2.544 - 2.741 \text{ \AA}$	C_1	+0.33	
$\text{Ni}_3(\text{CO})_9^+$ iso 3	 $d_{\text{Ni-Ni}} = 2.639 - 2.739 \text{ \AA}$	C_1	+0.67	
$\text{Ni}_3(\text{CO})_9^+$ iso 4	 $d_{\text{Ni-Ni}} = 2.725 - 2.838 \text{ \AA}$	C_1	+0.76	

List of Publications

This thesis is based in part on the following publications:

- I. Swart, F.M.F. de Groot, B.M. Weckhuysen, D.M. Rayner, G. Meijer, and A. Fielicke, *Cationic Late Transition Metal Carbonyl Clusters in the Gas-phase, insights from Vibrational Spectroscopy and Density Functional Theory*, to be submitted.
- I. Swart, P. Gruene, A. Fielicke, G. Meijer, B.M. Weckhuysen, and F.M.F. de Groot, *Molecular Adsorption of H₂ on Small Cationic Nickel Clusters*, Phys. Chem. Chem. Phys. in press (2008)
- I. Swart, F.M.F. de Groot, B.M. Weckhuysen, D.M. Rayner, G. Meijer, and A. Fielicke, *The Effect of Charge on the CO Binding in Rhodium Carbonyls: from Bridging to Terminal CO*. J. Am. Chem. Soc. (Communication), **130**, 2126 (2008)
- I. Swart, F.M.F. de Groot, B.M. Weckhuysen, P. Gruene, G. Meijer, and A. Fielicke, *H₂ Adsorption on 3d Transition Metal Clusters: a Combined Infrared Spectroscopy and Density Functional Study*, J. Phys. Chem. A, **112**, 1139 (2008)
- I. Swart, A. Fielicke, D.M. Rayner, G. Meijer, B.M. Weckhuysen, and F.M.F. de Groot, *Controlling the Bonding of CO on Cobalt Clusters by Coadsorption of H₂*, Angew. Chem. Int. Ed., **46**, 5317 (2007)
- I. Swart, A. Fielicke, B. Redlich, G. Meijer, B.M. Weckhuysen and F.M.F. de Groot, *Hydrogen-Induced Transition from Dissociative to Molecular Chemisorption of CO on Vanadium Clusters*, J. Am. Chem. Soc., **129**, 2516 (2007)

Other publications by the author:

- E. de Smit, I. Swart, J.F. Creemer, G.H. Hoveling, M.K. Gilles, T. Tyliczszak, C. Morin, P.J. Kooyman, H.W. Zandbergen, B.M. Weckhuysen and F.M.F. de Groot, *Nanoscale Chemical Imaging of a Working Catalyst by Scanning Transmission X-Ray Microscopy*, submitted.
- E. Stavitski, M.F. Kox, I. Swart, F.M.F. de Groot, and B.M. Weckhuysen, *In-situ Synchrotron-based IR Microspectroscopy to study Catalytic Reactions in Zeolite Crystals*, Angew. Chem. Int. Ed., **47**, 3543 (2008)
- J.M. Szarko, J.K. Song, C.W. Blackledge, I. Swart, S.R. Leone, S. Li, and Y. Zhao, *Optical Injection Probing of Single ZnO Tetrapod Lasers*, Chem. Phys. Lett., **404**, 171 (2005)

-
- M. Di Vece, I. Swart, and J.J. Kelly, *Electrochemical Kinetics of Hydrogen Intercalation in Gadolinium Switchable Mirrors*, *J. Appl. Phys.*, **94**, 4659 (2003)
 - S.F. Wuister, I. Swart, F. van Driel, S.G. Hickey, and C. de Mello Donega, *Highly Luminescent Water-Soluble CdTe Quantum Dots*, *Nanoletters*, **3**, 503 (2003)

Acknowledgements

Although this Ph.D. thesis has only one author, it would not have been possible to complete this thesis without the help of many people. Here, I would like to acknowledge those people.

First of all, I would like to thank my two advisors: Frank de Groot and Bert Weckhuysen. Four years ago, the field of cluster science was as new for you as it was for me. Nevertheless, you have given me (and perhaps I took) the freedom to pursue my own research interests. Frank, you were always enthusiastic about the research and convinced of my abilities. Your broad scientific interests have been a great stimulus. Bert, you provided a framework of thinking. Your door was always open and you have encouraged me and challenged me. It has been a pleasure to work with you both.

Collaborations are often fruitful, and in my experience always pleasurable. During my Ph.D. research, I had the privilege to collaborate with many different people. First of all, I would like to thank André Fielicke, Philipp Grüne, Gerard Meijer, and Karsten Reuter of the Fritz-Haber-Institut der Max-Planck-Gesellschaft in Berlin, Germany. André, thank you for the invaluable help with the experimental work and the critical reading of my manuscripts. If I had yet another question, you were always there to answer it. Your contributions are also reflected by the fact that you have become my co-advisor. Philipp, without your help, chapters 3 and 4 would have looked considerably different. Good luck with finishing your own Ph.D. thesis! Gerard, thank you for your contributions to the articles and the opportunity to visit the institute in Berlin. Karsten, I would like to thank you for sharing your time and knowledge of DFT calculations with me. Although the theoretical analysis of the effects associated with the co-adsorption of H₂ and CO on cobalt clusters remains an unfinished issue, I have learned a great deal about DFT calculations during my visit to your group.

Next, I would like to thank David Rayner of the Steacie Institute for Molecular Sciences, in Ottawa, Canada. Your contributions to the interpretation of the cobalt/H₂/CO and metal-carbonyl data have been a great help.

The experiments described in this Ph.D. thesis would not have been possible without the free-electron laser FELIX. My gratitude goes out to the FELIX-staff, and in particular to Britta Redlich, for the excellent conditions under which the experiments could be performed.

I also owe gratitude to dr. Joop van Lenthe for the insightful discussions on quantum mechanics and his help with the computer problems.

Dennis van Dorp has been a great help in preparing the isotopically enriched nickel target rod, which was instrumental for the hydrogen adsorption experiments.

I would also like to thank Lars Pettersson of Stockholm University, Sweden, for his help with the calculations that led to the charge-density-difference plots shown in chapter 6, 7, and 8.

At the beginning of my Ph.D. research, I had the opportunity to visit the group of Delphine Cabaret at the Université Pierre et Marie Curie, in Paris, France. Delphine, thank you for introducing me to world of DFT.

During the last four years, I was in the fortunate position to also be involved in research, other than what is described in this Ph.D. thesis. One of those research projects dealt with the characterization of catalytic materials under reaction conditions using X-ray microscopy. This was a joint project with Emiel de Smit. Emiel, let's hope our paper gets published in the journal we are aiming for! I am going to miss our trips to California.

In addition, I would like to thank Marianne Kox and Eli Stavitski for getting me involved in their research. My 'excursion' into the field of organic molecules in zeolites was most entertaining. It has been great to work with you!

My (former) roommates Daphne Keller, Arjan Plomp, and Mariska Wolters have made everyday life in room N209 enjoyable. Thank you for your sincere interest in my research and the discussions that we had, scientific and otherwise. I sincerely hope that we keep in touch!

A special word of thanks for my former colleagues Rudy Wagemans and Joost van Lingen for their help with setting up the calculations and the discussions about quantum chemistry.

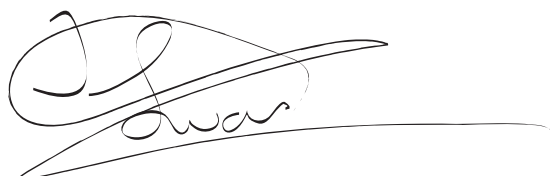
The secretaries of the Inorganic Chemistry and Catalysis group, Dymph Serrée and Monique Lamers, have been a great help with all administrative issues.

Of course, I am grateful to all the past and present members of the Inorganic Chemistry and Catalysis group for the pleasant working atmosphere and the good times during drinks, coffee breaks, Italiano sandwiches, barbecues, and group outings.

Finally, I would like to acknowledge my friends and family for their contributions to all the aspects of life besides science. Anna, Annemieke, Arjan, Ashwin, Claudia, Giovanni, Marieke, Nathaniel, Onno, and Quirine, thank you for all the nice things we have done and experienced together over the last couple of years. Your friendship means a great deal to me.

My family, Koos, Antje, Justin and Kim, Detmer, Anja, and Frans have always had confidence in me and have unconditionally supported me. Without you, it would not have been possible to complete this thesis.

The last words are for you, Charlotte. It is finished! Thank you for all your love and support. Together with you, I am ready for the future.

A handwritten signature in black ink, appearing to read 'Ingmar Swart', with a long horizontal flourish extending to the right.

Ingmar Swart, August 2008

About the author

Ingmar Swart was born in Opsterland, the Netherlands, on December 5th, 1980. In 1999 he obtained his Gymnasium diploma at the Comenius College in Hilversum. That same year, he started with undergraduate studies in chemistry and physics at Utrecht University. The Master of Science degree was received in June 2004 (cum laude). Several research projects were carried out in the 'Condensed Matter and Interfaces' group, under supervision of prof. dr. J.J. Kelly and prof. dr. A. Meijerink. From January 2004 until June 2004 he worked in the group of prof. dr. S.R. Leone at the University of California at Berkeley and the Lawrence Berkeley National Laboratory, California, USA. Besides his chemistry studies, he also completed several courses in business administration at the Erasmus University, Rotterdam.

In September 2004, he joined the Inorganic Chemistry and Catalysis group at Utrecht University as a Ph.D. student under supervision of dr. F.M.F. de Groot and prof. dr. ir. B.M. Weckhuysen. The results of this research have been published in scientific journals and are described in this Ph.D. thesis. During his studies, Ingmar was a teaching assistant for a quantum chemistry course for freshman students, as well as for several laboratory courses. He was a member (2004-2007) and chairman (2006-2007) of the Ph.D. committee of the Debye Institute for NanoMaterials Science. As such, he was a co-organizer of the Debye winterschool 2006 and the DOI!-days 2007 (two-day symposium for all Ph.D. students of the institute).

As of September 2008, he is a post-doctoral research fellow in the group of prof. dr. D.A.M. Vanmaekelbergh at Utrecht University.

